TECHNISCHE
UNIVERSITÄT
MÜNCHEN

WALTHER-
MEISSNER-
INSTITUT

BAYERISCHE
AKADEMIE DER
WISSENSCHAFTEN

Tuning the Amplitude of the Spin Hall Magnetoresistance

Master's thesis
Monika Scheufele

Supervisor: Prof. Dr. Rudolf Gross
Advisor: Dr. Stephan Geprägs

Garching – December 1, 2021

Contents

1. Motivation

Given the approaching end of Moore's Law [1], new technologies are needed to ensure adequate data processing and storage in future. The demand for higher data storage capacities at smaller and smaller device dimensions has the consequence of increasing energy consumpion due to Joule heating induced by charge transport [2, 3]. This contributes to the emission of greenhouse gases and thus to global warming and the climate change challenge faced by humanity [4]. Next to (electron) charge-current based electronics, the field of spintronics takes advantage of the spin of electrons by enabling device concepts being based on spin currents. Pure spin currents are the flow of angular momentum without a net charge current [5]. Since spin currents can also appear in insulators, heat losses could be reduced significantly. Additionally, spintronics utilizing antiferromagnetic insulators reveal fast switching dynamics and robustness against external, disturbing magnetic fields due to their vanishing net magnetization [6, 7]. However, this makes the control and readout of magnetization in antiferromagnets challenging as well. The spin Hall magnetoresistance effect (SMR) represents a possibility to overcome this challenge.

The spin Hall magnetoresistance is based on spin currents in a heavy metal, which are generated and detected by the combined action of spin Hall and inverse spin Hall effects, manipulated by the magnetization of an adjacent magnetically ordered insulator by spin transfer torque effects. This results in a dependence of the resistivity in the heavy metal on the direction of the sublattice magnetizations in the magnetic ordered insulator [8]. Since the SMR is sensitive on the direction of the sublattice magnetizations and not on that of the net magnetization, the resistivity of a bilayer sample measured in a magnetic field $\mathbf{H}$ rotated in the layer plane exhibits a phase shift of $90°$ for antiferromagnetic insulators compared to ferrimagnetic insulators (FMI) [9]. This is due to the sublattice magnetizations following the magnetic field rotation with the sublattices being collinear to $\mathbf{H}$ in ferrimagnetic insulators and being perpendicular to $\mathbf{H}$ in antiferromagnetic insulators.

Although the phase of the SMR has been intensively explored in recent years, its amplitude and the mechanisms that affect it are not well understood. For the prototype heterostructure $Y_3Fe_5O_{12}$ (YIG)/Pt a ferrimagnetic SMR amplitude of 1.3×10^{-3} is measured [10]. However, Fischer *et al.* reported a large antiferromagnetic SMR amplitude of 2.5×10^{-3} in α-Fe_2O_3/Pt bilayers [11, 12]. The origin of the large SMR amplitude in α-Fe_2O_3/Pt heterostructures is still under debate and thus this thesis aims to provide clues to clarify this question. From a theoretical point of view, the SMR amplitude depends on the density n_s of magnetic moments at the magnetic ordered insulator/ heavy metal interface [13, 14]. By doping the magnetic ordered insulator, n_s can be modified and therefore also the SMR amplitude. Within this thesis, special emphasis is placed on bilayers composed of the heavy metal platinum (Pt) and the antiferromagnetic insulator α-Fe_2O_3 (hematite) as well as the ferrimagnetic insulator γ-Fe_2O_3 (maghemite), whose SMR amplitudes are tuned by doping the corresponding magnetic ordered insulator at different doping concentrations and with various types of dopants.

In contrast to the antiferromagnetic, hexagonal insulator α-Fe_2O_3 (hematite) and the spinel, ferrimagnetic insulator γ-Fe_2O_3 (maghemite) the iron oxide Fe_3O_4 (magnetite) is a poor conductor at room temperature exhibiting a metal to insulator transition at low temperature [12, 15–20]. To investigate the effect of this change in resistivity on the SMR amplitude, Fe_3O_4/Pt bilayers are investigated as well. Therefore, the present work provides an overview of thin films as well as bilayers of the most common iron oxides α-Fe_2O_3, γ-Fe_2O_3 and Fe_3O_4 regarding their structural, magnetic and magnetotransport properties also covered with Pt electrodes.

This thesis is structured as follows: First, the theoretical concepts are explained that are essential for understanding the spin Hall magnetoresistance in α-Fe_2O_3/Pt and γ-Fe_2O_3/Pt heterostructures (Chapter 2). The same chapter includes an overview of the physical properties of iron oxides, in particular of α-Fe_2O_3 (hematite), γ-Fe_2O_3 (maghemite) and Fe_3O_4 (magnetite). Additionally, the effect of doping of α-Fe_2O_3 and γ-Fe_2O_3 thin films on the crystallographic and magnetic properties is discussed. Subsequently, the experimental results are extensively investigated with focus on the SMR effect. Thereby, in Chapter 3, undoped α-Fe_2O_3, γ-Fe_2O_3 and Fe_3O_4 thin films as well as bilayers with Pt electrodes on top are characterized in terms of their structural, magnetic and magnetotransport properties. In Chapter 4 doped α-Fe_2O_3/Pt and γ-Fe_2O_3/Pt heterostructures are investigated with respect to their physical properties. Last but not least, Chapter 5 provides a summary of the key findings of this thesis together with an outlook on possible continuing experiments to get more insight into the mechanisms affecting the SMR amplitude.

2. Theoretical background

In the following, the basic theoretical concepts are discussed, on which the experimental results of this thesis are based on. Therefore, a brief explanation of spin currents and the spin Hall effect (SHE) and inverse spin Hall effect (ISHE) is given in Chapters 2.1 and 2.2. Subsequently, the spin Hall magnetoresistance (SMR) effect in heterostructures consisting of a magnetic ordered insulator (MOI) and a heavy metal (HM) is extensively described and explained in Chapter 2.3. The final Chapter 2.4 provides an overview of the physical properties of iron oxides, in particular of α-Fe_2O_3 (hematite), γ-Fe_2O_3 (maghemite) and Fe_3O_4 (magnetite), which are used as MOI in MOI/HM heterostructures to investigate its SMR amplitude. Chapter 2.4 also includes a discussion on the effect of doping on the properties of α-Fe_2O_3/Pt and γ-Fe_2O_3/Pt heterostructures.

2.1. Spin currents

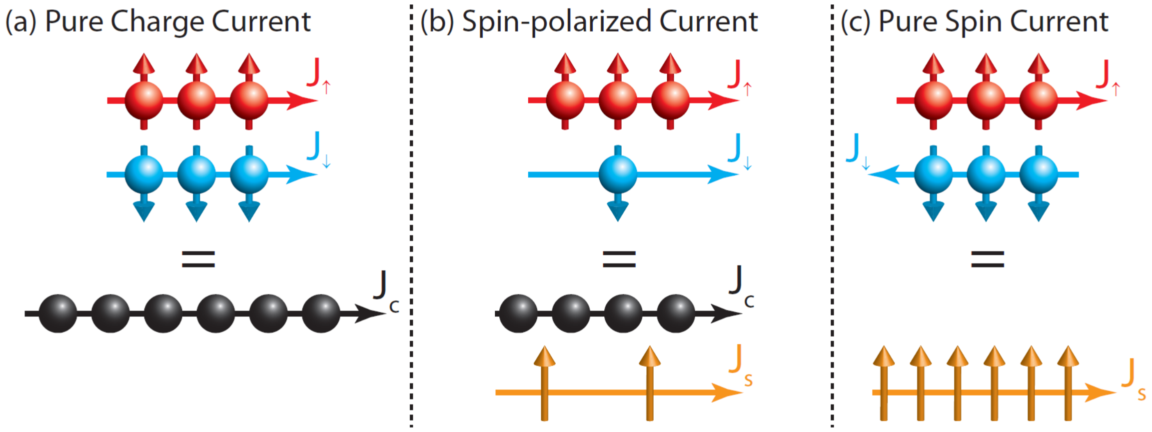

Figure 2.1.1.: Illustration of charge currents $\mathbf{J}_c$ and spin currents $\mathbf{J}_s$. Within a two channel model, $\mathbf{J}_c$ consists of a charge current $\mathbf{J}_\uparrow$ induced by spin-up electrons and a charge current $\mathbf{J}_\downarrow$ induced by spin-down electrons. (a) Pure charge current with $\mathbf{J}_s = 0$ due to $\mathbf{J}_\uparrow = \mathbf{J}_\downarrow$. (b) Spin-polarized current with $\mathbf{J}_c \neq 0$ and $\mathbf{J}_s \neq 0$ originating from an unequal number of spin-up and spin-down electrons at the Fermi level. (c) Pure spin current with $\mathbf{J}_c = 0$. The equal number of spin-up and spin-down electrons is flowing in opposite directions resulting in $\mathbf{J}_\uparrow = -\mathbf{J}_\downarrow$. Figure adapted from Ref. [21].

In electrical conductors, the charge current is carried by mobile charge carriers, e.g. electrons in normal metals such as platinum, aluminum or chopper. Additionally to the charge degree of freedom, charge carriers such as electrons also exhibit a spin degree of freedom.

Thereby, the spin s of an electron collinear to the quantization axis is given by $s = \pm\hbar/2$, resulting in a differentiation into spin-up ($s = +\hbar/2 = |\uparrow\rangle$) and spin-down ($s = -\hbar/2 = |\downarrow\rangle$) polarized electrons. Taking into account a two-spin channel model [22], the charge current $\mathbf{J}_\mathrm{c}$ is the sum of the current by the spin-up electrons ($\mathbf{J}_\uparrow$) and that of the spin-down electrons ($\mathbf{J}_\downarrow$) and thus leading to [23]

$$\mathbf{J}_\mathrm{c} = \mathbf{J}_\uparrow + \mathbf{J}_\downarrow. \tag{2.1}$$

The flow of charge carriers implies a charge current as well as a spin current, which can be described by

$$\mathbf{J}_\mathrm{s} = -\frac{\hbar}{2e}(\mathbf{J}_\uparrow - \mathbf{J}_\downarrow), \tag{2.2}$$

where $\hbar$ is the reduced Planck constant and $-e$ the charge of an electron [23]. Thereby, the same amount of spin-up and spin-down electrons moving in the same direction ($\mathbf{J}_\uparrow = \mathbf{J}_\downarrow$) leads to a pure charge current $\mathbf{J}_\mathrm{c}$ and zero spin current $\mathbf{J}_\mathrm{s}$ (cf. Fig. 2.1.1 (a)). An unequal number of spin-up and spin-down electrons at the Fermi level results in a charge as well as in a spin current leading to a spin-polarized current (cf. Fig. 2.1.1 (b)). This holds for ferromagnetic conductors with a dominating type of spin polarized electrons at the Fermi level. If the same amount of spin-up and spin-down electrons moves in opposite directions ($\mathbf{J}_\uparrow = -\mathbf{J}_\downarrow$), the net charge current is zero and a pure spin current is accomplished (cf. Fig. 2.1.1 (c)).

2.2. Spin Hall effect and inverse spin Hall effect

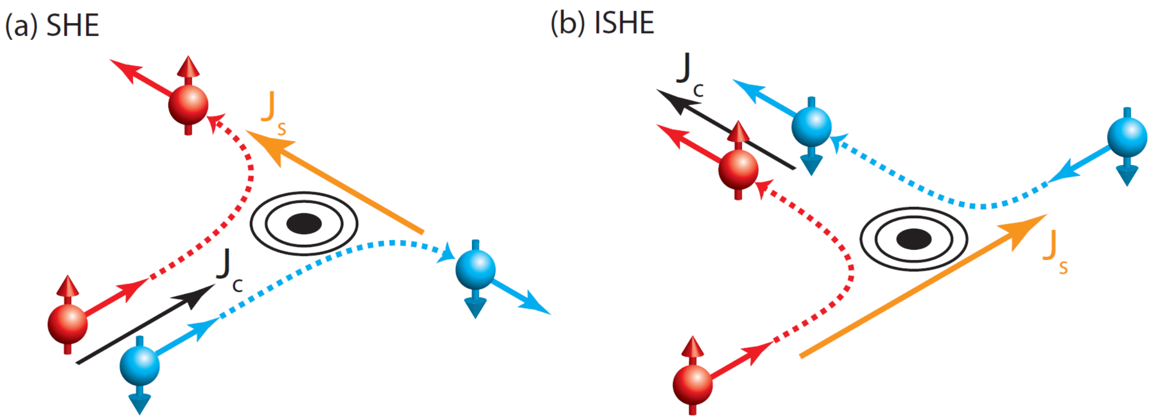

Figure 2.2.1.: (a) Spin Hall effect and (b) inverse spin Hall effect originating from spin dependent scattering of the charge carriers (here spin-up electrons in red and spin-down electrons in blue). The spin Hall effect is described by a charge current $\mathbf{J}_\mathrm{c}$ converted into a transverse spin current $\mathbf{J}_\mathrm{s}$. The inverse spin Hall effect represents the conversion of a spin current into a transverse charge current. Figure taken from Ref. [21].

Mobile charge carriers flowing through a conductor with strong spin orbit coupling (SOC) exhibit a transverse deflection. Due to the Z^4 dependence of the SOC, heavy metals are thereby in favor, where the charge is carried by electrons [24]. The deflection is spin dependent and thus spin-up electrons are deflected in the opposite direction of spin-down electrons. The scattering processes originate from extrinsic effects such as spin dependent scattering at impurities (skew and side jump scattering [25, 26]) and intrinsic, bandstructure effects described by the Berry curvature [27]. The deflection of the electrons in paramagnetic conductors leads to a spin current $\mathbf{J}_\mathrm{s}$ perpendicular to the initial charge current $\mathbf{J}_\mathrm{c}$ and also perpendicular to the spin polarisation s (cf. Fig. 2.2.1 (a)). This so-called spin Hall effect (SHE) can be described by

$$\mathbf{J}_\mathrm{s}^\mathrm{SHE} = -\alpha_\mathrm{SH}\frac{\hbar}{2e}\mathbf{J}_\mathrm{c} \times \mathbf{s} \tag{2.3}$$

with the spin Hall angle α_SH [13]. This spin Hall angle α_SH represents the efficiency of the interconversion of a charge current into a spin current, which is particularly large for heavy metals (HM). For the HM Pt, e.g., α_SH is 0.11 [28, 29]. The opposite effect, i.e. a conversion of a spin current into a charge current, is called inverse spin Hall effect (ISHE) (cf. Fig. 2.2.1 (b)) and described by

$$\mathbf{J}_\mathrm{c}^\mathrm{ISHE} = -\alpha_\mathrm{SH}\frac{2e}{\hbar}\mathbf{J}_\mathrm{s} \times \mathbf{s}. \tag{2.4}$$

2.3. Spin Hall magnetoresistance

In the following, the spin Hall magnetoresistance (SMR) is explained in more detail. Therefore in Section 2.3.1, the SMR effect in magnetic ordered insulator (MOI)/ heavy metal (HM) heterostructures is discussed. The MOI can either be a ferro-/ferrimagnetic or an antiferromagnetic insulator. In Section 2.3.2, the domain structure in antiferromagnetic insulators (AFI) is considered within the SMR theory. Additionally, the SMR amplitude and its dependence on the spin mixing conductance is discussed in Section 2.3.3.

2.3.1. SMR in magnetic ordered insulator/ heavy metal bilayers

In magnetic ordered insulator (MOI)/ heavy metal (HM) bilayers, the spin Hall magnetoresistance (SMR) effect arises from the dependence of the resistivity ρ in the HM on the direction of the magnetization M in the MOI [5, 8]. In a HM, a pure charge current $\mathbf{J}_\mathrm{c}$ along the $\mathbf{j}$ direction (cf. coordinate system in Fig. 2.3.1) generates a perpendicular spin current $\mathbf{J}_\mathrm{s}^\mathrm{SHE}$ via the SHE. A spin accumulation $\boldsymbol{\mu}_\mathrm{s} = \boldsymbol{\mu}_\uparrow - \boldsymbol{\mu}_\downarrow$ at the edges of the HM is formed and therefore a gradient in the spin dependent electrochemical potentials $\boldsymbol{\mu}_\uparrow$ and $\boldsymbol{\mu}_\downarrow$ [30]. This gradient drives a diffusive spin current $\mathbf{J}_\mathrm{s}^\mathrm{diff}$ compensating $\boldsymbol{\mu}_\mathrm{s}$ by flowing in the opposite direction of the initial spin current $\mathbf{J}_\mathrm{s}^\mathrm{SHE}$. Via the ISHE $\mathbf{J}_\mathrm{s}^\mathrm{diff}$ generates again a charge current $\mathbf{J}_\mathrm{c}^\mathrm{ISHE}$ perpendicular to $\mathbf{J}_\mathrm{s}^\mathrm{diff}$ and s and along the initial direction of $\mathbf{J}_\mathrm{c}$.

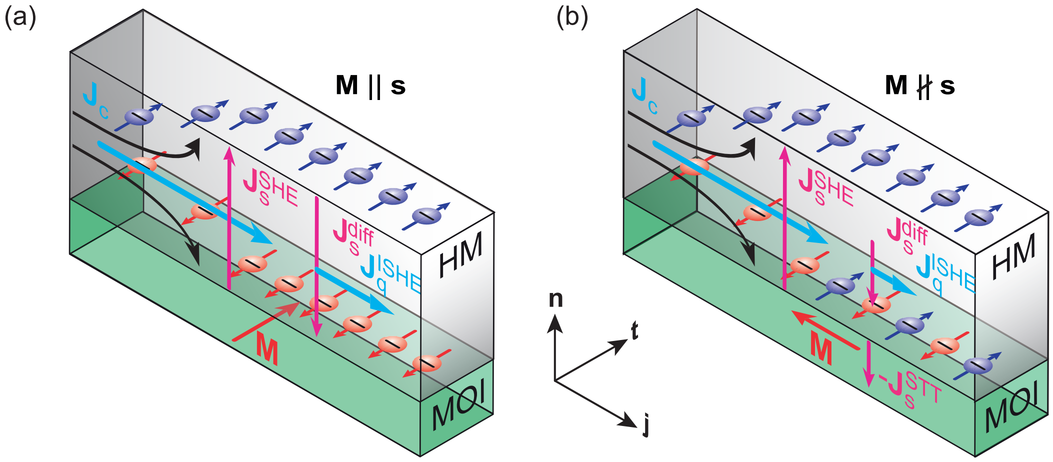

Figure 2.3.1.: A charge current $\mathbf{J}_\mathrm{c}$ injected into a heavy metal (HM) adjacent to a magnetic ordered insulator (MOI) with magnetization $\mathbf{M}$. Via the spin Hall effect (SHE) $\mathbf{J}_\mathrm{c}$ is converted into a transverse spin current $\mathbf{J}_\mathrm{s}^\mathrm{SHE}$. A spin accumulation $\boldsymbol{\mu}_\mathrm{s}$ occurs at the edges of the HM. (a) If $\mathbf{M}$ is collinear to the spin polarization s of the HM electrons, $\boldsymbol{\mu}_\mathrm{s}$ is compensated by a diffusive spin current $\mathbf{J}_\mathrm{s}^\mathrm{diff}$ counteracting $\mathbf{J}_\mathrm{s}^\mathrm{SHE}$. $\mathbf{J}_\mathrm{s}^\mathrm{diff}$ generates a charge current $\mathbf{J}_\mathrm{c}^\mathrm{ISHE}$ via the inverse spin Hall effect (ISHE). (b) For $\mathbf{M} \nparallel \mathrm{s}$ the spin accumulation exerts a spin transfer torque (STT) on $\mathbf{M}$ resulting in a spin current $-\mathbf{J}_\mathrm{s}^\mathrm{STT}$ accross the HM/MOI interface. This represents an additional loss channel for $\mathbf{J}_\mathrm{s}^\mathrm{diff}$ and thus a reduced $\mathbf{J}_\mathrm{c}^\mathrm{ISHE}$ in the HM. Figure adapted from Ref. [31].

Bringing a MOI adjacent to the HM, a dependence of $\mathbf{J}_\mathrm{c}^\mathrm{ISHE}$ on the magnetization orientation in the MOI is observed (cf. Fig. 2.3.1). If the spin polarization s in the HM and the magnetization $\mathbf{M}$ in the MOI are collinear to each other, the already discussed open circuit condition appears, where the spin current is reflected at the interface of MOI and HM and converted into a charge current (cf. Fig. 2.3.1 (a)). Hereby, the generation of magnons in the MOI due to spin-scattering at the MOI/HM interface is neglected. This is valid for $T = 0\,\mathrm{K}$. For finite temperatures a finite spin current accross the interface is expected, since the spin accumulation in the HM creates and annihilates magnons in the MOI depending on the orientation of $\boldsymbol{\mu}_\mathrm{s}$ [32].

If $\mathbf{M}$ is not collinear to $\mathbf{s}$, spin angular momentum is transferred across the interface reducing $\boldsymbol{\mu}_\mathrm{s}$ and also $\mathbf{J}_\mathrm{s}^\mathrm{diff}$ and $\mathbf{J}_\mathrm{c}^\mathrm{ISHE}$ (short circuit condition, cf. Fig. 2.3.1 (b)). This is decribed by a spin transfer torque (STT) of $\boldsymbol{\mu}_\mathrm{s}$ exerted on $\mathbf{M}$ resulting in a spin current $\mathbf{J}_\mathrm{s}^\mathrm{STT}$ accross the interface [33]. $\mathbf{J}_\mathrm{s}^\mathrm{STT}$ is therefore proportional to $(g_\mathrm{i}^{\uparrow\downarrow} + g_\mathrm{r}^{\uparrow\downarrow}\mathbf{M}\times)(\boldsymbol{\mu}_\mathrm{s} \times \mathbf{M})$, depending on the real and the imaginary part of the complex spin mixing conductance $g^{\uparrow\downarrow} = g_\mathrm{r}^{\uparrow\downarrow} + i g_\mathrm{i}^{\uparrow\downarrow}$ [34]. The spin mixing conductance is a quantity describing the efficiency of spin transport across the HM/MOI interface [35]. All in all, an additional loss channel for the charge transport appears in the HM so that the longitudinal resistivity ρ_long of the HM increases and reaches a maximum for $\mathbf{M} \perp \mathrm{s}$. Analogously, a minimum in ρ_long is observed for $\mathbf{M} \parallel \mathrm{s}$.

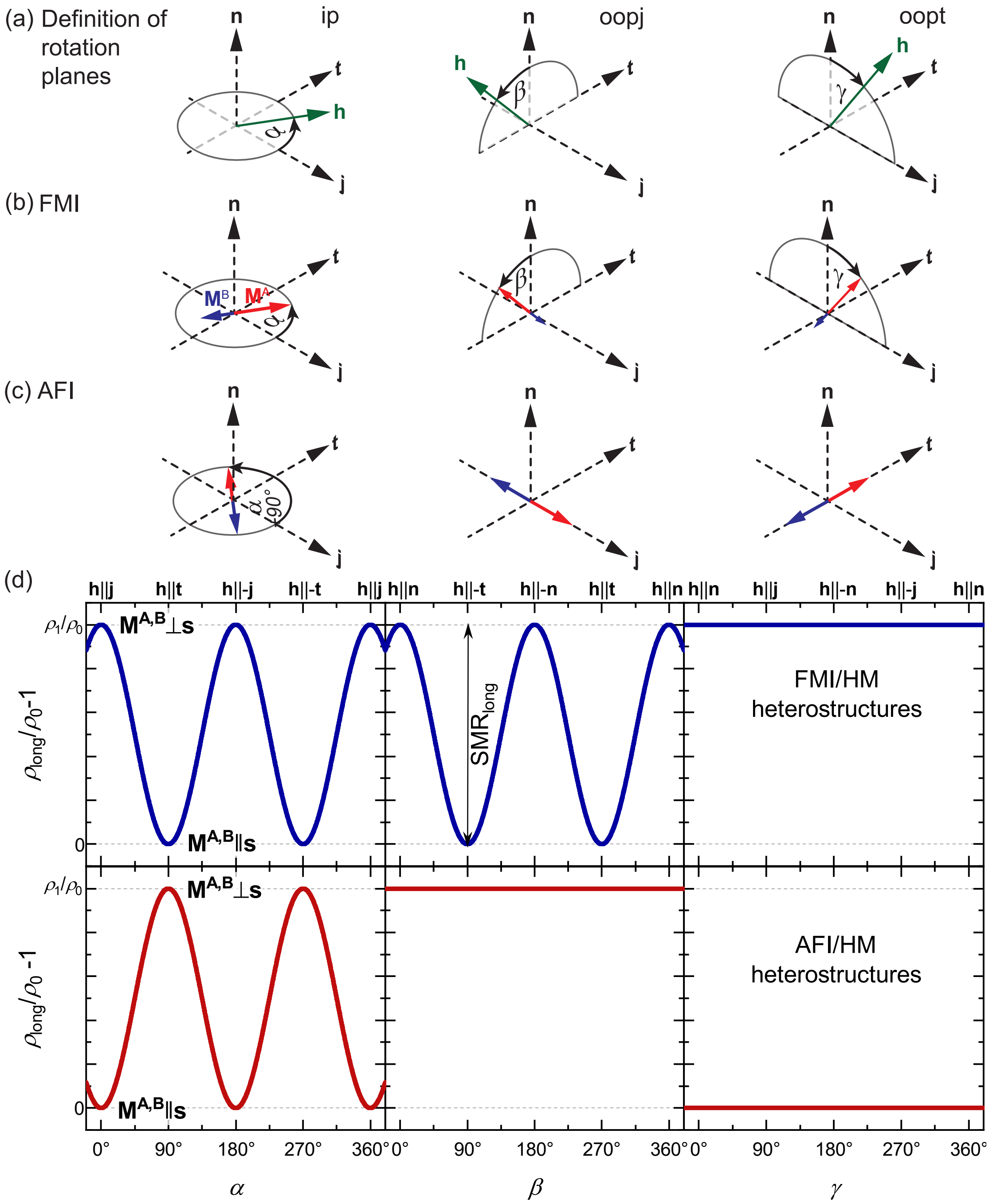

Figure 2.3.2.: (a) Definition of the rotation planes: the external magnetic field direction **h** is rotated in the thin film plane (ip, angle α), out of the plane perpendicular to **j** (oopj, angle β) and out of the plane perpendicular to **t** (oopt, angle γ). Corresponding rotation of two magnetic sublattices with magnetizations $\mathbf{M}^{\mathrm{A}}$ and $\mathbf{M}^{\mathrm{B}}$ (b) for a FMI with $|\mathbf{M}^{\mathrm{A}}| > |\mathbf{M}^{\mathrm{B}}|$ collinear to **h** and (c) for an AFI with $|\mathbf{M}^{\mathrm{A}}| = |\mathbf{M}^{\mathrm{B}}|$ perpendicular to **h** in the magnetic easy plane of the AFI. (d) Theoretical angle dependencies of the longitudinal resistivity ρ_{long} in a FMI/HM and an AFI/HM bilayer. ρ_{long} is normalized to ρ_0. Figures (a)-(c) taken from Ref. [10].

Since the SMR is a function of the angle between **M** and **s**, angle-dependent magnetoresistance (ADMR) measurements are a tool for investigating the SMR effect. In ADMR measurements an external magnetic field **H** with direction $\mathbf{h} = \mathbf{H}/H$ is rotated in three planes (cf. Fig. 2.3.2 (a)), which are orthogonal to each other: in the thin film plane with the rotation angle α (in-plane, ip), out of the thin film plane perpendicular to the charge current direction $\mathbf{j}$ with the rotation angle β (out-of-plane perpendicular to $\mathbf{j}$, oopj) and out-of-plane perpendicular to the transverse direction $\mathbf{t}$ with the corresponding angle γ (out-of-plane perpendicular to $\mathbf{t}$, oopt).

The longitudinal resistivity ρ_{long}, i.e. the resistivity measured along $\mathbf{J}_\text{c}$, can be expressed within the SMR theory as

$$\rho_{\text{long}} = \rho_0 + \frac{1}{2}\sum_{\text{X = A}}^{\text{B}} \rho_1^{\text{X}}\left(1 - (\mathbf{m}^{\text{X}} \cdot \mathbf{t})^2\right) = \rho_0 + \frac{1}{2}\sum_{\text{X = A}}^{\text{B}} \rho_1^{\text{X}}\left(1 - (m_t^{\text{X}})^2\right), \tag{2.5}$$

considering two magnetic sublattices A and B in the MOI [9, 33]. Thereby, ρ_0 is approximately the normal resistivity of the HM and ρ_1 is the longitudinal SMR coefficient, which is assumed to be equal for the two magnetic sublattices. The sublattice magnetizations $\mathbf{M}^{\text{X}}$ are normalized to the respective saturation magnetization M_{S} yielding $\mathbf{m}^{\text{X}} = \mathbf{M}^{\text{X}}/M_{\text{S}}$. So ρ_{long} depends on the projection m_t^{X} of the direction of the sublattice magnetization $\mathbf{m}^{\text{X}}$ on $\mathbf{t}$. The resistivity ρ_{trans} measured along the transverse direction $\mathbf{t}$ is a function of the transverse SMR coefficient ρ_3 and the anomalous Hall effect type coefficient ρ_2. Taking into account the projections of $\mathbf{m}^{\text{X}}$ on the directions $\mathbf{j}$, $\mathbf{t}$, $\mathbf{n}$ ρ_{trans} yields [10, 28]

$$\rho_{\text{trans}} = \frac{1}{2}\sum_{\text{X = A}}^{\text{B}} \left(\rho_3^{\text{X}} m_j^{\text{X}} m_t^{\text{X}} + \rho_2^{\text{X}} m_n^{\text{X}}\right). \tag{2.6}$$

The factor $1/2$ in Eqs. (2.5) and (2.6) stems from the contribution of two magnetic sublattices. In case of a ferrimagnetic insulator, both sublattice magnetizations $\mathbf{M}^{\text{A}}$ and $\mathbf{M}^{\text{B}} \neq \mathbf{M}^{\text{A}}$ are collinear to $\mathbf{h}$ for sufficiently large magnetic field magnitudes and thus the net magnetization $\mathbf{M} = \mathbf{M}^{\text{A}} + \mathbf{M}^{\text{B}}$ is pointing along the external magnetic field direction (cf. Fig. 2.3.2 (b)). If $\mathbf{h}$ is parallel to $\mathbf{j}$, also $\mathbf{M}$ is parallel to $\mathbf{j}$. Therefore, $\mathbf{M}$ is perpendicular to s, resulting in ρ_{long} being maximum. Applying $\mathbf{h}$ perpendicular to $\mathbf{j}$ leads to ρ_{long} being minimum, since $\mathbf{M}$ is then collinear to s. The angular dependencies of ρ_{long} as well as of ρ_{trans} for all three magnetic field rotations can be expressed as

$$\rho_{\text{long}}^{\text{ip}} = \rho_0 + \frac{\rho_1}{2}(1+\cos(2\alpha)), \quad \rho_{\text{long}}^{\text{oopj}} = \rho_0 + \frac{\rho_1}{2}(1+\cos(2\beta)), \quad \rho_{\text{long}}^{\text{oopt}} = \rho_0 + \rho_1, \tag{2.7}$$

$$\rho_{\text{trans}}^{\text{ip}} = \frac{\rho_3}{2}\sin(2\alpha), \quad \rho_{\text{trans}}^{\text{oopj}} = \rho_2\cos(\beta), \quad \rho_{\text{trans}}^{\text{oopt}} = \rho_2\cos(\gamma). \tag{2.8}$$

In antiferromagnetic insulators the situation is different as depicted in Fig. 2.3.2 (c). The sublattice magnetizations are the same in their magnitude, pointing in opposite directions ($\mathbf{M}^{\text{A}} = -\mathbf{M}^{\text{B}}$). The Néel vector $\mathbf{l} = (\mathbf{m}^{\text{A}} - \mathbf{m}^{\text{B}})/2$ describes the orientation of the magnetic sublattices [9, 10]. A sufficiently large external magnetic field leads to the alignment of $\mathbf{M}^{\text{A}}$ and $\mathbf{M}^{\text{B}}$ perpendicular to $\mathbf{h}$. Consequently, the SMR in AFI/HM bilayers exhibits a 90° phase shift compared to the one in FMI/HM bilayers while rotating the magnetic field in the **j**-**t**-plane, since ρ_{long} is now minimum for $(\mathbf{h} \parallel \mathbf{j}) \perp \mathbf{l}$ and maximum for $(\mathbf{h} \perp \mathbf{j}) \parallel \mathbf{l}$. Therefore, Eqs. (2.5) and (2.6) yields the resistivities

$$\rho^{\text{ip}}_{\text{long}} = \rho_0 + \frac{\rho_1}{2}(1 - \cos(2\alpha)), \qquad \rho^{\text{oopj}}_{\text{long}} = \rho_0 + \rho_1, \qquad \rho^{\text{oopt}}_{\text{long}} = \rho_0, \tag{2.9}$$

$$\rho^{\text{ip}}_{\text{trans}} = -\frac{\rho_3}{2}\sin(2\alpha), \qquad \rho^{\text{oopj}}_{\text{trans}} = 0, \qquad \rho^{\text{oopt}}_{\text{trans}} = 0, \tag{2.10}$$

for the three magnetic field rotations. Hereby, no finite canting of the sublattices is taken into account and a single domain state is considered. For an illustration of the differences of the ferri- and the antiferromagnetic SMR effect, the angle dependence of the normalized longitudinal resistivities ρ_{long} according to Eqs. 2.7 and 2.9 is depicted in Fig. 2.3.2 (d). The resistivities are normalized to ρ_0, respectively, to be able to directly determine the SMR amplitude $\text{SMR}_{\text{long}} = \rho_1/\rho_0$. Complementary, the transverse SMR amplitude is defined as $\text{SMR}_{\text{trans}} = \rho_3/\rho_0$.

2.3.2. SMR in multidomain antiferromagnetic insulator/ heavy metal bilayers

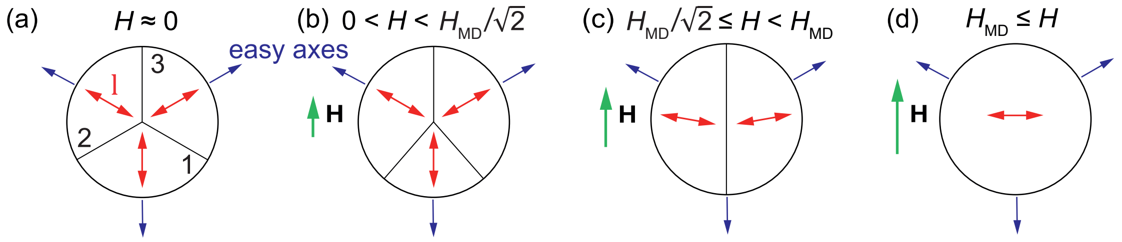

Figure 2.3.3.: Magnetic domain structure in an easy plane antiferromagnet under variation of the magnitude H of an applied magnetic field $\mathbf{H}$. The magnetically easy axes are marked as blue arrows and the Néel vectors $\mathbf{l}$ of each domain $k = 1, 2, 3$ as red double arrows, indicating the non-distinguishable antiferromagnetic 180° domains. H_{MD} is the monodomainization field, reaching a single domain state. (a) $H \approx 0$: Equal distribution of the three domains with $\mathbf{l}$ of each domain oriented in 120° to each other. (b) $0 < H < H_{\text{MD}}/\sqrt{2}$: Domain wall motion towards the energetically unfavorable magnetic domains. (c) $H_{\text{MD}}/\sqrt{2} \leq H < H_{\text{MD}}$: Additional reorientation of the domains. (d) $H_{\text{MD}} \leq H$: Single domain state with $\mathbf{l} \perp \mathbf{H}$. Figure adapted from Ref. [9].

Due to its anisotropy energy, easy plane antiferromagnetic insulators such as α-Fe_2O_3 (hematite) form magnetic domains [36, 37], which are not yet considered in the SMR theory, but affecting it remarkably [12]. With the absence of an applied magnetic field, α-Fe_2O_3 consists of three equally distributed, distinguishable magnetic domains. The magnetic sublattices of those domains are oriented to each other with an angle of 120° in the easy plane (cf. Fig. 2.3.3 (a)). Thereby, 180° domains with Néel vectors $\pm\mathbf{l} = \pm(\mathbf{m}^{\text{A}} - \mathbf{m}^{\text{B}})/2$ can not be distinguished. Equations (2.5) and (2.6) describing the SMR effect in general can be modified to involve the domain structure in an AFI. Therefore the fractions ξ_k of the domains k with $\sum_k \xi_k = 1$ are taken into account resulting in the longitudinal and transverse resistivities [9–11]

$$\rho_{\text{long}} = \rho_0 + \rho_1 \sum_k \xi_k \big(1 - (l_t^k)^2\big), \qquad \rho_{\text{trans}} = \rho_3 \sum_k \xi_k l_j^k l_t^k. \tag{2.11}$$

l_j^k and l_t^k represent the projections of $\mathbf{l}^k$ on the directions $\mathbf{j}$ and $\mathbf{t}$ of each domain (cf. Fig. 2.3.2 (c)). For $H = 0$ the fractions of the domains $k = 1$, 2 and 3 are $\xi_1 = \xi_2 = \xi_3 = 1/3$.

Applying an external magnetic field within the easy plane changes the domain structure in the AFI, since the three domains are not energetically degenerated anymore due to the additional Zeeman energy. The domain walls move towards the energetically unfavorable domains and therefore decreasing its fraction (Fig. 2.3.3 (b)). If the remaining domains are not already oriented perpendicular to $\mathbf{H}$, increasing the magnetic field further leads to an additional reorientation $\mathbf{l}^k$ of the remaining domains (Fig. 2.3.3 (c)). For magnetic fields larger than the monodomainization field M_{MD}, a single domain state is obtained with the magnetic sublattices being perpendicular to $\mathbf{H}$ (Fig. 2.3.3 (d)).

The fractions and orientations of the magnetic domains are determined by three distinct energy contributions, the anisotropy energy E_{a}, the Zeeman energy E_{Zee} and the destressing energy E_{dest}. E_{a} is responsible for the domain structure, when the external magnetic field is absent [9, 38]. E_{Zee} and E_{dest} are competing energies, since the Zeeman forces a single domain state for high enough fields, but E_{dest} favors a multi domain state [11, 39]. The destressing energy can be seen as an analogon to the demagnetization energy in ferromagnets [40]. Minimizing the total energy $E_{\text{tot}} = E_{\text{a}} + E_{\text{Zee}} + E_{\text{dest}}$ with respect to the fractions ξ_k and the orientations $\mathbf{l}^k$ of the magnetic domains yields the longitudinal and transverse resistivities in ip magnetic field rotation, i.e. [11]

$$\rho_{\text{long}}^{\text{ip}} = \rho_0 + \frac{\rho_1}{2}\left(1 - \frac{H^2}{H_{\text{MD}}^2}\cos(2\alpha)\right), \qquad \rho_{\text{trans}}^{\text{ip}} = -\frac{\rho_3}{2}\frac{H^2}{H_{\text{MD}}^2}\sin(2\alpha). \tag{2.12}$$

H_{MD} is the monodomainization field with $H_{\text{MD}} = 2\sqrt{H_{\text{dest}}H_{\text{ex}}}$, where H_{dest} is the destressing field of the destressing energy contribution and H_{ex} the exchange field stemming from the Zeeman energy contribution. For $H \geq H_{\text{MD}}$ the single domain state is reached apart from indistinguishable antiferromagnetic 180° domains (Fig. 2.3.3 (d)) and the SMR effect can therefore be described by Eqs. (2.9) and (2.10). For $H < H_{\text{MD}}$ the longitudinal SMR amplitude can be approximated to

$$\text{SMR}_{\text{long}} \approx \frac{\rho_1}{\rho_0}\frac{H^2}{H_{\text{MD}}^2} \tag{2.13}$$

with $\rho_1 \ll \rho_0$ [9]. In ip ADMR measurements, ρ_{long} oscillates around $\rho_0 + \rho_1/2$ reaching a maximum in its amplitude for $H \geq H_{\text{MD}}$. In oopj and oopt magnetic field rotations a finite projection of $\mathbf{H}$ on the magnetic easy plane has to be considered that modifies the in Fig. 2.3.2 (d) depicted high resistive state in oopj and low resistive state in oopt rotation.

For **H** $\parallel$ **n** this projection is zero leading to a multi domain state with $\rho_{\text{long}}^{\text{oopj, oopt}} = \rho_0 + \rho_1/2$ in analogon to the ip zero field case depicted in Fig. 2.3.3 (a). While rotating **H** towards the magnetic easy plane, the ip projection of **H** increases and therefore the projections l_j^k and l_t^k of each domain change. Once the ip projection of **H** is larger than H_{MD}, a single domain state occurs and therefore $\rho_{\text{long}}^{\text{oopj}} = \rho_0 + \rho_1$ and $\rho_{\text{long}}^{\text{oopt}} = \rho_0$. The overall magnetic field dependence of the longitudinal resistivities in oopj and oopt magnetic field rotation is described by [10]

$$\rho_{\text{long}}^{\text{oopj, oopt}} = \rho_0 + \frac{\rho_1}{2}\left(1 \pm \frac{H^2}{H_{\text{MD}}^2}\sin(\beta,\gamma)\right). \tag{2.14}$$

The derivations of the equations given in this section including the free energy minimization are given in Ref. [11]. Thereby, the domain states depicted in Fig. 2.3.3 are also discussed in more detail for different orientations of **H**.

2.3.3. Amplitude of the SMR

The SMR amplitude is a function of multiple quantities. In particular for $g_{\text{r}}^{\uparrow\downarrow} \gg g_{\text{i}}^{\uparrow\downarrow}$ the longitudinal SMR amplitude is given by

$$\text{SMR}_{\text{long}} = \frac{2\lambda_{\text{sf}}^2 \rho_{\text{HM}} \alpha_{\text{SH}}^2 t_{\text{HM}}^{-1} g_{\text{r}}^{\uparrow\downarrow} \tanh^2\left(\frac{t_{\text{HM}}}{2\lambda_{\text{sf}}}\right)}{he^{-2} + 2\lambda_{\text{sf}}\rho_{\text{HM}} g_{\text{r}}^{\uparrow\downarrow}\coth\left(\frac{t_{\text{HM}}}{\lambda_{\text{sf}}}\right)}, \tag{2.15}$$

with Planck's constant h [5, 13]. Hence, SMR_{long} is mostly dependent on properties of the HM, such as the spin Hall angle α_{SH}, the layer thickness t_{HM}, the spin diffusion length λ_{sf} and the resistivity ρ_{HM}. Due to spin-flip scattering processes the spin state of an electron ($s = |\uparrow\rangle$ or $|\downarrow\rangle$) is finite and decays after a characteristic length scale, the so-called spin diffusion length [35]. For electrons in Pt λ_{sf} is approximately $1.5\,\text{nm}$ [28]. SMR_{long} is therefore maximum, if $t_{\text{HM}} = 2\lambda_{\text{sf}}$. Additionally, SMR_{long} is also dependent on the real part of the spin mixing conductance

$$g_{\text{r}}^{\uparrow\downarrow} \propto J_{\text{sd}}^2 n_{\text{s}}\left(\langle S_{\parallel}^2\rangle - \frac{\langle S_{\perp}^2\rangle}{2}\right), \tag{2.16}$$

with the s-d interface exchange coupling J_{sd}, the density n_{s} of magnetic moments at the MOI surface in units of m^{-2} and the components $S_{\parallel}$ and $S_{\perp}$ of the spin operator S parallel and perpendicular to **H** [14, 41]. Vélez *et al.* derived Eq. (2.16) by theoretically introducing an additional HM layer between MOI and HM, which includes impurities magnetically coupled to each other analogously to the magnetic moments at the MOI surface [14]. Hence, J_{sd} is the coupling constant describing the s-d hybridization between the localized d-orbitals of the impurities and the s-orbitals of the HM electrons. Therefore, the spin mixing conductance strongly depends on the interface morphology. In Ref. [42] for instance, the authors report an increase of $g_{\text{r}}^{\uparrow\downarrow}$ by increasing the surface roughness of the MOI layer. Since $g_{\text{r}}^{\uparrow\downarrow}$ is proportional to the magnetic moment surface density n_{s}, also the SMR amplitude SMR_{long} is depending on n_{s}.

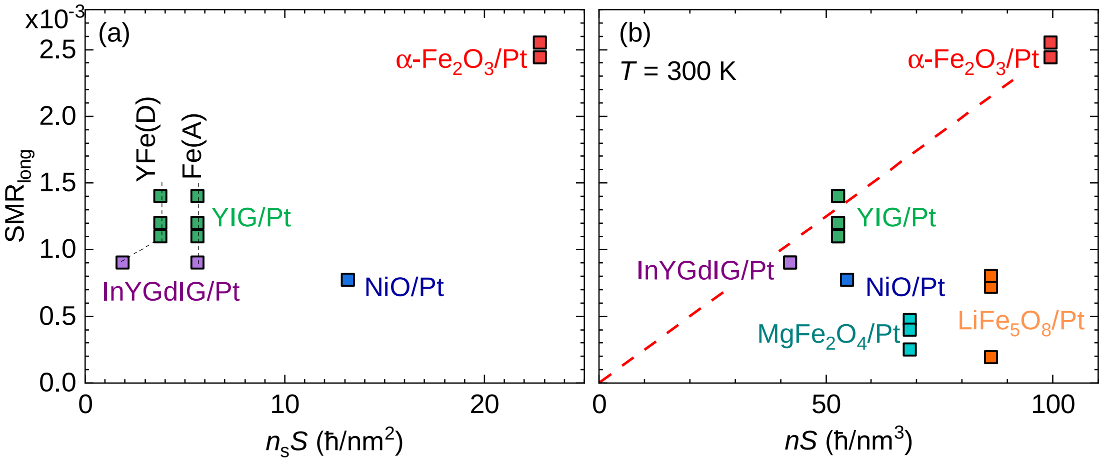

Figure 2.3.4.: Longitudinal SMR amplitude $\mathrm{SMR_{long}}$ of different magnetic ordered insulator/Pt (MOI/Pt) heterostructures fabricated and measured at the WMI. (a) $\mathrm{SMR_{long}}$ as a function of the magnetic moment surface density $n_\mathrm{s}S$ at the interface between MOI and Pt. (b) $\mathrm{SMR_{long}}$ as a function of the magnetic moment volume density nS in the MOI. In (b) the dashed red line indicates a potential linear dependence of $\mathrm{SMR_{long}}(nS)$. The data are summarized by M. Opel and supplemented by the SMR amplitudes of $MgFe_2O_4$/Pt and $LiFe_5O_8$/Pt obtained in Ref. [43].

Figure 2.3.4 provides an overview of MOI/Pt heterostructures fabricated at the WMI. Thereby, the longitudinal SMR amplitude $\mathrm{SMR_{long}} = \rho_1/\rho_0$ of these heterostructures is depicted as (a) a function of the magnetic moment surface density $n_\mathrm{s}S$ and (b) a function of the magnetic moment volume density nS in units of $\hbar\mathrm{nm}^{-2}$ and $\hbar\mathrm{nm}^{-3}$, respectively. In the first case the number of magnetic moments on the MOI surface at the interface between MOI and Pt is considered, since Eqs. (2.15) and (2.16) claim a dependence of $\mathrm{SMR_{long}}$ on n_s. In the second case, a finite diffusion of angular momentum from the Pt layer into the MOI volume is assumed and thus the number of magnetic moments in the total MOI volume is considered. In Fig. 2.3.4 (a) no clear dependence is visible, while in Fig. 2.3.4 (b) the heterostructures InYGdIG/Pt, YIG/Pt and α-Fe_2O_3/Pt exhibit a linear increase of $\mathrm{SMR_{long}}$ with increasing nS. But this empirical observation can not be confirmed by Ref. [43], where the SMR amplitudes of $MgFe_2O_4$/Pt and $LiFe_5O_8$/Pt are significantly smaller than expected. Hence, the assumption of a linear dependence of $\mathrm{SMR_{long}}(nS)$ could be too simple and has to be investigated in more detail. Since $MgFe_2O_4$ and $LiFe_5O_8$ exhibit complicated spinel structures [44, 45], it is not trivial to predict their magnetic behavior.

Therefore, in this thesis, the SMR amplitude is attempted to be tuned by doping thin films of α-Fe_2O_3 (hematite, $nS = 99.4\,\hbar/\mathrm{nm}^3$) and γ-Fe_2O_3 (maghemite, $nS = 92.2\,\hbar/\mathrm{nm}^3$ assuming a cubic spinel structure) with non-magnetic ions. α-Fe_2O_3/Pt bilayers exhibit a large SMR amplitude of 2.5×10^{-3} (see Ref. [12] and Sec. 3.1.3). The aim is to decrease this SMR amplitude by Ga doping and to analyze $\mathrm{SMR_{long}}$ as a function of nS. In contrast to $MgFe_2O_4$ and $LiFe_5O_8$, the antiferromagnetic iron oxide α-Fe_2O_3 does not crystallize in a complicated spinel structure with two differently coordinated sites, but in a hexagonal lattice [46–48]. This should make it easier to predict the effect of doping on the magnetic structure. Furthermore, the spinel, ferrimagnetic γ-Fe_2O_3 is investigated and corresponding γ-Fe_2O_3/Pt bilayers are doped [49, 50]. The crystal structure of γ-Fe_2O_3 is simpler compared to $MgFe_2O_4$ and $LiFe_5O_8$, which makes γ-Fe_2O_3/Pt bilayers a tool for investigating the SMR effect in spinel based systems. To complete the investigation of the most known iron oxides, also Fe_3O_4 (magnetite, $nS = 94.7\,\hbar/\mathrm{nm}^3$) thin films are fabricated and characterized, among others in terms of magnetoresistive effects.

2.4. Physical properties of iron oxides

To investigate the SMR amplitude in bilayers composed of different magnetically ordered insulators (MOI) and platinum, the vast group of iron oxides as MOI is used. Therefore, this Chapter provides an overview of the physical properties of common iron oxides. In Section 2.4.1 the antiferromagnet α-Fe_2O_3 (hematite) is discussed concerning its structural and magnetic properties. The ferrimagnetic insulator γ-Fe_2O_3 (maghemite) is then described in Section 2.4.2. In Section 2.4.3, ferrimagnetic Fe_3O_4 (magnetite) is analyzed in terms of crystallography and magnetism. Addtionally, Chapter 2.4.4 discusses the effect of doping on the properties of α-Fe_2O_3/Pt and γ-Fe_2O_3/Pt bilayers.

2.4.1. Physical properties of α-Fe_2O_3

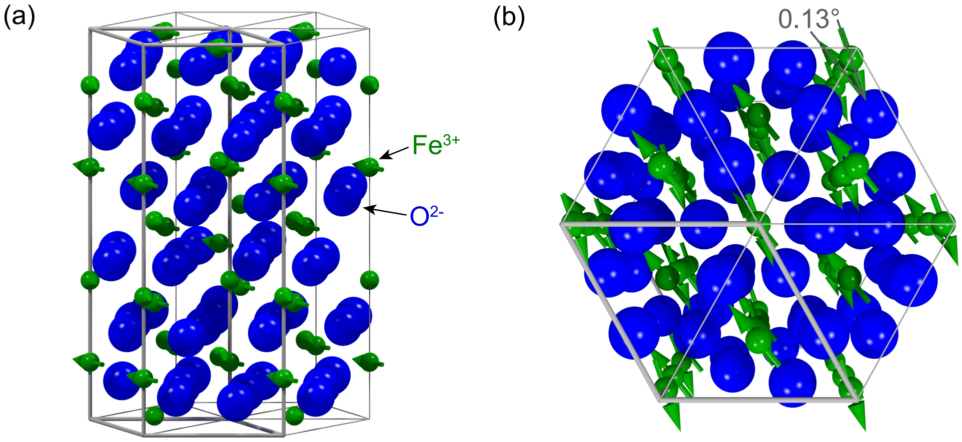

Figure 2.4.1.: Hexagonal unit cell of α-Fe_2O_3 with the Fe^{3+} ions depicted as green and the O^{2-} ions depicted as blue spheres. This conventional unit cell consists of three trigonal unit cells. One of them is indicated by thicker grey lines. Additionally, the magnetic moments of the Fe^{3+} ions are shown as arrows. (a) Side view and (b) top view illustrating the canting of the magnetic sublattices with a canting angle of $\delta = 0.13°$ [51].

α-Fe_2O_3 (hematite) crystallizes in a hexagonal (rhombohedral) lattice with an in-plane lattice contant $a = 0.5034\,\mathrm{nm}$ and an out-of-plane lattice constant $c = 1.3752\,\mathrm{nm}$ (see Fig. 2.4.1 (a)) [48]. The Fe^{3+} ions with a spin quantum number of $S = 5/2\hbar$ are surrounded octahedrally by O^{2-} ions and each unit cell contains six formula units of α-Fe_2O_3 [46, 48]. α-Fe_2O_3 is fully insulating and antiferromagnetic below $T_\mathrm{N} = 953\,\mathrm{K}$, which makes it a possible material for antiferromagnetic spintronics in particular for SMR experiments. At approximately $T_\mathrm{M} = 263\,\mathrm{K}$ a spin reorientation occurs, the so-called Morin transition [15]. Therefore, at $T_\mathrm{M} < T < T_\mathrm{N}$ the magnetic moments lie in the magnetically easy α-Fe$_2$O$_3$ (0001) plane with a ferromagnetic ordering within each plane and an antiferromagnetic coupling between neighboring planes with the stacking sequence "$+ - -+$" [46]. Due to the Dzyaloshinskii–Moriya interaction (DMI) the magnetic sublattices are slightly canted with a canting angle $\delta = 0.13°$ resulting in a weak net magnetization of $2.5\,\mathrm{kA\,m^{-1}}$ at a temperature of $300\,\mathrm{K}$ (see Fig. 2.4.1) [51, 52]. For $T < T_\mathrm{M}$ the magnetic moments align along the [0001]-axis with ferromagnetic coupling in the (0001) planes and antiferromagnetic coupling between those planes [15]. The spin reorientation is a result of a sign change in the uniaxial magnetic anisotropy leading to a transition from a magnetic (0001) easy plane above T_M to a magnetically [0001] easy axis below T_M [53]. In the magnetic easy plane for $T_\mathrm{M} < T < T_\mathrm{N}$, the threefold crystal symmetry results in the formation of three magnetic domains rotated by 120° as discussed previously in Sec. 2.3.2.

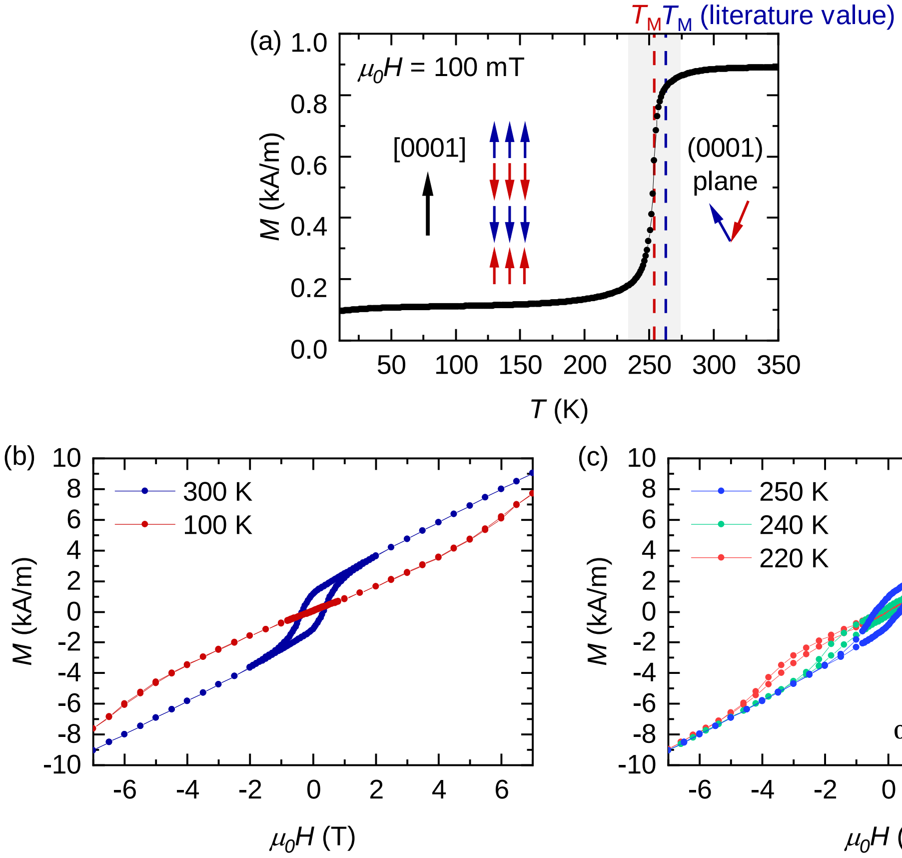

Figure 2.4.2.: SQUID magnetometry measurement results of α-Fe$_2$O$_3$ powder. (a) The temperature dependence of the magnetization M reveals a Morin transition at $T_\mathrm{M} = 254\,\mathrm{K}$ (dashed red line) slightly smaller than the literature value of $263\,\mathrm{K}$ (dashed blue line) [15]. For $T > T_\mathrm{M}$ the magnetic sublattices are canted in the (0001) thin film plane, for $T < T_\mathrm{M}$ a reorientation occurs with the magnetic moments antiferromagnetically aligned along the [0001] direction [46, 53]. $M(T)$ is measured at an applied magnetic field of $\mu_0 H = 100\,\mathrm{mT}$. (b) Hysteresis curves far above ($300\,\mathrm{K}$) and far below ($100\,\mathrm{K}$) T_M and (c) hysteresis curves at different T near T_M.

Figure 2.4.2 depicts the results of superconducting quantum interference device (SQUID) magnetometry measurements performed on polycrystalline α-Fe_2O_3 powder. In Fig. 2.4.2 (a), the temperature dependence of the magnetization M exhibits the characteristic Morin transition at approximately $254\,\mathrm{K}$, slightly smaller than the literature value. This could be due to the dependence of the Morin transition on the grain size. With decreasing grain size also T_M decreases [54]. Above T_M the magnetic sublattice canting in a magnetic field of $\mu_0 H = 100\,\mathrm{mT}$ results in a small net magnetization of $0.9\,\mathrm{kA\,m^{-1}}$. This value is significantly smaller than the literature value of $2.5\,\mathrm{kA\,m^{-1}}$, also due to the polycrystalline structure of the α-Fe_2O_3 powder, which leads to different oriented grains at low $\mu_0 H$. Below T_M the magnetic moments are aligned along the crystallographic c axes of the individual grains, but the orientation of those grains is statistically distributed. Therefore, the Morin transition is not sharp (cf. Ref. [54]). The finite field leads to a small magnetization measured below T_M.

M as a function of $\mu_0 H$ shown in Fig. 2.4.2 (b) exhibits a distinct hysteretic behavior at $300\,\mathrm{K}$ far above T_M and no hysteresis at $100\,\mathrm{K}$ far below T_M. With increasing $\mu_0 H$ the magnetic sublattices of the grains align perpendicular to the magnetic field direction $\mathbf{h}$ and a field induced canting of the magnetic sublattices occurs. For $T = 300\,\mathrm{K}$ the DMI induced spin canting and therefore the finite net magnetization leads to the hysteretic behavior, while orienting the individual grain magnetizations perpendicular to $\mathbf{h}$. In the temperature range of the Morin transition, the hysteresis curves measured at $220\,\mathrm{K}$, $240\,\mathrm{K}$ and $250\,\mathrm{K}$ reveal a transition from a double hysteresis at higher $\mu_0 H$ to a single hysteresis around zero magnetic field with increasing T (cf. Fig. 2.4.2 (c)). Hence, the system becomes magnetically soft close to T_M with the result of a reduction of the critical magnetic field for spin-flop transitions.

2.4.2. Physical properties of γ-Fe_2O_3

γ-Fe_2O_3 (maghemite) crystallizes in a cubic or a tetragonal inverse spinel structure [17, 55], similar to the structure of Fe_3O_4 (see Fig. 2.4.3). The lattice constant of the cubic unit cell is $a = 0.8332\,\mathrm{nm}$, whereas the tetragonal supercell exhibits an approximately three times larger out-of-plane lattice constant of $c = 2.5113\,\mathrm{nm}$ [56]. The Fe^{3+} ions with $S = 5/2\hbar$ are located on octahedral as well as on tetrahedral lattice sites surrounded by O^{2-} ions. Additionally, Fe^{3+} vacancies are distributed on the octahedral sites [57]. In total, the cubic unit cell consists of eight units of $Fe^{3+}_A(Fe^{3+}_{5/3}\square_{1/3})_B O^{2-}_4$, where $\square$ denotes the vacancies, the index A the tetrahedral and the index B the octahedral sites [58]. Therefore, the vacancies partially compensate the positive charge of the Fe^{3+} ions to get charge neutrality in γ-Fe_2O_3. Depending on the degree of vacancy disorder, γ-Fe_2O_3 can be classified into the cubic crystal structure or the tetragonal one as extensively discussed in Ref. [55]. The insulating γ-Fe_2O_3 is ferrimagnetic below $T_\mathrm{C} = 950\,\mathrm{K}$ [50]. One ferromagnetic sublattice is formed by the Fe^{3+} moments on the octahedral sites, the other by the Fe^{3+} moments on the tetrahedral sites [17]. This results in a ferrimagnetic order, since the two sublattices are

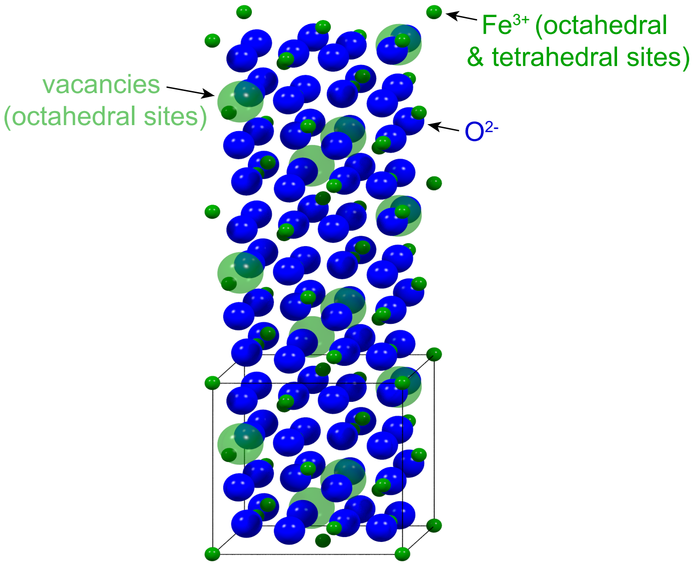

Figure 2.4.3.: Tetragonal unit cell of γ-Fe_2O_3 with Fe^{3+} ions in green, O^{2-} ions in blue, vacancies as larger, green, transparent spheres. The out of plane lattice constant c is three times the in plane lattice constant a. In case of disordered vacancy sites, γ-Fe_2O_3 appears in a cubic structure.

coupled antiferromagnetically to each other and more Fe^{3+} ions occupy octahedral sites than tetrahedral ones [59]. The ferrimagnetic structure results in a net magnetization of $400\,\mathrm{kA\,m^{-1}}$ at a temperature of $300\,\mathrm{K}$ [60].

2.4.3. Physical properties of Fe_3O_4

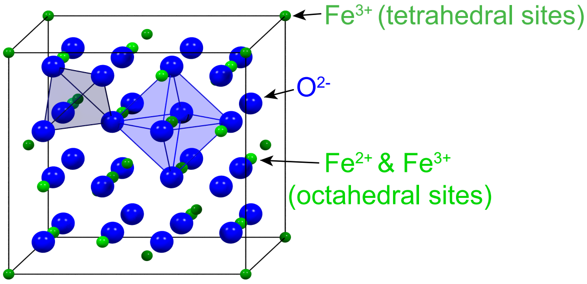

Figure 2.4.4.: Cubic unit cell of Fe_3O_4 ($Fe^{2+,3+}$ ions in green, O^{2-} ions in blue). The tetrahedral sites of Fe are depicted in dark green spheres and the octahedral sites in light green. Exemplarily, a tetrahedron and an octrahedron is shown in grey and blue, respectively.

Fe_3O_4 (magnetite) crystallizes in a cubic, inverse spinel structure similar to γ-Fe_2O_3 with a lattice constant $a = 0.8394\,\mathrm{nm}$ [61]. Thereby, Fe_3O_4 exhibits mixed Fe^{3+} and Fe^{2+} valences with $S = 5/2\hbar$ and $S = 2\hbar$, respectively. The Fe^{3+} ions occupy all tetrahedral A-sites and half of the octahedral B-sites. The other half of the octahedral B-sites is occupied by the Fe^{2+} ions. Analogous to γ-Fe_2O_3, also a Fe_3O_4 unit cell consists of eight formula units with the stoichiometry $Fe_A^{3+}(Fe^{3+}Fe^{2+})_B O_4^{2-}$ (cf. Fig. 2.4.4) [18]. Magnetite is ferrimagnetic below a Curie temperature of $T_C = 858\,\mathrm{K}$ with the ferromagnetically ordered sublattices formed by the dominating octahedral $Fe^{3+,2+}$ sites and by the tetrahedral Fe^{3+} sites [20, 62]. The magnetic sublattices are antiferromagnetically coupled with each other due to super exchange [18]. Bulk Fe_3O_4 reveals a magnetization of $471\,\mathrm{kA\,m^{-1}}$ at room temperature [63]. Fe_3O_4 shows structural and electronic phase transitions at the so-called Verwey transition temperature $T_V = 120\,\mathrm{K}$ [64, 65]. Above T_V Fe_3O_4 is a poor conductor, while below T_V it becomes insulating, which entails a phase change to a monoclinic crystal structure [19, 66]. The origin of this metal-insulator transition is the freeze-out of double exchange induced electron hopping between the octahedral Fe^{3+} and the octahedral Fe^{2+} ions [67, 68].

2.4.4. Effect of doping on the physical properties of α-Fe_2O_3 and γ-Fe_2O_3

Within this thesis α-Fe_2O_3 and γ-Fe_2O_3 thin films are doped using different dopants and varying the corresponding concentration level. In the following discussion, the occupation of interstital and vacancy sites or lattice disorder in general is neglected for simplification.

α-Fe_2O_3 thin films are doped with diamagnetic Ga^{3+} ions with $3d^{10}$ electronic configuration, which replace the octahedrally coordinated Fe^{3+} ions. Since the ionic radius r of Ga^{3+} is slightly smaller than the one of Fe^{3+} (cf. Table 2.4.1), a small decrease in the lattice constants and thus in the unit cell volume of α-Fe_2O_3 is expected. The magnetic sublattices of α-Fe_2O_3 are identical, but antiferromagnetically coupled to each other with a finite canting angle of the sublattices above the Morin temperature T_M. Replacing the magnetic Fe^{3+} ions with diamagnetic Ga^{3+} ions with completely filled $3d$-levels would lead to a statistically equal distribution of Ga^{3+} ions on octahedral lattice sites of both sublattices and therefore to a reduction of the net magnetization of α-Fe_2O_3 above T_M, assuming no effect on the Dzyaloshinskii-Moriya interaction and therefore on the canting angle δ. Below T_M, α-Fe_2O_3 exhibits an antiferromagnetic easy-axis with no net magnetization. Therefore, Ga^{3+}-doping of α-Fe_2O_3 should reduce the net sublattice magnetization. The Morin transition can be tuned drastically by doping due to the sensitivity of the competing magnetic-dipolar anisotropy and single-ion anisotropy on small changes. The magnetic-dipolar anisotropy prefers ip orientation of the magnetic Fe^{3+} moments, whereas the single-ion anisotropy prefers oop orientation, instead [53]. For instance, the incorporation of Ga^{3+} or Al^{3+} ions leads to a decrease in both anisotropy contributions [53, 69]. But since the single-ion anisotropy is more affected, an overall decrease of T_M occurs with increasing doping. Ab initio studies based on density functional theory within the local density approximation (LDA) reveal an insulating electric behavior of α-Fe_2O_3 doped with Ga^{3+} [70]. Therefore, α-$Fe_{2-x}Ga_xO_3$/Pt bilayers are still suitable candiates for the investigation of the SMR amplitude as a function of doping.

The effect of doping on the structural and magnetic properties of γ-Fe_2O_3 is not trivial due to the possibility of dopants occupying the octahedral as well as the tetrahedral Fe^{3+} lattice sites. With the incorporation of ions with similar, but slightly smaller ionic radii than Fe^{3+} ions, the unit cell volume should decrease. This should be the case for the dopants Al^{3+} with $2p^6$ electronic configuration and Ga^{3+} with $3d^{10}$ electronic configuration (cf. Table 2.4.1) [71]. In a simple picture taking only the ionic radii into account, Al^{3+} and Ga^{3+} dopants should slightly prefer the tetrahedral sites than the octahedral ones due to a stronger binding. This would lead to an increase in the magnetization M of γ-Fe_2O_3 as the magnetic moments on the tetrahedral sites oppose those on the octahedral sites.

Using Ir as a dopant in γ-Fe_2O_3 one has to consider the most common valence states, i.e. Ir^{3+} with $5d^6$ electronic configuration and Ir^{4+} with $5d^5$ electronic configuration, as presented in Table 2.4.1. Ir^{3+} has a slightly smaller and Ir^{4+} a slightly larger ionic radius than Fe^{3+}. Therefore, Ir^{3+} dopants lead to a decrease of the lattice constants and Ir^{4+} dopants to an increase of the lattice constants in γ-Fe_2O_3 [72]. Anyhow, due to their size the Ir ions are suggested to replace the Fe ions on the octahedral sites. Hence, a reduction in the magnetization is expected. Additionally, doping with Ir^{4+} ions could change the electronic structure of γ-Fe_2O_3 and thus changing the valence state of Fe^{3+}. The extra electron of Ir^{4+} compared to Fe^{3+} might partially reduce Fe^{3+} to Fe^{2+}. This might lead to double exchange mechanism between Fe^{3+} and Fe^{2+} ions as observed in Fe_3O_4 and thus increase the magnetization as well as the conductivity of the layer. However, due to large correlations, the mobility accompanied by a double exchange mechanism is expected to be suppressed as discussed for tetravalent doping of α-Fe_2O_3 [70].

The dopants Zn^{2+} and Ce^{4+} with $3d^{10}$ and $5p^6$ electronic configuration have greater ionic radii than Fe^{3+}. Therefore, doping γ-Fe_2O_3 with Zn^{2+} or Ce^{4+} should increase the unit cell volume [73, 74]. The larger ionic radii compared to Fe^{3+} should also lead to a preferred occupation of the octahedral lattice sites in γ-Fe_2O_3, which results in a decrease in M. The divalent Zn^{2+} and tetravalent Ce^{4+}-ions should further change the electronic properties of γ-Fe_2O_3. Similar to Ir^{4+}, the extra electron of Ce^{4+} might lead to finite Fe^{2+}-ions in the γ-Fe_2O_3 lattice [73]. This increases the magnetization of γ-Fe_2O_3 in analogy to γ-Fe_2O_3 doped with Ir^{4+}. In case of Zn^{2+}, the missing electron is expected to create a hole in the oxygen valence band, which should be easily ionized leading to a more p-type semiconductor behavior [70]. However, since γ-Fe_2O_3 crystallizes in the inverse spinel structure with $Fe_A^{3+}(Fe^{3+}_{5/3}\square_{1/3})_B O_4^{2-}$ (see Sec. 2.4.2), the dopands can also occupy vacancies on the octahedral B-sites or increase the vacancy disorder within the γ-Fe_2O_3-lattice. This demonstrates that the prediction of the magnetic and electric properties of doped γ-Fe_2O_3 is a challenging task.

	Al^{3+}	Ga^{3+}	Ir^{4+}	Fe^{3+}	Ir^{3+}	Zn^{2+}	Ce^{4+}
r (Å), octahedral sites	0.535	0.62	0.625	0.645	0.68	0.74	0.87
r (Å), tetrahedral sites	0.39	0.47		0.49		0.6	

Table 2.4.1.: Ionic radii r of the dopants Al^{3+}, Ga^{3+}, $Ir^{3+,4+}$, Zn^{2+} and Ce^{4+} according to Ref. [75] in an octahedral and a tetrahedral oxygen environment. The values for Fe^{3+} ions are given as a reference.

3. Investigation of the iron oxides α-Fe_2O_3, γ-Fe_2O_3 and Fe_3O_4

The following chapter provides a detailed analysis of thin films of α-Fe_2O_3 (hematite, Chapter 3.1), γ-Fe_2O_3 (maghemite, Chapter 3.2) and Fe_3O_4 (magnetite, Chapter 3.3) with respect to their structural, magnetic and magnetotransport properties. In particular, the spin Hall magnetoresistance (SMR) of thin films of these oxides covered with a top platinum (Pt) electrode is discussed. In conclusion (Chapter 5.1) all three iron oxides are compared to each other for a better understanding of their physical differences.

3.1. Physical properties of α-Fe_2O_3 thin films

The variety of structural, magnetic and magnetotransport properties of hematite thin films is discussed in the next Chapters 3.1.1, 3.1.2 and 3.1.3. Particular emphasis is placed on the properties of α-Fe_2O_3/Pt bilayers with respect to the antiferromagnetic spin Hall magnetoresistance (SMR).

3.1.1. Fabrication and structural analysis of α-Fe_2O_3 thin films

Hematite (α-Fe_2O_3) thin films are grown by pulsed laser deposition (PLD) on (0001)-oriented single crystalline sapphire (Al_2O_3) substrates. The PLD process is carried out utilizing a substrate temperature $T_S = 320\,^\circ\mathrm{C}$ in a pure oxygen atmosphere with a total pressure of $p_{O_2} = 25\,\mu\mathrm{bar}$ to avoid oxygen vacancies. An energy density at the target of $\rho_L = 2.5\,\mathrm{J\,cm^{-2}}$ and a repetition rate of $f = 2\,\mathrm{Hz}$ is used. In total, 20000 pulses devided in packages of 250 pulses with a relaxation time of $t_R = 10\,\mathrm{s}$ inbetween the packages is used. For α-Fe_2O_3/Pt bilayers platinum (Pt) is evaporated at room temperature and a pressure of about $2 \times 10^{-7}\mathrm{mbar}$ on top by electron beam evaporation (EVAP) in situ, without breaking the vacuum. Here the desired Pt thickness is set to $5\,\mathrm{nm}$ with a rate of $0.4\,\mathrm{Å\,s^{-1}}$. For a detailed description of the fabrication techniques it is referred to the Appendix A.1.1. The epitaxial relation between the hexagonal materials α-Fe_2O_3 and Al_2O_3 is as follows: α-Fe_2O_3 $[10\bar{1}0] \| Al_2O_3$ $[10\bar{1}0]$ and α-Fe_2O_3 $[0001] \| Al_2O_3$ $[0001]$. Since the lattice constants of the hexagonal unit cell of hematite ($a_{\alpha\text{-}Fe_2O_3,\,\mathrm{bulk}} = 0.5034\,\mathrm{nm}$, $c_{\alpha\text{-}Fe_2O_3,\,\mathrm{bulk}} = 1.3752\,\mathrm{nm}$) and sapphire ($a_{Al_2O_3} = 0.4759\,\mathrm{nm}$, $c_{Al_2O_3} = 1.2997\,\mathrm{nm}$) differ greatly, the respective large lattice mismatch of $\epsilon = (a_{\alpha\text{-}Fe_2O_3,\,\mathrm{bulk}} - a_{Al_2O_3})/a_{Al_2O_3} = 5.8\,\%$ should result in a fully relaxed growth of α-Fe_2O_3 on Al_2O_3 [48, 76].

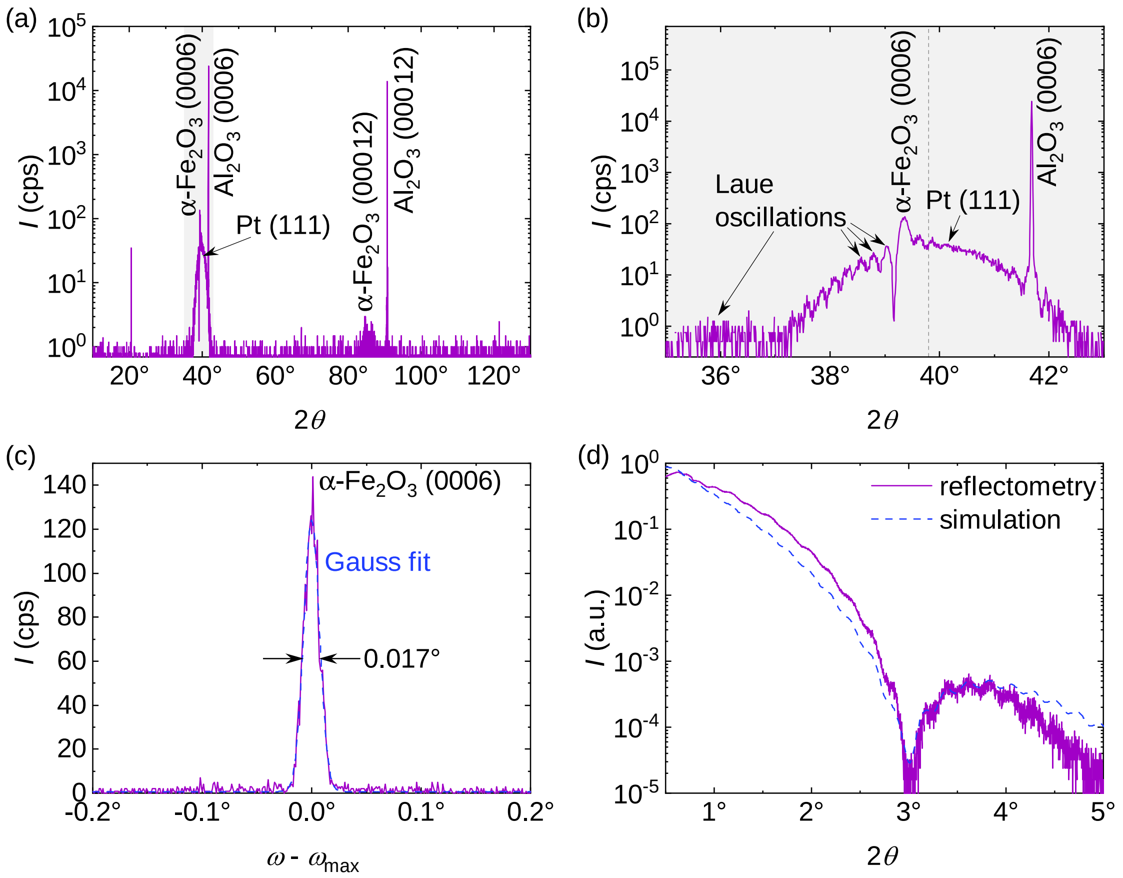

Figure 3.1.1.: High resolution X-ray diffraction of a α-Fe_2O_3/Pt bilayer on a Al_2O_3 (0001) substrate. (a) 2θ-ω scan containing the (0006) and (000 12) reflections of both the α-Fe_2O_3 thin film and the Al_2O_3 substrate. Additionally, the Pt (111) reflection appears beneath the α-Fe_2O_3 (0006) reflection. (b) For a better illustration it is zoomed into the grey region, where Laue oscillations around the α-Fe_2O_3 and the Pt thin film reflections are visible. The bulk value for Pt (111) is displayed as a dashed grey line [11]. (c) Rocking curve around the α-Fe_2O_3 (0006) reflection having a small full width at half maximum (FWHM) of $0.017°$ extracted from the Gauss fit shown as dashed blue lines. ω is shifted by its maximum value ω_{max}. (d) X-ray reflectivity data (purple line) and simulation (blue dashed line) to obtain the layer thicknesses of α-Fe_2O_3 and Pt.

The crystalline quality, the thicknesses as well as the epitaxial strain of the α-Fe_2O_3/Pt bilayers on Al_2O_3 (0001) are analyzed by high-resolution X-ray diffractometry (HR-XRD, see Appendix A.1.2.1 for further information). Figure 3.1.1 provides an overview of the measurement results of a α-Fe_2O_3/Pt bilayer. The 2θ-ω scan in (a) over a large range from $2\theta = 10°$ to $2\theta = 130°$ reveals the Bragg reflections (0006) and (000 12) of the thin film and the substrate. The thin film (substrate) reflections are located at $39.36°$ ($41.68°$) and at $84.61°$ ($90.71°$) for the (0006) and (000 12) reflection, respectively. Using the Bragg condition (see Eq. (A.1)) and the 2θ value of α-Fe_2O_3 (0006) an out-of-plane lattice constant of $c_{\alpha\text{-}Fe_2O_3} = (1.372 \pm 0.003)\,\mathrm{nm}$ can be calculated. Additionally, a background appears beneath the α-Fe_2O_3 (0006) reflection, which can be identified as the Pt (111) reflection so that also the Pt electrode is in a crystalline state. The peak at $2\theta = 20.50°$ can be attributed to the Al_2O_3 (0003) substrate reflection, which should be ideally forbidden. Otherwise the 2θ-ω scan reveals only Bragg reflections of the substrate, the thin film and the platinum electrode and no other crystalline phases.

For a more detailed analysis it is zoomed into the grey region of the wide range 2θ-ω scan (see Fig. 3.1.1 (b)). Clearly visible are Laue oscillations around the α-Fe_2O_3 (0006) reflection and the Pt (111) reflection indicating a coherent growth and thus a good crystalline quality of the thin films. The dashed vertical line marks the bulk value of Pt (111) of $39.8°$ [11]. The rocking curve around α-Fe_2O_3 (0006) is fitted with a Gaussian function with a small full width at half maximum (FWHM) of $0.017°$ (see Fig. 3.1.1 (c)). This result shows a low mosaic spread and again confirms a high crystalline quality of the α-Fe_2O_3 thin film on Al_2O_3. To obtain the thicknesses of the α-Fe_2O_3 thin film and the Pt electrode X-ray reflectometry scans from $2\theta = 0.5°$ to $5°$ are performed and simulated with the software LEPTOS (see Fig. 3.1.1 (d)). There the wider Kiessig fringes are associated with the Pt layer and the narrow fringes with the α-Fe_2O_3 thin film. From the simulation of the reflectometry data a thickness of $t_{\alpha\text{-Fe}_2\text{O}_3} = (37.6 \pm 0.3)\,\mathrm{nm}$ and $t_{\mathrm{Pt}} = (3.2 \pm 0.1)\,\mathrm{nm}$ is extracted. For the α-Fe_2O_3 layer a thickness of approximately $45\,\mathrm{nm}$ is expected assuming the same growth rate as reported by Fischer *et al.* [11, 12]. The value for $t_{\alpha\text{-Fe}_2\text{O}_3}$ indicates a slightly smaller growth rate. The thickness of the Pt layer is approximately twice the spin diffusion length of electrons in Pt ($\lambda_{\mathrm{sf}} \approx 1.5\,\mathrm{nm}$) and therefore favorable for a maximum SMR signal (cf. Sec. 2.3.3). In summary the above given growth parameters for the PLD and EVAP deposition process yield α-Fe_2O_3/Pt bilayers with excellent structural properties.

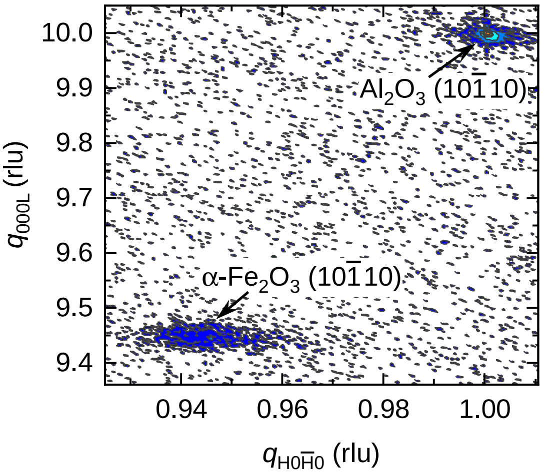

Figure 3.1.2.: Reciprocal space mapping around the asymmetric $(10\bar{1}\,10)$ substrate and thin film reflections of a α-Fe_2O_3/Pt bilayer. The units are given in terms of the reciprocal lattice vector of the Al_2O_3 substrate.

To get further information about the strain state of the α-Fe_2O_3 thin film on Al_2O_3 (0001) a reciprocal space mapping around the asymmetric $(10\bar{1}\,10)$ reflection is carried out, which is shown in Fig. 3.1.2 (given in units of the reciprocal lattice vector of Al_2O_3). The thin film reflection is located far away from the substrate reflection, indicating a relaxed growth of α-Fe_2O_3 on Al_2O_3 (0001). For a precise determination of the positions of the reflections line scans are executed along the $[H0\bar{H}0]$- and the $[000L]$-direction through the thin film and the substrate reflection. From fitting these line scans with a Gaussian function the exact peak positions can be extracted and therefore the lattice constants can be calculated with Eq. (A.6) (see Appendix A.1.2.1). The Gauss fits reveal the position of the α-Fe_2O_3 $(10\bar{1}\,10)$ reflection at $q_{\mathrm{H0\bar{H}0}} = 0.9442\,\mathrm{rlu}$ and $q_{\mathrm{000L}} = 9.4496\,\mathrm{rlu}$, which leads to an in-plane lattice constant of $a_{\alpha\text{-Fe}_2\text{O}_3} = (0.504 \pm 0.003)\,\mathrm{nm}$ and an out-of-plane lattice constant of $c_{\alpha\text{-Fe}_2\text{O}_3} = (1.375 \pm 0.001)\,\mathrm{nm}$. The epitaxial strain in the thin film plane is $\epsilon_{\mathrm{xx}} = (a_{\alpha\text{-Fe}_2\text{O}_3} - a_{\alpha\text{-Fe}_2\text{O}_3,\,\mathrm{bulk}})/a_{\alpha\text{-Fe}_2\text{O}_3,\,\mathrm{bulk}} = 0.1\,\%$, which is small confirming a nearly fully relaxed growth of α-Fe_2O_3 on Al_2O_3 (0001). Since also the out-of-plane strain is small ($\epsilon_{\mathrm{zz}} = (c_{\alpha\text{-Fe}_2\text{O}_3} - c_{\alpha\text{-Fe}_2\text{O}_3,\,\mathrm{bulk}})/c_{\alpha\text{-Fe}_2\text{O}_3,\,\mathrm{bulk}} = -0.03\,\%$), the change in the unit cell volume is negligible. This demonstrates the growth of a relaxed α-Fe_2O_3 thin film and indicates the correct stochiometry.

3.1.2. Magnetic properties of α-Fe_2O_3 thin films

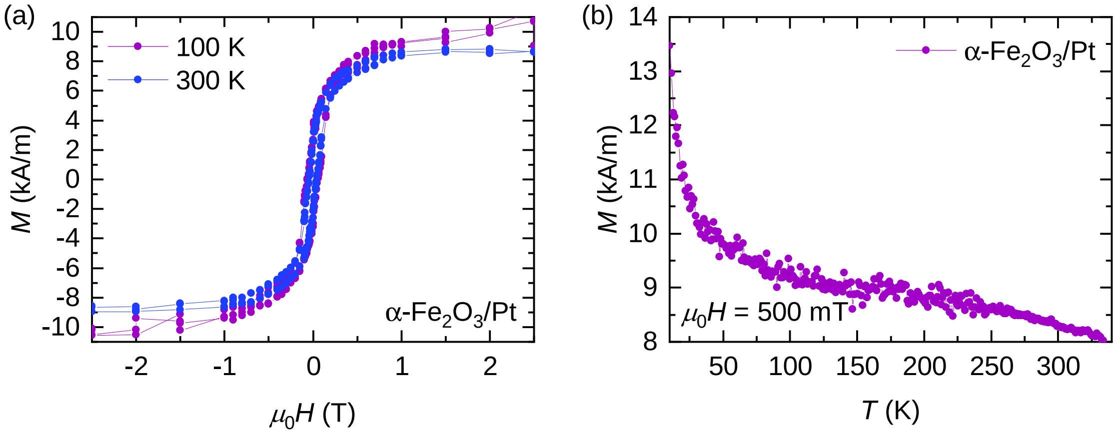

Figure 3.1.3.: In-plane SQUID magnetometry measurements performed on a α-Fe_2O_3/Pt bilayer. A linear background including the diamagnetic signal of the Al_2O_3 substrate was subtracted to obtain (a) the magnetic field and (b) the temperature dependence of the thin film magnetization. The narrow hysteresis loops measured at $100\,\mathrm{K}$ and $300\,\mathrm{K}$ saturate approximately at $10\,\mathrm{kA\,m^{-1}}$ and $8.7\,\mathrm{kA\,m^{-1}}$ at a magnetic field of $1.5\,\mathrm{T}$. For the temperature dependent measurement of the magnetization a magnetic field of $500\,\mathrm{mT}$ is used after cooling the sample in a magnetic field of $7\,\mathrm{T}$.

The magnetic properties of the α-Fe_2O_3/Pt bilayer are investigated via superconducting quantum interference device (SQUID) magnetometry (see also Appendix A.1.2.3 for technical details). In Fig. 3.1.3 (a) the in-plane hysteresis loops measured at $100\,\mathrm{K}$ and $300\,\mathrm{K}$ are depicted. A linear background is subtracted beforehand, which is originating from the diamagnetic Al_2O_3 substrate, the paramagnetic Pt electrode and the increasing spin canting in α-Fe_2O_3 with increasing magnetic field $\mu_0 H$. Above the Morin-transition, α-Fe_2O_3 is a canted antiferromagnet resulting in a continuous increase of M with $\mu_0 H$ due to the increasing canting of the sublattice magnetizations. Because of the linear background subtraction this contribution to M is also deducted. The saturation magnetization M_{S} is here (Fig. 3.1.3 (a)) defined as the point, where the hysteresis just starts to saturate because of the finally reached monodomainization of the thin film. M_S is then the result of the DMI induced canting of the magnetic sublattices. This leads to $M_S = (10\pm2)\,\mathrm{kA\,m^{-1}}$ at $(1.5\pm0.5)\,\mathrm{T}$ at $100\,\mathrm{K}$ and $M_S = (8.7\pm0.2)\,\mathrm{kA\,m^{-1}}$ at $(1.5\pm0.5)\,\mathrm{T}$ and $300\,\mathrm{K}$. The value at $300\,\mathrm{K}$ is slightly reduced in comparison to a literature value of approximately $10\,\mathrm{kA\,m^{-1}}$ at $350\,\mathrm{K}$ [12]. Another α-Fe_2O_3 thin film, which was fabricated and will not be further discussed in this thesis, reveals a M_S of $(14.0 \pm 0.3)\,\mathrm{kA\,m^{-1}}$ at $300\,\mathrm{K}$. Therefore, on average the obtained M_S of the α-Fe_2O_3 thin films seem to agree with other reported values [10, 12]. Comparing the hysteresis loops measured at $300\,\mathrm{K}$ and $100\,\mathrm{K}$, i.e., above and below the Morin transition temperature $T_{\mathrm{M,\,bulk}} = 263\,\mathrm{K}$ [77], no obvious changes are observed except for the higher M_S value at $100\,\mathrm{K}$. The coercitive fields H_c are very small with $(57 \pm 3)\,\mathrm{mT}$ at $100\,\mathrm{K}$ and $(45.8 \pm 0.2)\,\mathrm{mT}$ at $300\,\mathrm{K}$.

The temperature dependence of the magnetization M over a range of $10\,\mathrm{K}$ to $340\,\mathrm{K}$ and an in-plane applied magnetic field of $\mu_0 H = 500\,\mathrm{mT}$ is shown in Fig. 3.1.3 (b). Before the $M(T)$ measurement the sample was cooled down in a magnetic field of $7\,\mathrm{T}$. The Morin transition cannot be observed in the α-Fe_2O_3 thin film in contrast to the measured polycrystalline α-Fe_2O_3 powder in Fig. 2.4.2. The suppression of the Morin transition can be based on multiple possibilities leading to a change in the magnetic anisotropy. Above T_M an orientation of the magnetic moments in the thin film plane (c plane) is preferred (cf. Sec. 2.4.1). An additional induced anisotropy in the thin films can shift T_M towards lower temperatures so that an in-plane orientation of the magnetic moments is energetically favorable over a wider temperature range. Firstly, the general reduction of T_M with decreasing thin film thickness can be due to a possible strain-induced magnetic anisotropy [78, 79] or due to size effects of the thin films [77]. But the α-Fe_2O_3 thin films discussed in this thesis exhibit a nearly relaxed growth on the Al_2O_3 substrates compared to bulk α-Fe_2O_3, which makes a strain-induced magnetic anisotropy less likely. In case of ferromagnetic thin films a reduction in the magnetic stray fields is obtained by a preferred in-plane orientation of the magnetic moments. But here, the canted antiferromagnet α-Fe_2O_3 just has a small net magnetization, which makes stray fields and thus size effects also negligibly small. Additionally, a finite density of oxygen vacancies could also cause the absence of the Morin transition due to a possible partial reduction of the Fe^{3+} ions to Fe^{2+} and therefore a change in the magnetic anisotropy (cf. Ref. [80]). The magnetic hysteresis loops as well as the temperature dependence of the magnetization thus reveal that the magnetic moments in the α-Fe_2O_3 thin film lie in the magnetic easy plane with a finite canting between the magnetic sublattices down to $10\,\mathrm{K}$. The corresponding canting angle δ can be calculated with $\sin(\delta) = M_S/(2S\mu_B n_{Fe^{3+}})$. Here the Fe^{3+} ions in α-Fe_2O_3 have a spin quantum number of $S = 5/2$ and an ion density of $n_{Fe^{3+}} = 39.76\,\mathrm{nm^{-3}}$. With $M_S = 8.68\,\mathrm{kA\,m^{-1}}$ (at $300\,\mathrm{K}$) and Bohr's magneton μ_B one gets $\delta = 0.27°$ at a magnetic field of $1.5\,\mathrm{T}$. This is comparable to values found for previous α-Fe_2O_3 thin films [12]. In addition in Fig. 3.1.3 (b) a slight increase of M is observed at low T most likely due to the existance of localized magnetic moments in the Al_2O_3 substrate.

3.1.3. Magnetotransport measurements on α-Fe$_2$O$_3$/Pt bilayers

To investigate the spin Hall magnetoresistance (SMR) of α-Fe$_2$O$_3$/Pt bilayers, angle-dependent magnetoresistance (ADMR) measurements are carried out. To this end, the Pt thin film is patterned into two Hall bar mesa-structures via optical lithography and argon ion milling (see Appendix A.1.1.3 for technical details). The Hall bars are perpendicular to each other and parallel to the corresponding sample edges so that the applied current I_c of 100 µA flows parallel and perpendicular to the crystallographic [$10\bar{1}0$] direction. The ADMR measurements are performed at 300 K in all three different rotations of the magnetic field direction $\mathbf{h}$ in relation to the thin film plane and the charge current direction $\mathbf{j}$ (ip, oopj and oopt, see Sec. 2.3). Thereby, the longitudinal and transverse voltages V_{long} and V_{trans} are measured in a standard four probe technique using the current reversal method. For further information about ADMR measurements and the current reversal method it is referred to Appendix A.1.2.5. The corresponding resistivities are calculated according to $\rho_{\mathrm{long}} = V_{\mathrm{long}} w t_{\mathrm{Pt}}/(I_c l)$ and $\rho_{\mathrm{trans}} = V_{\mathrm{trans}} t_{\mathrm{Pt}}/I_c$ with a charge current of $I_c = 100\,\mu\mathrm{m}$, a Hall bar width of $w = 80\,\mu\mathrm{m}$ and a distance of $l = 600\,\mu\mathrm{m}$ between contacted Hall bar pads. The resistivities are normalized to the normal resisitivity ρ_0 of the Pt electrode, which is approximately $458\,\mathrm{n\Omega\,m}$ and thus in good agreement with reported values for Pt [81]. For the data shown in Fig. 3.1.4, the voltages are recorded while applying a magnetic field magnitude of $\mu_0 H = 7\,\mathrm{T}$.

An applied magnetic field $\mu_0 H = 7\,\mathrm{T}$ is large enough to align the Néel vector $\mathbf{l}$ along $\mathbf{h}$. For ρ_{long} and ρ_{trans} measured in the thin film plane the expected spin Hall magnetoresistance (SMR) effect for antiferromagnetic insulator/ heavy metal (AFI/HM) bilayers is observed and can be explained analogously to the theory presented in Sec. 2.3. Thereby, the 90° phase shift in $\rho_{\mathrm{long,\,ip}}$ in comparison to ferrimagnetic insulator/heavy metal (FMI/HM) bilayers should be emphasized. As indicated in Fig. 3.1.4, the longitudinal SMR amplitude $\mathrm{SMR}_{\mathrm{long}} = \rho_1/\rho_0$ can be determined via the oscillation amplitude and the transverse SMR amplitude $\mathrm{SMR}_{\mathrm{trans}} = \rho_3/\rho_0$ as twice the oscillation amplitude in ip-ADMR measurements. The ip-data are fitted to Eqs. (2.9) and (2.10). In oopj (oopt) rotation ρ_{long} stays in its maximum (minimum) resistive state except for $\beta(\gamma) \approx 0°, 180°$ and $360°$, i.e., for $\mathbf{h} \parallel \mathbf{n}$. As discussed in Sec. 2.3.2 a complex domain structure exists within the magnetically easy plane of α-Fe$_2$O$_3$. For the ip rotation the high magnetic field magnitude of 7 T leads to a monodomainization, whereas for $\mathbf{h} \parallel \mathbf{n}$ with the magnetic field aligned perpendicular to the easy plane, a multi domain state in the plane of α-Fe$_2$O$_3$ exists. This minimizes (maximizes) the resistivity, because not every Néel vector $\mathbf{l}$ of the respective domains is perpendicular (parallel) to the spin polarization s of the conduction electrons in the Pt electrode. But in contrast to the theory (see Eq. (2.14)), $\rho_{\mathrm{long,\,oop}}$ does not reach $\rho_{\mathrm{long}}/\rho_0 - 1 = \mathrm{SMR}_{\mathrm{long}}/2$ at $\beta = \gamma = 0°$ and $180°$. This might be due to deviations from the theoretical three-domain structure in terms of an unequal distribution of the domains. The domains are then affecting ρ_{long} differently depending on their fractions ξ_k. The deviation might be explained by a small misalignment of the sample with respect of the magnetic field rotation

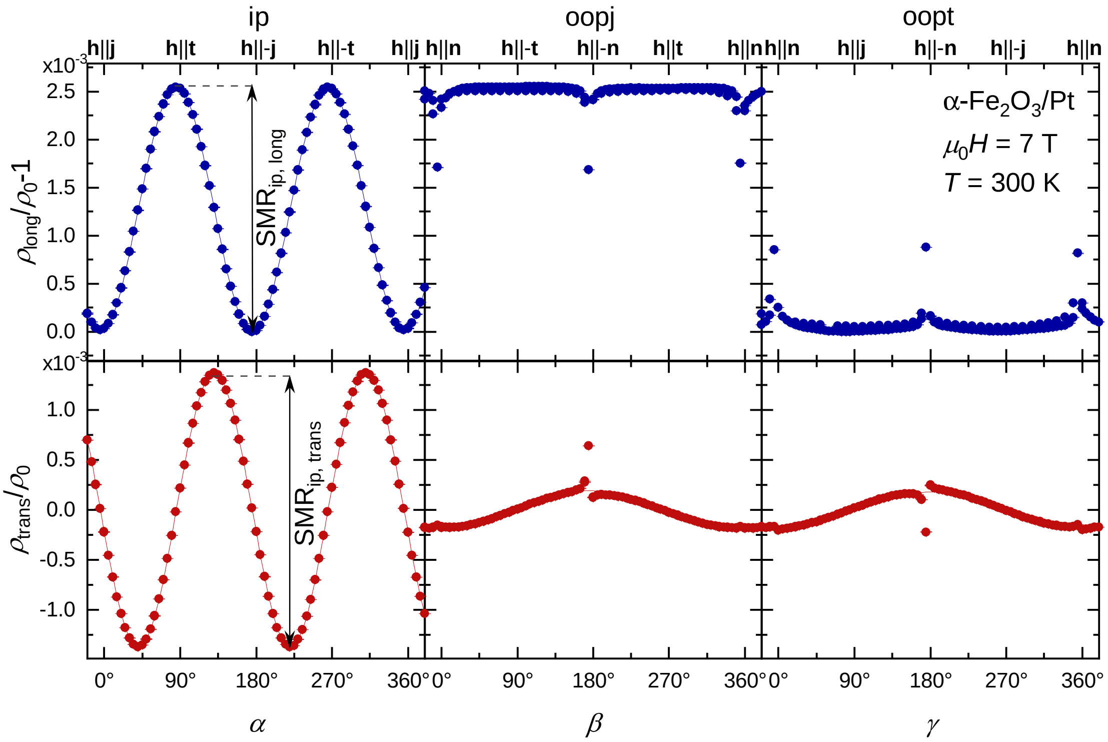

Figure 3.1.4.: ADMR of a α-Fe$_2$O$_3$/Pt bilayer using three rotation planes of the magnetic field (ip, oopj and oopt) at 300 K and 7 T. The normalized longitudinal resistivities (top panels) are depicted as blue and the transverse resistivites as red dots (bottom panels). The lines are fits to the ip-data according to Eqs. (2.9) and (2.10) describing the antiferromagnetic SMR effect and to the transverse oop-data according to Eqs. (2.8).

plane resulting in a finite magnetic field contribution in the plane of the thin film even for a nominal alignment of the magnetic field perpendicular to the plane ($\mathbf{h} \parallel \mathbf{n}$). The abrupt jumps in ρ_{oop} for $\mathbf{h}$ close to $\mathbf{n}$ indicate an abrupt change of the domain configuration of α-Fe$_2$O$_3$ from a multi-domain state to a single-domain state caused by the finite in-plane projection of the magnetic field and because of a small monodomainization field $\mu_0 H_{\text{MD}}$. Equations (2.10) claim zero transverse resistivity in oopj and oopt magnetic field rotations, but instead finite angle-dependence around zero with a periodicity of 360° is visible in Fig. 3.1.4. So the projections $m_{\text{n}}^{\text{A, B}}$ of the sublattice magnetizations $\mathbf{m}^{\text{A, B}}$ on the surface normal $\mathbf{n}$ do not stay zero during a full 360° rotation of $\mathbf{h}$ around $\mathbf{j}$ (oopj) and $\mathbf{t}$ (oopt). This might additionally prove a small but finite misalignment of the sample with respect to the rotation plane of the magnetic field.

To get a better understanding of the SMR amplitude and its magnetic field dependence ip ADMR measurements are performed at different magnetic field magnitudes starting from 7 T down to 0 T at a constant temperature of 300 K. The extracted SMR amplitudes SMR$_{\text{ip, long}}$ and SMR$_{\text{ip, trans}}$ are depicted in Fig. 3.1.5. In (a) a saturation of both SMR$_{\text{ip, long}}$ and SMR$_{\text{ip, trans}}$ is clearly visible at about 3 T. Surprisingly, this value is much larger than the monodomainization field of 0.24 T previously reported for thin films α-Fe$_2$O$_3$ [10] and also larger than $\mu_0 H_{\text{S}} = 1.5$ T determined via SQUID magnetometry. This could be due

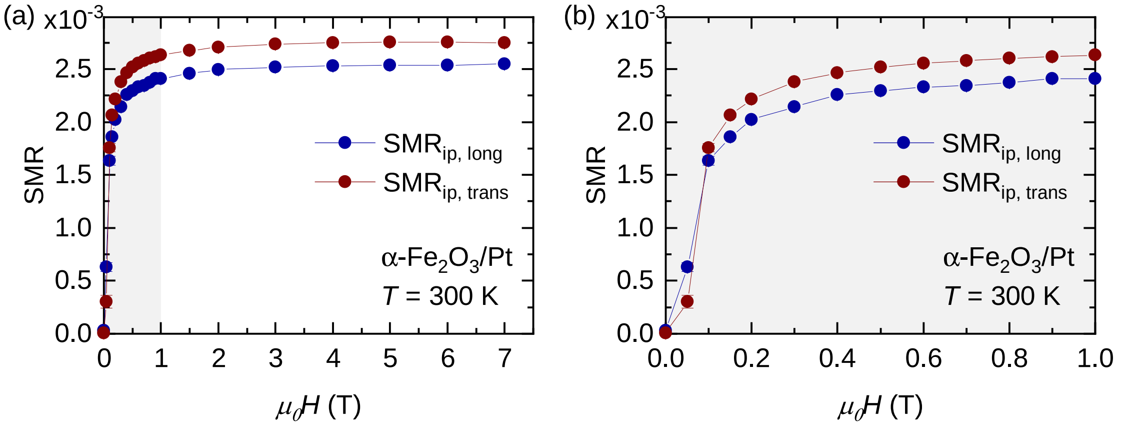

Figure 3.1.5.: Longitudinal (blue) and transverse (red) SMR amplitudes as a function of the applied magnetic field $\mu_0 H$ at 300 K. The amplitudes were extracted from the in-plane ADMR measurements at different magnetic fields (see Fig. 3.1.4). (b) Zooming into the grey region reveals that $\mathrm{SMR}_{\mathrm{ip,\,trans}}$ exceeds $\mathrm{SMR}_{\mathrm{ip,\,long}}$ at small magnetic fields.

to pinning effects of the domain walls in α-Fe_2O_3 [10]. The SMR amplitudes reach a maximum value of 2.55×10^{-3} and 2.75×10^{-3} for the in-plane longitudinal and transverse SMR, respectively. This is close to the $\mathrm{SMR}_{\mathrm{ip,\,long}}$ value reported in Ref. [12] indicating a similar high quality of the α-Fe_2O_3/Pt bilayer. At magnetic fields larger than 100 mT, $\mathrm{SMR}_{\mathrm{ip,\,trans}}$ exceeds $\mathrm{SMR}_{\mathrm{ip,\,long}}$, which could be explained once again by the domain structure in α-Fe_2O_3. The magnetic domains could be big enough to exceed the width w of the Hall bar, but not the distance l between Hall bar pads, where V_{long} is measured. The domain walls lead to a reduction of $\mathrm{SMR}_{\mathrm{ip,\,long}}$ also far above the monodomainization field, since it is not possible to eliminate 180° domains (see Sec. 2.3.2) [12]. In Fig. 3.1.5 (b) the behavior of the SMR at small magnetic fields ($H < H_{\mathrm{MD}}$) exhibits similar values for $\mathrm{SMR}_{\mathrm{ip,\,long}}$ and $\mathrm{SMR}_{\mathrm{ip,\,trans}}$ from 0 T to 0.1 T. Very special is the large SMR amplitude of α-Fe_2O_3/Pt of $\mathrm{SMR}_{\mathrm{ip,\,long}} = 2.55 \times 10^{-3}$ in comparison to $\mathrm{SMR}_{\mathrm{ip,\,long}} = 1.3 \times 10^{-3}$ for $Y_3Fe_5O_{12}$(YIG)/Pt bilayers [10]. A possible explanation for the enhanced SMR effect could be found in analyzing the influence of the magnetic moment density on the SMR, which will be discussed in Chapter 4. Zhou *et al.* demonstrated an even higher SMR amplitude of 3.5×10^{-3} for a α-Fe_2O_3/Pt bilayer on Al_2O_3 measured at 300 K and 5 T [82]. In their case the Pt thickness is larger ($t_{\mathrm{Pt}} = 5\,\mathrm{nm}$), which should result in an even larger SMR amplitude for bilayers with a Pt thickness of 3 nm used in the framework of this theis. However, this crucially depends on the diffusion length of the used Pt [28]. The difference in the SMR amplitudes could stem from differences in the interface quality.

3.2. Physical properties of γ-Fe_2O_3 thin films

In this chapter the γ-phase of Fe_2O_3 is analyzed. For the spinel structured, ferrimagnetic γ-Fe_2O_3 thin films, the structural and magnetic properties are presented in Sections 3.2.1 and 3.2.2. Finally, Section 3.2.3 deals with the magnetotransport properties of γ-Fe_2O_3/Pt bilayers with respect to their spin Hall magnetoresistance effect.

3.2.1. Fabrication and structural analysis of γ-Fe_2O_3 thin films

Fe_2O_3 can exist in a variety of possible cystalline structures with different magnetic arrangements. Besides the antiferromagnetic, hexagonal α-Fe_2O_3 (hematite), also the ferrimagnetic γ-Fe_2O_3 (maghemite) is prominent, which orders in a cubic or tetragonal structure depending on the iron vacancies (see Sec. 2.4.2, Ref. [55]). For the realization of γ-Fe_2O_3 thin films the same growth parameters are used as for the α-Fe_2O_3 thin films (Sec. 3.1.1) such as $f = 2\,\mathrm{Hz}$, $\rho_L = 2.5\,\mathrm{J\,cm^{-2}}$, $T_S = 320\,°\mathrm{C}$ and $p_{O_2} = 25\,\mathrm{\mu bar}$. However, cubic MgO (001) substrates are used instead of hexagonal Al_2O_3 (0001) substrates for providing an in-plane cubic structure for the PLD thin film growth. In addition to γ-Fe_2O_3 thin films, also γ-Fe_2O_3/Pt bilayers are fabricated, where the Pt layer is deposited on top of the γ-Fe_2O_3 thin film in situ, without breaking the vacuum using EVAP with similar parameters as discribed in Sec. 3.1.1. One γ-Fe_2O_3 unit cell grows on four MgO unit cells so that the lattice mismatch is $\epsilon = (a_{\gamma\text{-}Fe_2O_3,\,\mathrm{bulk}} - 2a_{\mathrm{MgO}})/(2a_{\mathrm{MgO}}) = -1.1\,\%$ with $a_{\gamma\text{-}Fe_2O_3,\,\mathrm{bulk}} = 0.8332\,\mathrm{nm}$ and $a_{\mathrm{MgO}} = 0.4212\,\mathrm{nm}$ [56, 83]. Hereby, the epitaxial relation is γ-Fe_2O_3 [100]||MgO [100] and γ-Fe_2O_3 [001]||MgO [001].

Analogously to the characterization of α-Fe_2O_3/Pt in Chapter 3.1.1, HR-XRD scans (Fig. 3.2.1) are performed on the γ-Fe_2O_3 thin film without Pt on top (blue) and on the γ-Fe_2O_3/Pt bilayer (purple). Figure 3.2.1 (a) depicts a 2θ-ω scan over the entire 2θ-range revealing the reflections γ-Fe_2O_3 (004) and MgO (002) as well as γ-Fe_2O_3 (008) and MgO (004). No other crystalline iron oxide phases are visible. Zooming into the region around the MgO (002) reflection reveals Laue oscillations not only for the single γ-Fe_2O_3 thin film, but also for the γ-Fe_2O_3/Pt bilayer sample indicating a coherent high crystalline growth of γ-Fe_2O_3. From the 2θ positions of the γ-Fe_2O_3 (004) reflections of $43.39°$ and $43.43°$ for the single γ-Fe_2O_3 thin film and γ-Fe_2O_3/Pt bilayer sample the out-of-plane lattice constant c is calculated, resulting in $(0.833 \pm 0.004)\,\mathrm{nm}$ (γ-Fe_2O_3 sample) and $(0.834 \pm 0.004)\,\mathrm{nm}$ (γ-Fe_2O_3/Pt sample). In Fig. 3.2.1 (c) the rocking curves around the γ-Fe_2O_3 (004) reflection are fitted with Gaussian functions with FWHMs of only $0.019°$ and $0.015°$, which confirms a good crystalline quality of the γ-Fe_2O_3 thin films of both samples. But in case of the γ-Fe_2O_3/Pt bilayer (purple line), multiple peaks can be observed due to the MgO substrate consisting of several crystallites. The simulations of the reflectometry scans (cf. Fig. 3.2.1 (d)) provide a γ-Fe_2O_3 thin film thicknesses of $t_{\gamma\text{-}Fe_2O_3} = (44.6 \pm 0.3)\,\mathrm{nm}$ and $t_{\gamma\text{-}Fe_2O_3} = (18.4 \pm 0.3)\,\mathrm{nm}$ for the single γ-Fe_2O_3 thin film and γ-Fe_2O_3/Pt bilayer samples, respectively. Furthermore, a thickness of $t_{\mathrm{Pt}} = (3.6 \pm 0.1)\,\mathrm{nm}$ of the Pt layer of the γ-Fe_2O_3/Pt bilayer sample can be extracted. Although the same growth parameters with a number of 20000 pulses are used for both γ-Fe_2O_3 thin films, the growth rates and so the thicknesses differ greatly. The measured energy at the target at the beginning of the growth process is just slightly smaller for the γ-Fe_2O_3/Pt bilayer than for the thin film without Pt on top ($48.33\,\mathrm{mJ}$ in comparison to $50.76\,\mathrm{mJ}$). This cannot explain the huge difference in

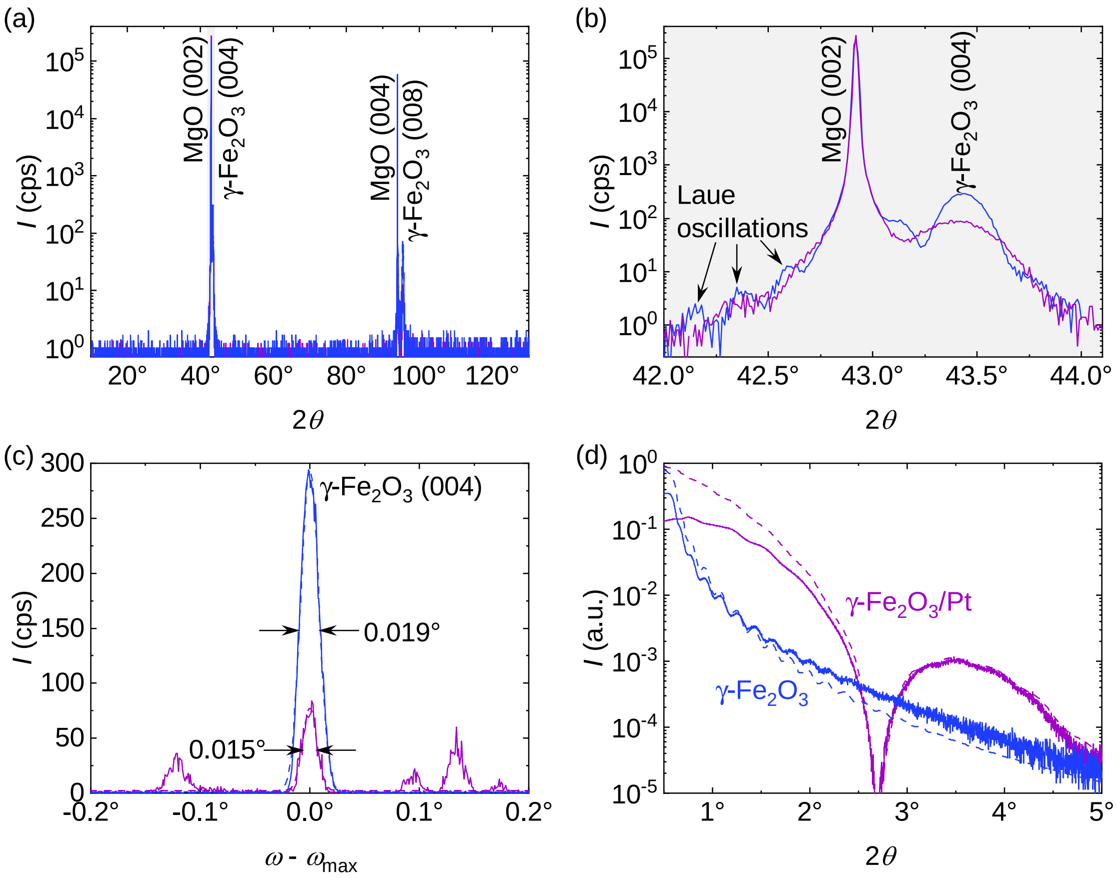

Figure 3.2.1.: X-ray diffraction of a γ-Fe_2O_3 thin film (in blue) and a γ-Fe_2O_3/Pt bilayer (in purple) on MgO (001) substrates. (a) 2θ-ω scan exhibiting only the (004) and the (008) reflections of γ-Fe_2O_3 together with the corresponding substrate reflections. Laue oscillations around the MgO (002) reflection are visible in the enlargement in (b). (c) Rocking curves around the γ-Fe_2O_3 (004) reflection fitted with Gaussian functions with FWHMs of $0.019°$ and $0.015°$. The additional reflections stem from the non-single crystallinity of the MgO substrate. The ω-angle is shifted by the angle of the maximum intensity $\omega_{\max}$. (d) X-ray reflectometry scans (solid lines) of the γ-Fe_2O_3 thin film sample and the γ-Fe_2O_3/Pt bilayer sample. For both samples the reflectometry scans are simulated to extract the thickness of the γ-Fe_2O_3 layer $t_{\mathrm{Fe_2O_3}}$ and the Pt thickness t_{Pt} (simulation curves in dashed lines).

growth rate. However, in case of the γ-Fe_2O_3/Pt bilayer, the excimer laser hit the target on an outer position than usual. This could have affected the growth rate. More important is the fact that t_{Pt} is in a range, for which the SMR amplitude shows a maximum value, i.e., at twice the spin diffusion length λ_{sf} of approximately $1.5\,\mathrm{nm}$ (see Sec. 2.3.3).

Additionally, reciprocal space maps (RSMs) of the γ-Fe_2O_3 thin film (without Pt on top) are shown in Fig. 3.2.2. The mappings are done around the symmetric MgO (002) and γ-Fe_2O_3 (004) reflections (a) and the asymmetric MgO (204) and γ-Fe_2O_3 (408) reflections (b). The same applies for the RSM of the γ-Fe_2O_3/Pt bilayer in Fig. A.3.1. For further information about the RSM of the γ-Fe_2O_3/Pt bilayer it is referred to the Appendix A.3. From the position of the γ-Fe_2O_3 (004) reflection $q_{00\mathrm{L}} = 2.0224$ the out-of-plane lattice constant $c_{\gamma\text{-}\mathrm{Fe_2O_3}}$ is determined by using Eq. (A.6) and taking into account a tetragonal

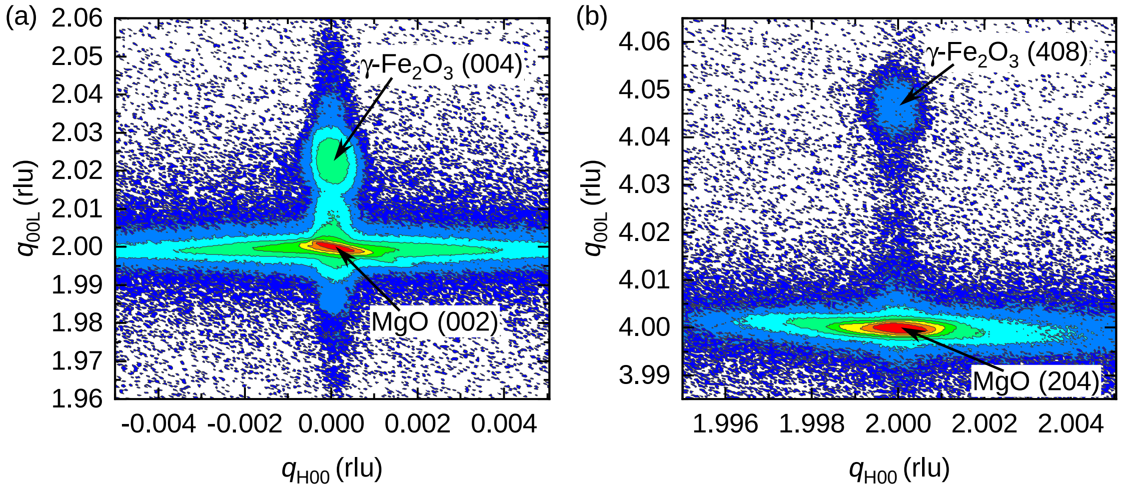

Figure 3.2.2.: Reciprocal space mapping around (a) the symmetric γ-Fe_2O_3 (004) and (b) the asymmetric γ-Fe_2O_3 (408) reflection of the γ-Fe_2O_3 thin film without a top Pt electrode. The corresponding substrate reflections are (a) MgO (002) and (b) MgO (204) and the units are given in reciprocal lattice units (rlu) with respect to the MgO substrate.

symmetry. This results in $c_{\gamma\text{-Fe}_2\text{O}_3} = (0.833 \pm 0.002)\,\text{nm}$. In the RSM around the asymmetric γ-Fe_2O_3 (408) reflection, the thin film reflection is located at $q_{\text{H00}} = 1.999\,98\,\text{rlu}$ and $q_{\text{00L}} = 4.0463\,\text{rlu}$, which leads to an in-plane lattice constant of $a_{\gamma\text{-Fe}_2\text{O}_3} = (0.8423 \pm 0.0004)\,\text{nm}$ and an out-of-plane lattice constant of $c_{\gamma\text{-Fe}_2\text{O}_3} = (0.833 \pm 0.001)\,\text{nm}$. Averaging over all measurement methods (2θ-ω scan, RSM around the symmetric and the asymmetric reflections) gives an out-of-plane lattice constant $c_{\gamma\text{-Fe}_2\text{O}_3} = (0.8327 \pm 0.0004)\,\text{nm}$ of the thin film without a Pt electrode on top. As already visible in the RSM around the asymmetric reflection in Fig. 3.2.2, $a_{\gamma\text{-Fe}_2\text{O}_3}$ reaches a value near two times the lattice constant of the MgO substrate a_{MgO}. The in-plane epitaxial strain of the γ-Fe_2O_3 thin film is $\epsilon_{\text{xx}} = (a_{\gamma\text{-Fe}_2\text{O}_3} - a_{\gamma\text{-Fe}_2\text{O}_3,\,\text{bulk}})/a_{\gamma\text{-Fe}_2\text{O}_3,\,\text{bulk}} = 1.1\,\%$ and the out-of-plane strain is $\epsilon_{\text{zz}} = (c_{\gamma\text{-Fe}_2\text{O}_3} - a_{\gamma\text{-Fe}_2\text{O}_3,\,\text{bulk}})/a_{\gamma\text{-Fe}_2\text{O}_3,\,\text{bulk}} = -0.05\,\%$. The tensile in-plane strain is in its value the same as the lattice mismatch indicating a fully epitaxial strained thin film. The volume change $\Delta V/V$ relative to the volume V of a bulk unit cell is $1.0\,\%$ for the γ-Fe_2O_3 thin film without Pt. The increase in volume could be due to finite oxygen vacancies although an oxygen atmosphere is applied during the PLD.

For an investigation of the surface topography of the γ-Fe_2O_3 thin film sample and the γ-Fe_2O_3/Pt bilayer sample atomic force microscopy (AFM) images with an area of $1.17 \times 1.17\mu\text{m}^2$ are presented in Fig. 3.2.3. The root-mean square (RMS) roughness of γ-Fe_2O_3 thin film sample is $R_{\text{RMS}} = 1.16\,\text{nm}$ and the one of the Pt of the bilayer sample is $R_{\text{RMS}} = 0.46\,\text{nm}$. So the Pt electrode on top of the γ-Fe_2O_3 thin film exhibits a smaller surface roughness than the single γ-Fe_2O_3 thin film, which might be due to crystallites visible in the images. The image of the γ-Fe_2O_3 thin film without Pt on top shows a few brighter spots with a maximum height of $21.91\,\text{nm}$ (see Fig. 3.2.3 (a)). Also in Fig. 3.2.3 (b) small grains of up to $9.96\,\text{nm}$ height are visible. Together with Figs. 3.2.1 (c) and A.3.1 these regions can be identified as crystallites.

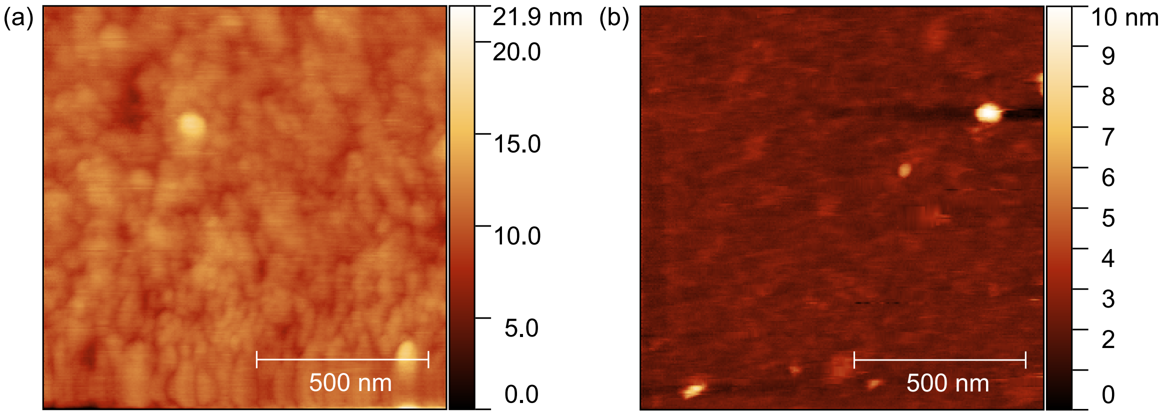

Figure 3.2.3.: Atomic force microscopy (AFM) images of a $1.17 \times 1.17 \mu m^2$ lateral area of (a) the γ-Fe_2O_3 thin film sample and (b) the γ-Fe_2O_3/Pt bilayer sample with roughnesses of $R_{RMS} = 1.16$ nm and $R_{RMS} = 0.46$ nm.

3.2.2. Magnetic properties of γ-Fe_2O_3 thin films

The magnetic properties of the γ-Fe_2O_3 thin films are again characterized by SQUID magnetometry. In Figs. 3.2.4 (a) and (b) the hysteresis curves of the γ-Fe_2O_3 thin film (blue) and the γ-Fe_2O_3/Pt bilayer (purple) at 300 K are shown after subtracting a linear background including the diamagnetic contribution of the MgO substrate. Surprisingly, the thin film without a Pt electrode on top exhibits a 15 % larger saturation magnetization M_S than the one with Pt on top. At a saturation field of $\mu_0 H_S = (3 \pm 0.5)$ T the saturation magnetization is (197 ± 4) kA m^{-1} for the γ-Fe_2O_3 thin film without a Pt electrode and (171.1 ± 0.3) kA m^{-1} for the one with Pt on top. In the enlargement of the grey area indicated in Fig. 3.2.4 (a) the respective coercitive fields $\mu_0 H_c$ can be determined to $\mu_0 H_c = (3.9 \pm 0.2)$ mT for the γ-Fe_2O_3 thin film sample with a Pt electrode and $\mu_0 H_c = (8.09 \pm 0.05)$ mT for the thin film sample without a Pt electrode at 300 K. The corresponding magnetization data at a temperature of 100 K are shown in the Appendix, Fig. A.4.1. All extracted values of M_S, $\mu_0 H_S$ and $\mu_0 H_c$ are summarized in Table 3.2.1.

	T (K)	M_S (kA m^{-1})	$\mu_0 H_S$ (T)	$\mu_0 H_c$ (mT)
γ-Fe_2O_3/Pt	300	171 ± 1	3.0 ± 0.5	3.9 ± 0.2
γ-Fe_2O_3	300	197 ± 4	3.0 ± 0.5	8.1 ± 0.1
γ-Fe_2O_3/Pt	100	183 ± 2	3.0 ± 0.5	30 ± 1
γ-Fe_2O_3	100	207 ± 22	3.0 ± 0.5	22.6 ± 0.5

Table 3.2.1.: Extracted values of M_S, $\mu_0 H_S$ and $\mu_0 H_c$ from SQUID magnetometry measurements at 300 K and 100 K on the γ-Fe_2O_3 thin film sample as well as the γ-Fe_2O_3/Pt bilayer.

The temperature dependence of the magnetization M shown in Fig. 3.2.4 (c) has in contrast to the magnetic hysteresis loops a larger M for the γ-Fe_2O_3/Pt bilayer accross the whole temperature range from 10 K to 330 K. The data are recorded in a magnetic field of 500 mT after cooling down in a magnetic field of 7 T. Both $M(T)$ curves show a $1/T$-

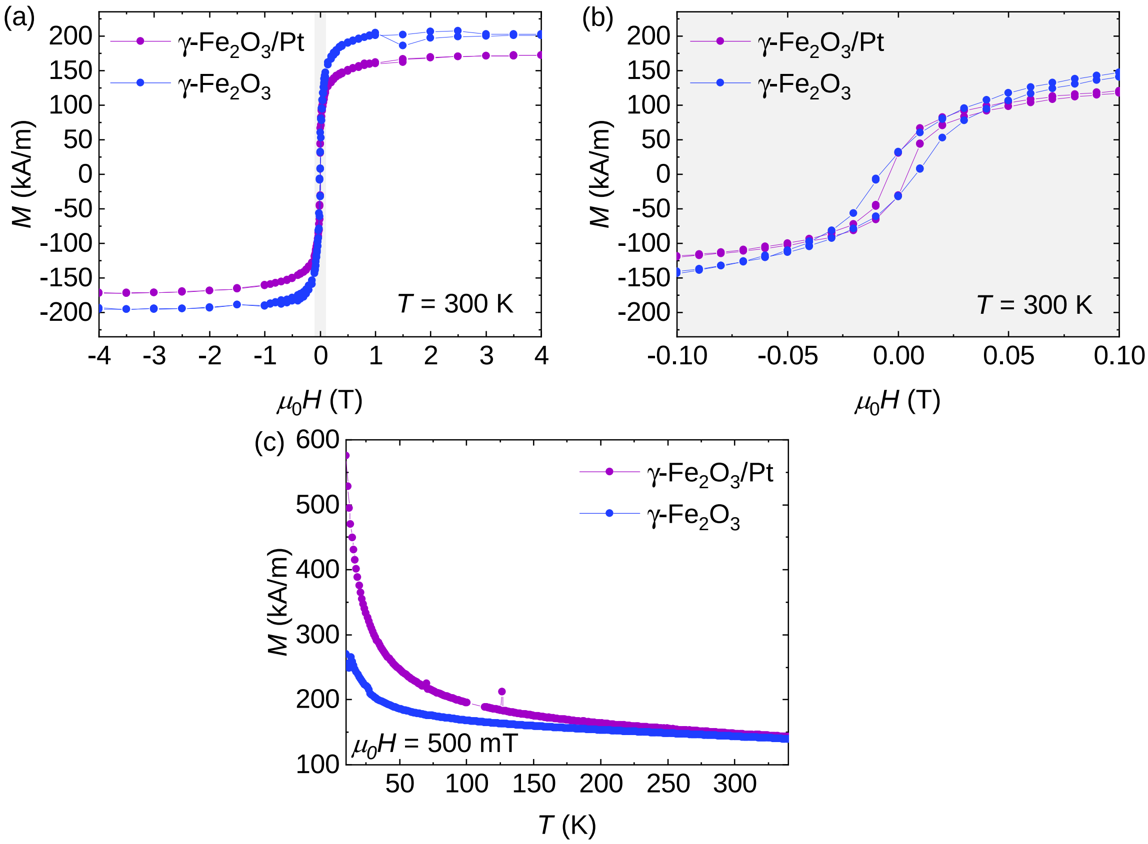

Figure 3.2.4.: SQUID magnetometry measurements performed on γ-Fe$_2$O$_3$ thin films with (purple dots) and without Pt on top (blue dots). (b) For a better analysis of the hysteresis loops in (a) at $300\,\mathrm{K}$ it is zoomed into the grey area. (c) Temperature dependence of the magnetization M measured with a magnetic field of $500\,\mathrm{mT}$ after field-cooled the sample using a magnetic field of $7\,\mathrm{T}$.

dependence as a function of temperature. A MgO substrate was measured with SQUID magnetometry before the thin film deposition and showed the same T dependence (see Fig. A.4.2). So the low-temperature behavior of the magnetization of the γ-Fe$_2$O$_3$ thin film as well as the γ-Fe$_2$O$_3$ bilayer sample originates from the MgO substrates exhibiting diamagnetism as well as paramagnetic contributions stemming from localized magnetic moments. In addition, the thin film $M(T)$ curves exhibit no significant changes at $263\,\mathrm{K}$ (Morin transition of α-Fe$_2$O$_3$) or at $120\,\mathrm{K}$ (Verwey transition of Fe$_3$O$_4$, cf. Ref. [65]). Together with the XRD results in Sec. 3.2.1, this indicates single-phase γ-Fe$_2$O$_3$ thin films with no other iron oxide phases.

Comparing the determined M_S values of the samples at $300\,\mathrm{K}$ with the bulk value of $400\,\mathrm{kA\,m^{-1}}$ reveals a reduction of M_S in γ-Fe$_2$O$_3$ thin films to about the half of the bulk value [60]. Among other things the saturation magnetization of γ-Fe$_2$O$_3$ thin films depends on the fabrication method, the thin film quality and the thin film thickness, since different values for M_S in γ-Fe$_2$O$_3$ thin films are reported (e.g. $270\,\mathrm{kA\,m^{-1}}$ in Ref. [84]). An explanation for the strong reduction of M_S in γ-Fe$_2$O$_3$ thin films compared to bulk γ-Fe$_2$O$_3$ could be made by considering so-called antiphase boundaries (Refs. [84, 85] for more details). In the growth process on the MgO substrate different crystalline γ-Fe_2O_3 regions start to arise and grow larger and larger. These regions then meet each other and form ionic bonds. Since γ-Fe_2O_3 grows on four MgO unit cells, bonds connecting a full γ-Fe_2O_3 unit cell with half of a unit cell can occur breaking the translation symmetry of the γ-Fe_2O_3 thin film. These defects are called antiphase boundaries (APBs). In most cases the APBs couple neighboring regions antiferromagnetically with each other and thus reduce the overall magnetization in the thin film. In general the density of such APBs increases with decreasing film thickness, which could explain the reduction in M_S compared to bulk γ-Fe_2O_3. Furthermore, it might also explain the smaller M_S value of the γ-Fe_2O_3 thin film of the γ-Fe_2O_3/Pt bilayer compared to the single γ-Fe_2O_3 thin film sample, which has a much larger thickness. For the prototype YIG/Pt bilayer for SMR experiments a similar reduction of M_S has been observed [86, 87]. Here, a smaller M_S value of YIG/Pt bilayers compared to YIG films without Pt on top has been reported. This is explained by a diffusion of Al^{3+} ions of the $Y_3Al_5O_{12}$ substrate into the YIG thin film during the EVAP process. This leads to an antiferromagnetic $Y_3Fe_{5\text{-}x}Al_xO_{12}$-phase and a reduction of the magnetization. To the best of our knowledge there is no similar effect reported in MgO//γ-Fe_2O_3/Pt. So further investigations have to be done and additional γ-Fe_2O_3 thin films have to be fabricated. Furthermore, detailed measurements of the APBs, which would require advanced microscopy techniques such as transmission electron microscopy (TEM), is needed to investigate the dependence of M_S on the density of the APBs.

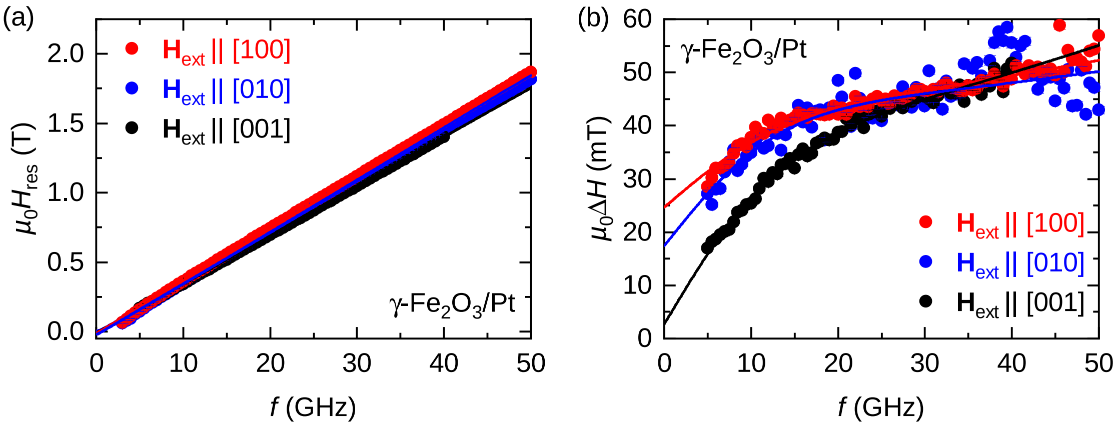

Figure 3.2.5.: Broadband ferromagnetic resonance (bbFMR) measurements of the γ-Fe_2O_3/Pt bilayer. The measurements are performed with the external magnetic field $\mathbf{H}_{ext}$ being parallel to the crystallographic [100], [010] and [001] directions of the γ-Fe_2O_3 thin film (cf. Fig. A.1.7). (a) Extracted resonance fields $\mu_0 H_{res}$ as well as (b) line widths $\mu_0 \Delta H$. The respective line widths $\mu_0 \Delta H$ are fitted according to Eq. (3.1) (solid lines in (b)).

In addition to SQUID magnetometry, also broadband ferromagnetic resonance (bbFMR) measurements are performed with the external magnetic field aligned along the crystallographic directions [001], [010] and [001] of the γ-Fe_2O_3 thin film (cf. Fig. A.1.7) to study the anisotropy and magnetization dynamics parameters of the thin film. Figure 3.2.5 shows the resonance field $\mu_0 H_{res}$ and resonance linewidth $\mu_0 \Delta H$ as a function of the driving field frequency f for the γ-Fe_2O_3/Pt bilayer. Complementary the FMR results for the γ-Fe_2O_3 thin film without Pt on top are depicted in Fig. A.5.1. From fitting the FMR with the ip-Kittel equation for $\mathbf{H}_{\text{ext}} \parallel [100]$ and $[010]$ and the oop-Kittel equation for $\mathbf{H}_{\text{ext}} \parallel [001]$ the effective magnetization $M_{\text{eff}} = M_{\text{S}} - H_{\text{ani}}$, the anisotropy field H_{ani} and the gyromagnetic ratio γ can be determined. The parameters are shown in Table 3.2.2. In oop configuration $g = \gamma\hbar/\mu_{\text{B}}$ exhibits a slightly larger value than in the ip configurations, where the results are quite similar. The fit in case of the oop orienation of $\mathbf{H}_{\text{eff}}$ gives a negative M_{eff} indicating the complete compensation of M_{S} by the strain-induced anisotropy of the γ-Fe_2O_3 thin film. A small effective magnetization could be useful for nonlocal magnetotransport measurements as a reduced M_{eff} leads to a more circular precession of the magnetization and thus suppressing nonlinear damping effects. This, in turn, increases the magnon conductivity [88]. In comparison to maghemite the prototype material YIG exhibits a larger effective magnetization of $\mu_0 M_{\text{eff}} = 140\,\text{mT}$ [89]. Taking a closer look on Fig. 3.2.5 (a) reveals an almost identical $\mu_0 H_{\text{res}}(f)$-dispersion in all three geometric measurement configurations indicating an isotropic magnetic behavior although uniaxial anisotropy is expected in thin films. The results are in agreement with the bbFMR measurements of the γ-Fe_2O_3 thin film without Pt on top, which are presented in Appendix A.5.

In Fig. 3.2.5 (b) the line widths $\mu_0\Delta H$ of the corresponding FMR are shown. Here, besides the linear Gilbert damping a slow relaxer damping contribution is considered, since $\mu_0\Delta H(f)$ is not a fully linear function over the whole frequency range from $5\,\text{GHz}$ to $50\,\text{GHz}$. The slow relaxer damping contribution can be described as follows: An impurity atom is exchange coupled to the surrounding magnetic moments in a magnetic material. The precession of the magnetic moments influences the splitting of the energy level of the impurity and thus also the thermal population of this level. The exchange coupling is anisotropic, since the splitting depends on the magnetization direction. A thermal relaxation of the impurity atom takes place in delay to the precession of the magnetic moments, which can be described by the relaxation time τ. Due to this thermal population and relaxation a fluctuation in the local magnetic field occurs that acts on the magnetic moments. All in all, the interaction with impurities leads to an additional damping contribution on the precession of the magnetic moments [90], which leads to [91]

$$\Delta H(f) = H_{\text{inh}} + \frac{4\pi f}{|\gamma|\mu_0}(\alpha + \text{Re}(\alpha_{\text{slow}}(2\pi f))), \tag{3.1}$$

where

$$\alpha_{\text{slow}}(\omega) = CF(T)\left(\frac{\tau}{1+(\omega\tau)^2} - i\frac{\omega\tau^2}{1+(\omega\tau)^2}\right) \tag{3.2}$$

is the slow relaxer damping term with

$$C = \frac{|\gamma| N_{\text{slow}}}{8 M_{\text{S}} k_{\text{B}} T}\left(\left(\frac{\partial E_{\text{slow}}}{\partial\phi}\right)^2 + \left(\frac{\partial E_{\text{slow}}}{\partial\theta}\right)^2\right) \tag{3.3}$$

and

$$F(T) = \mathrm{sech}^2\left(\frac{E_{\mathrm{slow}}}{k_{\mathrm{B}}T}\right). \tag{3.4}$$

N_{slow} is the slow-relaxer impurity concentration, E_{slow} the exchange energy and k_{B} Boltzmann's constant. The term in the outer brackets in Eq. (3.3) with the angular derivatives of E_{slow} describes the anisotropic exchange interaction between the impurity and the magnetic moment [90, 91]. For the γ-Fe$_2$O$_3$/Pt bilayer τ is fixed to 7.5 ps such that $\omega\tau = 1$ is fullfilled at the position of the peak in $\mu_0\Delta H$ in Fig. 3.2.5 (b), to avoid overfitting. The possible application of the slow relaxer damping term could indicate the existance of impurities and defects in the γ-Fe$_2$O$_3$ thin films. The previously mentioned antiferromagnetically coupled APBs could be seen as those defects coupling to the ferrimagnetic domains. But also other impurities occuring during the growth process could lead to the slow-relaxer damping contribution. So this has to be analyzed in more detail in the future.

	$\mu_0 M_{\mathrm{eff}}$ (mT)	g ($\gamma = g\mu_{\mathrm{B}}/\hbar$)	$\mu_0 H_{\mathrm{ani}}$ (mT)	α (10^{-3})	$\mu_0 H_{\mathrm{inh}}$ (mT)
$\mathbf{H}_{\mathrm{ext}} \parallel [100]$	-10.0 (fixed)	1.897 ± 0.002	-19 ± 1	5.3 ± 0.1	24.6 ± 0.8
$\mathbf{H}_{\mathrm{ext}} \parallel [010]$	-10.0 (fixed)	1.936 ± 0.002	-30 ± 1	5.5 ± 0.3	17.4 ± 2.1
$\mathbf{H}_{\mathrm{ext}} \parallel [001]$	-10.0 ± 0.1	2.023 ± 0.001		10.5 ± 0.2	2.7 ± 0.6

Table 3.2.2.: Extracted effective Magnetization $\mu_0 M_{\mathrm{eff}}$, g-factor g, anisotropy field $\mu_0 H_{\mathrm{ani}}$, damping parameter α and inhomogeneity field $\mu_0 H_{\mathrm{inh}}$ from fittings of the bbFMR data of a γ-Fe$_2$O$_3$ sample using Eqs. (A.13), (A.14) and (3.1).

Strikingly, the damping parameter for the γ-Fe$_2$O$_3$/Pt bilayer is approximately twice as high as the one for the γ-Fe$_2$O$_3$ thin film without a top Pt electrode (cf. Table A.5.1). The larger α of the γ-Fe$_2$O$_3$/Pt bilayer could be a result of spin pumping from the FMI γ-Fe$_2$O$_3$ into the HM Pt (cf. Ref. [92]). Here, the magnetization of the FMI is excited by the driving field generated by the coplanar waveguide (see Appendix A.1.2.4). The precessing magnetization then injects a spin current into the adjacent Pt layer, which creates an additional loss channel for the angular momentum and thus a damping contribution to the magnetization precession in the FMI. The damping α is also larger in the oop measurement compared to the ip measurements, which could indicate an anisotropic spin pumping. Compared to the damping in γ-Fe$_2$O$_3$, the prototype YIG exhibits a smaller Gilbert damping of $\alpha \simeq 2 \times 10^{-3}$, extracted from bbFMR measurements with an external magnetic field pointing oop [88]. For a more detailed explanation of the FMR setup and the physics behind FMR (including the fit equations) it is referred to the Appendix A.1.2.4.

3.2.3. Magnetotransport measurements on γ-Fe$_2$O$_3$/Pt bilayers

To investigate the spin Hall magnetoresistance (SMR) in γ-Fe$_2$O$_3$/Pt bilayers ADMR measurements are performed on two Hall bar structures with the same measurement methods and Hall bar dimensions as described in Sec. 3.1.3. The results of ADMR measurements at 300 K rotating the magnetic field in ip, oopj and oopt planes using a magnitude of 7 T are presented in Fig. 3.2.6. Here $\rho_{\mathrm{long}}/\rho_0 - 1$ (blue dots) as well as $\rho_{\mathrm{trans}}/\rho_0$ (red dots) shows the

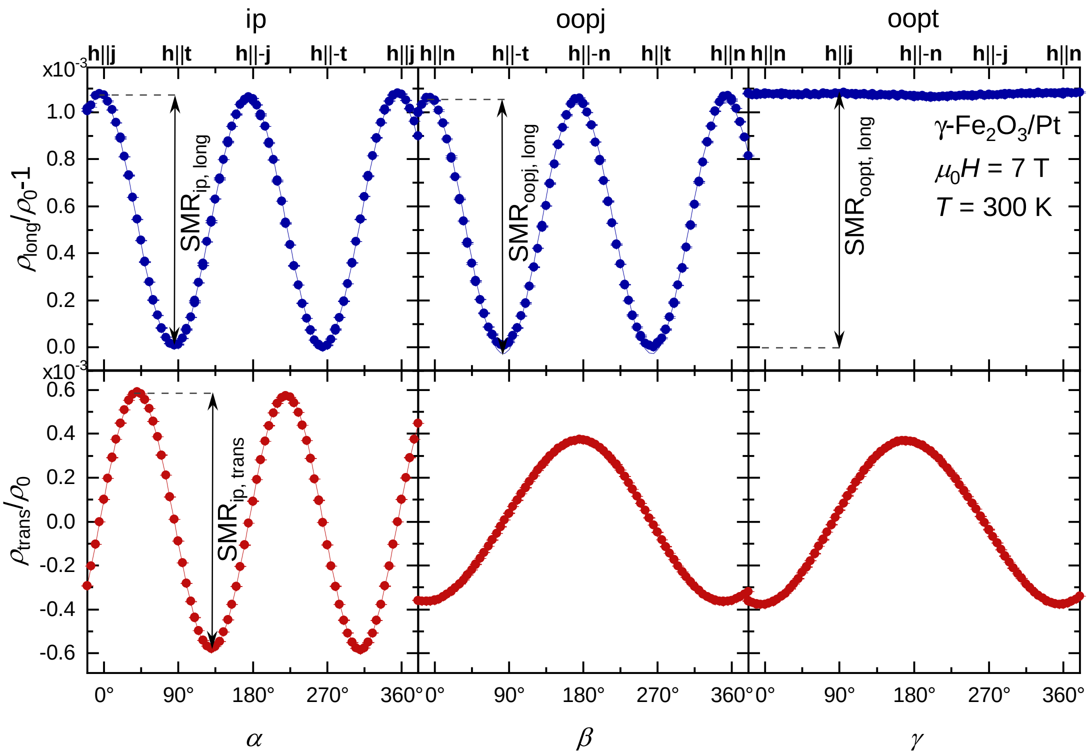

Figure 3.2.6.: ADMR of a γ-Fe$_2$O$_3$/Pt bilayer in ip, oopj and oopt magnetic field rotations (angles α, β and γ) at 300 K and 7 T. The normalized longitudinal resistivities are depicted as blue and the transverse resistivites as red dots with its corresponding fit curves according to Eqs. (2.7) and (2.8) describing the ferrimagnetic SMR effect. The longitudinal and transverse SMR amplitudes (SMR$_{\text{ip, long}}$, SMR$_{\text{oopj, long}}$, SMR$_{\text{oopt, long}}$ SMR$_{\text{trans}}$) of the ip and oop measurements are indicated by vertical arrows.

characteristic behavior of the ferrimagnetic SMR effect in all three rotation planes (ip, oopj and oopt) with a normal resistivity of Pt of $\rho_{0,\text{ip}} = 398\,\text{n}\Omega\,\text{m}$. The solid lines are fits to the data according to Eqs. (2.7) and (2.8) revealing a zero phase shift for the ip ADMR of ρ_{long}. For both the ip and the oopj magnetic field rotations a maximum (minimum) resistive state can be observed at 0°, 180° and 360° (90° and 270°), whereas ρ_{long} remains in its maximum value during a full 360° magnetic field rotation perpendicular to the transverse direction **t** (oopt). Also the angle-dependence of the transverse resistivity ρ_{trans} exhibits the expected behavior for FMI/HM bilayers (cf. Sec. 2.3.1).

ADMR measurements are carried out at different magnetic field magnitudes from 7 T down to 0 T at a temperature of 300 K for all possible magnetic field rotations. In case of the ip measurements, the SMR magnitudes of the two Hall bars are averaged. In addition, T-dependent oopj and oopt ADMR measurements are performed at 7 T from 10 K up to 300 K. Extracting the SMR amplitudes from these H- and T-dependent ADMR measurements yields the curves shown in Fig. 3.2.7 with the longitudinal SMR amplitudes (SMR$_{\text{ip, long}}$, SMR$_{\text{oopj, long}}$, SMR$_{\text{oopt, long}}$) depicted as blue and the transverse SMR amplitudes (SMR$_{\text{ip, trans}}$) as red symbols. For SMR$_{\text{long}}$ and SMR$_{\text{trans}}$ in ip and oopj rotations a similar magnetic field dependence can be observed. Moreover, SMR$_{\text{ip, long}}$ and SMR$_{\text{oopj, long}}$

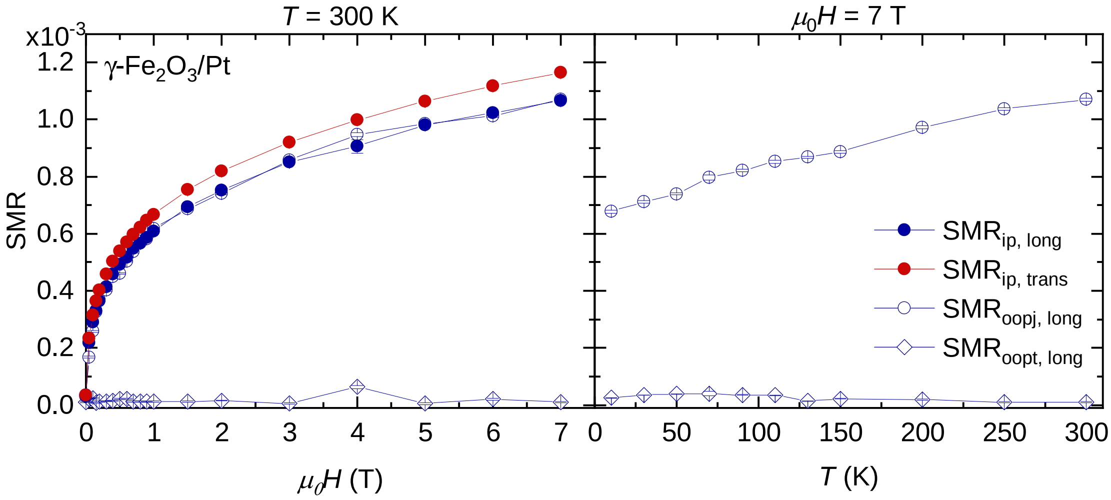

Figure 3.2.7.: From ADMR measurements extracted SMR amplitudes as a function of the applied magnetic field $\mu_0 H$ at 300 K (left figure) and of the temperature T at 7 T (right figure). The ip SMR amplitudes $\mathrm{SMR}_{\mathrm{ip,\,long}}$ and $\mathrm{SMR}_{\mathrm{ip,\,trans}}$ are depicted as blue and red dots and the longitudinal oop SMR amplitudes $\mathrm{SMR}_{\mathrm{oopj,\,long}}$ and $\mathrm{SMR}_{\mathrm{oopt,\,long}}$ as open blue symbols.

are almost identical in magnitude. As expected, the oscillation amplitude of $\rho_{\mathrm{oopt,\,long}}$ (here defined as $\mathrm{SMR}_{\mathrm{oopt,\,long}}$) is vanishingly small.

The non-saturating, square root magnetic field dependence of $\mathrm{SMR}_{\mathrm{ip}}$ and $\mathrm{SMR}_{\mathrm{oopj,\,long}}$ is striking, since it is contrary to the saturation field observed in the SQUID magnetometry measurements in Fig. 3.2.4. Thereby, the magnetization M already saturates at 3 T at a temperature of 300 K. Therefore, above 3 T no increase in the SMR amplitude is expected, because all magnetic moments should be aligned along the external magnetic field direction and thus maximizing the projection of $\mathbf{M}$ on $\mathbf{t}$ at $\alpha, \beta = 90°$. Equally striking is that $\mathrm{SMR}_{\mathrm{ip,\,trans}}$ is larger than $\mathrm{SMR}_{\mathrm{ip,\,long}}$. A general increase in the saturation field H_S could be explained by taking into account the existance of antiphase boundaries (cf. Sec. 3.2.2). The APBs could cause domain wall pinning in particular at the interface between FMI and Pt so that it takes a stronger external magnetic field to align the orientation of the magnetic domains along the magnetic field direction (cf. Ref. [93]). The existance of magnetic domains even at magnetic fields of up to 7 T could also lead to a higher value of $\mathrm{SMR}_{\mathrm{trans}}$ compared to $\mathrm{SMR}_{\mathrm{long}}$. Similar to the discussion of the SMR amplitudes in the α-Fe_2O_3/Pt bilayer (see Sec. 3.1.3) the magnetic domains in γ-Fe_2O_3 could exceed the width of the Hall bar, but not the distance between contacted pads for the longitudinal measurement. Thus, the magnetic domains could have an influence on the longitudinal resistivity, but no or just a vanishingly small influence on the transverse resistivity.

At 300 K and 7 T a longitudinal SMR amplitude of 1.07×10^{-3} and a transverse SMR amplitude of 1.16×10^{-3} can be extracted from Fig. 3.2.7. These values reach only 42 % of the values of the α-Fe_2O_3/Pt bilayer (see Fig. 3.1.5). Comparing γ-Fe_2O_3/Pt with the prototype bilayer YIG/Pt $\mathrm{SMR}_{\mathrm{long}}$ exhibits just a slightly smaller value, since for YIG/Pt bilayers a $\mathrm{SMR}_{\mathrm{long}}$ amplitude of 1.3×10^{-3} is observed [10]. The value is also comparable to other reported values in γ-Fe_2O_3/Pt bilayers with a SMR amplitude of approximately 1.1×10^{-3} at $300\,\mathrm{K}$ and $5\,\mathrm{T}$ [82]. In case of the temperature dependent oop-measurement at $7\,\mathrm{T}$ (right part of Fig. 3.2.7), $\mathrm{SMR}_{\mathrm{oopj,\,long}}$ exhibits a nearly linear dependence with increasing T with a small kinck at $150\,\mathrm{K}$, which is in agreement with the T-dependence of the SMR effect in YIG/Pt [81]. The $\mathrm{SMR}_{\mathrm{oopt,\,long}}$ amplitude shows a vanishingly small magnitude over a large temperature range, which indicates that no anisotropic magnetoresistance is present [94].

3.3. Physical properties of Fe_3O_4 thin films

Reducing the oxygen content in γ-Fe_2O_3 leads to Fe_3O_4 (magnetite) and thus to new structural (Sec. 3.3.1) and magnetic phenomenons (Sec. 3.3.2). As a half metallic material, magnetite offers magnetoresistive effects different from that in magnetic insulator (MI)/ heavy metal (HM) bilayers such as α-Fe_2O_3/Pt and γ-Fe_2O_3/Pt. These are discussed in Sec. 3.3.3.

3.3.1. Fabrication and structural analysis of Fe_3O_4 thin films

Fe_3O_4 (magnetite) thin films are fabricated on MgO (001) substrates by PLD. Therefore nearly the same growth parameters are used as for the γ-Fe_2O_3 thin films (see Sec. 4.3.1), but for the formation of Fe_3O_4 a reduction in oxygen compared to γ-Fe_2O_3 is required. This is realized by growing in an argon atmosphere with a partial pressure of $p_{\mathrm{Ar}} = 10\,\mathrm{\mu bar}$. In addition, one of the Fe_3O_4 thin films is covered by a Pt electrode deposited via EVAP using a deposition rate of $r = 0.1\,\mathrm{Å\,s^{-1}}$. Analogously to γ-Fe_2O_3 on MgO (001), also in the case of Fe_3O_4 one unit cell is growing on four MgO (001) unit cells with lattice vectors pointing in the same directions. So the epitaxial relation is Fe_3O_4 [100]||MgO [100] and Fe_3O_4 [001]||MgO [001]. The literature value for the in-plane lattice constant of Fe_3O_4 of $a_{\mathrm{Fe_3O_4,\,bulk}} = 0.8394\,\mathrm{nm}$ results in a small lattice mismatch of $\epsilon = (a_{\mathrm{Fe_3O_4,\,bulk}} - 2a_{\mathrm{MgO}})/(2a_{\mathrm{MgO}}) = -0.36\,\%$ on MgO (001) [61]. Compared to γ-Fe_2O_3, the Fe_3O_4 thin film should exhibit less, but still finite tensile strain in the thin film plane.

For an investigation of the crystalline quality, the epitaxial relations and the film thicknesses HR-XRD measurements of a single Fe_3O_4 thin film sample and a Fe_3O_4/Pt bilayer sample are presented in Fig. 3.3.1. The wide range 2θ-ω scan in (a) of the Fe_3O_4/Pt bilayer reveals the thin film (substrate) reflections Fe_3O_4 (004) (MgO (002)) and Fe_3O_4 (008) (MgO (004)) together with the Pt (111) reflection at $2\theta = 39.87°$. No other crystalline phases occur such as α-Fe_2O_3 or FeO. Laue oscillations are visible on both samples as an indicator of a high-crystalline coherent growth of Fe_3O_4 (see Fig. 3.3.1 (b)). The 2θ positions of the thin film reflections of 43.13° and 43.11° are quite similar for the thin films without and with Pt, respectively. Taking into account these 2θ values the out-of-plane lattice constants can be calculated to $c_{\mathrm{Fe_3O_4}} = (0.838 \pm 0.003)\,\mathrm{nm}$ (thin film without Pt) and $c_{\mathrm{Fe_3O_4}} = (0.839 \pm 0.003)\,\mathrm{nm}$ (thin film with Pt). The determined lattice constants c are closer to the bulk value of Fe_3O_4 than compared to the γ-Fe_2O_3 sample ($c_{\gamma\text{-}\mathrm{Fe_2O_3,\,bulk}} = 2.5113\,\mathrm{nm}$).

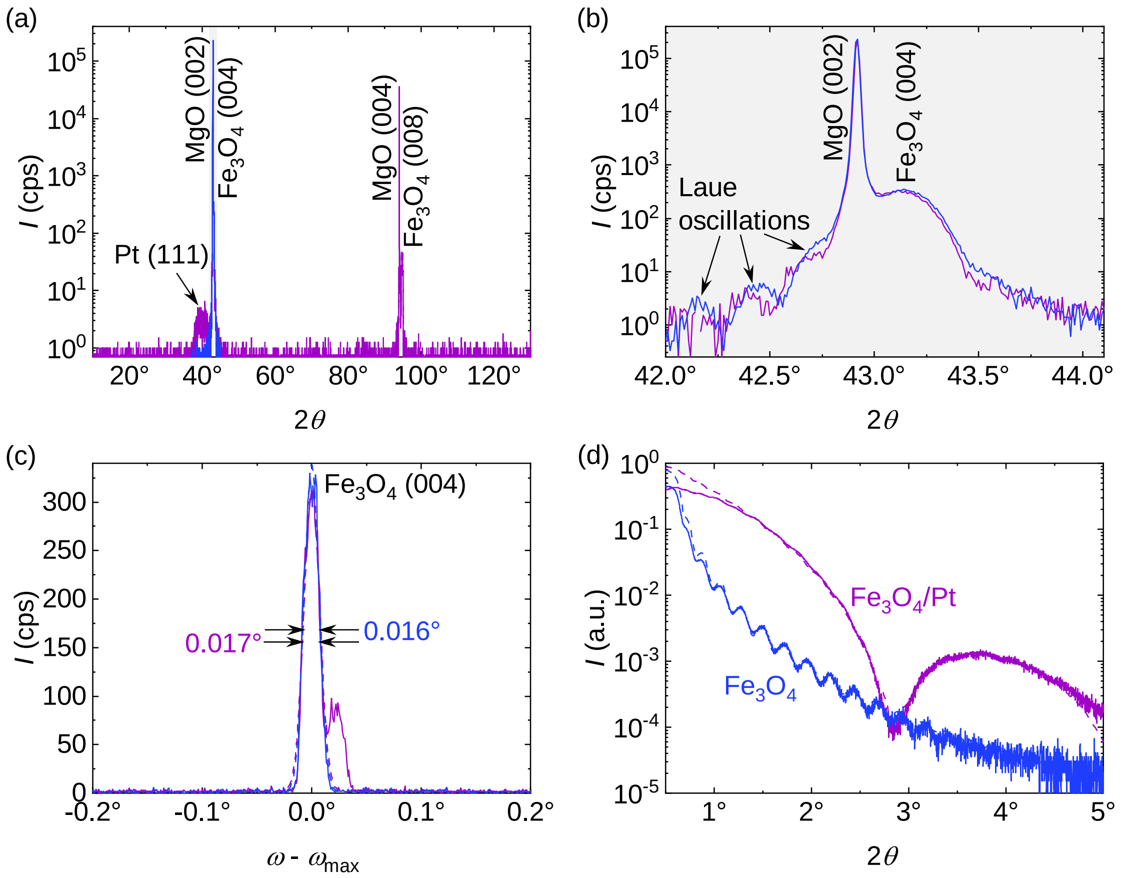

Figure 3.3.1.: High resolution X-ray diffraction of a Fe_3O_4 thin film (in blue) and a Fe_3O_4/Pt bilayer (in purple) on MgO (001) substrates. (a) The 2θ-ω scan shows the (004) and the (008) reflections of Fe_3O_4, the corresponding substrate reflections as well as the Pt (111) reflection. (b) Laue oscillations are visible around the Fe_3O_4 (004) reflection. (c) Rocking curves around the Fe_3O_4 (004) reflection fitted with Gaussian functions with FWHMs of $0.016°$ and $0.017°$. (d) X-ray reflectometry scans as solid lines and their simulation as dashed lines.

The Gauss fits of rocking curves around the Fe_3O_4 (004) reflections reveal small FWHMs of $0.016°$ of the thin film without Pt and $0.017°$ of the Fe_3O_4/Pt bilayer sample, revealing a low mosaic spread. But as in the case of the γ-Fe_2O_3/Pt bilayer in the previous section also the rocking curve of the Fe_3O_4/Pt bilayer (purple line) shows additional reflections due to the existance of multiple crystallites in the MgO substrate. The thickness of the Fe_3O_4 thin films as well as the Pt layer are determined by XRR (see Fig. 3.3.1 (d)). The LEPTOS simulations (dashed lines) reveals $t_{Fe_3O_4} = (35.9 \pm 0.3)\,\mathrm{nm}$ for the Fe_3O_4 thin film without Pt on top and $t_{Fe_3O_4} = (35.2 \pm 0.3)\,\mathrm{nm}$ together with $t_{Pt} = (3.4 \pm 0.1)\,\mathrm{nm}$ for the Fe_3O_4/Pt bilayer sample. Comparing the thin film thicknesses with each other reveals nearly the same growth rates for the two films of about $0.004\,\mathrm{nm\,s^{-1}}$. Also the value of t_{Pt} is a qualitatively good result, since it is comparable to the thicknesses of the already mentioned Pt electrodes on α-Fe_2O_3 and γ-Fe_2O_3 and approximately twice the spin diffusion length of Pt possibly providing a maximum SMR signal. For the latter it has to be taken into account that also the anisotropic magnetoresistance (AMR) effect plays a crucial role in Fe_3O_4/Pt bilayers (see Sec. 3.3.3).

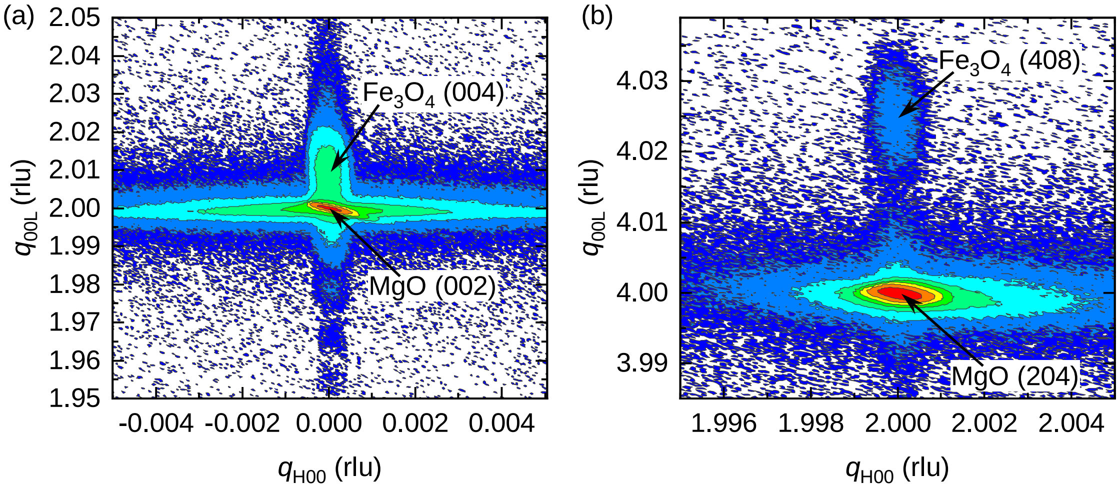

Figure 3.3.2.: Reciprocal space mapping of the Fe_3O_4 thin film (without Pt on top) around (a) Fe_3O_4 (004) and MgO (002) as well as (b) Fe_3O_4 (408) and MgO (204). The units are given in reciprocal lattice units (rlu) with respect to the MgO substrate.

To calculate the elastic strain and thus determine the in-plane lattice constant $a_{Fe_3O_4}$ reciprocal space mappings (RSMs) are performed for the Fe_3O_4 thin film without a Pt electrode (Fig. 3.3.2) and the Fe_3O_4 thin film with a Pt electrode (Fig. A.3.1). In Fig. 3.3.2 (a) the RSM around the symmetric MgO (002) and Fe_3O_4 (004) reflections shows Laue oscillations below the substrate reflection. Together with Eqs. (A.6) and (A.3) the position of the Fe_3O_4 (004) reflection ($q_{00L} = 2.0097\,\mathrm{rlu}$) leads to $c_{Fe_3O_4} = (0.838 \pm 0.003)\,\mathrm{nm}$. Figure 3.3.2 (b) yields the lattice constants $a_{Fe_3O_4} = (0.8423 \pm 0.0001)\,\mathrm{nm}$ and $c_{Fe_3O_4} = (0.837 \pm 0.001)\,\mathrm{nm}$ for the thin film reflection at $q_{H00} = 1.9999\,\mathrm{rlu}$ and $q_{00L} = 4.0247\,\mathrm{rlu}$. Taking all measurements (2θ-ω scan, RSMs of the symmetric and asymmetric reflections) into account this results in an out-of-plane lattice constant of $c_{Fe_3O_4} = (0.838 \pm 0.001)\,\mathrm{nm}$ on average. So an epitaxial strain in the thin film can be assessed to $\epsilon_{xx} = (a_{Fe_3O_4} - a_{Fe_3O_4,\,bulk})/a_{Fe_3O_4,\,bulk} = 0.34\,\%$ in the plane and to $\epsilon_{zz} = (c_{Fe_3O_4} - c_{Fe_3O_4,\,bulk})/c_{Fe_3O_4,\,bulk} = -0.18\,\%$ out of the plane. The small, but finite tensile ip strain is comparable to the lattice mismatch of $0.36\,\%$. The change in the unit cell volume relative to the bulk volume $\Delta V/V = 0.16\,\%$ is negligible. Therefore, the Fe_3O_4 thin films are fully strained and exihibit the correct stochiometry. The lattice constants indicate the desired growth of Fe_3O_4, since their values differ noticeable from the ones for γ-Fe_2O_3. Further investigations to differentiate between Fe_3O_4 and γ-Fe_2O_3 are done in Secs. 3.3.2 and A.2, where the magnetic and electric properties of the thin films give rise to a more substantial analysis.

3.3.2. Magnetic properties of Fe_3O_4 thin films

SQUID magnetometry measurements of the Fe_3O_4 thin film sample as well as the Fe_3O_4/Pt bilayer depicted in Fig. 3.3.3 entail more magnetically soft hysteresis curves at 300 K as for the γ-Fe_2O_3 thin film samples (cf. Fig. 3.3.3 and Fig. 3.2.4). The saturation magnetizations

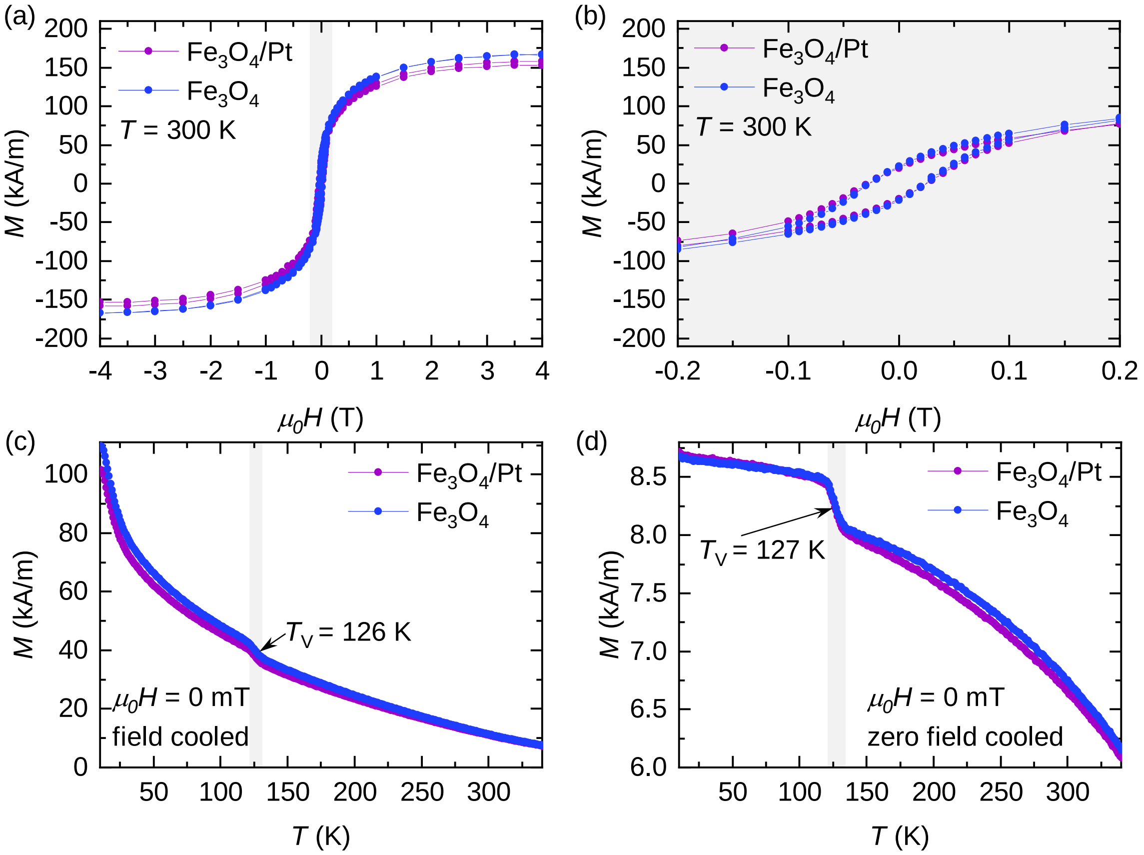

Figure 3.3.3.: SQUID magnetometry measurements performed on Fe_3O_4 thin films with and without a Pt electrode. (a) Hysteresis loops at 300 K and (b) zoom into the grey area of (a). (c) Field-cooled and (d) zero-field cooled temperature dependent measurements of M reveal a Verwey transition temperature of approximately 126 K and 127 K, depending on the measurement method (highlighted by the grey area).

of both samples are close to each other and result in an average value of $M_S = 161\,\mathrm{kA\,m^{-1}}$ at a magnetic saturation field of 3.5 T. The low field magnetic behavior shown in Fig. 3.3.3 (b) reveals a coercitive field of 26.1 mT for both samples. Table 3.3.1 summarizes the obtained values for M_S, $\mu_0 H_S$ and $\mu_0 H_c$ for the two samples. The values measured at 100 K and the hysteresis curves, respectively, are shown in the Appendix A.4. Unlike the γ-Fe_2O_3 samples the Fe_3O_4 thin films covered with and without Pt exhibit no significant difference in magnetization to each other. Surprisingly the Fe_3O_4 samples exhibit even smaller saturation magnetizations than the γ-Fe_2O_3 thin film samples, although for magnetite a higher M_S is expected. Compared to the bulk value of $M_S = 471\,\mathrm{kA\,m^{-1}}$ at room temperature the fabricated Fe_3O_4 thin films have a 66 % smaller M_S on average and thus a very significant reduction in M [63]. This could be again attributed to the existance of antiphase boundaries as extensively discussed in Sec. 3.2.2 for the reduction in M of the γ-Fe_2O_3 thin films compared to bulk γ-Fe_2O_3.

To be able to make further statements about the existance and quality of the Fe_3O_4 phase in the fabricated thin films the T-dependence of M is additionally measured. Figure 3.3.3

(c) and (d) depict $M(T)$ at $0\,\mathrm{T}$ for the field cooled and for the zero field cooled case. In the former case before the measurements a magnetic field of $7\,\mathrm{T}$ is applied while cooling down to $10\,\mathrm{K}$. In the latter case the samples are cooled down without applying an external magnetic field. Since in (c) all magnetic moments are aligned along $\mathbf{H}$, the magnitude of $\mathbf{M}$ is higher than in (d). In (c) as well as in (d) $M(T)$ exhibits a step like behavior in the grey highlighted region, which is better visible in the zero field cooled case. This indicates the Verwey transition in Fe_3O_4 from a conductive to an insulating state while going to lower T. Such a metal-insulator transition entails a change from a cubic to a monoclinic crystal and also a reorientation of the magnetic moments. This is due to a change of an in-plane easy axis along the [100] direction to an out-of-plane easy axis along Fe_3O_4 [001] [95]. The Verwey transitions occur at around $T_\mathrm{V} = 126\,\mathrm{K}$ (c) and $127\,\mathrm{K}$ (d) and are just slightly larger than the literature bulk value of $120\,\mathrm{K}$ [95]. All in all, the presence of the Verwey transition in the fabricated thin films indicates a good crystalline quality with correct stochiometry of the Fe_3O_4 thin films.

	T (K)	M_S $\left(\mathrm{kA\,m^{-1}}\right)$	$\mu_0 H_\mathrm{S}$ (T)	$\mu_0 H_\mathrm{c}$ (mT)
Fe_3O_4/Pt	300	155 ± 2	3.5 ± 0.5	26 ± 1
Fe_3O_4	300	166 ± 1	3.5 ± 0.5	26 ± 1
Fe_3O_4/Pt	100	195 ± 1	3.5 ± 0.5	72 ± 4
Fe_3O_4	100	203 ± 1	3.5 ± 0.5	72 ± 4

Table 3.3.1.: Extracted values of M_S, $\mu_0 H_\mathrm{S}$ and $\mu_0 H_\mathrm{c}$ of the Fe_3O_4 thin film sample and the Fe_3O_4/Pt bilayer sample measured at $300\,\mathrm{K}$ and $100\,\mathrm{K}$.

3.3.3. Magnetotransport measurements on Fe_3O_4/Pt bilayers

To investigate the spin Hall magnetoresistance in Fe_3O_4/Pt, first the temperature dependence of the resistance of a single Fe_3O_4 thin film sample is measured and compared with that of a Fe_3O_4/Pt bilayer sample as well as a single γ-Fe_2O_3 thin film sample. For the temperature dependent resistance measurements a voltage V of $50\,\mathrm{V}$ ($150\,\mathrm{V}$) is applied on the Hall bars of the Fe_3O_4 (γ-Fe_2O_3) thin film samples. The Hall bars are perpendicular to each other and parallel to the corresponding sample edges with a width of $w = 80\,\mathrm{\mu m}$ and a distance of $l = 1000\,\mathrm{\mu m}$ between the contacted Hall bar pads. The measured current I is used to calculate the resistance $R = V/I$. In case of the Fe_3O_4/Pt bilayer, a standard four probe measurement with a current of $I = 100\,\mathrm{\mu A}$ is performed analogously to the ADMR measurements presented in the previous sections with a seperation of the contact pads of $l = 600\,\mathrm{\mu m}$. Figures 3.3.4 (a) and (b) juxtapose the measured resistances R of the Fe_3O_4 and the γ-Fe_2O_3 thin film samples at $0\,\mathrm{T}$ and as a function of T. Hereby, the thin films without Pt on top are depicted as blue and the Fe_3O_4/Pt bilayer as purple dots. In (a) the resistance is given in several hundred Ω and in (b) in several tens of $\mathrm{G\Omega}$, obviously indicating the fully insulating behavior of γ-Fe_2O_3 compared to the conducting Fe_3O_4. Both iron oxides become more and more insulating going to lower temperatures, but especially

Fe_3O_4 exhibits an abrupt increase in R below 100 K. At 300 K the calculated resistivity for Fe_3O_4 is $\rho = 37\,\mathrm{m\Omega\,cm}$ and therefore one order of magnitude higher than in bulk Fe_3O_4 at room temperature ($4\,\mathrm{m\Omega\,cm}$). A possible explanation could be a much higher density of antiphase boundaries in Fe_3O_4 thin films compared to bulk Fe_3O_4. The APBs increase the resistivity and the region of the Verwey transition is broadened [95]. Furthermore, surface scattering in the Fe_3O_4 thin film becomes more important leading to an increase of the resistivity. The Fe_3O_4/Pt bilayer shows an increase of the resistance with T. For low T the Pt contribution and for high T the Fe_3O_4 contribution in Fe_3O_4/Pt dominates leading to the fact that at low T the applied current prefers to flow through the Pt layer and at high T through the Fe_3O_4 layer. This results in a maximum R of 590 Ω at 155 K. Comparing Figs. (a) and (b) with each other is in total a good tool to distinguish Fe_3O_4 from γ-Fe_2O_3 due to the high resistance of γ-Fe_2O_3. For the Fe_3O_4 thin film with a Pt electrode the temperature dependent resistance is also measured at a finite magnetic field of 7 T to calculate the magnetoresistance according to $\mathrm{MR} = (R(7\,\mathrm{T}) - R(0\,\mathrm{T}))/R(0\,\mathrm{T})$. Figure 3.3.4 (c) presents the resulting MR behavior of one of the Hall bars. A clear dip is visible not at the Verwey transition of $T_\mathrm{V} \approx 126\,\mathrm{K}$, but at a much higher temperature of $T = 180\,\mathrm{K}$. The temperature dependence of the resistance of the Fe_3O_4/Pt bilayer sample indicates that the spin Hall magnetoresistance (SMR) can be observed in the insulating phase of Fe_3O_4, i.e., below $\approx 100\,\mathrm{K}$, while at higher temperatures an additional anisotropic magnetoresistance (AMR) is expected due to the higher conductivity of the Fe_3O_4 thin film.

To investigate possible SMR and AMR effects, ADMR measurements are performed on Fe_3O_4 thin film samples with and without Pt on top considering all three magnetic field rotations: ip, oopj and oopt. Therefore a current of 100 µA is applied on both Hall bars on the samples. For the ip measurements the MR results of the two Hall bars are averaged. In Fig. 3.3.5 the results for a single Fe_3O_4 thin film without a Pt electrode recorded at 300 K and 7 T are depicted. Since the SQUID measurements reveal a saturation field of $\mu_0 H_\mathrm{S} = 3.5\,\mathrm{T}$, the applied field of 7 T should be large enough to align $\mathbf{M}$ along the magnetic field direction. The longitudinal resistivities ρ_long are normalized to their corresponding minimal values. The transverse resistivities ρ_trans are therefore normalized to $\rho_\mathrm{min} = \rho_\mathrm{long,\,min}$. These measurements reveal the anisotropic magnetoresistance (AMR) effect of Fe_3O_4 at 300 K, i.e., in the conducting phase of Fe_3O_4. To explain the ADMR of Fe_3O_4, the symmetry of the crystal has to be taken into account [96]. To this end, it is assumed that the (001)-oriented Fe_3O_4 thin film exhibits a cubic symmetry with a tetragonal distortion due to the finite lattice mismatch to the MgO substrate. With this assumption, a $\cos^2$-dependence of ρ_long is expected in all three magnetic field rotations. For a more theoretical explanation including the resistivity tensor of a cubic crystal symmetry with a tetragonal distortion it is referred to Sec. A.2 and to Ref. [97].

Addionally, the ADMR measurements on the blank Fe_3O_4 thin film are executed at different magnetic fields from 7 T down to 0 T. The extracted MR values as a function of H are shown in Fig. A.2.1. No saturation of the AMR amplitude is found with a maximum

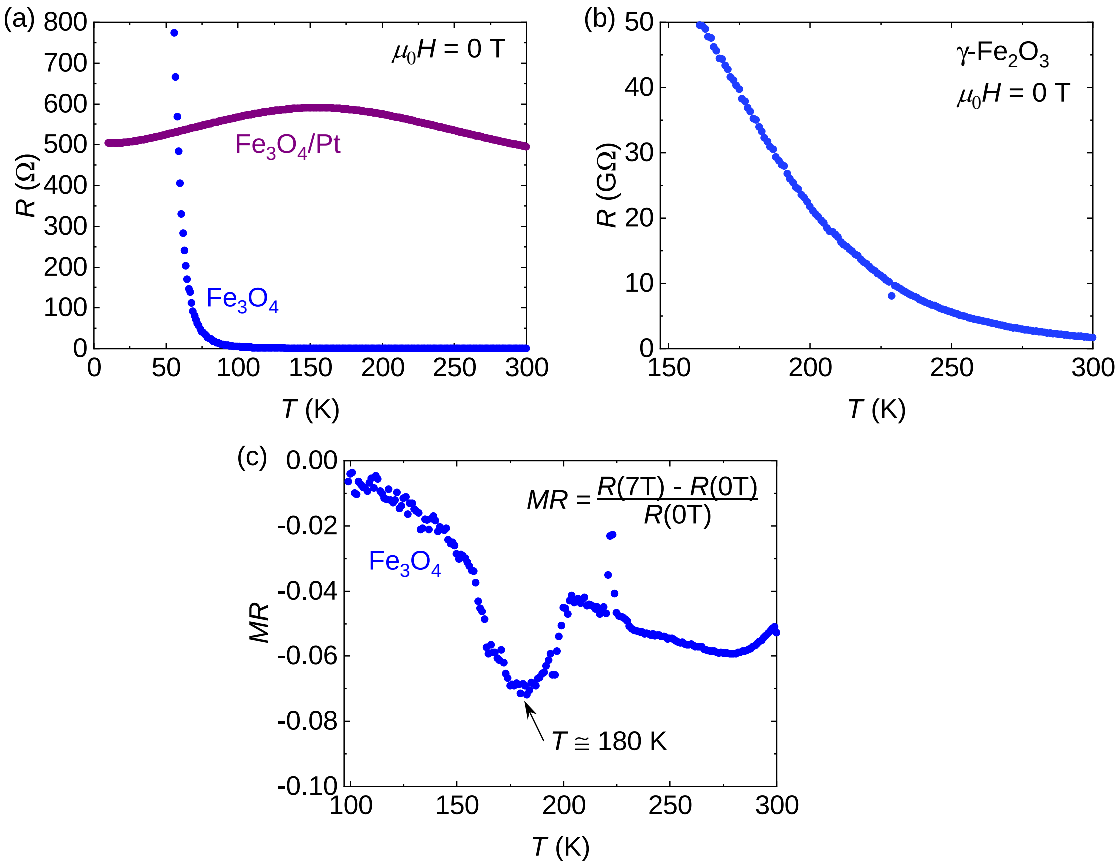

Figure 3.3.4.: Temperature dependence of the resistance R measured at $0\,\mathrm{T}$ of (a) Fe_3O_4 with (purple dots) and without a Pt electrode (blue dots) and (b) a γ-Fe_2O_3 single thin film sample. Note the different magnitudes of the resistance (Ω in (a) and $\mathrm{G}\Omega$ in (b)). For the Fe_3O_4 thin film (without Pt on top) R is also measured at $7\,\mathrm{T}$ to calculate the magnetoresistance $\mathrm{MR} = (R(7\,\mathrm{T}) - R(0\,\mathrm{T}))/R(0\,\mathrm{T})$. (c) $\mathrm{MR}(T)$ exhibiting a dip at approximately $180\,\mathrm{K}$.

AMR amplitude of $\rho_{\mathrm{ip,\,long}}$ of 1.95×10^{-3} at $7\,\mathrm{T}$. For Fe_3O_4 thin films also higher AMR magnitudes are reported. For example Ding and coworkers found an AMR amplitude of 2.6×10^{-3} in a $6\,\mathrm{nm}$ thick Fe_3O_4 thin film at room temperature with a magnetic field of $2\,\mathrm{T}$ [98]. The difference might be again due to the density of APBs in the respective Fe_3O_4 thin film sample.

Analogously to the ADMR measurements on the single Fe_3O_4 thin film sample, ADMR measurements are carried out on the Fe_3O_4/Pt bilayer sample (see Fig. 3.3.6). Hereby, the longitudinal resistivities and their corresponding fits are shown in blue in case of the measurement at $300\,\mathrm{K}$ and in cyan in case of the measurement at $50\,\mathrm{K}$. The resistivities are normalized again to their minimal values ρ_{min}. For $\rho_{\mathrm{ip,\,long}}$ this value is approximately $207\,\mathrm{n}\Omega\,\mathrm{m}$ at room temperature and in agreement with the normal resistivites of Pt in Ref. [81]. Based on Fig. 3.3.4 (a) the current in the Fe_3O_4/Pt bilayer prefers to flow through the Pt layer at low temperatures and through the Fe_3O_4 layer at high temperatures. Therefore, different dominating MR effects are expected at $300\,\mathrm{K}$ and at $50\,\mathrm{K}$. At $300\,\mathrm{K}$ the AMR and at $50\,\mathrm{K}$ the SMR effect should dominate. The amplitude of the in-plane resistivity de-

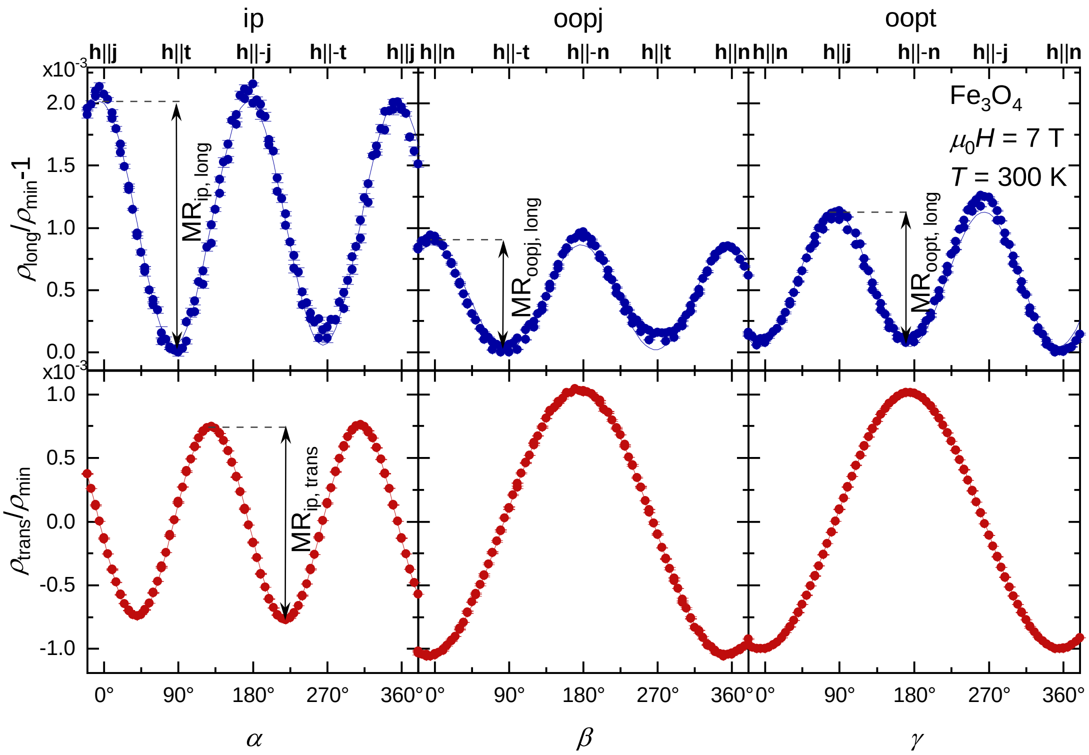

Figure 3.3.5.: ADMR of the single Fe_3O_4 thin film sample in ip, oopj and oopt magnetic field rotations at 300 K and 7 T. The longitudinal ρ_{long} (blue dots) and the transverse ρ_{trans} resistivites (red dots) are normalized to the corresponding minimal values of ρ_{long}. The fit curves (blue and red lines) follow a $\cos^2(\phi)$ (longitudinal) and a $\sin(2\phi)$ and $\cos(\phi)$ (transverse) dependence, respectively (with $\phi = \alpha$, β and γ). The AMR amplitudes $\text{MR}_{\text{ip, long}}$, $\text{MR}_{\text{oopj, long}}$, $\text{MR}_{\text{oopt, long}}$ and $\text{MR}_{\text{ip, trans}}$ are indicated by vertical arrows.

creases by 27 % from 300 K down to 50 K. This strong decrease could be explained by the AMR exhibiting higher values than the SMR. But the reduction could be also explained by the general decrease of the SMR amplitude with decreasing T (cf. Fig. 3.2.7). Since the SMR as well as the AMR theory claim the same ip $\cos^2(\alpha)$ dependence, the ADMR in the β and γ rotation planes of the magnetic field has to be taken into account for a more specific analysis and differentiation of the SMR and the AMR. In particular, in the measurement with rotating the magnetic field perpendicular to **t** (oopt) an oscillation is expected at 300 K at which the AMR of Fe_3O_4 is dominating (see Fig. 3.3.5). At 50 K, i.e. in the insulating state of Fe_3O_4, the Fe_3O_4/Pt should behave in accordance to the SMR theory and a high resistive state is expected. However, the measurement results reveal a small, but not negligible, oscillation of ρ_{long} for both temperatures together with a change in phase. For 300 K ρ_{long} is maximum at 90° and at 270°, but for 50 K the maximum value is reached at 0°, 180° and at 360°.

At 300 K the behavior is similar to that of the Fe_3O_4 thin film without Pt on top shown in Fig. 3.3.5. Both resistivity oscillations exhibit the same phase but different amplitudes. The different MR amplitudes of the oopj- and oopt-measurements at 300 K could be explained by the additional SMR effect present in the Fe_3O_4/Pt bilayer sample. Still astonishing is

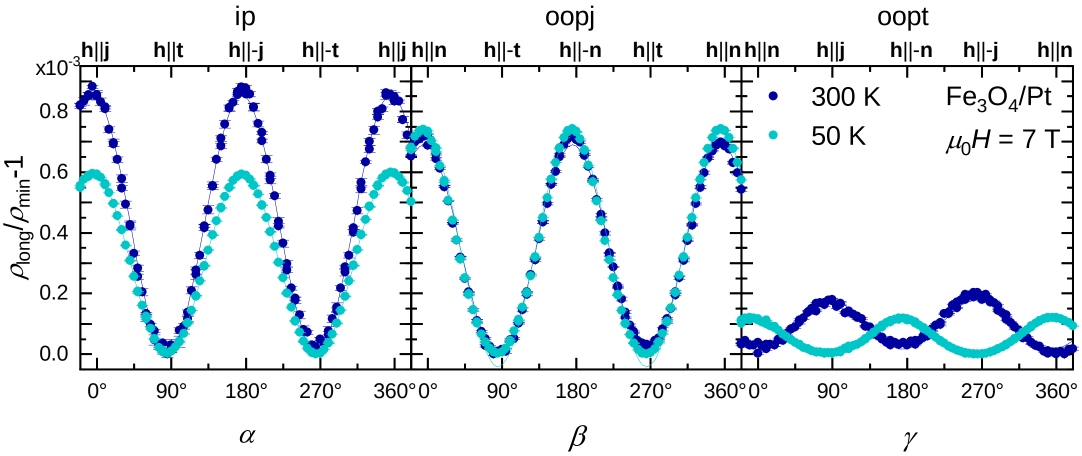

Figure 3.3.6.: ADMR of the Fe_3O_4/Pt bilayer (ip, oopj and oopt rotation) at a magnetic field of 7 T and a temperature of 300 K (blue dots) and 50 K (cyan dots). The normalization of the data and the fit curves follow the same procedure as in Fig. 3.3.5.

the finite amplitude together with the phase change of ρ_{long} in oopt magnetic field rotations at 50 K. The amplitude is too large to be explained only by a misalignment of the Hall bars with respect to the rotation plane of the magnetic field. One possibility for the finite angle-dependence at low temperatures could be the crystalline Pt electrode (cf. Fig. 3.3.1 (a)), which should be considered in the SMR theory. Furthermore, there could be a small but finite current flowing through the Fe_3O_4 thin film, which results in a finite AMR contribution also at low temperatures. Due to a change in crystal symmetry below the Verwey transition, a phase shift of the AMR of Fe_3O_4 could occur. However, this is still under debate, since the SMR theory with no angle-dependence of ρ_{long} in oopt rotation in Fe_3O_4/Pt bilayers was recently confirmed by Pham and coworkers [42].

ADMR measurements on the Fe_3O_4/Pt bilayer are performed in all three magnetic field rotation planes (ip, oopj and oopt) at different magnetic field magnitudes and temperatures. Figure 3.3.7 depicts the ADMR oscillation amplitudes $\mathrm{MR}_{\text{long}}$ (upper panels) and the corresponding phases ϕ (lower panels) as a function of $\mu_0 H$ (left panels) and of T (right panels). Hereby, the results for the ip rotation are shown as blue, full circles, the ones for the oopj rotation as open circles and the ones for the oopt rotation as open diamonds. In addition to that, the field dependent oop measurement is performed at 300 K (blue symbols) as well as at 50 K (cyan symbols). The grey highlighted areas indicate the changes in phase of $\rho_{\text{oopt, long}}$ as a function of $\mu_0 H$ and T.
Figure 3.3.7 shows similar magnetic field dependencies for ip and oopj rotation at 300 K and 50 K (see top left panel). These are comparable to the results of the γ-Fe_2O_3/Pt bilayer shown in Fig. 3.2.7. Therefore, the non-saturation above the determined saturation field $\mu_0 H_S = 3.5$ T is again attributed to the presence of antiphase boundaries. At 7 T and 300 K the MR in ip rotation yields 0.86×10^{-3}. At 70 K the ip MR amplitude is 0.65×10^{-3} and so slightly higher than 0.46×10^{-3} reported at 77 K [42]. The finite MR amplitude in oopt rotation is not comparable to the SMR behavior of γ-Fe_2O_3/Pt bilayers shown in Fig. 3.2.7.

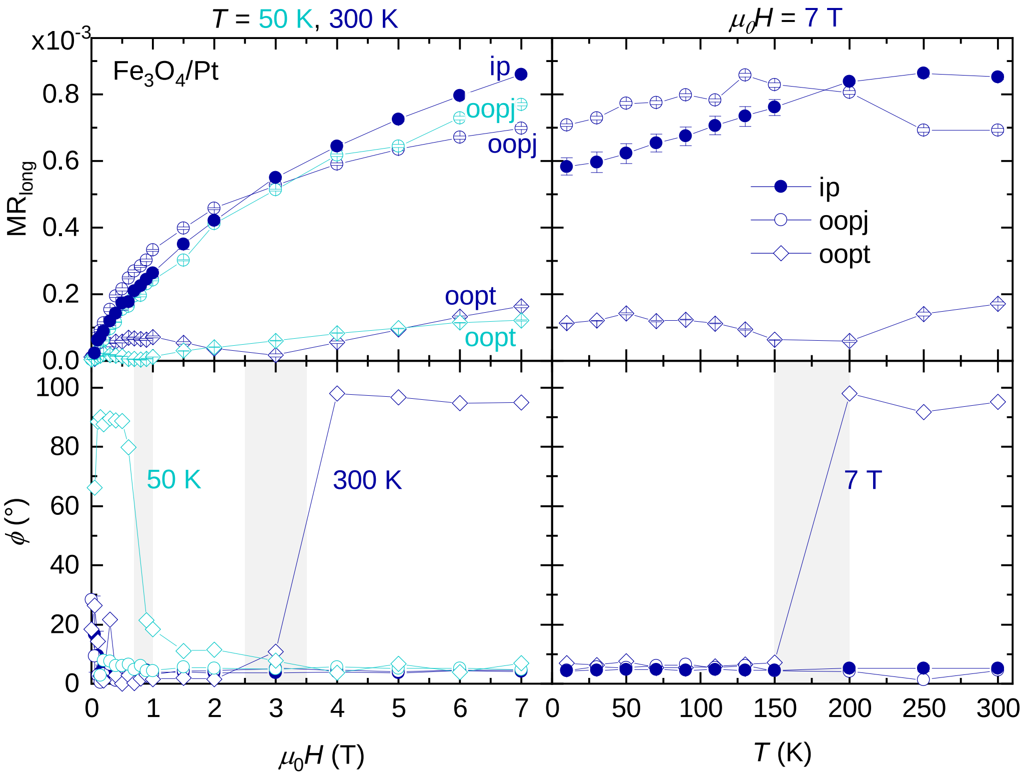

Figure 3.3.7.: From ADMR measurements extracted amplitudes $\mathrm{MR}_{\mathrm{long}}$ und phases ϕ of the Fe_3O_4/Pt bilayer as a function of $\mu_0 H$ at 300 K and 50 K (left panels) and of T at 7 T (right panels). The longitudinal ip magnetoresistances are depicted as blue, full circles and the longitudinal oop (oopj and oopt) magnetoresistances as open blue (at 300 K or 7 T) and cyan (at 50 K) symbols. Below are the corresponding phases ϕ of the resistivities depicted, also as a function of $\mu_0 H$ (lower left panel) and of T (lower right panel). The longitudinal oopt ADMR measurements exhibit a change in the phase ϕ_{oopt} of about 90° in the grey highlighted areas.

In addition, $\rho_{\mathrm{oopt,\,long}}$ undergoes a phase change at around 3 T and 0.9 T at 300 K and 50 K, respectively (see lower left panel in Fig. 3.3.7).

The temperature dependence of the longitudinal MR amplitudes depicted in the top right panel of Fig. 3.3.7 exhibits a similar temperature dependence for the ip rotation as in the case of $\mathrm{SMR}_{\mathrm{long,\,ip}}$ in Fig. 3.2.7. Contrary to that the oopj rotation shows a small increase in $\mathrm{MR}_{\mathrm{long}}$ up to 130 K and then a decrease, which seems to gradually saturate. $\mathrm{MR}_{\mathrm{long,\,oopt}}(T)$ undergoes a change in phase at approximately 175 K (see lower right panel). The ip and oopj rotations, instead, reveal no phase change ($\phi \approx 0°$) as expected.

The behavior of ϕ as a function of the external magnetic field and the temperature is the result of a complex interplay between SMR and AMR effects considering a finite current flowing through the Fe_3O_4 thin film also at low temperature. The lower right panel of Fig. 3.3.7 reveals that the dominating effect at high T and at 7 T is the AMR effect with a maximum in $\rho_{\mathrm{oopt,\,long}}$ at 90°. Decreasing T leads to an increased contribution of the SMR effect. However, aforementioned, a finite AMR is still present at low temperature, indicating a finite charge current also flowing through the Fe_3O_4 thin film leading to a phase shift with a maximum in $\rho_{\mathrm{oopt,\,long}}$ at 0°.

Taking a closer look on the magnetic field dependence of ϕ exhibits also various phase changes. At $50\,\mathrm{K}$ the dominant SMR effect can just develop its full potential, when $\mu_0 H$ is large enough to align the magnetization $\mathbf{M}$ of the Fe_3O_4 thin film along $\mathbf{h}$. So at lower H a smaller SMR amplitude is expected than at higher H. At high fields the same behavior of ϕ at $50\,\mathrm{K}$ is expected as in the case for ϕ at $7\,\mathrm{T}$ and low T. Therefore the same explanations could be applied. Correspondingly, at low fields and $50\,\mathrm{K}$ the SMR effect is not as strong and might lead to a more AMR dominant behavior, since a pure AMR amplitude increases with decreasing T (cf. Ref. [94]). The AMR effect would then lead to a phase change with a maximum in $\rho_{\text{oopt, long}}$ at $90°$. Going up to a higher temperature of $300\,\mathrm{K}$ and then observing the H dependence leads to the opposite behavior. The phase is nearly zero at low H and approximately $90°$ at higher H. As already mentioned the AMR effect dominates at $300\,\mathrm{K}$ leading to $\phi = 0°$.

3.4. Summary

Thin films of the iron oxides α-Fe_2O_3, γ-Fe_2O_3 and Fe_3O_4 were fabricated by PLD and Pt electrodes were deposited on top by EVAP. HR-XRD measurements reveal a high crystalline quality of the iron oxide thin films confirmed by finite thickness fringes and narrow rocking curves around the thin film reflections. Reflectometry measurements indicate similar thicknesses of $t_{\mathrm{Pt}} \approx 3\,\mathrm{nm}$ for all Pt layers of about twice the spin diffusion length of Pt. The α-Fe_2O_3 thin films grew fully relaxed on the (0001)-oriented, hexagonal Al_2O_3 substrates, whereas the γ-Fe_2O_3 and the Fe_3O_4 thin films on (001)-oriented, cubic MgO substrates are fully strained.

SQUID magnetometry measurements of the α-Fe_2O_3 thin films reveal no Morin transition indicating that the α-Fe_2O_3 thin films exhibit no spin reorientation and a magnetically easy plane down to $10\,\mathrm{K}$. The γ-Fe_2O_3 thin films also exhibit no phase transitions in temperature dependent magnetization measurements. In particular no Morin or Verwey transition was found. This is an indicator of the growth of γ-Fe_2O_3 thin films without other iron oxide parasitic phases. The Fe_3O_4 thin films, instead, reveal the expected Verwey transition at $127\,\mathrm{K}$. The γ-Fe_2O_3 and Fe_3O_4 spinel thin films grown on MgO have a strong reduction in the saturation magnetization compared to the bulk values most probably due to the antiferromagnetic coupling of possible antiphase boundaries. In addition, bbFMR measurements of the γ-Fe_2O_3 thin films exhibit a vanishingly small effective magnetization, which is attractive for magnon transport measurements. A reduced effective magnetization leads to a more circular precession of the magnetization and thus suppressing nonlinear damping effects, which should increase the magnon conductivity in γ-Fe_2O_3 as demonstrated for strained YIG [88]. The resonance line widths $\mu_0 \Delta H$ were fitted considering a slow relaxer damping contribution.

The comparison of the temperature dependent resistance $R(T)$ of the γ-Fe_2O_3 and the Fe_3O_4 thin films leads to much higher values in the $\mathrm{G}\Omega$ range for the γ-Fe_2O_3 thin film.

The two crystallographic very similar γ-Fe_2O_3 and Fe_3O_4 phases can also be distinguished by considering the electronic properties of the thin films. ADMR measurements on the α-Fe_2O_3/Pt bilayer can be described within the framework of the theory of the antiferromagnetic SMR considering a trigonal domain structure in the easy plane of α-Fe_2O_3. This includes the $90°$ phase shift of the in-plane angle-dependence of the resistivity compared to the ferrimagnetic SMR effect. In oopj and oopt magnetic field rotation, a discontinuous angle-dependence of the resistivity at $0°$, $180°$ and $360°$ is visible. This can be explained by the trigonal domain structure in α-Fe_2O_3, when the magnetic field points along the surface normal $\mathbf{n}$. For the α-Fe_2O_3/Pt bilayer a longitudinal SMR amplitude of 2.55×10^{-3} can be extracted, which is similar to the previously reported values [12] and therefore confirm the large SMR amplitude in α-Fe_2O_3/Pt. In the γ-Fe_2O_3/Pt bilayer, the angle-dependence of ρ_{long} reveals the ferrimagnetic SMR with a $\cos^2(\phi)$ dependence in ip and oopj magnetic field rotation and a constant high resistive state in oopt magnetic field rotation. A SMR amplitude of 1.07×10^{-3} can be extracted, which is similar to the prototype ferrimagnetic YIG/Pt bilayer. The Fe_3O_4/Pt bilayer reveals a complex interplay between SMR and AMR including a temperature as well as magnetic field dependent phase change of the angle-dependence of the longitudinal resistivity in oopt measurements. Due to the metal to insulator transition at the Verwey transition temperature T_{V} of Fe_3O_4, solely a SMR is expected below T_{V} and an additional dominating AMR effect above T_{V}. Surprisingly, at $50\,\mathrm{K} < T_{\mathrm{V}}$ a finite oscillation of the longitudinal resistivity in oopt magnetic field rotations appear with a phase change with respect to the oopt measurements at $300\,\mathrm{K}$. This might be explained by a finite AMR caused by a finite current through the Fe_3O_4 near the interface to Pt. Unlike the α-Fe_2O_3/Pt bilayer, the bilayers grown on MgO show a nonsaturating SMR amplitude up to $7\,\mathrm{T}$, which might be traced back to the existance of antiphase boundaries in the spinel ferrimagnets γ-Fe_2O_3 and Fe_3O_4. This chapter reveals that in particular the iron oxide materials α-Fe_2O_3 and γ-Fe_2O_3 are suitable candidates for the investigation of the SMR amplitude in magnetic ordered insulator/Pt heterostructures. Therefore, in the next chapter, the influence of doping of these iron oxide materials on the SMR amplitude are investigated in detail.

4. Doping of α-Fe_2O_3 and γ-Fe_2O_3 thin films

In the following Chapter, the effect of doping of α-Fe_2O_3 and γ-Fe_2O_3 on the spin Hall magnetoresistance is discussed. To this end the crystallographic, magnetic and magnetotransport properties of doped α-Fe_2O_3 and γ-Fe_2O_3 thin films are analyzed. First, the influence of Ga doping in α-Fe_2O_3 thin films is reported in Chapter 4.1. Due to the unstable α-Fe_2O_3 phase in these Ga:α-Fe_2O_3 thin films, a undoped α-Fe_2O_3 seed layer are introduced between the substrate and the Ga:α-Fe_2O_3 thin films. The properties of the thus resulting trilayers are discussed in Chapter 4.2. Subsequently, the physical properties of γ-Fe_2O_3 thin films doped with Ga (Chapter 4.3) and a variety of other dopants such as Al, Zn, Ce and Ir are presented (Chapter 4.4). In Chapter 4.5 the relevant results of iron oxide thin films doped with these ions are summarized.

4.1. Ga doping of α-Fe_2O_3

In the next Sections 4.1.1 and 4.1.2, the effect of Ga doping on the crystallographic and magnetic properties of hematite thin films is investigated. Additionally, in Section 4.1.3, ADMR measurements on Ga:α-Fe_2O_3/Pt bilayers are performed to evaluate the effect of Ga doping in α-Fe_2O_3 on the spin Hall magnetoresistance (SMR) amplitude.

4.1.1. Structural analysis of Ga:α-Fe_2O_3/Pt bilayers

For the pulsed laser deposition (PLD) of α-$Fe_{2-x}Ga_xO_3$ thin films with $x = 0.1$ and $x = 0.2$ polycrystalline Ga-doped α-Fe_2O_3 targets (cf. Appendix A.7) together with the same PLD growth parameters and substrates as for the fabrication of α-Fe_2O_3 thin films discussed in Sec. 3.1.1 are used. Subsequently, Pt is deposited in-situ on top of the thin films by electron beam evaporation (EVAP).

The crystalline structure of the Ga:α-Fe_2O_3/Pt bilayers are characterized and compared to the undoped α-Fe_2O_3 thin films by HR-XRD (see Fig. 4.1.1 with α-Fe_2O_3/Pt depicted as purple, α-$Fe_{1.9}Ga_{0.1}O_3$/Pt as blue and α-$Fe_{1.8}Ga_{0.2}O_3$/Pt as cyan lines). In the 2θ-ω scans, the (0006) and (000 12) reflections of the thin films, the corresponding Al_2O_3 substrates as well as the Pt (111) reflection are visible and no other crystalline phases (see Fig. 4.1.1 (a)). The 2θ-ω scans around the Ga:α-Fe_2O_3 (0006) and the Pt (111) reflections reveal Laue oscillations. These fringes are slightly less pronounced for the Ga doped thin films. The top Pt layer is crystalline for all samples, since the Pt (111) reflection emerges below the α-$Fe_{2-x}Ga_xO_3$ (0006) reflection near the theoretical 2θ position of Pt (111) depicted as vertical

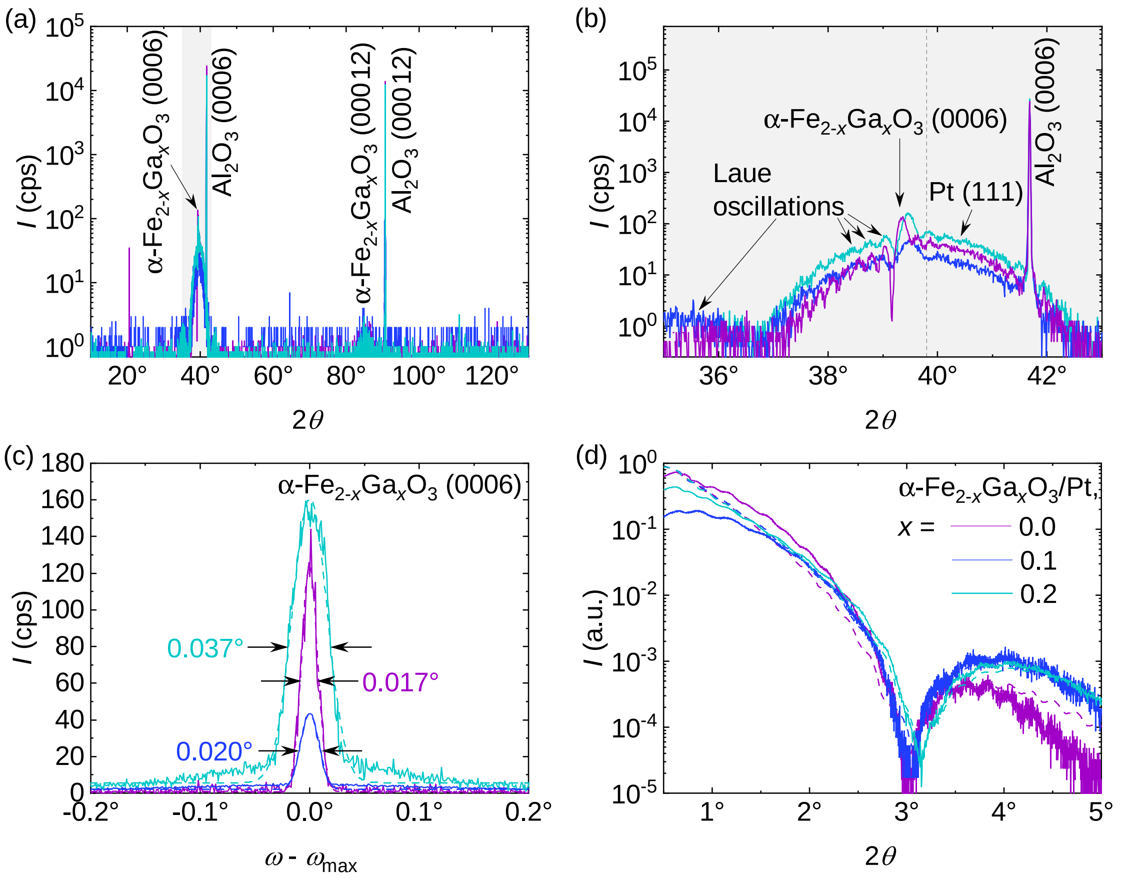

Figure 4.1.1.: HR-XRD of α-$Fe_{2-x}Ga_xO_3$/Pt bilayer samples with $x = 0.1$ and 0.2 together with the undoped α-Fe_2O_3/Pt bilayer sample. The undoped bilayer is depicted in purple, the α-$Fe_{1.9}Ga_{0.1}O_3$/Pt bilayer in blue and the α-$Fe_{1.8}Ga_{0.2}O_3$/Pt bilayer in cyan. (a) Long range 2θ-ω scan including the (0006) and the (000 12) reflections of the Al_2O_3 substrates and Ga:α-Fe_2O_3 thin films and (b) zoom-in around the (0006) reflections. (c) Corresponding rocking curves around the thin film (0006) reflections and Gauss fits in dashed lines. (d) X-ray reflectometry scans in solid and simulations in dashed lines.

dashed line in Fig. 4.1.1 (b). The α-Fe_2O_3 thin film reflections show a shift to higher 2θ values with the incorporation of Ga ions into α-Fe_2O_3. Under consideration of Bragg's law, this entails a decrease of the out-of-plane lattice constant c. The Gauss fits of the rocking curves yield slightly higher FWHMs for the Ga doped hematite thin films of $0.020°$ and $0.037°$ for $x = 0.1$ and 0.2 (cf. Fig. 4.1.1 (c)). Furthermore, the intensity of the Ga:α-Fe_2O_3 (0006) reflections are reduced for $x = 0.1$. Therefore, the 2θ-ω scans as well as the rocking curves reveal a small reduction in the crystalline quality of Ga:α-Fe_2O_3 thin films compared to the undoped one. X-ray reflectometry scans shown in Fig. 4.1.1 (d) are simulated to get the respective thin film and Pt thicknesses. The results are given in Table 4.1.1 together with the FWHMs of all α-$Fe_{2-x}Ga_xO_3$/Pt thin films. The Ga doped hematite thin film thicknesses are in a range from about 20 nm ($x = 0.1$) to almost 40 nm ($x = 0.0$) mainly due to differences in the energy at the target measured just before the respective PLD processes. The Pt layer thicknesses t_{Pt} of all bilayers are approximately the same in their value, in fact, twice the spin diffusion length of Pt. Thus the bilayers are reaching a maximum in the thickness dependent SMR amplitude.

x	FWHM (°)	$t_{\alpha\text{-Fe}_{2-x}\text{Ga}_x\text{O}_3}$ (nm)	t_{Pt} (nm)
0.0	0.0170 ± 0.0001	37.6 ± 0.3	3.2 ± 0.1
0.1	0.0200 ± 0.0002	20.1 ± 0.3	3.2 ± 0.1
0.2	0.0370 ± 0.0003	28.9 ± 0.3	3.0 ± 0.1

Table 4.1.1.: FWHMs of the Gauss fits of the rocking curves shown in Fig. 4.1.1 (c) and layer thickness extracted from the simulations of the X-ray reflectometry scans in Fig. 4.1.1 (d).

Reciprocal space maps are measured around the asymmetric $(10\bar{1}\,10)$ reflections of α-$Fe_{2-x}Ga_xO_3$ and Al_2O_3 and presented in Fig. 4.1.2. The thin film reflections are located far away from the substrate reflections, since the thin films grow fully relaxed on the substrates. Due to the low intensity of the α-$Fe_{1.9}Ga_{0.1}O_3$ $(10\bar{1}\,10)$ reflection, the reflection position is determined by performing multiple rocking curves and detector scans around the area, where the thin film reflection is supposed to be (red lines in Fig. 4.1.2 (a)). The final rocking curve with maximum intensity of the thin film reflection is fitted with a Gaussian function. The hereby extracted ω value of the peak is converted into reciprocal lattice units together with the fixed 2θ value (see Appendix A.1.2.1, Eqs. (A.9) and (A.10)). The resulting position of the α-$Fe_{1.9}Ga_{0.1}O_3$ $(10\bar{1}\,10)$ reflection is marked as the intersection of the two red lines depicted in Fig. 4.1.2. These lines represent the final rocking curve (line from left to right) and the final detector scan (line from top to bottom) in the reciprocal space. For the α-$Fe_{1.8}Ga_{0.2}O_3$/Pt sample the α-$Fe_{1.8}Ga_{0.2}O_3$ $(10\bar{1}\,10)$ reflection is well visible in the lower left corner of the RSM. Here, the reflection position is determined by line scans along the $[H0\bar{H}0]$- and the $[000L]$-direction. Together with the distance d_{hkl} between neighboring lattice planes in a hexagonal crystal, the ip and the oop lattice constants a and c can be calculated. The results are shown in Table 4.1.2. Hereby, c is the average of the oop lattice constant determined from Bragg's law and the 2θ value in Fig. 4.1.1 (b) and the oop lattice constant extracted from the reflection position in the RSM in Fig. 4.1.2. In addition to a and c, the volume change ΔV relative to the bulk volume V of α-Fe_2O_3 are presented in Table 4.1.2.

Additionally, the lattice constants are depicted as a function of the Ga concentration x in Fig. 4.1.3. Therefore, a is shown as green and c as yellow dots together with the respective bulk values of undoped α-Fe_2O_3 ($a_{\alpha\text{-Fe}_2\text{O}_3,\,\text{bulk}} = 0.5034\,\text{nm}$ and $c_{\alpha\text{-Fe}_2\text{O}_3,\,\text{bulk}} = 1.3752\,\text{nm}$ [48]). The undoped thin film exhibits lattice constants near the literature values. The lattice constant a increases slightly and c decreases more noticeably with the incorporation of Ga^{3+} ions into the thin film. But a clear dependence of a on the Ga content x is not visible within the given errors. Since the changes in a and c are very small, just a small expansion in the unit cell volume compared to bulk α-Fe_2O_3 is found (cf. Table 4.1.2).

The low intensity of the α-$Fe_{1.9}Ga_{0.1}O_3$ reflection, the less pronounced Laue oscillations in Fig. 4.1.1 (b) and the increased FWHM of the rocking curve in Fig. 4.1.1 (c) indicate a slightly lower thin film quality of α-$Fe_{1.9}Ga_{0.1}O_3$ compared to the other α-$Fe_{2-x}Ga_xO_3$

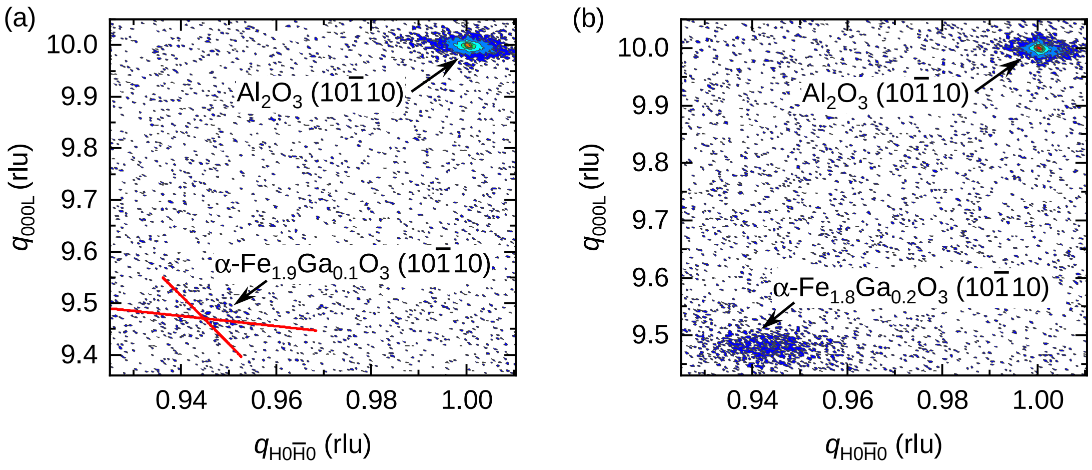

Figure 4.1.2.: Reciprocal space maps around the $(10\bar{1}\,10)$ reflections of Al_2O_3 and α-$Fe_{2-x}Ga_xO_3$ with $x = 0.1$ and 0.2. (a) RSM of the α-$Fe_{1.9}Ga_{0.1}O_3$/Pt and (b) of the α-$Fe_{1.8}Ga_{0.2}O_3$/Pt bilayer. Due to the low intensity, the position of the α-$Fe_{1.9}Ga_{0.1}O_3$ $(10\bar{1}\,10)$ reflection is marked as the intersection of a rocking curve and a detector scan performed after the RSMs and here shown as two red lines. The units are given in reciprocal lattice units (rlu) with respect to the Al_2O_3 substrate.

x	a (nm)	c (nm)	$\Delta V/V$ (%)
0.0 (bulk)	0.5034	1.3752	
0.0	0.504 ± 0.003	1.374 ± 0.001	0.2
0.1	0.505 ± 0.005	1.370 ± 0.002	0.3
0.2	0.505 ± 0.007	1.370 ± 0.001	0.2

Table 4.1.2.: Lattice constants a and c and corresponding relative volume change $\Delta V/V$ of the α-$Fe_{2-x}Ga_xO_3$ thin films. The change in volume (ΔV) is relative to the volume V of a bulk unit cell of α-Fe_2O_3. Literature values for bulk α-Fe_2O_3 are given as a reference [48].

thin films.

The investigation of the lattice constants of the bulk Ga:α-Fe_2O_3 targets by HR-XRD reveals an increase in a and a decrease in c with increasing Ga concentration x up to $x = 0.3$ (cf. Appendix A.7). Overall, the unit cell volume decreases. These results are consistent with those of Bhowmik *et al.*, where a increases with a Ga content of up to $x = 0.36$. But they report also an increase of the lattice constant c and the unit cell volume [99].

Since the ionic radius of Ga^{3+} is 0.62 Å and thus smaller than the one of Fe^{3+} (0.645 Å) [75], in a simple picture a decrease in the lattice constants and the unit cell volume is expected with increasing x. But this can be perturbed by disorder in the crystal lattice [100]. Khan *et al.* confirm the decrease in unit cell volume for Al doping in α-Fe_2O_3 thin films, where Al^{3+} also has a smaller ionic radius than Fe^{3+} [71]. The decrease in the thin film lattice constant c with increasing x (Fig. 4.1.3) fulfills the mentioned expectations. But the behavior of a is still under debate due to the fact that the changes occur on a small scale with large uncertainties. A possible explanation for an increase in a could be made by taking into account the occupation of interstitial sites [101].

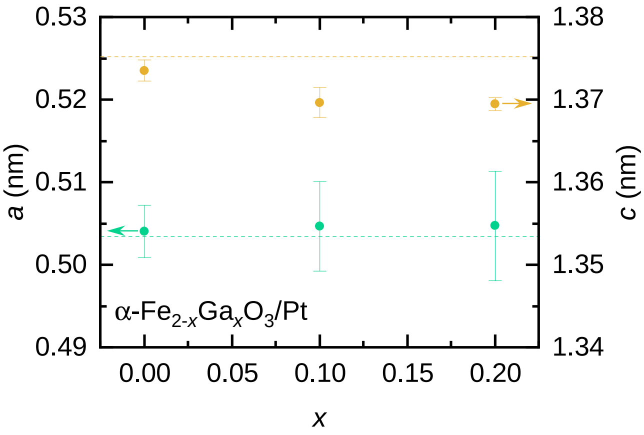

Figure 4.1.3.: In-plane a (green dots) and out-of-plane c (yellow dots) lattice constants of the α-$Fe_{2-x}Ga_xO_3$ thin films of the α-$Fe_{2-x}Ga_xO_3$/Pt bilayer samples. The horizontal dashed lines indicate the bulk values of α-Fe_2O_3 of $a_{\alpha\text{-Fe}_2\text{O}_3,\,\text{bulk}} = 0.5034\,\text{nm}$ and $c_{\alpha\text{-Fe}_2\text{O}_3,\,\text{bulk}} = 1.3752\,\text{nm}$ [48].

4.1.2. Magnetic properties of Ga:α-Fe_2O_3/Pt bilayers

SQUID magnetometry measurements of the α-$Fe_{2-x}Ga_xO_3$/Pt heterostructures shown in Fig. 4.1.4 reveal narrow hysteresis loops and the absence of the Morin transition down to $10\,\text{K}$ for all Ga:α-Fe_2O_3 thin films [77]. The magnetic hysteresis loops show a strong increase in the saturation magnetizations M_S and a strong reduction in the coercive fields H_c of the Ga doped thin films compared to the undoped α-Fe_2O_3 thin film. The saturation magnetization is again defined as the point, where the hysteresis loop (shown in Fig. 4.1.4 (a)) just starts to saturate and a single domain state is reached in the thin film. The extracted values for M_S, $\mu_0 H_\text{S}$ and $\mu_0 H_\text{c}$ are summarized in Table 4.1.3. α-$Fe_{1.9}Ga_{0.1}O_3$ has a more than eight times higher M_S and α-$Fe_{1.8}Ga_{0.2}O_3$ a nearly five times higher M_S than α-Fe_2O_3. In case of $\mu_0 H_\text{c}$, the value of α-$Fe_{1.9}Ga_{0.1}O_3$ is $90\,\%$ smaller and the value of α-$Fe_{1.8}Ga_{0.2}O_3$ $87\,\%$ smaller than the one of α-Fe_2O_3.

A general decrease of the sublattice magnetization with increasing Ga concentration in Ga:α-Fe_2O_3 thin films is expected due to the replacement of magnetic Fe^{3+} ions with non-magnetic Ga^{3+} ions. Since this replacement should be statistically equally distributed, the same amount of magnetic moments is removed in both sublattices. The reduction in the number of canted magnetic moments leads to a decrease in the net magnetization assuming a constant Dzyaloshinskii-Moriya interaction and therefore a constant canting angle δ. Instead, a strong increase in M for α-$Fe_{1.9}Ga_{0.1}O_3$ and α-$Fe_{1.8}Ga_{0.2}O_3$ is visible in Fig. 4.1.4 (a). This counteracts the theoretical expectation of the simple picture aforementioned and might be a result of enhanced spin canting indicated by the calculated canting angle δ in Table 4.1.3. This suggests an increase of the Dzyaloshinskii-Moriya-Interaction in Ga doped α-Fe_2O_3 thin films compared to undoped α-Fe_2O_3 thin films. However, as already mentioned before, structural imperfection might also play a dominant role in modifiying the magnetic properties.

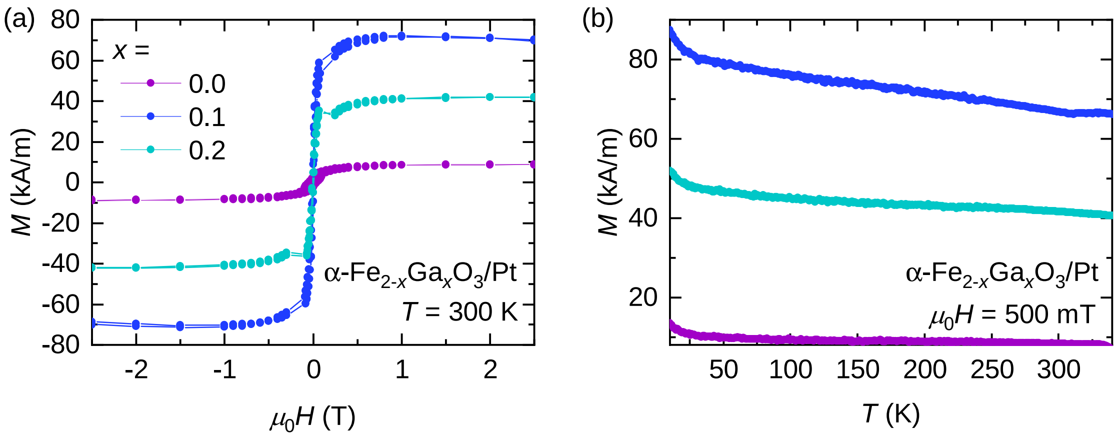

Figure 4.1.4.: SQUID magnetometry measurements of α-$Fe_{2-x}Ga_xO_3$/Pt bilayer samples ($x = 0.0$ in purple, $x = 0.1$ in blue and $x = 0.2$ in cyan). (a) Hysteresis loops recorded at $T = 300\,\mathrm{K}$ with a magnetic field applied in-plane. (b) Temperature-dependence of the magnetization measured with $\mu_0 H = 500\,\mathrm{mT}$ after field-cooled the samples in $\mu_0 H = 7\,\mathrm{T}$.

Figure 4.1.4 (b) reveals that also Ga doped α-Fe_2O_3 thin films do not show any sign of a Morin transition. This might be due to strain effects, size effects or a finite density of oxygen vacancies as discussed in Chapter 3.1.2. The incorporation of dopants such as Ga^{3+} or Al^{3+} into α-Fe_2O_3 supports a decrease in T_M. The magnetic-dipolar (preferring ip orientation of the magnetic moments) as well as the counteracting single-ion anisotropy (preferring oop orientation of the magnetic moments) is reduced by Ga and Al doping [53, 69]. But since the latter anisotropy contribution is more affected by doping (cf. Secs. 2.4.1 and 2.4.4), T_M decreases with increasing doping content in total [53]. A not intended diffusion of Al^{3+} ions from the Al_2O_3 substrates into the Ga:α-Fe_2O_3 thin films could occur next to the intended Ga doping [35]. The reduction in the single ion anisotropy due to doping can also be responsible for the strong decrease in $\mu_0 H_\mathrm{c}$ presented in Table 4.1.3, since in Ref. [102] a connection between Ga doping and decrease in $\mu_0 H_\mathrm{c}$ is claimed. Additionally, in Fig. 4.1.4 (b), a slight increase of M is observed going to very low temperatures. This might be attributed to the existance of localized magnetic moments in the normally diamagnetic Al_2O_3 substrates.

x	M_S $(\mathrm{kA\,m^{-1}})$	$\mu_0 H_\mathrm{S}$ (T)	$\mu_0 H_\mathrm{c}$ (mT)	δ (°)
0.0	8.7 ± 0.2	1.5 ± 0.5	45.5 ± 0.5	0.27
0.1	71.3 ± 0.4	1.0 ± 0.5	4.6 ± 0.1	2.33
0.2	41.9 ± 0.1	2.0 ± 0.5	5.8 ± 0.5	1.45

Table 4.1.3.: Extracted values of M_S, $\mu_0 H_\mathrm{S}$ and $\mu_0 H_\mathrm{c}$ from SQUID magnetometry measurements at 300 K together with the calculated canting angle δ.

4.1.3. Spin Hall magnetoresistance of Ga:α-Fe_2O_3/Pt bilayers

To investigate the SMR effect in α-$Fe_{2-x}Ga_xO_3$/Pt bilayers with $x = 0.1$ and 0.2, ADMR measurements are performed analogously to the ones on the undoped α-Fe_2O_3/Pt bilayer

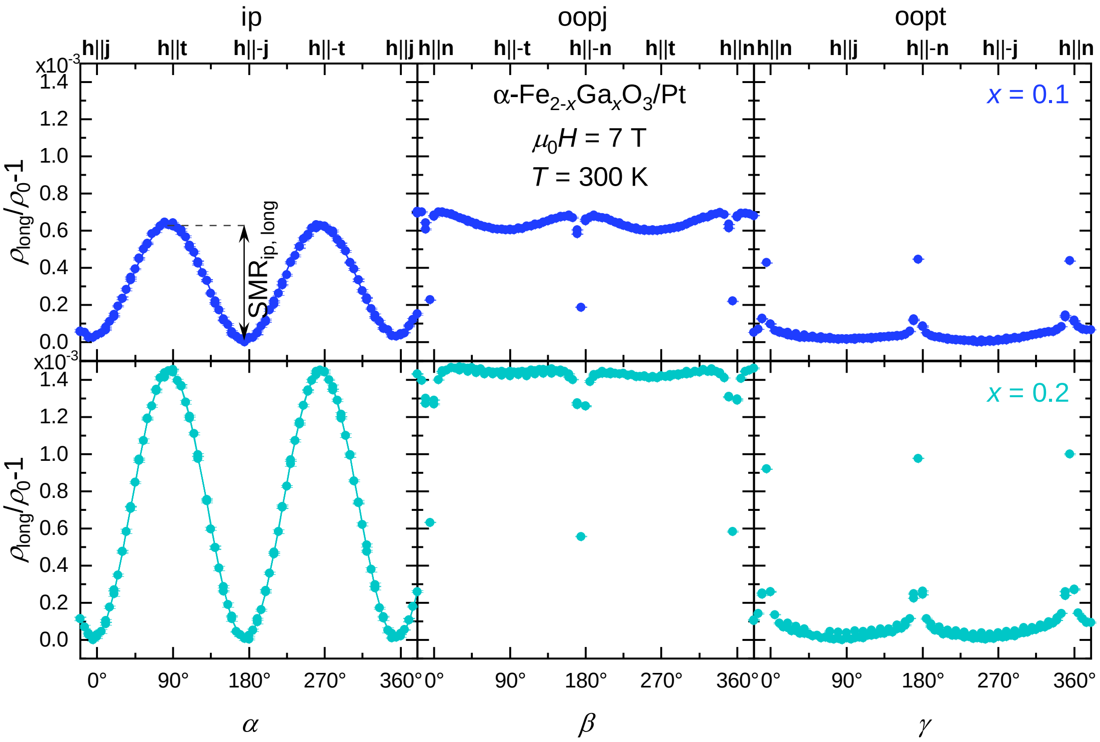

Figure 4.1.5.: ADMR of the α-Fe$_{1.9}$Ga$_{0.1}$O$_3$/Pt (blue dots) and the α-Fe$_{1.8}$Ga$_{0.2}$O$_3$/Pt bilayer (cyan dots) in ip, oopj and oopt rotation of $\mathbf{h}$ at 7 T and 300 K. The data are normalized to ρ_0, respectively. The solid lines of the ip-ADMR measurements are fits to Eq. (2.9). Exemplarily for $x = 0.1$, the longitudinal SMR amplitude SMR$_{\text{ip, long}}$ in ip magnetic field rotation is indicated by the vertical arrow.

discussed in Sec. 3.1.3. The results of the normalized longitudinal resistivity $\rho_{\text{long}}/\rho_0 - 1$ at $T = 300$ K are presented in Fig. 4.1.5 for all rotation planes of $\mathbf{h}$ (ip, oopj and oopt) for $x = 0.1$ (blue dots) and $x = 0.2$ (cyan dots). The normal resistivities of the Pt electrode are for all bilayers in the same order of magnitude ($\rho_0 = 458\,\mathrm{n\Omega\,m}$ (x = 0.0), $301\,\mathrm{n\Omega\,m}$ (x = 0.1) and $270\,\mathrm{n\Omega\,m}$ (x = 0.2)). Hence, the small differences in ρ_0 have no strong influence on the SMR amplitude ρ_1/ρ_0. The applied magnetic field of $\mu_0 H = 7$ T is well above the saturation fields determined in Sec. 4.1.2 ($\mu_0 H_S \leq 2$ T) and thus high enough for a monodomainization of the thin films apart from antiferromagnetic 180° domains. The Ga doped bilayers exhibit the same angular dependencies as for the undoped α-Fe$_2$O$_3$/Pt bilayer sample, i.e. for an antiferromagnetic SMR effect under consideration of a three domain structure (cf. Chpts. 2.3.2 and 3.1.3).

Taking a closer look on the ADMR of the α-Fe$_{1.9}$Ga$_{0.1}$O$_3$/Pt bilayer in oopj magnetic field rotation, exhibits a small oscillation with $\cos(2\beta)$ dependence. This oscillation could be explained by a small misalignment of the Hall bars with respect to the rotation planes of the magnetic field. Additionally, the large applied magnetic field magnitude leads to an increase in the canting of the two magnetic sublattices. Neglecting spin canting ($\delta = 0°$) would result in $\mathbf{m}^{\text{A, B}}$ being perpendicular to $\mathbf{t}$ for $\beta \neq 0°, 180°$, where the AFI is in a single domain state. Therefore, in this case is the projection on $\mathbf{t}$ is zero: $m_t = 0$. Considering a finite canting ($\delta \neq 0°$) a non-zero projection of the magnetic sublattices on $\mathbf{t}$ appears that oscillates with β. According to Eq. (2.5) the projection of $\mathbf{m}^{\mathrm{A,B}}$ on $\mathbf{t}$ leads to a $\cos(2\beta)$ dependence. For ip-ADMR measurements, the finite canting reduces m_t for $\alpha = 0°$ and increases it for $\alpha = 90°$. Therefore, ρ_{long} exhibits a decrease in the oscillation amplitude in ip magnetic field rotations. In case of oopt magnetic field rotations, m_t is generally reduced due to a finite spin canting. By fitting the angle-dependence of the resistivity recorded while rotating the magnetic field in the oopj-plane, a canting angle of $46°$ is calculated, which is much larger than the canting angle $2.33°$ derived from SQUID magnetometry measurements (cf. Table 4.1.3). A canting angle of $2.33°$ would lead to a very small oscillation amplitude of the resistivity of approximately 3×10^{-7}. Therefore, this result rather confirms the assumption of a misalignment of the Hall bars.

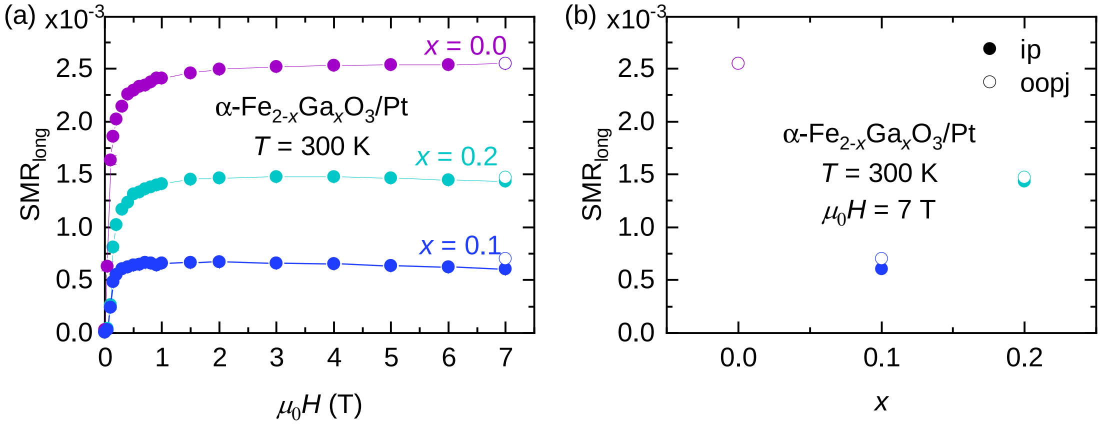

Figure 4.1.6.: From ADMR measurements extracted longitudinal SMR amplitudes SMR$_{\mathrm{long}}$ as (a) a function of $\mu_0 H$ measured at 300 K and (b) a function of the Ga concentration x recorded at 7 T of the α-Fe$_{2-x}$Ga$_x$O$_3$/Pt bilayers with $x = 0.0$ (purple), 0.1 (blue) and 0.2 (cyan). Full circles indicate the amplitudes of ip and open circles the ones of the oopj rotation measurements.

ADMR measurements are performed at magnetic field magnitudes from 7 T down to 0 T at a temperature of 300 K. By using fits to Eq. 2.9, the longitudinal SMR amplitudes of the ip-ADMR measurements (full circles) and by determining the maximum values of $\rho_{\mathrm{long}}/\rho_0 - 1$, the longitudinal SMR amplitudes of the oopj-ADMR measurements (open circles) of the α-Fe$_{2-x}$Ga$_x$O$_3$/Pt bilayers are extracted and shown in Fig. 4.1.6 as (a) a function of $\mu_0 H$ and (b) of x at a fixed magnetic field magnitude of 7 T. SMR$_{\mathrm{ip,\,long}}$ saturates at (3 ± 1) T for $x = 0.0$ and $x = 0.2$. In case of $x = 0.1$, the saturation of SMR$_{\mathrm{ip,\,long}}$ is already reached at (1.5 ± 0.5) T. These results are slightly larger than the saturation fields determined with SQUID magnetometry, but still comparable within the errors (cf. Table 4.1.3). This slight increase in $\mu_0 H_{\mathrm{S}}$ might be, again, due to pinning effects of the domain walls. The smaller $\mu_0 H_{\mathrm{S}}$ for $x = 0.1$ indicates a smaller monodomainization field of the thin film compared to the thin films with $x = 0.0$ and $x = 0.2$. Additionally, the Ga doped bilayers undergo a small decrease in SMR$_{\mathrm{ip,\,long}}$ at magnetic fields larger than the respective saturation field. This decrease might be a result of increased spin canting of the sublattice magnetizations with increasing $\mu_0 H$, which should reduce the SMR amplitude as discussed above.

The SMR amplitudes of the Ga:α-Fe$_2$O$_3$/Pt bilayers are strongly reduced compared to the undoped α-Fe$_2$O$_3$/Pt bilayer (cf. Fig. 4.1.6). The α-Fe$_{1.9}$Ga$_{0.1}$O$_3$/Pt bilayer exhibits a reduction of $76\,\%$ in SMR$_{\text{ip, long}}$ and the α-Fe$_{1.8}$Ga$_{0.2}$O$_3$/Pt bilayer of $44\,\%$ in SMR$_{\text{ip, long}}$ relative to the value of the α-Fe$_2$O$_3$/Pt bilayer of SMR$_{\text{ip, long}}$ $= 2.55 \times 10^{-3}$ at $7\,\mathrm{T}$. The replacement of Fe^{3+} ions with diamagnetic Ga^{3+} ions leads to a reduction in the magnetic moment surface density n_s at the bilayer interface, to which the real part of the effective spin mixing conductance $g_\mathrm{r}^{\uparrow\downarrow}$ is proportional to. Due to the dependence of the SMR amplitude on the effective spin mixing conductance according to Eq. (2.15), a decrease in SMR$_{\text{long}}$ is expected for increasing Ga content. But for $x = 0.1$ a smaller SMR$_{\text{long}}$ is observed than for $x = 0.2$. As the saturation magnetization M_S is larger for the $x = 0.1$ sample than for the $x = 0.2$ one, this result suggests an inverse dependence of the SMR amplitude SMR$_{\text{ip, long}}$ on M_S. As the oscillation amplitude of the ADMR measurements depends only on the direction of the sublattice magnetizations in the framework of the SMR theory (see Sec. 2.3.1), the inverse dependence of SMR$_{\text{ip, long}}$ on M_S might be explained by a different canting angle δ of the $x = 0.1$ sample compared to the $x = 0.2$ layer. However, the change in δ for the two different samples is too small to be solely responsible for the difference in SMR$_{\text{ip, long}}$. Therefore, other effects like changes of the sublattice magnetizations of Ga:α-Fe$_2$O$_3$ or interface effects play a dominant role in the dependence of SMR$_{\text{ip, long}}$ on x.

4.2. α-Fe$_2$O$_3$/Ga:α-Fe$_2$O$_3$/Pt trilayers

The previous section showed a different magnetic behavior of the α-Fe$_{2-x}$Ga$_x$O$_3$/Pt bilayer sample with $x = 0.1$ compared to the Ga-doped α-Fe$_2$O$_3$/Pt bilayer sample with $x = 0.2$. This can mainly be attributed to the polycrystalline α-Fe$_{1.9}$Ga$_{0.1}$O$_3$ target used for the PLD process of the Ga-doped α-Fe$_2$O$_3$ thin film. This target, which was fabricated with a final annealing step at $1000\,^\circ$C, had a low-density, porous texture. This resulted in small regions with concentrated target material on the surface of the α-Fe$_{1.9}$Ga$_{0.1}$O$_3$ thin film. The target was once again annealed, this time at $1200\,^\circ$C and thus leading to a more dense state. However, the α-phase of Fe$_2$O$_3$ appears to be unstable while growing additional α-Fe$_2$O$_3$ thin films on Al$_2$O$_3$ substrates (see XRD results in the Appendix, Fig. A.6.1). Even further optimization of the PLD growth process such as a variation of the oxygen pressure in the PLD chamber from $25\,\mathrm{\mu bar}$ to $75\,\mathrm{\mu bar}$ did not lead to the expected α-Fe$_{1.9}$Ga$_{0.1}$O$_3$ phase. Instead, 2θ-ω scans reveal a thin film reflection near the theoretical expected γ-Fe$_2$O$_3$ (222) reflection, leading to the assumption of the growth of cubic Ga:γ-Fe$_2$O$_3$ on hexagonal Al$_2$O$_3$ (0001). A possible solution to overcome the growth of the γ-phase on Al$_2$O$_3$ substrates is to first deposit an undoped α-Fe$_2$O$_3$ seed layer followed by the Ga-doped Fe$_2$O$_3$ thin film. Therefore, in the following Section, trilayers consisting of α-Fe$_2$O$_3$, Ga:α-Fe$_2$O$_3$ and Pt will be discussed. Next to the properties related to the crystal structure of the trilayers (Sec. 4.2.1), also the magnetic properties (Sec. 4.2.2) together with the results of the respective ADMR measurements (Sec. 4.2.3) are discussed. The latter includes an analysis of the SMR effect in α-Fe_2O_3/α-$Fe_{2-x}Ga_xO_3$/Pt trilayers.

4.2.1. Structural analysis of α-Fe_2O_3/Ga:α-Fe_2O_3/Pt trilayers

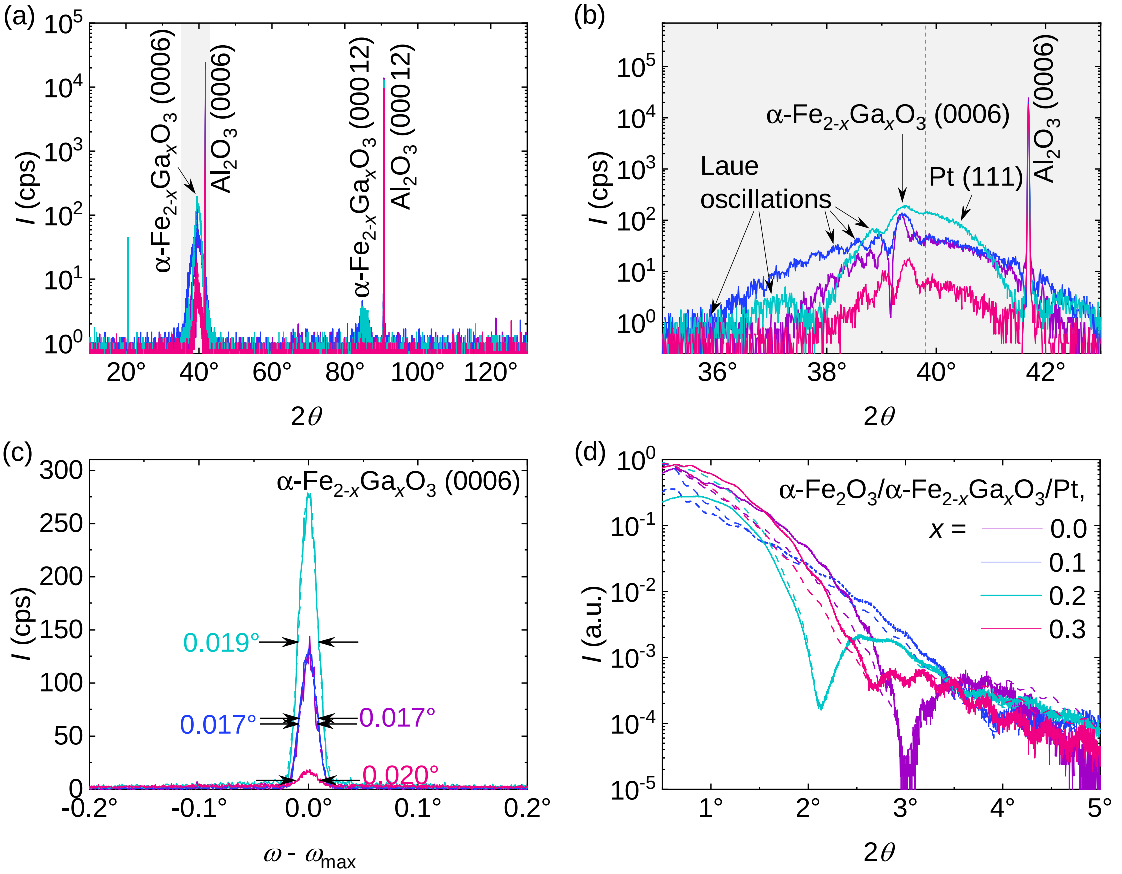

Figure 4.2.1.: HR-XRD of α-Fe_2O_3/α-$Fe_{2-x}Ga_xO_3$/Pt trilayers with $x = 0.1$ in blue, $x = 0.2$ in cyan and $x = 0.3$ in pink and the α-Fe_2O_3/Pt bilayer as a reference in purple. (a) Wide range 2θ-ω scan of the (0006) and (000 12) thin film and substrate reflections and (b) zoom into the 2θ-ω scan around the (0006) reflections together with the Pt (111) reflection and its theoretical position in dashed lines. (c) Rocking curves around the (0006) thin film reflections with the corresponding Gauss fits in dashed lines. (d) X-ray reflectometry scans and respective simulations in dashed lines.

Besides the α-$Fe_{2-x}Ga_xO_3$/Pt bilayers, a trilayer series is fabricated with α-Fe_2O_3 seed layers between the Al_2O_3 (0001) substrates and the α-$Fe_{2-x}Ga_xO_3$ thin films. This results in the stacking sequence Al_2O_3//α-Fe_2O_3/α-$Fe_{2-x}Ga_xO_3$/Pt with $x = 0.1$, 0.2 and 0.3. For the thin film deposition of the iron oxide layers the same growth parameters are used as in Secs. 3.1.1 and 4.1.1 except for the total pulse number of the α-Fe_2O_3 layer. For the seed layer the number of pulses is set to 5000, afterwards the respective α-$Fe_{2-x}Ga_xO_3$ thin films are grown by using 20000 pulses hitting the respective target. The α-Fe_2O_3 seed layer should provide better growth conditions for the α-$Fe_{2-x}Ga_xO_3$ thin films due to the same crystal symmetry and the strongly reduced lattice mismatch compared to that of α-Fe_2O_3

thin films on Al_2O_3 substrates.

x	FWHM (°)	$t_{\alpha\text{-}Fe_{2-x}Ga_xO_3}$ (nm)	t_{Pt} (nm)
0.0	0.0170 ± 0.0001	38 ± 1	3.2 ± 0.1
0.1	0.0170 ± 0.0001	26 ± 2	2.2 ± 0.1
0.2	0.0190 ± 0.0001	27 ± 5	4.9 ± 0.1
0.3	0.0200 ± 0.0004	28 ± 3	3.6 ± 0.1

Table 4.2.1.: Structural parameters of the α-Fe_2O_3/α-$Fe_{2-x}Ga_xO_3$/Pt trilayers: FWHMs of the rocking curves depicted in Fig. 4.2.1 (c) together with the layer thicknesses of α-$Fe_{2-x}Ga_xO_3$ and Pt.

HR-XRD measurements of the α-Fe_2O_3/α-$Fe_{2-x}Ga_xO_3$/Pt trilayers reveal that the seed layers lead to the desired growth of the hexagonal Ga:α-Fe_2O_3 phase. Since the undoped seed layers are expected to be much thinner than the α-$Fe_{2-x}Ga_xO_3$ layers, reflections in 2θ-ω scans can be attributed mostly to the α-$Fe_{2-x}Ga_xO_3$ thin film layer. In Fig. 4.2.1 (a), only the (0006) and the (000 12) reflections of the hexagonal α-Fe_2O_3 phase together with the Pt (111) reflection are visible for all trilayers. Figure 4.2.1 (b) confirms the coherent growth of crystalline Ga:α-Fe_2O_3/Pt layers on Al_2O_3//α-Fe_2O_3 with the appearence of Laue oscillations. Therefore, in contrast to Fig. A.6.1 demonstrating the growth of γ-$Fe_{2-x}Ga_xO_3$ on Al_2O_3 substrates, the fabrication of α-$Fe_{2-x}Ga_xO_3$ thin films with $x = 0.1$, 0.2 and 0.3 is feasible using undoped α-Fe_2O_3 seed layers on Al_2O_3 substrates. In Fig. 4.2.1 (c) all rocking curves around the (0006) reflections exhibit small FWHMs $\leq 0.02°$, indicating a low mosaic spread. Additionally in Fig. 4.2.1 (d), the simulated X-ray reflectometry scans give the Pt thicknesses t_{Pt} summarized in Table 4.2.1. Hereby, t_{Pt} is strongly reduced for $x = 0.1$ and strongly increased for $x = 0.2$. Only the α-Fe_2O_3/α-$Fe_{1.7}Ga_{0.3}O_3$/Pt trilayer has a Pt thickness comparable to the undoped α-Fe_2O_3/Pt bilayer and thus $t_{Pt} \approx 2\lambda_{sf}$. Since it is not possible to distinguish between the α-$Fe_{2-x}Ga_xO_3$ and the α-Fe_2O_3 layer in terms of the thickness simulation, the layer thickness of α-$Fe_{2-x}Ga_xO_3$ is determined by taking into account the Laue oscillations shown in Fig. 4.2.1 (b) and using $t_{\alpha\text{-}Fe_{2-x}Ga_xO_3} = \lambda(n_1 - n_2)/[2(\sin(\theta_1) - \sin(\theta_2))]$ [103]. The neighboring 2θ positions of the Laue oscillations ($n_1 - n_2 = -1$) and averaging over all calculated $t_{\alpha\text{-}Fe_{2-x}Ga_xO_3}$ leads to the values given in Table 4.2.1. For the α-Fe_2O_3 seed layers a constant growth rate is assumed resulting in $t_{\alpha\text{-}Fe_2O_3} = 7\,\text{nm}$ for all trilayers.

Reciprocal space mappings around the asymmetric α-$Fe_{2-x}Ga_xO_3$ $(10\bar{1}\,10)$ reflections shown in Fig. 4.2.2 face the difficulty of low reflection intensities. In case of (a) $x = 0.1$, the $(10\bar{1}\,10)$ reflection is still visible, but for (b) $x = 0.2$ this is hardly possible anymore. The α-Fe_2O_3/α-$Fe_{1.7}Ga_{0.3}O_3$/Pt trilayer already revealed low intensities of the symmetric out-of-plane reflections shown in Fig. 4.2.1 and so in the corresponding RSM no thin film reflection is visible. The RSM for $x = 0.3$ is attached to the Appendix, Fig. A.3.3. But for all trilayers it is possible to perform rocking curves and detector scans around the supposed reflection areas. Analogously to the reflection determination of α-$Fe_{1.9}Ga_{0.1}O_3$ $(10\bar{1}\,10)$ in Fig. 4.1.2, here the reflection positions are determined by the final rocking curves with a

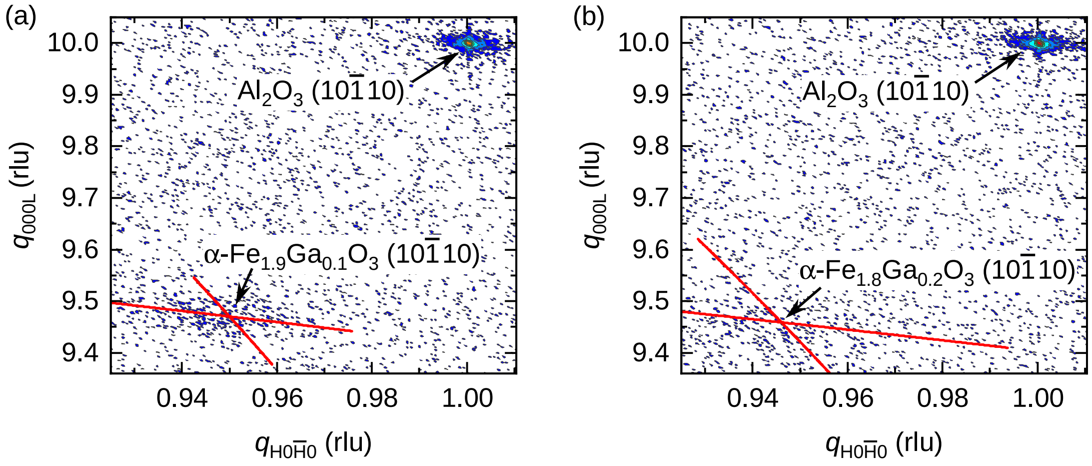

Figure 4.2.2.: RSMs around the asymmetric α-$Fe_{2-x}Ga_xO_3$ $(10\bar{1}\,10)$ and Al_2O_3 $(10\bar{1}\,10)$ reflections with (a) $x = 0.1$ and (b) $x = 0.2$. Multiple rocking curves and detector scans are performed for a better determination of the reflection positions. The final rocking curves and the final detector scans shown in red lines lead to the reflection positions indicated by the corresponding line intersections.

fixed 2θ value and an extracted ω value, at which the intensity is maximum. The thin film reflection positions are marked as the line intersections depicted in Fig. 4.2.2. Hereby, the red lines represent the final rocking curves and detector scans.

The thus obtained in-plane lattice constants a as well as out-of-plane lattice constants c averaged over the results of the 2θ-ω scans in Fig. 4.2.1 (b) and the RSMs are given in Table 4.2.2 together with the unit cell volume of the trilayers compared to bulk α-Fe_2O_3. The variation of the unit cell volume ΔV is small for all fabricated trilayers demonstrating low oxygen vacancies and therefore the right stochiometry of the Ga-doped α-Fe_2O_3 thin films.

x	a (nm)	c (nm)	$\Delta V/V$ (%)
0.0 (bulk)	0.5034	1.3752	
0.0	0.504 ± 0.003	1.374 ± 0.001	0.2
0.1	0.502 ± 0.005	1.371 ± 0.001	-0.9
0.2	0.503 ± 0.008	1.371 ± 0.002	-0.5
0.3	0.503 ± 0.007	1.369 ± 0.001	-0.6

Table 4.2.2.: Lattice constants a and c and relative volume change $\Delta V/V$ for the α-Fe_2O_3/Pt bilayer and all α-Fe_2O_3/α-$Fe_{2-x}Ga_xO_3$/Pt trilayers. The α-Fe_2O_3 bulk values are given as a reference and taken from Ref. [48]. V is defined as the corresponding unit cell volume of bulk α-Fe_2O_3.

The lattice constants are plotted as a function of the Ga content x in α-$Fe_{2-x}Ga_xO_3$ in Fig. 4.2.3. The ip lattice constant a (green dots) does not change within the given errors and remains near the bulk value of α-Fe_2O_3 indicated in dashed, green lines. The errors, however, are large due to the low intensity of the α-$Fe_{2-x}Ga_xO_3$ $(10\bar{1}\,10)$ reflections and the accompanying difficulties in determining the reflection positions. The oop lattice constant c (yellow), instead, reveals a decrease with increasing x compared to the lattice constant of undoped hematite. Within the errors, these results are in agreement with the results of the Ga:α-Fe$_2$O$_3$/Pt bilayers in Fig. 4.1.3. Therefore, the behavior of a as a function of x remains unclear, since a decrease of a is expected due to the smaller ionic radius of the Ga^{3+} ions compared to the Fe^{3+} ions. The out-of-plane lattice constant c instead indicates the expected behavior of a decrease with increasing Ga concentration. All in all, the unit cell volume also decreases with the incorporation of Ga^{3+} ions.

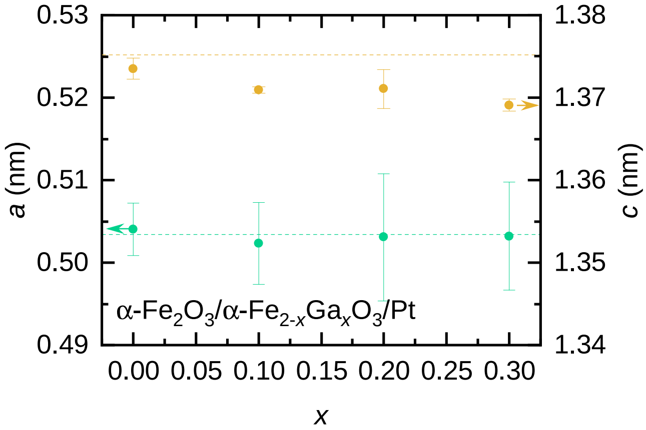

Figure 4.2.3.: In-plane lattice constants a (green dots) and out-of-plane lattice constants c (yellow dots) of α-Fe$_{2-x}$Ga$_x$O$_3$ as a function of the Ga concentration x in α-Fe$_2$O$_3$/α-Fe$_{2-x}$Ga$_x$O$_3$/Pt trilayers. The dashed lines indicate the bulk lattice constants of α-Fe$_2$O$_3$ ($a_{\alpha\text{-Fe}_2\text{O}_3,\,\text{bulk}} = 0.5034\,\text{nm}$, $c_{\alpha\text{-Fe}_2\text{O}_3,\,\text{bulk}} = 1.3752\,\text{nm}$ [48]).

4.2.2. Magnetic properties of α-Fe$_2$O$_3$/Ga:α-Fe$_2$O$_3$/Pt trilayers

The magnetic properties of α-Fe$_2$O$_3$/Ga:α-Fe$_2$O$_3$/Pt trilayers are investigated by SQUID magnetometry. Measurements of the magnetization M as a function of $\mu_0 H$ at 300 K and as a function of T at 500 mT are presented in Fig. 4.2.4 for all trilayers including the undoped α-Fe$_2$O$_3$/Pt bilayer ($x = 0.0$ (purple), $x = 0.1$ (blue), $x = 0.2$ (cyan) and $x = 0.3$ (pink)). The linear background mainly due to the diamagnetic contribution of the Al$_2$O$_3$ substrates was subtracted before and M represents the net magnetization of both, the Ga:α-Fe$_2$O$_3$ layer and the undoped α-Fe$_2$O$_3$ seed layer beneath, since SQUID magnetometry is an integral measurement method and cannot distinguish between the two magnetic layers. The hysteresis loops in (a) for $x = 0.1$ and $x = 0.2$ are reduced in M compared to undoped hematite and have similar values for the saturation magnetization M_S (cf. Table 4.2.3) that is defined as the net magnetization of the DMI induced sublattice canting. The saturation field increases with increasing x from 1.5 T for $x = 0.0$ and $x = 0.1$ to 2.5 T for $x = 0.3$. At the same time the coercive field decreases with increasing x. The measured M_S differ greatly from the results of the Ga:α-Fe$_2$O$_3$/Pt bilayers (cf. Fig. 4.1.4), but at least for $x = 0.1$ and $x = 0.2$ the expected decrease in M_S with Ga doping is visible. For $x = 0.3$ a larger value of M_S is observed, which suggests either that one magnetic sublattice is preferred over the other in terms of replacing Fe^{3+} ions with nonmagnetic Ga^{3+} ions or an increased

DMI, which results in a stronger spin canting. The canting angle δ presented in Table 4.2.3 is calculated from the saturation magnetization $M_{\mathrm{S},\,\alpha\text{-Fe}_{2-x}\text{Ga}_x\text{O}_3}$ of the α-$Fe_{2-x}Ga_xO_3$ thin film only, assuming a statistically equal distribution of Ga^{3+} ions in the α-Fe_2O_3 lattice. Therefore a thickness of 7 nm is assumed for the α-Fe_2O_3 seed layer and the corresponding $M(H)$ of α-Fe_2O_3 is subtracted from the hysteresis loop shown in Fig. 4.2.4 (a) to get the net magnetization of the α-$Fe_{2-x}Ga_xO_3$ layer. The canting angle reflects the M_S dependence on x and shows a decrease up to $x = 0.2$, while the larger canting angle of the α-$Fe_{1.7}Ga_{0.3}O_3$ thin film suggests a stronger spin canting.

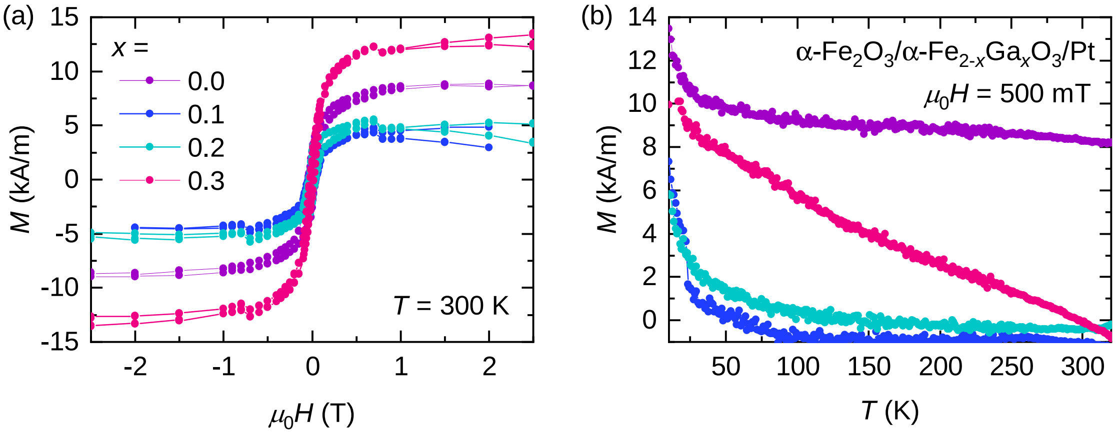

Figure 4.2.4.: SQUID magnetometry with (a) M measured as a function of $\mu_0 H$ at 300 K and (b) M measured as a function of T at 500 mT. The α-Fe_2O_3/α-$Fe_{2-x}Ga_xO_3$/Pt trilayers are depicted in blue ($x = 0.1$), cyan ($x = 0.2$) and pink ($x = 0.3$) and the undoped α-Fe_2O_3/Pt bilayer in purple dots. A linear background of the magnetic hysteresis in (a) mainly caused by the diamagnetic contribution of the Al_2O_3 substrate is subtracted beforehand.

x	M_S $(\mathrm{kA\,m^{-1}})$	$\mu_0 H_S$ (T)	$\mu_0 H_c$ (mT)	$M_{\mathrm{S},\,\alpha\text{-Fe}_{2-x}\text{Ga}_x\text{O}_3}$ $(\mathrm{kA\,m^{-1}})$	δ (°)
0.0	8.7 ± 0.2	1.5 ± 0.5	46 ± 1		0.27
0.1	4.3 ± 0.3	1.5 ± 0.5	43 ± 3	3.8 ± 0.1	0.12
0.2	5.0 ± 0.3	2.0 ± 0.5	36 ± 2	3.7 ± 0.4	0.13
0.3	13 ± 0.3	2.5 ± 0.5	21 ± 1	14.1 ± 0.3	0.52

Table 4.2.3.: Extracted values of M_S, $\mu_0 H_S$ and $\mu_0 H_c$ from SQUID magnetometry measurements at 300 K. The canting angle δ is calculated from the saturation magnetization $M_{\mathrm{S},\,\alpha\text{-Fe}_{2-x}\text{Ga}_x\text{O}_3}$ of the α-$Fe_{2-x}Ga_xO_3$ layer only, after subtracting the magnetization of the approximately 7 nm thick α-Fe_2O_3 seed layer.

In case of the temperature dependent magnetization curves shown in Fig. 4.2.4 (b), the Morin transition is absent for all trilayers as also observed and already explained for the α-$Fe_{2-x}Ga_xO_3$/Pt bilayers in Sec. 4.1.2. The α-Fe_2O_3/α-$Fe_{1.7}Ga_{0.3}O_3$/Pt trilayer exhibits a $M(T)$ behavior different from that of the other thin films and thus not typical for a canted antiferromagnet. $M(T)$ strongly increases with decreasing T in a nearly linear way. For $x = 0.1$ and $x = 0.2$ a negative magnetization is derived at higher temperatures after subtracting the diamagnetic contribution from the Al_2O_3 substrate. Since the applied magnetic field of 500 mT is well below the saturation fields, magnetic domains in the thin films, which lead to a net magnetization not pointing along the external magnetic field direction, are most likely responsible fot the negative signal. All trilayers exhibit a slight increase of M at low T, being most propably attributed to the existance of localized magnetic moments in the Al$_2$O$_3$ substrates.

4.2.3. Spin Hall magnetoresistance of α-Fe$_2$O$_3$/Ga:α-Fe$_2$O$_3$/Pt trilayers

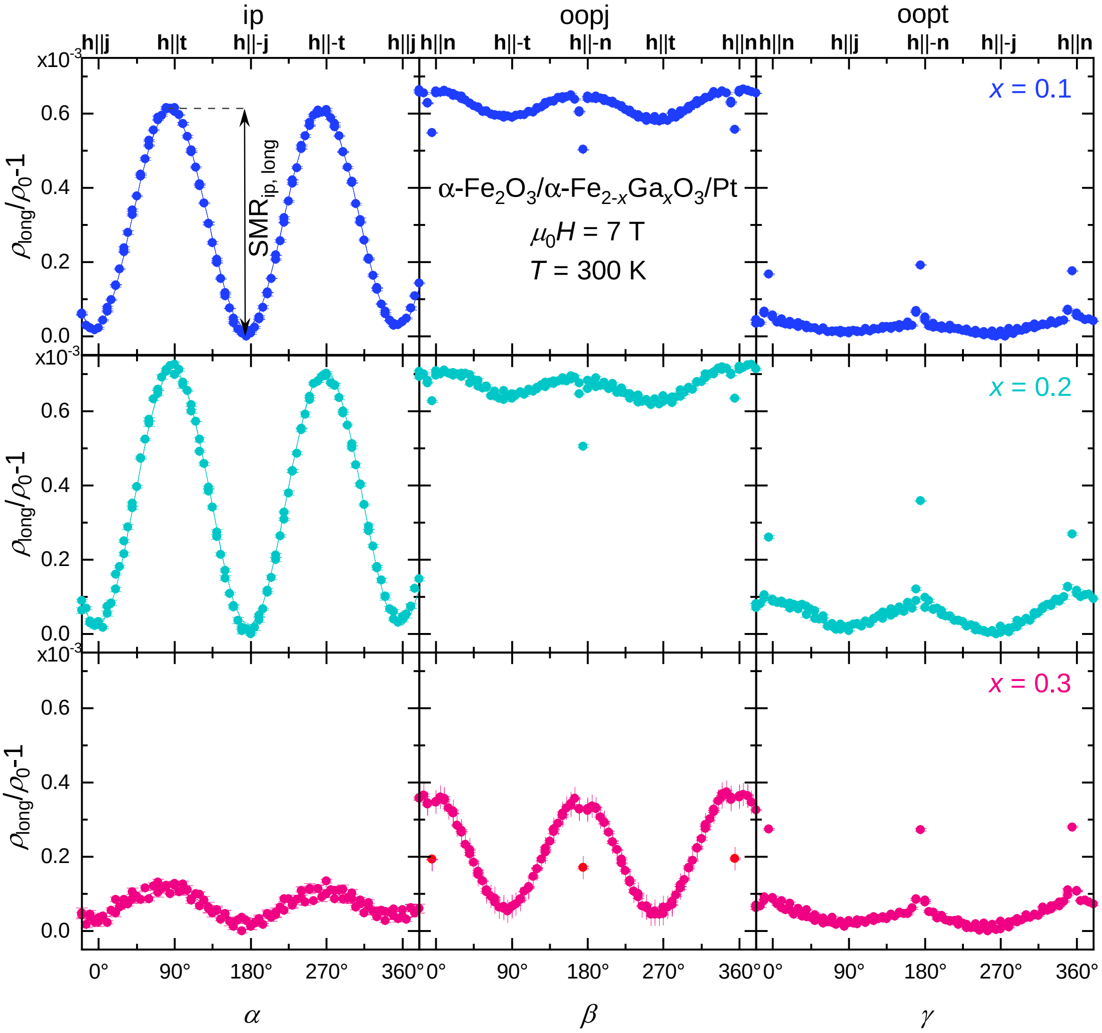

Figure 4.2.5.: ADMR measurements of the α-Fe$_2$O$_3$/α-Fe$_{2-x}$Ga$_x$O$_3$/Pt trilayers in ip, oopj and oopt rotation of **h** at 7 T and 300 K with $x = 0.1$ (blue), $x = 0.2$ (cyan) and $x = 0.3$ (pink). Fits to Eq. (2.9) of the ip-ADMR measurements are depicted by solid lines. For $x = 0.1$ in ip magnetic field rotation, the longitudinal SMR amplitude SMR$_{\text{ip, long}}$ is indicated by the vertical arrow.

For the investigation of the SMR in α-Fe$_2$O$_3$/Ga:α-Fe$_2$O$_3$/Pt trilayers, ADMR measurements are performed at various magnetic field magnitudes. The measurements are executed in ip, oopj and oopt rotations of the magnetic field at 300 K. The derived longitudinal resistivities ρ_{long} at 7 T depicted in Fig. 4.2.5 are normalized to ρ_0, respectively. For $x = 0.1$ (blue dots) ρ_0 is 343 nΩ m, for $x = 0.2$ (cyan dots) it is 195 nΩ m and for $x = 0.3$ (pink dots) it is $241\,\mathrm{n\Omega\,m}$. So ρ_0 exhibits comparable values for all trilayers. Since the applied magnetic field is above the saturation fields summarized in Table 4.2.3, a single domain state is expected at 7 T for ip-ADMR measurements apart from indistinguishable $180°$ domains.

The ADMR measurements are in agreement with the SMR in AFI/HM bilayers (cf. Chapter 3.1.3). However, there are deviations from the expected behavior. First a strong decrease of the ADMR amplitude for ip magnetic field rotations of the α-Fe$_{1.7}$Ga$_{0.3}$O$_3$/Pt bilayer is visible. Furthermore, oscillations of ρ_{long} for oopj and oopt magnetic field rotations are detectable, most pronounced for the α-Fe$_{1.7}$Ga$_{0.3}$O$_3$/Pt bilayer. As described in Sec. 4.1.3, this additional $\cos(2\phi)$ dependence might stem from an increased canting of the magnetic sublattices in Ga:α-Fe$_2$O$_3$. This leads to a change in the projection m_{t} of the sublattice magnetizations $\mathbf{m}^{\mathrm{A,\,B}}$ on the transverse direction $\mathbf{t}$. For the $x = 0.3$ bilayer, the $\cos(2\beta)$ dependence even dominates compared to the expected high resistive state for AFI/HM interfaces. Since the canting angle of $\delta = 0.52°$ extracted from SQUID magnetometry measurements would result in a small oscillation in oopj rotation plane with an amplitude of approximately 2×10^{-9}, this strong angle-dependence of ρ_{long} cannot be explained solely by a finite spin canting. In particular, the different values obtained for $\beta = 0°$, $180°$ and $360°$ and $\gamma = 0°$, $180°$ and $360°$, i.e. for $\mathbf{h} \parallel \mathbf{n}$, point to an additional misalignment of the Hall bar with respect to the oopj-rotation plane in the oopj-ADMR measurement.

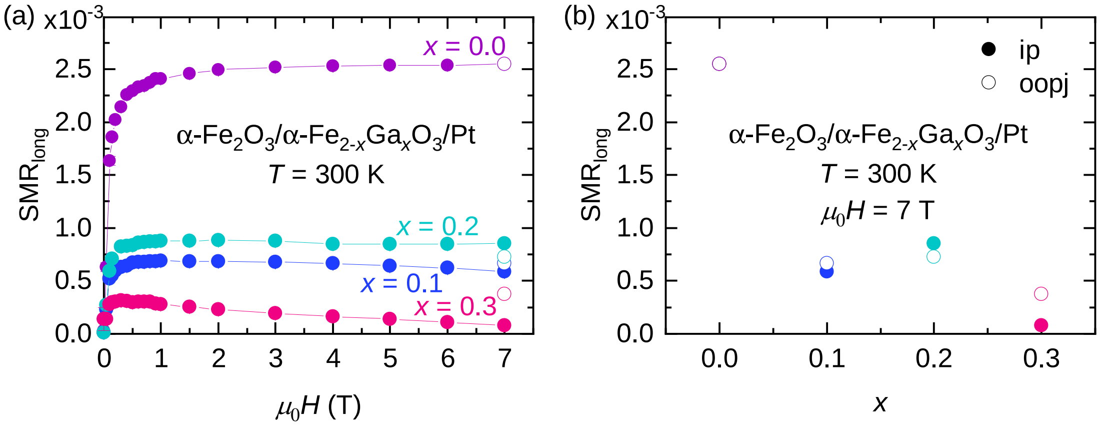

Figure 4.2.6.: SMR$_{\mathrm{long}}$ amplitude of α-Fe$_2$O$_3$/α-Fe$_{2-x}$Ga$_x$O$_3$/Pt trilayers with $x = 0.0$ (purple), $x = 0.1$ (blue), $x = 0.2$ (cyan) and $x = 0.3$ (pink) at 300 K as (a) a function of the magnetic field magnitude $\mu_0 H$ and (b) of the Ga content x at 7 T. The ip rotation results are represented by full circles and the oopj rotation results by open circles. SMR$_{\mathrm{long}}$ in ip magnetic field rotation is determined as the oscillation amplitude of $\rho_{\mathrm{long}}/\rho_0 - 1$ and SMR$_{\mathrm{long}}$ in oopj magnetic field rotation as the maximum value of $\rho_{\mathrm{long}}/\rho_0 - 1$. For the $x = 0.2$ trilayer, the SMR amplitude is corrected due to the larger Pt thickness of $4.9\,\mathrm{nm}$ by taking into account the Pt thickness dependence reported in Ref. [28].

ADMR measurements are further performed at different magnitudes of $\mathbf{H}$ to get the magnetic field dependence of SMR$_{\mathrm{long}}$ depicted in Fig. 4.2.6 (a). The SMR amplitude is strongly reduced for all trilayers compared to the undoped α-Fe$_2$O$_3$/Pt bilayer. All values are below 1×10^{-3}, more specifically, SMR$_{\mathrm{ip,\,long}}$ is 0.59×10^{-3} for $x = 0.1$, 0.86×10^{-3} for $x = 0.2$ and 0.08×10^{-3} for $x = 0.3$ at 7 T. The SMR amplitude is corrected for $x = 0.2$

due the much thicker Pt electrode ($t_{Pt} = 4.9\,\mathrm{nm}$) compared to the other trilayers. Thereby, SMR_{long} is calculated for a Pt thickness of $3\,\mathrm{nm}$ according to the t_{Pt} dependence of the SMR amplitude reported in Ref. [28]. This leads to an increase in SMR_{long} for the α-Fe_2O_3/α-$Fe_{1.8}Ga_{0.2}O_3$/Pt trilayer. The saturation field decreases with the incorporation of Ga^{3+} ions ($\mu_0 H_S = (1 \pm 0.5)\,\mathrm{T}$ for $x = 0.1$, $(1 \pm 0.4)\,\mathrm{T}$ for $x = 0.2$ and $(0.5 \pm 0.3)\,\mathrm{T}$ for $x = 0.3$). This tendency is contradictory to the trend observed in the SQUID measurements (cf. Table 4.2.3), where $\mu_0 H_S$ generally increases with x and might be explained by a different dependence of the magnetic properties as a function of the external magnetic field at the interface to Pt compared to that of the whole iron oxide thin films. Furthermore, a reduction in $SMR_{ip,\,long}$ at high magnetic fields is observable for all trilayers, but affects especially the α-Fe_2O_3/α-$Fe_{1.7}Ga_{0.3}O_3$/Pt trilayer, which also exhibits a very small $\mu_0 H_S$. The SMR amplitude SMR_{long} as a function of the Ga concentration x at 7 T and 300 K reveals a strong decrease with the incorporation of Ga^{3+} ions in general, but no clear dependence on x (see Fig. 4.2.6 (b)). A continuous decrease with increasing x is expected due to the reduction in the number of magnetic moments at the AFI/HM interface, on which a spin transfer torque can be exerted on. This is only fulfilled by excluding the SMR amplitude measured for the trilayer with a Ga content of $x = 0.1$. However, interestingly, the dependence of SMR_{long} on the Ga concentration x of the α-Fe_2O_3/α-$Fe_{2-x}Ga_xO_3$/Pt trilayer samples with $x = 0.1$ and 0.2 is similar to that of the α-$Fe_{2-x}Ga_xO_3$/Pt bilayers shown in Fig. 4.1.6 (b) although the SQUID magnetometry measurements reveal different magnetic properties of these samples. Anyhow, the influence of the Ga doping in α-Fe_2O_3 on the SMR amplitude needs to be further clarified in future experiments. In particular, the different temperature dependence together with the strong reduction in SMR amplitude of the $x = 0.3$ trilayer sample needs to be clarified.

4.3. Ga doping of γ-Fe_2O_3

Analogous to the doping of α-Fe_2O_3 with Ga^{3+} ions, also γ-Fe_2O_3 thin films are doped with Ga^{3+} ions and characterized in the next Section. Therefore, the structural (Sec. 4.3.1), magnetic (Sec. 4.3.2) and magnetotransport properties (Sec. 4.3.3) will be discussed. Particular emphasis is placed on the latter, including the SMR effect in γ-Fe_2O_3/Pt bilayers.

4.3.1. Structural analysis of Ga:γ-Fe_2O_3/Pt bilayers

Ga:γ-Fe_2O_3 thin films on (100)-oriented MgO substrates are fabricated by PLD using the same growth parameters as described in Sec. 3.2.1. A Pt electrode is deposited in-situ on top of the γ-$Fe_{2-x}Ga_xO_3$ thin films by EVAP. The structural properties of the bilayers are characterzied by HR-XRD as shown in Fig. 4.3.1. The 2θ-ω scan depicted in Fig. 4.3.1 (a) confirms the crystalline growth of the Ga:γ-Fe_2O_3 phase only. The (004) and the (008) thin film reflections occur together with the (002) and the (004) MgO substrate reflections. The Pt electrode is cystalline for all bilayers except for $x = 0.2$, where no Pt (111) reflection is visible. The 2θ-ω scans further reveal Laue oscillations with different degrees of distinctness (see Fig. 4.3.1 (b)). These Laue oscillations indicate a coherent growth of all bilayers. The large shift of the 2θ-position of the γ-Fe$_{2-x}$Ga$_x$O$_3$ (004) reflection to lower 2θ values even at small doping concentrations is striking. For $x = 0.05$ (blue line) the 2θ position of the (004) reflection is only visible as a shoulder of the MgO (002) reflection. For higher Ga concentrations this shoulder vanishes and the thin film reflection is hidden under the substrate reflection with higher intensity. Therefore, a finite Ga doping of γ-Fe$_2$O$_3$ entails a sudden increase of the out-of-plane lattice constant c, which further increases with x.

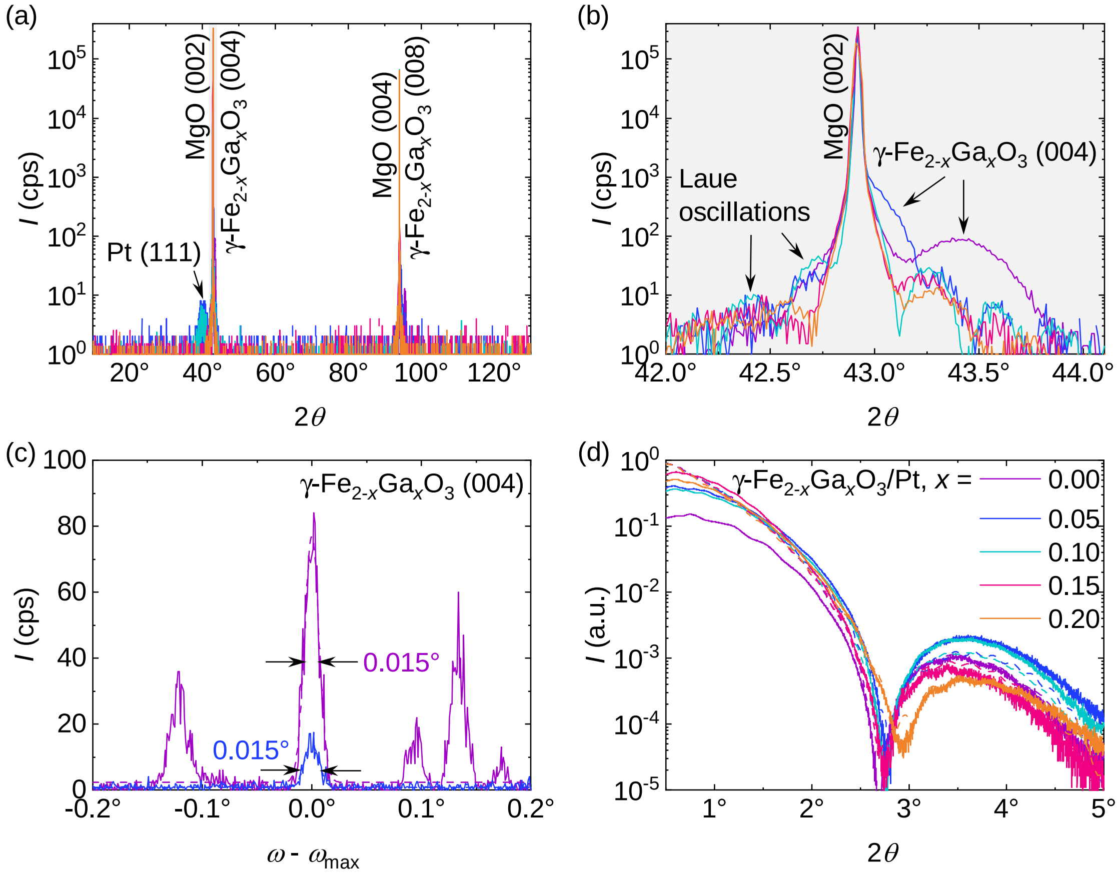

Figure 4.3.1.: HR-XRD of γ-Fe$_{2-x}$Ga$_x$O$_3$/Pt bilayers with $x = 0.0$ (purple line), 0.05 (blue line), 0.1 (cyan line), 0.15 (pink line) and 0.2 (orange line). (a) 2θ-ω scan from 10° to 130° around the γ-Fe$_{2-x}$Ga$_x$O$_3$ (004) and γ-Fe$_{2-x}$Ga$_x$O$_3$ (008) reflections with the respective MgO and Pt reflections. (b) Zoom into the grey region depicted in (a) reveals Laue oscillations around the γ-Fe$_{2-x}$Ga$_x$O$_3$ thin film reflections. (c) Rocking curves around the γ-Fe$_{2-x}$Ga$_x$O$_3$ (004) thin film reflections with $x = 0$ and $x = 0.2$ together with the corresponding Gauss fits in dashed lines. The additional reflections of the rocking curve of the undoped γ-Fe$_2$O$_3$ are caused by additional crystallites within the MgO substrate (see Sec. 3.2.1). (d) X-ray reflectometry scans of the bilayers in solid and simulations in dashed lines.

Rocking curves are performed around the γ-Fe$_{2-x}$Ga$_x$O$_3$ (004) reflections as shown in Fig. 4.3.1 (c). Due to the overlap of the MgO (002) substrate reflection and the γ-Fe$_2$O$_3$ (004) thin film reflection with finite Ga doping the measurement of rocking curves around the respective reflections is difficult. Only rocking curves for bilayer samples with $x = 0$

and $x = 0.2$ are presented in Fig. 4.3.1 (c). Both rocking curves have a small FWHM of $0.015°$ demonstrating a high crystalline quality with low mosaic spread.

x	FWHM (°)	$t_{\gamma\text{-Fe}_{2-x}\text{Ga}_x\text{O}_3}$ (nm)	t_{Pt} (nm)
0.00	0.0150 ± 0.0005	18.4 ± 0.3	3.6 ± 0.1
0.05		41.8 ± 0.3	3.5 ± 0.1
0.10		32.3 ± 0.3	3.6 ± 0.1
0.15		34.6 ± 0.3	3.6 ± 0.1
0.20	0.0150 ± 0.0004	26.0 ± 0.3	3.3 ± 0.1

Table 4.3.1.: From Gauss fits to the rocking curves shown in Fig. 4.3.1 (c) extracted FWHM values as well as the layer thicknesses $t_{\gamma\text{-Fe}_{2-x}\text{Ga}_x\text{O}_3}$ and t_{Pt} determined from simulations of the XRR scans displayed in Fig. 4.3.1 (d) of the γ-$Fe_{2-x}Ga_xO_3$/Pt bilayer samples.

The X-ray reflectometry scans of all γ-$Fe_{2-x}Ga_xO_3$/Pt bilayers and the corresponding simulations in dashed lines are shown in Fig. 4.3.1 (d). All bilayers exhibit similar thicknesses t_{Pt} of the Pt layer between $3.3\,\text{nm}$ and $3.6\,\text{nm}$ expecting a maximum SMR amplitude. The extracted values for t_{Pt} are summarized in Table 4.3.1 together with the thin film thicknesses $t_{\gamma\text{-Fe}_{2-x}\text{Ga}_x\text{O}_3}$. Although the same number of pulses are used for the PLD of the Ga-doped γ-Fe_2O_3 thin films $t_{\gamma\text{-Fe}_{2-x}\text{Ga}_x\text{O}_3}$ varies from approximately $18\,\text{nm}$ to nearly $42\,\text{nm}$, indicating that the growth rates of the Ga doped γ-Fe_2O_3 thin film depositions differ greatly.

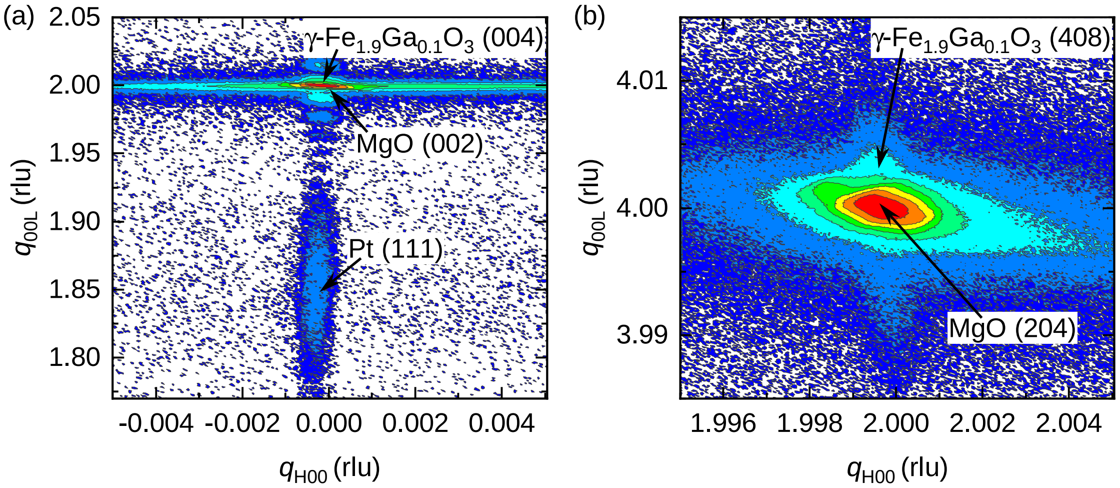

Figure 4.3.2.: RSMs around (a) the symmetric γ-$Fe_{1.9}Ga_{0.1}O_3$ (004) and (b) the asymmetric γ-$Fe_{1.9}Ga_{0.1}O_3$ (408) reflection. The units are given in reciprocal lattice units (rlu) with respect to the MgO substrate.

Reciprocal space mappings (RSMs) are executed for all γ-$Fe_{2-x}Ga_xO_3$/Pt bilayers around the symmetric γ-$Fe_{2-x}Ga_xO_3$ (004) (MgO (002)) and the asymmetric γ-$Fe_{2-x}Ga_xO_3$ (408) (MgO (204)) reflections. For the γ-$Fe_{1.9}Ga_{0.1}O_3$/Pt bilayer the RSMs of the symmetric and the asymmetric reflection is presented in Fig. 4.3.2. For the γ-$Fe_{2-x}Ga_xO_3$/Pt bilayers with $x = 0.05, 0.15$ and 0.2 the RSMs are summarized in the Appendix, Fig. A.3.4. In Fig. 4.3.2 (a), also the Pt (111) reflection and Laue oscillations beneath the MgO (002) reflection are visible. In Fig. 4.3.2 (a) a shift of the MgO (002) and the Pt (111) reflections and in (b) a shift of the MgO (204) reflection towards smaller q_{H00} values are visible. The small shifts indicate a small tilt of the thin film lattice planes with respect to that of the MgO substrate, which might be due to a large miscut of the MgO substrate. This leads to changes in the reflection positions, although it is aligned to the substrate reflections before. However, the narrow Pt (111) reflection visible in Fig. 4.3.2 (a) reveals a high crystalline quality of the Pt electrode on top of the γ-$Fe_{1.9}Ga_{0.1}O_3$ thin film. Furthermore, no strain relaxation of the γ-$Fe_{1.9}Ga_{0.1}O_3$ thin film could be detected (see Fig. 4.3.2 (b)).

x	a (nm)	c (nm)	$\Delta V/V$ (%)
0.00 (bulk)	0.8332	0.8332	
0.00	0.8422 ± 0.0004	0.8328 ± 0.0002	1.1
0.05	0.8422 ± 0.0003	0.8408 ± 0.0002	2.0
0.10	0.8424 ± 0.0004	0.8420 ± 0.0001	2.2
0.15	0.8422 ± 0.0006	0.8423 ± 0.0001	2.2
0.20	0.8423 ± 0.0005	0.8420 ± 0.0001	2.2

Table 4.3.2.: Lattice constants a and c and change in the unit cell volume $\Delta V/V$ of γ-$Fe_{2-x}Ga_xO_3$ compared to bulk γ-Fe_2O_3. Literature values for bulk γ-Fe_2O_3 are given as a reference [56].

From the 2θ-ω scans and the RSMs the lattice constants a and c are calculated. Therefore, the results from the 2θ-ω scan and both RSMs are averaged to get the out-of-plane lattice constant c. Since for $x = 0$ two and for $x = 0.2$ three different thin films are fabricated, it is also averaged over all fabricated samples to get precise values of a and c (see Table 4.3.2). The change in the respective unit cell volume ΔV compared to the volume V of bulk γ-Fe_2O_3 is also given. The in-plane lattice constant exhibits nearly no change in its value with the incorporation of Ga^{3+} into the thin films. The out-of-plane lattice constant c, instead, increases strongly for Ga:γ-Fe_2O_3 compared to undoped γ-Fe_2O_3. Also the relative unit cell volume increases up to $2.2\,\%$.

The dependence of the lattice constants a and c as a function of x are shown in Fig. 4.3.3 with a depicted as green and c depicted as yellow dots. The lower dashed line marks the lattice constant $a_{\gamma\text{-}Fe_2O_3}$ of bulk γ-Fe_2O_3 ($a_{\gamma\text{-}Fe_2O_3} = 0.8332\,\mathrm{nm}$ Ref. [56]) and the upper one indicates twice the lattice constant of bulk MgO ($a_{\mathrm{MgO}} = 0.4212\,\mathrm{nm}$ Ref. [83]). Since one unit cell of Ga:γ-Fe_2O_3 grows on four unit cells of MgO, the in-plane lattice constant a is approximately $2a_{\mathrm{MgO}}$ for all thin films from $x = 0$ to $x = 0.2$, hence all bilayers are fully epitaxially strained. In case of c, an increase with Ga^{3+} incorporation is visible. Already very small Ga concentrations have a big impact on c. The undoped thin film exhibits an oop lattice constant close to the bulk value of γ-Fe_2O_3. For $x = 0.05$ a clear increase of c occurs, which saturates at about $2a_{\mathrm{MgO}}$ for higher Ga concentrations. So the bilayers with $x = 0.1$, 0.15 and 0.2 do not only reveal similar lattice constants compared to each other, but also similar values for a and c within one thin film, indicating a nearly cubic symmetry of the crystalline thin films. In case of the Ga:α-Fe_2O_3 thin films mentioned in Secs. 4.1.1 and 4.2.1, a reduction in c is observed and thus contrary to the behavior of Ga:γ-Fe_2O_3

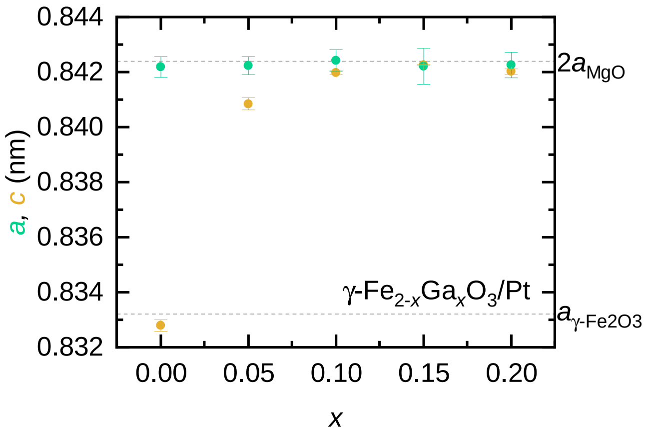

Figure 4.3.3.: Ip and oop lattice constants a and c as a function of the Ga content x in γ-$Fe_{2-x}Ga_xO_3$. The lower dashed line indicates the lattice constant of bulk γ-Fe_2O_3 ($a_{\gamma\text{-}Fe_2O_3} = 0.8332\,\mathrm{nm}$), the upper one of twice the value of bulk MgO ($a_{\mathrm{MgO}} = 0.4212\,\mathrm{nm}$) [56, 83].

depicted in Fig. 4.3.3. Here, the incorporation of Ga in γ-Fe_2O_3 could reduce the vacancy ordering in the lattice, which results in a cubic lattice symmetry (see Sec. 2.4.4). This could be an explanation for the unexpected increase of c in Ga:γ-Fe_2O_3.

The Ga^{3+} ions have the possibility of replacing Fe^{3+} ions on the tetrahedral as well as on the octahedral lattice sites of the γ-Fe_2O_3 spinel structure, since the ionic radius of Ga^{3+} is similar to that of Fe^{3+} (see Table 2.4.1). However, as it is slightly smaller than the ionic radii of Fe^{3+}, more Ga^{3+} ions might marginally replace Fe^{3+}-ions on the tetrahedral site. Generally, by replacing Fe^{3+} with Ga^{3+} ions in Fe_2O_3, a slight reduction in the unit cell volume is expected due to the smaller ionic radii of Ga^{3+} ions compared to Fe^{3+} ions [75]. However, Table 4.3.2 reveals an increase of the unit cell volume, which might be attributed to vacancy disorder in γ-Fe_2O_3.

In contrast to α-Fe_2O_3, dopants in γ-Fe_2O_3 can also fill vacancies on the octahedral sites [104]. The effect of vacancy occupation on the lattice constants is still pending. According to Ref. [104] a vacancy occupation with Ga^{3+} ions could be very likely and would lead to a decrease in the unit cell volume. Furthermore, non-crystalline parasitic GaO_x phases could also form during the deposition. But the existing of such phases on the unit cell volume of γ-$Fe_{2-x}Ga_xO_3$ remains an open question.

4.3.2. Magnetic properties of Ga:γ-Fe_2O_3/Pt bilayers

Analogous to the investigation of the magnetism in the undoped γ-Fe_2O_3/Pt bilayer in Sec. 3.2.2, the magnetic properties appearing in Ga doped γ-Fe_2O_3/Pt bilayers is analyzed by SQUID magnetometry and FMR measurements. The results of the magnetic hysteresis measurements performed at $300\,\mathrm{K}$ are depicted in Fig. 4.3.4 and the $M(H)$ loops recorded at $100\,\mathrm{K}$ as well as the temperature dependence of the magnetization measured at $500\,\mathrm{mT}$ are shown in the Appendix, Fig. A.4.6. The hysteresis loops of the γ-$Fe_{2-x}Ga_xO_3$/Pt bilayers with Ga concentrations of $x = 0.0, 0.05, 0.10, 0.15, 0.20$ are shown in Fig. 4.3.4 (a). In

Fig. 4.3.4 (b) the dependence of the extracted saturation magnetization M_S on the Ga concentration x is depicted. Except for the bilayer with $x = 0.1$, M_S of the γ-$Fe_{2-x}Ga_xO_3$/Pt bilayers is reduced compared to the undoped γ-Fe_2O_3/Pt bilayer sample. Surprisingly, those bilayers exhibit similar hysteresis loops with M_S being approximately $80\,\mathrm{kA\,m^{-1}}$ independent of x. The γ-$Fe_{1.9}Ga_{0.1}O_3$/Pt bilayer is an outlier with M_S being nearly twice as high as for the undoped γ-Fe_2O_3/Pt bilayer. Within the given error of $\pm 0.5\,\mathrm{T}$ all hysteresis loops saturate at approximately $3\,\mathrm{T}$. Additionally, $M(H)$ loops of the Ga:γ-Fe_2O_3/Pt bilayers reveal a reduced H_c relative to the $M(H)$ hysteresis of γ-Fe_2O_3/Pt. All extracted magnetic parameters are summarized in Table 4.3.3.

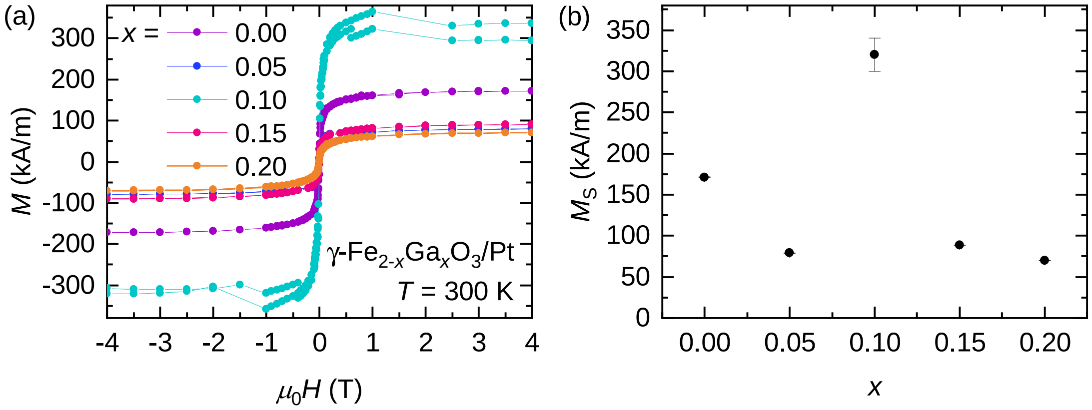

Figure 4.3.4.: SQUID magnetometry measurements of γ-$Fe_{2-x}Ga_xO_3$/Pt bilayers with $x = 0.0$ (purple), 0.05 (blue), 0.1 (cyan), 0.15 (pink) and 0.2 (orange). (a) Hysteresis loops measured at $300\,\mathrm{K}$ and (b) extracted saturation magnetization M_S.

Due to the replacement of magnetic Fe^{3+} ions with diamagnetic Ga^{3+} ions a reduction in M is expected for the Ga doped γ-Fe_2O_3 thin films, if the slightly different ionic radii of Ga^{3+} compared to Fe^{3+} is neglected and a statistical distribution of the dopants in the two antiferromagnetically coupled magnetic sublattices formed by the tetrahedral and octahedral sites of the spinel structure is assumed (see Sec. 2.4.4). Strikingly, the saturation magnetization does not decrease continously with increasing Ga concentration (cf. Fig. 4.3.4). Neglecting the outlier for $x = 0.1$ reveals a general reduction in M_S of the doped thin films, but no clear dependence of M_S on x. As already pointed out in the discussion of the lattice parameter of the Ga-doped γ-Fe_2O_3 thin films, the Ga^{3+} ions might occupy the octahedrally coordinated iron vacancies in the γ-Fe_2O_3 lattice. Therefore, the similar M_S values for $x = 0.05$, 0.15 and 0.2 could indicate a saturation in Fe^{3+} replacements and a vacancy occupation or the formation of GaO_x impurity phases at already low Ga concentrations. The outlier for $x = 0.1$ could be explained by an enhanced doping of the tetrahedral Fe^{3+} lattice sites in the spinel structure of γ-Fe_2O_3. This should lead to a reduction of the sublattice magnetization caused by the tetragonal sites and therefore to an increase of the total magnetization M in the ferrimagnetic γ-$Fe_{2-x}Ga_xO_3$ thin film measured by SQUID magnetometry (cf. Sec. 2.4.4).

Additionally, broadband FMR measurements are performed on the γ-$Fe_{2-x}Ga_xO_3$/Pt

x	M_S $\left(\mathrm{kA\,m^{-1}}\right)$	$\mu_0 H_S$ (T)	$\mu_0 H_c$ (mT)
0.00	171.2 ± 0.3	3.0 ± 0.5	3.9 ± 0.2
0.05	78.9 ± 0.3	3.0 ± 0.5	2.1 ± 0.1
0.10	320.0 ± 20.0	3.0 ± 0.5	1.4 ± 0.1
0.15	88.6 ± 0.2	2.5 ± 0.5	2.4 ± 0.2
0.20	69.8 ± 0.1	3.0 ± 0.5	1.1 ± 0.1

Table 4.3.3.: Magnetic properties M_S, $\mu_0 H_S$ and $\mu_0 H_c$ of γ-Fe$_{2-x}$Ga$_x$O$_3$/Pt bilayers measured at 300 K.

bilayers ($x = 0$, 0.05, 0.1, 0.15, 0.2) as well as on single γ-Fe$_{2-x}$Ga$_x$O$_3$ thin films with $x = 0$ and 0.2 without Pt on top. Thereby, the magnetic field $\mathbf{H}_{\text{ext}}$ is applied perpendicular to the surface of the thin films ($\mathbf{H}_{\text{ext}} \parallel [001]$). The from $\mu_0 H_{\text{res}}(f)$ and $\mu_0 \Delta H_{\text{res}}(f)$ extracted values for $\mu_0 M_{\text{eff}}$ and α are presented in Fig. 4.3.5 as a function of the Ga content x. Exemplarily, the resonance fields and the corresponding line widths as a function of f are shown for the γ-Fe$_{1.9}$Ga$_{0.1}$O$_3$/Pt bilayer and the γ-Fe$_{1.8}$Ga$_{0.2}$O$_3$ thin film in the Appendix, Fig. A.5.2. Additionally to the undoped maghemite thin film, the γ-Fe$_{1.9}$Ga$_{0.1}$O$_3$/Pt bilayer is the only sample, which shows indication of a slow relaxer damping contribution according to Eq. (3.1). The extracted values for $\mu_0 M_{\text{eff}}$, g, α and $\mu_0 H_{\text{inh}}$ of all thin films are summarized in the Appendix, Table A.5.2.

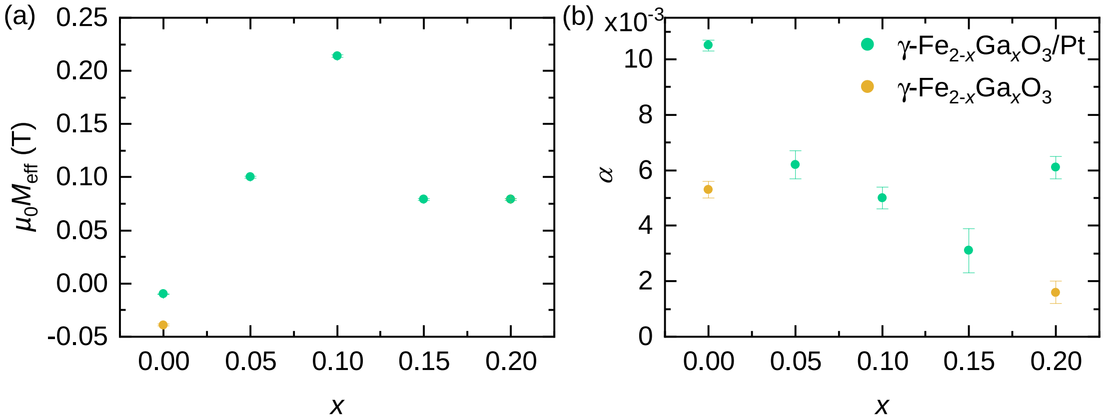

Figure 4.3.5.: From FMR measurements of γ-Fe$_{2-x}$Ga$_x$O$_3$/Pt bilayers and γ-Fe$_{2-x}$Ga$_x$O$_3$ thin films extracted values of (a) $\mu_0 M_{\text{eff}}$ and (b) α as functions of the Ga content x. The respective FMR measurements for $x = 0.1$ and $x = 0.2$ are exemplarily given in the Appendix, Fig. A.5.2.

The effective magnetization $\mu_0 M_{\text{eff}}$ exhibits a value between 100 mT and 79 mT for the bilayers with Ga contents of $x = 0.05$, 0.15 and 0.2. So the magnnetic properties of the bilayers with $x = 0.05$, 0.15 and 0.2 are confirmed to be very similar to each other by SQUID magnetometry as well as by FMR measurements. Analogous to the saturation magnetization determined by SQUID magnetometry measurements, M_{eff} of the γ-Fe$_{1.9}$Ga$_{0.1}$O$_3$/Pt bilayer is much higher than of all other bilayers. Overall, the Ga:γ-Fe$_2$O$_3$/Pt bilayers exhibit higher effective magnetizations than the undoped thin film with vanishingly small M_{eff}. Hence, M_S is not fully compensated by a possible strain-induced anisotropy in the bilayers. But compared to YIG ($\mu_0 M_{\text{eff}} = 140$ mT [89]), the results of the bilayers are still smaller. The γ-Fe$_{2-x}$Ga$_x$O$_3$/Pt bilayers reveal a continuous decrease in the damping parameter α with increasing Ga content of up to $x = 0.15$. Due to possible spin pumping the damping is generally higher for the Ga:γ-Fe$_2$O$_3$/Pt bilayers than for the γ-Fe$_{2-x}$Ga$_x$O$_3$ thin films. A decrease in α is surprising, since a higher damping of the magnetization precession is expected in the Ga:γ-Fe$_2$O$_3$ thin films due to a possible higher lattice disorder with respect to the iron vacancies (see Sec. 4.3.1) and possibly higher density of impurities in the thin films.

4.3.3. Spin Hall magnetoresistance of Ga:γ-Fe_2O_3/Pt bilayers

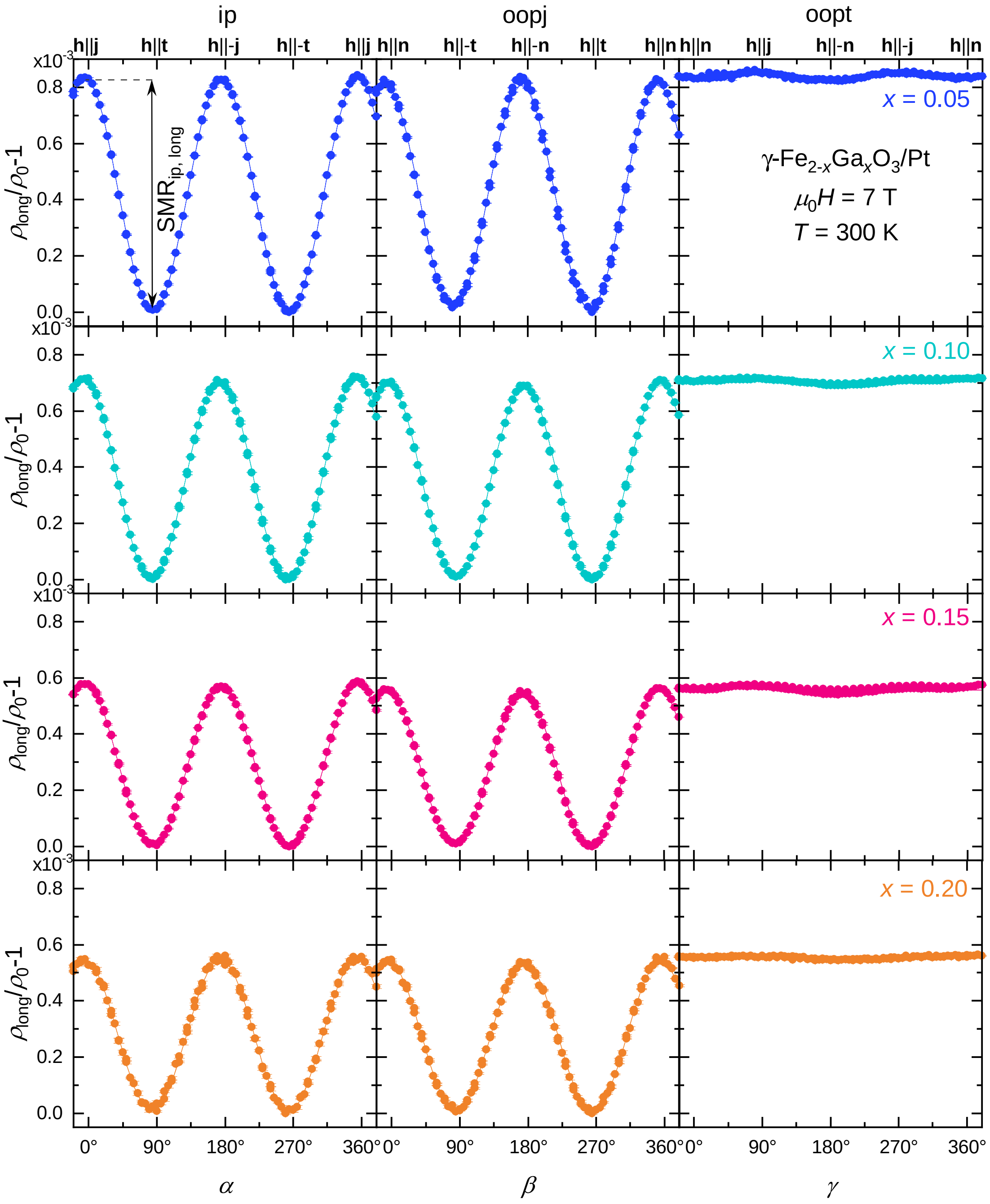

Figure 4.3.6.: ADMR measurements of the γ-$Fe_{2-x}Ga_xO_3$/Pt bilayers with $x = 0$ (purple), 0.05 (blue), 0.1 (cyan), 0.15 (pink) and 0.2 (orange) in ip, oopj and oopt rotation of $\mathbf{h}$. The ADMR measurements are executed at $7\,\mathrm{T}$ and $300\,\mathrm{K}$. Exemplarily for $x = 0.1$, the vertical arrow indicates the longitudinal SMR amplitude $\mathrm{SMR}_{\mathrm{ip,\,long}}$ in ip magnetic field rotation.

For the investigation of the SMR effect, ADMR measurements are performed on the γ-$Fe_{2-x}Ga_xO_3$/Pt bilayers at $300\,\mathrm{K}$ and in ip, oopj and oopt rotation of $\mathbf{h}$. In Fig. 4.3.6, the angle-dependence of the normalized longitudinal resistivities $\rho_{\mathrm{long}}/\rho_0$ and the respective fit curves are presented for $x = 0.05$ (blue), $x = 0.1$ (cyan), $x = 0.15$ (pink) and $x = 0.2$ (orange) recorded at an applied magnetic field of 7 T. The resistivities ρ_0 are all in a range expected for the Pt electrodes ($x = 0$: $398\,\mathrm{n\Omega\,m}$, $x = 0.05$: $352\,\mathrm{n\Omega\,m}$, $x = 0.1$: $372\,\mathrm{n\Omega\,m}$, $x = 0.15$: $443\,\mathrm{n\Omega\,m}$, $x = 0.2$: $257\,\mathrm{n\Omega\,m}$). All ADMR curves fulfill the expected, angle dependent behavior related to the SMR effect observed in FMI/HM bilayers (cf. Sec. 2.3.1). Hence, addionally to the $\cos^2(\phi)$ dependence in ip and oopj magnetic field rotations with maximum values at 0° and 180°, the measurements in oopt magnetic field rotations exhibit vanishingly small oscillations and a high resistive state over a whole 360° rotation. Those small oscillations could stem from a misalignment of the Hall bar structures with respect to the rotation plane and thus leading to an ip or an oopj ADMR contribution to the oopt signal. Therefore, the absence of strong oscillations in oopt rotation indicates the absence of the AMR effect in the Ga doped bilayers. Since for the AMR effect the magnetic thin film has to be conductive, this result leads to the assumption that the Ga doped γ-Fe_2O_3 thin films are insulating at 300 K in agreement with ab initio studies based on density functional theory [70]. This is further confirmed by $R(T)$ measurements (Appendix, Fig. A.8.1) of the γ-$Fe_{1.8}Ga_{0.2}O_3$ thin film over a temperature range from 160 K to 300 K.

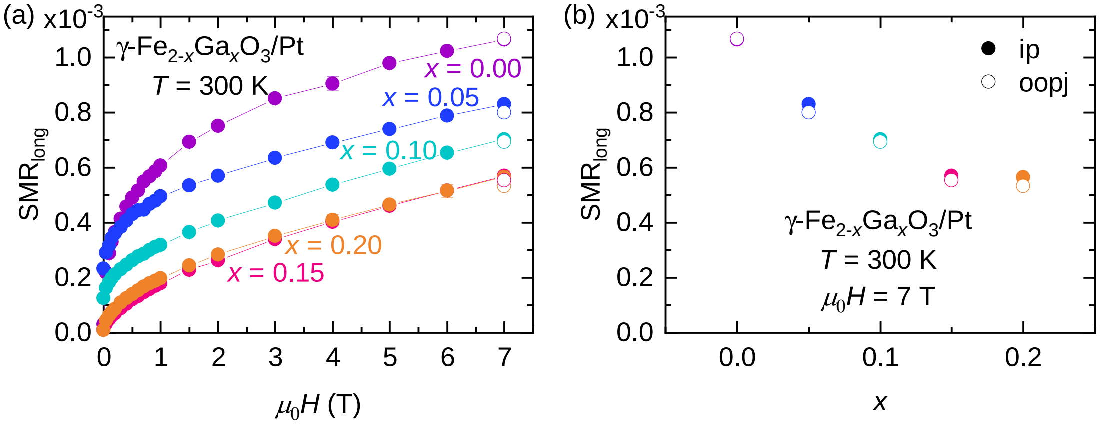

Figure 4.3.7.: SMR$_{long}$ of the γ-$Fe_{2-x}Ga_xO_3$/Pt bilayers with $x = 0.00$ (purple), $x = 0.05$ (blue), $x = 0.10$ (cyan), $x = 0.15$ (pink) and $x = 0.20$ (orange) as (a) a function of $\mu_0 H$ and (b) as a function of the Ga content x at 7 T. The corresponding ADMR measurements are performed at 300 K. Full circles display the ip, open circles the oopj rotation of **h**.

For a better analysis of the SMR amplitudes it is referred to Fig. 4.3.7 (a), where the longitudinal amplitude SMR$_{long}$ for the ip (full circles) and the oopj magnetic field rotation (open circles) is depicted as a function of $\mu_0 H$. The $\mathrm{SMR_{ip,\,long}}(\mu_0 H)$ curves exhibit similar unsaturated, square-root dependencies most likely due to the existance of antiphase boundaries in the γ-$Fe_{2-x}Ga_xO_3$/Pt thin films with spinel structure (cf. Sec. 3.2.3). SMR$_{long}$ is nearly the same for the γ-$Fe_{1.85}Ga_{0.15}O_3$/Pt and the γ-$Fe_{1.8}Ga_{0.2}O_3$/Pt bilayer. Taking a closer look on the dependence of SMR$_{long}$ on the Ga content x in Fig. 4.3.7 (b) reveals a continuous decrease of the SMR amplitude with increasing x up to 0.15 and then a possible saturation, since SMR$_{long}$ is nearly the same for $x = 0.15$ and $x = 0.2$.

Although the structural and magnetic properties of the Ga doped γ-Fe_2O_3/Pt bilayers are very similar except for the $x = 0.10$ compound, a clear dependence of the SMR amplitude as a function of the Ga content is observed. Surprisingly, the SMR amplitude of the γ-$Fe_{1.9}Ga_{0.1}O_3$/Pt bilayer, which exhibits clearly different magnetic properties, follows this trend. This might point to different properties of γ-Fe_2O_3 at the interface to Pt compared to the whole thin film.

4.4. Doping of γ-Fe_2O_3 using different dopants

In addition to the γ-$Fe_{2-x}Ga_xO_3$/Pt bilayer series with different Ga concentrations, also a γ-$Fe_{1.9}X_{0.1}O_3$/Pt bilayer series with a variety of dopants X is fabricated, where X stands for Al^{3+}, Ga^{3+}, $Ir^{3+,4+}$, Zn^{2+} and Ce^{4+}. The structural and magnetic properties of those thin films are discussed in Sections 4.4.1 and 4.4.2. Finally, in Section 4.4.3, the results of the ADMR measurements are presented and discussed in terms of the spin Hall magnetoresistance effect.

4.4.1. Structural analysis of doped γ-Fe_2O_3/Pt bilayers

The γ-$Fe_{1.9}X_{0.1}O_3$ thin films are fabricated by PLD with the same growth parameters given in Sec. 3.2.1. MgO (001) substrates are used to realize the growth of the γ-Fe_2O_3 phase. Polycrystalline, stochiometric targets with different dopants X are used. Hereby, all targets exhibit a dopant concentration of $5\,\%$. Afterwards, Pt layers are deposited in-situ on top of the thin films by EVAP.

For the characterization of the crystalline quality of the bilayers, HR-XRD measurements are performed and shown in Fig. 4.4.1. The Al, Ga, Ir, Zn and Ce doped thin films are depicted as purple, blue, cyan, pink and orange lines, respectively. The 2θ-ω scans reveal only the γ-$Fe_{1.9}X_{0.1}O_3$ (004) and γ-$Fe_{1.9}X_{0.1}O_3$ (008) reflections as well as the Pt (111) peaks together with the respective substrate reflections MgO (002) and MgO (004) (see Fig. 4.4.1 (a)). Indicated by the finite intensity of the Pt (111) reflections, the Pt electrodes of all bilayers are crystalline except for the Ce doped one.

In Fig. 4.4.1 (b), the 2θ-ω scans around the γ-$Fe_{1.9}X_{0.1}O_3$ (004) reflections exhibit that all thin film reflections are close to the substrate reflection. The γ-$Fe_{1.9}Al_{0.1}O_3$ (004) reflection is best visible, but also the reflections of the Ir and Zn doped thin films still appear as shoulders of the MgO (002) reflection. Hence, the crystalline thin films have an oop lattice constant c near the value of twice the substrate lattice constant a_{MgO}. Additionally, Laue oscillations occur around the γ-$Fe_{1.9}X_{0.1}O_3$ (004) reflections. These oscillations are most pronounced for the thin films including Ga, Ir and Zn dopants. The γ-$Fe_{1.9}Ce_{0.1}O_3$ thin film exhibits no Laue oscillations at all. So for all γ-$Fe_{1.9}X_{0.1}O_3$/Pt bilayers - except for the Ce doped one - a coherent growth of the γ-$Fe_{1.9}X_{0.1}O_3$ layers can be concluded. In case of these γ-$Fe_{1.9}X_{0.1}O_3$ (004) reflections no rocking curves can be measured due to the similar 2θ position of the thin film and the substrate reflections. Therefore, a high crystalline quality of the γ-$Fe_{1.9}X_{0.1}O_3$/Pt bilayers with $X =$ Al, Ga, Ir and Zn can only be

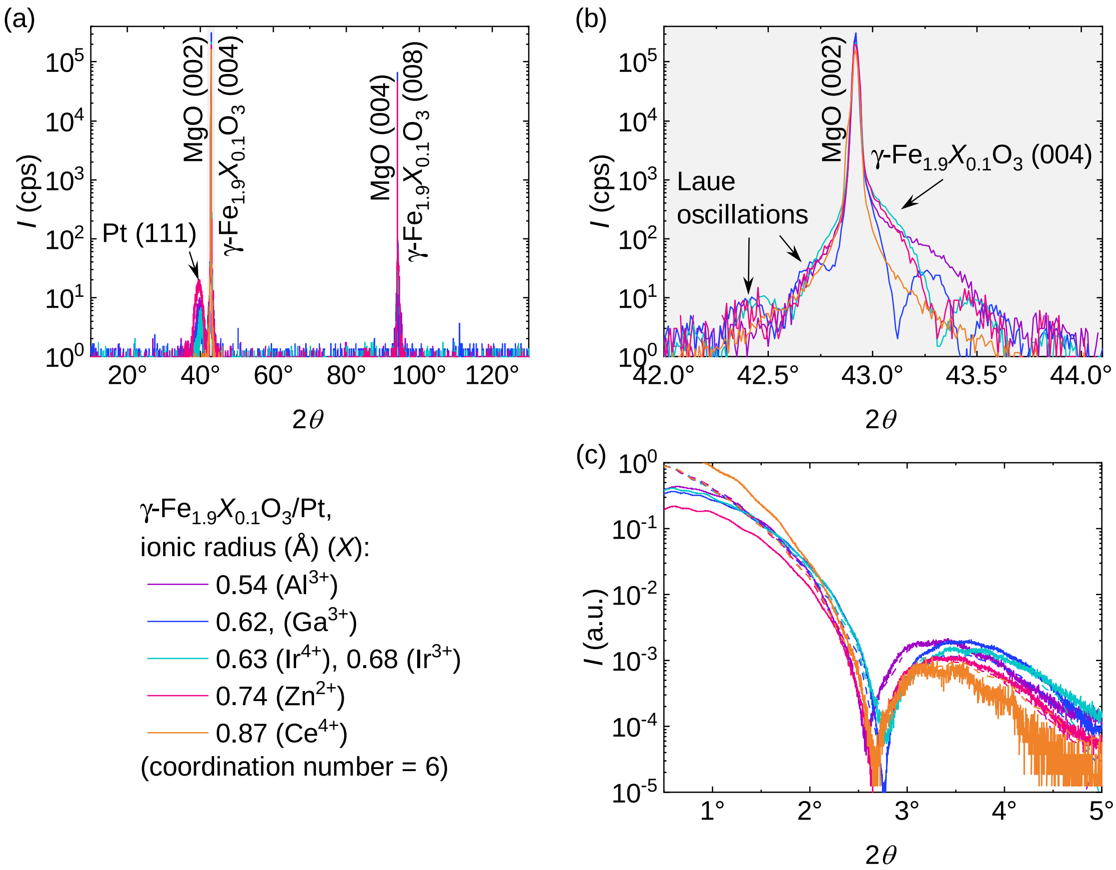

Figure 4.4.1.: HR-XRD of the γ-$Fe_{1.9}X_{0.1}O_3$/Pt bilayers with X = Al (purple), Ga (blue), Ir (cyan), Zn (pink), Ce (orange). (a) Long range 2θ-ω scan with the reflections γ-$Fe_{1.9}X_{0.1}O_3$ (004) (MgO (002)) and γ-$Fe_{1.9}X_{0.1}O_3$ (008) (MgO (004)) together with the (111) reflection of Pt. (b) 2θ-ω scan around the γ-$Fe_{1.9}X_{0.1}O_3$ (004) (MgO (002)) reflection. (c) X-ray reflectometry scans in solid and the corresponding simulations in dashed lines.

confirmed from 2θ-ω scans. The γ-$Fe_{1.9}Ce_{0.1}O_3$/Pt bilayer reveals neither a crystalline Pt electrode, nor Laue oscillations around the γ-$Fe_{1.9}Ce_{0.1}O_3$ reflections.

To get the layer thicknesses $t_{\gamma\text{-Fe}_{1.9}X_{0.1}O_3}$ and t_{Pt}, X-ray reflectometry scans are executed and simulated as shown in Fig. 4.4.1 (c). In Table 4.4.1, the layer thicknesses are presented for all γ-$Fe_{1.9}X_{0.1}O_3$/Pt bilayers. Thereby, the Ga, Ir and Zn doped γ-Fe_2O_3 thin films reveal similar growth rates with resulting layer thicknesses of about 30 nm. The Al and the Ce doped γ-Fe_2O_3 layers are much thinner with a thickness of approximately 18 nm for both thin films. The Pt layers have nearly the same thickness (3.6 nm - 3.7 nm) and thus a maximum SMR amplitude is expected considering the HM thickness dependence of the SMR.

Reciprocal space mappings of the γ-$Fe_{1.9}Zn_{0.1}O_3$/Pt bilayer are performed around the symmetric (004) and the asymmetric (408) reflections and depicted in Fig. 4.4.2. The RSMs of the remaining bilayers with the dopants Al, Ir and Ce are attached to the Appendix, Fig. A.3.5. The RSMs of the γ-$Fe_{1.9}Ga_{0.1}O_3$/Pt bilayer were already discussed in Sec. 4.3.1. In Fig. 4.4.2 (a), the γ-$Fe_{1.9}Zn_{0.1}O_3$ (004) reflection can be again seen as an asymmetric

X	$t_{\gamma\text{-Fe}_{1.9}X_{0.1}\text{O}_3}$ (nm)	t_{Pt} (nm)
Al	18.3 ± 0.3	3.8 ± 0.1
Ga	32.3 ± 0.3	3.6 ± 0.1
Ir	29.2 ± 0.3	3.6 ± 0.1
Zn	27.5 ± 0.3	3.7 ± 0.1
Ce	17.8 ± 0.3	3.7 ± 0.1

Table 4.4.1.: From XRR simulations shown in Fig. 4.4.1 (d) determined layer thicknesses $t_{\gamma\text{-Fe}_{1.9}X_{0.1}\text{O}_3}$ and t_{Pt} for the different dopants X.

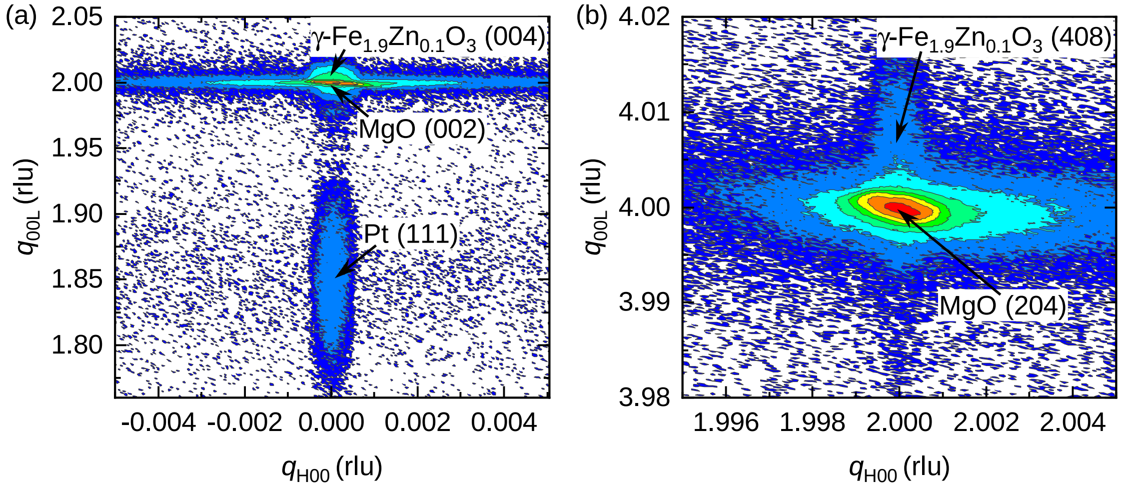

Figure 4.4.2.: RSMs around (a) the symmetric γ-$Fe_{1.9}Zn_{0.1}O_3$ (004) and (b) the asymmetric γ-$Fe_{1.9}Zn_{0.1}O_3$ (408) reflections. The units are given in reciprocal lattice units (rlu) with respect to the MgO substrate.

broadening of the MgO (002) reflection along the $[00L]$-direction towards higher $q_{00\text{L}}$ values. Additionally, Laue oscillations appear between the MgO (002) and the Pt (111) reflection. The asymmetric γ-$Fe_{1.9}Zn_{0.1}O_3$ (408) reflection shown in (b) is only indicated by a broad peak above the MgO (204) reflection.

X	r (Å)	a (nm)	c (nm)	$\Delta V/V$ (%)
Fe^{3+} (bulk)	0.645	0.8332	0.8332	
Al^{3+}	0.535	0.8420 ± 0.0004	0.8390 ± 0.0020	1.8
Ga^{3+}	0.62	0.8424 ± 0.0004	0.8420 ± 0.0001	2.2
Ir^{4+}	0.625	0.8423 ± 0.0009	0.8408 ± 0.0008	2.0
Zn^{2+}	0.74	0.8422 ± 0.0006	0.8412 ± 0.0006	2.1
Ce^{4+}	0.87	0.8420 ± 0.0010	0.8425 ± 0.0001	2.2

Table 4.4.2.: Lattice constants a and c and relative change in the unit cell volume $\Delta V/V$ compared to bulk γ-Fe_2O_3. The ionic radii r are given for a coordination number of six [75]. Literature values for bulk γ-Fe_2O_3 are taken from Ref. [56].

The thin film reflection positions in the 2θ-ω scans and the RSMs (Figs. 4.4.1, 4.3.2, 4.4.2 and in the Appendix, Fig. A.3.5) are fitted with Gaussian functions to obtain the ip and the oop lattice constants a and c. The results are given in Table 4.4.2 together with the relative change $\Delta V/V$ in the unit cell volume. The volume change is relative to bulk γ-Fe_2O_3 and its respective lattice constants (see Ref. [56]). All bilayers are fully strained and an increase in the unit cell volume of the γ-$Fe_{1.9}X_{0.1}O_3$ thin films can be observed.

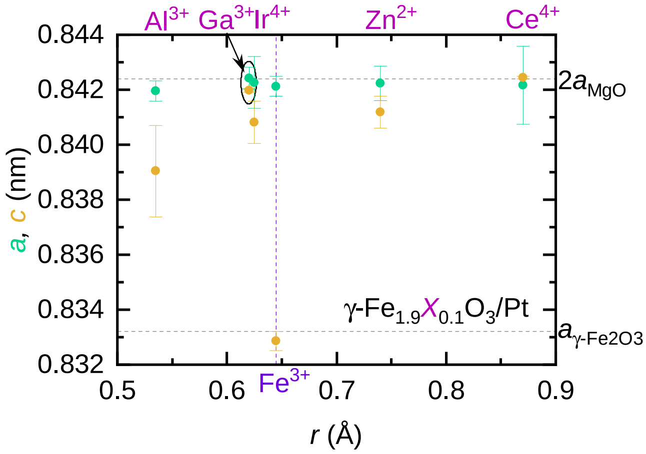

Figure 4.4.3.: Lattice constants a and c as functions of the ionic radius r of the dopants depicted as green and yellow dots, respectively. The respective dopants X (Al, Ga, Ir, Zn, Ce) are labelled in purple on top of the graph. For simplification only Ir^{4+} ions are assumed here. The upper dashed line indicates twice the lattice constant of bulk MgO, the lower dashed line the lattice constant of bulk γ-Fe_2O_3. For comparison, the lattice constants of γ-Fe_2O_3 of the undoped γ-Fe_2O_3/Pt bilayer are also given (cf. Sec. 3.2.1).

Figure 4.4.3 represents the lattice constants as functions of the ionic radius r of the dopants. Hereby, a is depicted as green and c as yellow dots. The dashed lines indicate the lattice constants of bulk γ-Fe_2O_3 and twice the lattice constant of bulk MgO ($a_{\gamma\text{-}Fe_2O_3} = 0.8332\,\mathrm{nm}$ and $a_{MgO} = 0.4212\,\mathrm{nm}$ [56, 83]). The in-plane lattice constant a is approximately $2a_{MgO}$ for all γ-$Fe_{1.9}X_{0.1}O_3$ thin films with $X =$ Al, Ga, Ir, Zn and Ce. The out-of-plane lattice constant c, instead, is increasing with increasing ionic radius r. Hereby, the Ga:γ-Fe_2O_3 thin film is an exception with its c value being slightly higher than for Ir:γ-Fe_2O_3 ($r_{Ga^{3+}} < r_{Ir^{4+}} < r_{Ir^{3+}}$).

Since the in-plane lattice constant a of the doped γ-Fe_2O_3 thin films is particularly influenced by the epitaxial strain induced by the MgO substrates, the effect of doping on the out-of-plane lattice constant c and relative change of the unit cell volume ΔV is discussed in more detail assuming a constant Poisson ratio. The dopants seem to generally increase c and thus the unit cell volume of doped maghemite with increasing ionic radius r. Due to the fact that Al^{3+}, Ga^{3+} and Ir^{4+} ions all have smaller ionic radii than Fe^{3+}, a reduction in the unit cell volume is expected compared to undoped γ-Fe_2O_3 [71]. Hereby, the Al^{3+} and the Ga^{3+} ions most likely occupy the tetrahedral sites of the γ-Fe_2O_3 spinel structure. Due to its ionic size, Ir^{4+} is expected to replace the Fe^{3+} ions on the octahedral sites. With the incorporation of Ir^{3+}, Zn^{2+} or Ce^{4+} into γ-Fe_2O_3, a volume expansion should occur due to the larger ionic radii of those dopants compared to Fe^{3+} [72–74]. Ir^{3+}, Zn^{2+} and Ce^{4+} should only go to the Fe^{3+} octahedral sites. All these expectations are based on the assumption that the dopants replace the Fe^{3+} ions on the respective sites. But for instance, vacancy disorder could lead to a decrease in the unit cell volume. Especially dopants with larger r than the one of Fe^{3+} could prefer other lattice sites than the ones of Fe^{3+} [104]. Also non-crystalline parasitic phases are possible and can influence the lattice constants of γ-Fe$_{1.9}X_{0.1}$O$_3$ in an unknown way.

Comparing the γ-Fe$_{1.9}X_{0.1}$O$_3$ thin films with each other reveals that the expectation of an increasing unit cell volume with increasing r is fulfilled by replacing the Fe^{3+} ions. But a comparison with the undoped γ-Fe$_2$O$_3$ thin film leads to a more complex behavior of the dopants in γ-Fe$_2$O$_3$, since the γ-Fe$_2$O$_3$ thin film exhibits a c lattice constant near the bulk value of $a_{\gamma\text{-Fe}_2\text{O}_3}$ and thus a smaller unit cell volume than the doped γ-Fe$_2$O$_3$ thin films. Hence, not only different doping concentrations (cf. Sec. 4.3.1) and different dopants affect the crystalline structure of γ-Fe$_2$O$_3$ thin films. The fact, that a small concentration of ions different from Fe^{3+} could induce vacancy disorder in the γ-Fe$_2$O$_3$ lattice has a great influence on the lattice constants, which needs to be investigated in more detail in the future.

4.4.2. Magnetic properties of doped γ-Fe$_2$O$_3$/Pt bilayers

The results of SQUID magnetometry measurements performed at $300\,\mathrm{K}$ are presented in Fig. 4.4.4 for the γ-Fe$_{1.9}X_{0.1}$O$_3$/Pt bilayers with X = Al (purple), Ga (blue), Ir (cyan), Zn (pink) and Ce (orange). In Fig. 4.4.4 (a), M is shown as a function of $\mu_0 H$ and in Fig. 4.4.4 (b), the extracted saturation magnetization M_S is depicted as a function of the ionic radius r of the dopants. The hysteresis loops of the thin films γ-Fe$_{1.9}$Al$_{0.1}$O$_3$ and γ-Fe$_{1.9}$Ir$_{0.1}$O$_3$ are quite similar to each other in their shape. The Ga and Zn doped γ-Fe$_2$O$_3$ thin films exhibit significantly larger saturation magnetizations. This is accompanied by a smaller $\mu_0 H_\mathrm{c}$ for both thin films compared to the Al and Ir doped thin films. The Ce:γ-Fe$_2$O$_3$ thin film has a very small saturation magnetization of only $17.9\,\mathrm{kA\,m^{-1}}$ and a much larger coercive field of $17\,\mathrm{mT}$. In addition, this thin film exhibits a comparatively strong shift of the hysteresis loop towards negative magnetic fields ($\mu_0 H_{\mathrm{c},-} = -23.1\,\mathrm{mT}$ and $\mu_0 H_{\mathrm{c},+} = 11.5\,\mathrm{mT}$). This might be due to an exchange-bias effect caused by a pinning of the ferrimagnetic phase by an antiferromagnetic one with an exchange bias field of $5.8\,\mathrm{mT}$. Therefore, in the Ce doped γ-Fe$_2$O$_3$ thin film antiferromagnetic and ferromagnetic phases could co-exist, which are exchange coupled with each other. All in all, the γ-Fe$_{1.9}X_{0.1}$O$_3$/Pt bilayers have a similar saturation field of $\mu_0 H_\mathrm{S} \approx 3\,\mathrm{T}$ in common. The saturation magnetizations and coercive fields differ in some parts greatly, which is demonstrated in Table 4.4.3.

The behavior of M_S as a function of the ionic radius r is depicted in Fig. 4.4.4 (b) and exhibits no clear dependence. The M_S-value of the undoped γ-Fe$_2$O$_3$/Pt bilayer is given as a reference. The ionic radii given in Fig. 4.4.4 (b) and Table 4.4.3 are the ones for a coordination number of six. In case of the Al and the Ga doped thin film, the dopants should slightly prefer the tetrahedral lattice sites over the octahedral ones due to their smaller ionic radii compared to Fe^{3+} (cf. Sec. 4.3.2). In the γ-Fe$_{1.9}X_{0.1}$O$_3$ thin films with X = Zn and Ce, the dopants should replace the Fe^{3+} ions on the octahedral sites and thus reduce the number of magnetic moments of the dominating magnetic sublattice (see

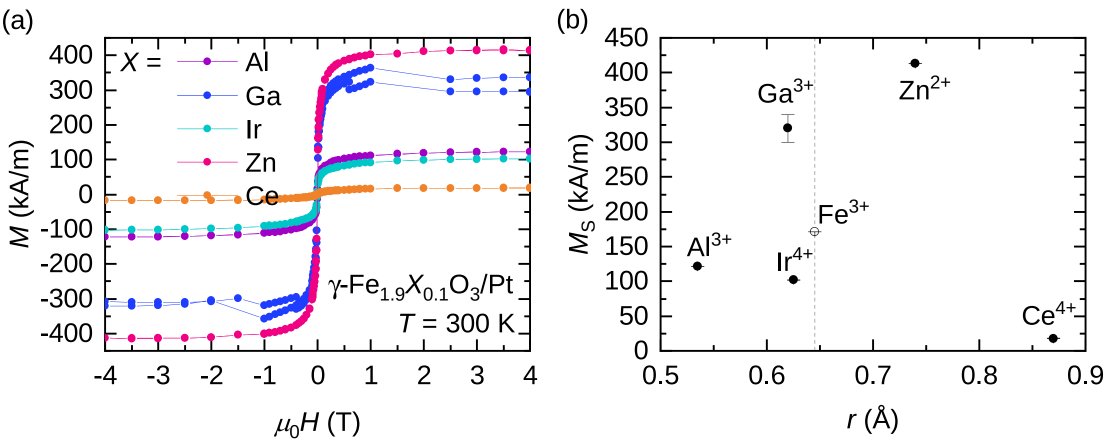

Figure 4.4.4.: SQUID magnetometry measurements of γ-$Fe_{1.9}X_{0.1}O_3$/Pt bilayers with X = Al (purple), Ga (blue), Ir (cyan), Zn (pink) and Ce (orange) performed at 300 K. (a) Magnetization M as a function of $\mu_0 H$ and (b) extracted saturation magnetization M_S as a function of the ionic radius r of the dopants X with a coordination number of six. As a reference, the M_S value of the undoped γ-Fe_2O_3/Pt bilayer is shown as open symbol.

Sec. 2.4.4). In conclusion, in a simple picture considering only the different ionic radii, the replacement of magnetic Fe^{3+} ions with the diamagnetic dopants should reduce the magnetization regardless of the dopant material. This is at least confirmed by Sharmin *et al.* for Al doped α-Fe_2O_3 [101], where two identical octahedral magnetic sublattices exist. However, the divalent and tetravalent Zn^{2+} and Ce^{4+} might induce holes in the valence band or reduce the valence state of Fe^{3+} to Fe^{2+} as discussed in Sec. 2.4.4. This might influence the magnetic properties of the γ-Fe_2O_3 doped thin films. Furthermore, the Ir^{4+} dopant itself exhibits a magnetic moment of $5/2\hbar$, which should be taken into account. However, as the ionic radius of Ir^{4+} is similar to the radius of Fe^{3+} (see Table 2.4.1), the Ir^{4+} ions might replace Fe^{3+} ions on the tetrahedral as well as on the octahedral sites, which makes a calculation of the net magnetization of the ferrimagnetic order without knowing the concentrations of the ions on the respective sites nearly impossible.

X	r (Å)	M_S $(\mathrm{kA\,m^{-1}})$	$\mu_0 H_S$ (T)	$\mu_0 H_c$ (mT)
Al^{3+}	0.535	121.4 ± 0.3	3.0 ± 0.5	2.9 ± 0.2
Ga^{3+}	0.62	320 ± 20	3.0 ± 0.5	1.4 ± 0.1
Ir^{4+}	0.625	101.7 ± 0.7	3.0 ± 0.5	2.3 ± 0.4
Fe^{3+} (undoped)	0.645	171.2 ± 0.3	3.0 ± 0.5	3.9 ± 0.2
Zn^{2+}	0.74	413.2 ± 0.3	2.5 ± 0.5	1.2 ± 0.1
Ce^{4+}	0.87	17.9 ± 0.4	3.0 ± 0.5	17 ± 6

Table 4.4.3.: Saturation magnetization M_S, saturation field $\mu_0 H_S$ and coercive field $\mu_0 H_c$ of γ-$Fe_{1.9}X_{0.1}O_3$/Pt bilayers measured at 300 K. X is the respective dopant in the γ-$Fe_{1.9}X_{0.1}O_3$ thin film. The values of the undoped γ-Fe_2O_3/Pt bilayer is given for comparison. The ionic radii r are given for a coordination number of six.

Surprisingly, Table 4.4.3 and Fig. 4.4.4 (b) reveal higher and lower saturation magnetizations compared to the undoped γ-Fe_2O_3/Pt bilayer. The Ga and the Zn doped thin films have larger saturation magnetizations than the undoped γ-Fe_2O_3. But the γ-$Fe_{1.9}Ga_{0.1}O_3$ thin film was already an outlier in Fig. 4.4.4, where all other Ga doped thin films exhibited a M_S of approximately $80\,\mathrm{kA\,m^{-1}}$. The enhanced magnetization could be explained by an increased reduction in magnetic moments on the tetrahedral sites and thus a non uniform distribution of the Ga^{3+} ions on the two sublattices. Zn^{2+}, instead, should not occupy tetrahedral sites at all due to its large ionic radius. Therefore, the increase in saturation magnetization might be explained by a magnetic hole state in the valence band of γ-Fe_2O_3 caused by the missing electron while doping with divalent Zn^{2+} [70]. As discussed in Sec. 2.4.4, the missing electron of Zn^{2+} most propably create a hole in the oxygen valence band, which should be ionized at room temperature.

4.4.3. Spin Hall magnetoresistance of doped γ-Fe$_2$O$_3$/Pt bilayers

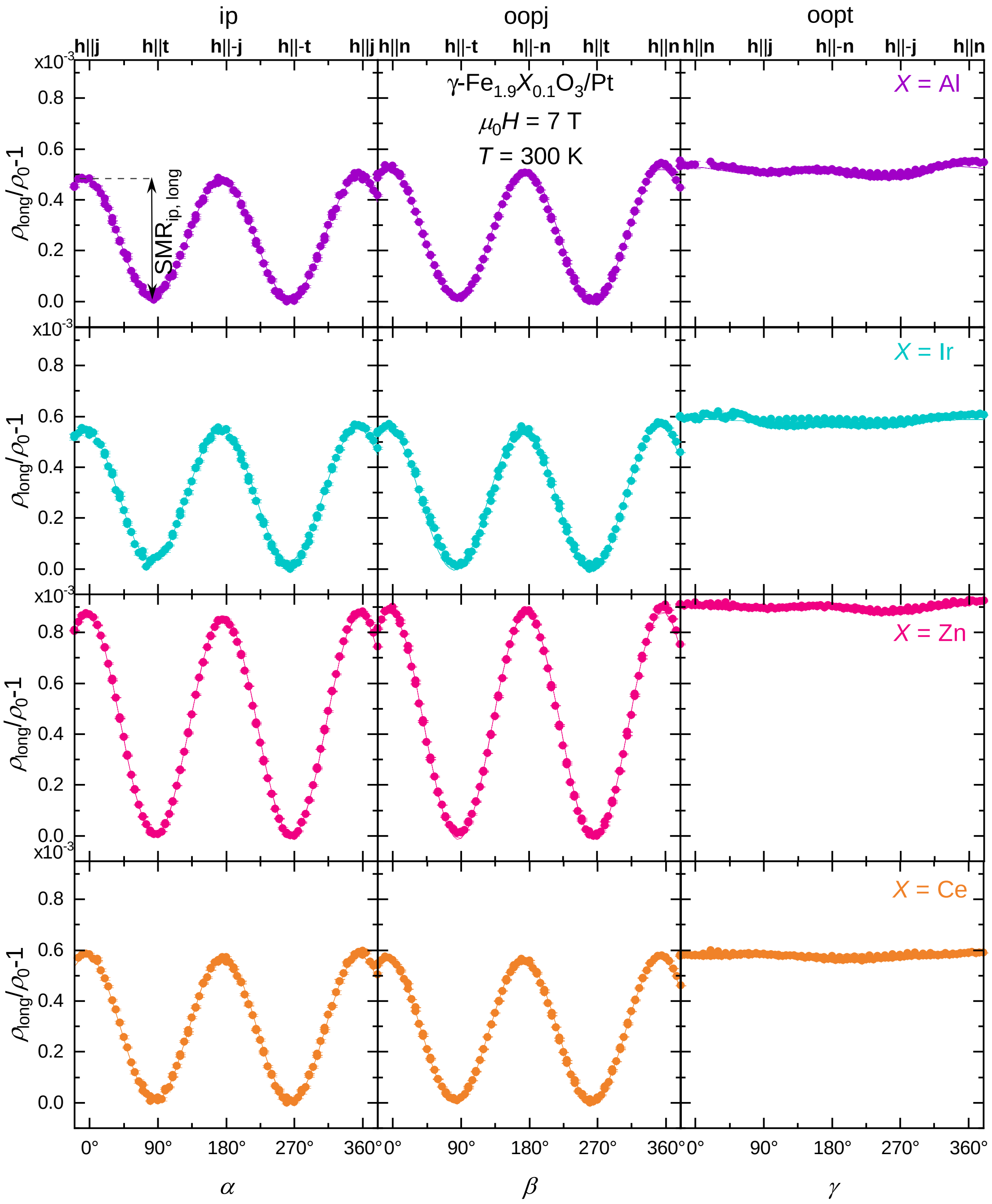

Figure 4.4.5.: Angle-dependence of the longitudinal resistivity ρ_{long} of the γ-Fe$_{1.9}X_{0.1}$O$_3$/Pt bilayers with X = Al (purple), Ir (cyan), Zn (pink) and Ce (orange) normalized to ρ_0 in ip, oopj and oopt rotations of $\mathbf{h}$ recorded at 300 K and 7 T. The $\cos^2$ functions are shown by solid lines. For γ-Fe$_{1.9}$Al$_{0.1}$O$_3$/Pt the ip, longitudinal SMR amplitude SMR$_{\text{ip, long}}$ is indicated by the vertical arrow.

ADMR measurements are performed at different magnetic field magnitudes to observe the SMR effect and its angular and magnetic field dependence. In Fig. 4.4.5, the normalized longitudinal resistivity $\rho_{\mathrm{long}}/\rho_0 - 1$ of the γ-Fe$_{1.9}X_{0.1}$O$_3$/Pt bilayers with X = Al (purple), X = Ir (cyan), X = Zn (pink) and X = Ce (orange) measured at 300 K and 7 T is shown for the three rotation planes of **h** (ip, oopj, oopt). The dots represent the data and the solid lines are fits to Eqs. 2.7. The resistivities ρ_0 of the Pt electrodes are in the same order of magnitude for all γ-Fe$_{1.9}X_{0.1}$O$_3$/Pt bilayers and thus comparable with each other (X = Al: $\rho_0 = 360\,\mathrm{n\Omega\,m}$, Ga: $372\,\mathrm{n\Omega\,m}$, Ir: $318\,\mathrm{n\Omega\,m}$, Zn: $290\,\mathrm{n\Omega\,m}$, Ce: $349\,\mathrm{n\Omega\,m}$). The ADMR curves in ip and oopj rotation exhibit the characteristic behavior of a FMI/HM bilayer with maximum resistivity at 0° and 180°. Additionally, a constant high resistive state is confirmed in oopt rotation. Therefore, the ADMR measurements are in agreement with the SMR theory (see Sec. 2.3.1). The small oscillations of the resistivity while rotating the magnetic field in the oopt-plane can be explained by a small misalignment of the Hall bar structures.

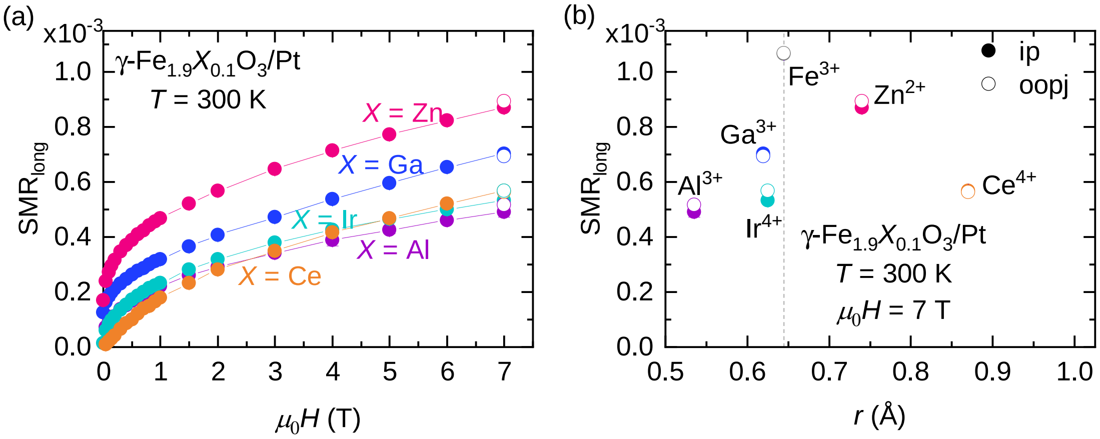

Figure 4.4.6.: SMR amplitude SMR$_{\mathrm{long}}$ of γ-Fe$_{1.9}X_{0.1}$O$_3$/Pt bilayers with X = Al, Ga, Ir, Zn and Ce measured at 300 K and 7 T as (a) a function of $\mu_0 H$ and (b) a function of the ionic radius r of the dopant. SMR$_{\mathrm{long}}$ in ip rotation of **h** is depicted in full circles and in oopj rotation in open circles. In (b) the SMR amplitude of the undoped γ-Fe$_2$O$_3$/Pt bilayer is given for comparison. The ionic radii of the dopants are given for a coordination number of six. For Ir, tetravalent Ir^{4+} is assumed as a dopant in γ-Fe$_2$O$_3$.

To investigate the magnetic field dependence of the longitudinal SMR amplitude ρ_1/ρ_0, ADMR measurements are performed at magnetic fields from 7 T down to 0 T. The extracted SMR amplitudes SMR$_{\mathrm{long}}$ are depicted in Fig. 4.4.6 (a) as a function of the magnetic field magnitude $\mu_0 H$ with the amplitude of the ip rotation shown as full circles and the amplitude of the oopj rotation as open circles. For all γ-Fe$_{1.9}X_{0.1}$O$_3$/Pt bilayers, SMR$_{\mathrm{ip,\,long}}$ does not reach saturation, although the hysteresis loops shown in Fig. 4.4.4 (a) do saturate at approximately 3 T. This might be traced back to APBs in the γ-Fe$_{1.9}X_{0.1}$O$_3$ thin films, which need much higher magnetic field magnitudes to fully align all magnetic moments along the magnetic field direction (see Sec. 3.2.3). For the Zn doped thin film the highest SMR amplitude is reached, followed by the thin films doped with Ga, Ce, Ir and Al. The Ce:γ-Fe$_2$O$_3$/Pt bilayer has the smallest SMR amplitude for $\mu_0 H < 3$ T, but SMR$_{\mathrm{ip,\,long}}$ increases with a larger slope than for the Al:γ-Fe$_2$O$_3$/Pt and the Ir:γ-Fe$_2$O$_3$/Pt bilayers resulting in a higher $\mathrm{SMR_{long}}$ value of Ce:γ-Fe_2O_3/Pt than for Al:γ-Fe_2O_3/Pt and Ir:γ-Fe_2O_3/Pt bilayers for $\mu_0 H > 5\,\mathrm{T}$.

In Fig. 4.4.6 (b) the longitudinal SMR amplitude at 7 T and 300 K is depicted as a function of the ionic radius r. For simplification, all ionic radii are given for a coordination number of six. Since the doping concentration of the X:γ-Fe_2O_3 thin films should be identical, it is expected that a similar amount of magnetic moments is removed from the magnetic sublattices of X:γ-Fe_2O_3 and thus the magnetic moment density is reduced at the interface between X:γ-Fe_2O_3 and Pt. This should lead to comparable SMR amplitudes, which are smaller than for undoped γ-Fe_2O_3/Pt. As obvious from Fig. 4.4.6 (b), all longitudinal SMR amplitudes are indeed smaller than for undoped γ-Fe_2O_3/Pt. However, a clear dependence of $\mathrm{SMR_{long}}$ on r is not observable.

The SMR amplitude $\mathrm{SMR_{long}}$ rather reflects the dependence of the saturation magnetization on the ionic radius r. The Zn- and Ga-doped γ-Fe_2O_3/Pt bilayers exhibit a high saturation magnetization as well as a larger SMR amplitude, while the Al-, Ir- and Ce-doped bilayers having a small saturation magnetization together with a smaller SMR amplitude.

4.5. Summary

The effect of doping on the crystallographic, magnetic and magnetotransport properties of α-Fe_2O_3 and γ-Fe_2O_3 thin films is investigated by HR-XRD, SQUID magnetometry, FMR and ADMR measurements. The α-Fe_2O_3 thin films are doped with Ga using two different stacking sequences: Al_2O_3 (0001)//α-$Fe_{2-x}Ga_xO_3$/Pt ($x = 0.1, 0.2$) and Al_2O_3 (0001)//α-Fe_2O_3/α-$Fe_{2-x}Ga_xO_3$/Pt ($x = 0.1, 0.2, 0.3$). In the latter case, the undoped α-Fe_2O_3 thin film is used as a seed layer for the Ga-doped α-Fe_2O_3 thin film. In case of the doped γ-Fe_2O_3 thin films, a series with different Ga concentrations and a series with various dopants at a dopant content of 5 % is analyzed. The respective bilayers grown on (001)-oriented MgO substrates are γ-$Fe_{2-x}Ga_xO_3$/Pt ($x = 0.05, 0.1, 0.15, 0.2$) and γ-$Fe_{1.9}X_{0.1}O_3$/Pt (X = Al, Ga, Ir, Zn, Ce).

HR-XRD measurements of the α-$Fe_{2-x}Ga_xO_3$/Pt bilayers and α-Fe_2O_3/α-$Fe_{2-x}Ga_xO_3$/Pt trilayers reveal in-plane lattice constants a being approximately the bulk value of α-Fe_2O_3, which demonstrates a nearly fully relaxed growth of α-Fe_2O_3 on Al_2O_3 (0001). Within the uncertainty no dependence of a on the doping concentration x is visible. The out-of-plane lattice constant c decreases with increasing x as expected due to the slightly smaller ionic radius of Ga^{3+} compared to Fe^{3+}. The γ-$Fe_{2-x}Ga_xO_3$/Pt bilayers also exhibit a nearly constant a at different Ga concentrations x, due to the fully epitaxial strained growth on MgO. The oop lattice constant c strongly increases with the incorporation of small Ga concentrations. This increase then saturates at higher concentrations x and could stem from dopant induced lattice disorder within the γ-Fe_2O_3 lattice, which leads to a cubic symmetry of the spinel structure. The lattice constants of the γ-$Fe_{1.9}X_{0.1}O_3$ thin films follow a similar behavior, where a stays constant and c increases with increasing ionic radius r of the dopant X as expected.

Doping with diamagnetic Ga^{3+} ions should lead to a reduction in the saturation magnetization M_S in α-Fe_2O_3 as well as in γ-Fe_2O_3. Instead, SQUID magnetometry measurements reveal a higher saturation magnetization of the Ga:α-Fe_2O_3/Pt bilayers compared to the undoped α-Fe_2O_3/Pt bilayer. Additionally, the α-Fe_2O_3/α-$Fe_{2-x}Ga_xO_3$/Pt trilayers have a higher magnetization for $x = 0.3$ and a lower one for $x = 0.1$ and 0.2 compared to the α-Fe_2O_3/Pt bilayer. The enhancement in M_S is mirrored in an increased spin canting, which might be induced by Ga doping. The Ga:γ-Fe_2O_3/Pt bilayers reveal the expected decrease in M_S for all Ga concentrations except for $x = 0.1$, for which the magnetization is enhanced as well. A clear dependence of M_S on the Ga content x cannot be concluded. Furthermore, the dopant series γ-$Fe_{1.9}X_{0.1}O_3$/Pt exhibits higher (X = Ga, Zn) as well as lower (X = Al, Ir, Ce) saturation magnetizations than M_S of undoped γ-Fe_2O_3.

ADMR measurements are performed to investigate the SMR effect in all doped bilayers and trilayers, where increasing the doping concentration should lead to a continous decrease in the SMR amplitude due to a reduction of the surface magnetic moment density. In case of the α-$Fe_{2-x}Ga_xO_3$/Pt bilayers a non-linear dependence of the longitudinal SMR amplitude SMR_{long} with the doping concentration x is observed. For the α-$Fe_{1.9}Ga_{0.1}O_3$/Pt bilayer, SMR_{long} is strongly reduced compared to the undoped α-Fe_2O_3/Pt bilayer and even smaller than for the bilayer with a Ga content of $x = 0.2$. This non-linear dependence is confirmed by the α-Fe_2O_3/α-$Fe_{2-x}Ga_xO_3$/Pt trilayers for $x = 0.1$ and 0.2. While almost the same value of SMR_{long} is observed for the $x = 0.1$ trilayer and bilayer samples, the amplitude SMR_{long} is lower in the $x = 0.2$ trilayer sample compared to the $x = 0.2$ bilayer sample. However, the similar dependence of the SMR amplitude of the Ga doped α-Fe_2O_3 bilayer and trilayer samples for $x = 0.1$ and 0.2 is surprising, since they exhibit completely different magnetic properties measured by SQUID magnetometry. This indicates similar interface properties at the SMR relevant α-$Fe_{2-x}Ga_xO_3$/Pt interface and different magnetic bulk properties. For the α-Fe_2O_3/α-$Fe_{1.7}Ga_{0.3}O_3$/Pt trilayer sample, a different temperature-dependence of the magnetization together with a different ADMR is observed, which needs to be further investigated in future experiments. The ADMR measurements of the Ga:γ-Fe_2O_3/Pt bilayers reveal the expected decrease in SMR_{long} with x with a possible saturation at a Ga content of $x = 0.15$. The clear dependence of SMR_{long} on x of these sample is remarkable, since they exhibit different magnetic bulk properties. Since for the dopant series a constant dopant concentration is used, in a similar picture, a similar reduction of the SMR amplitudes compared to the undoped γ-Fe_2O_3/Pt bilayer is expected for all γ-$Fe_{1.9}X_{0.1}O_3$/Pt samples. Indeed, the SMR amplitudes are all smaller than for γ-Fe_2O_3/Pt. However, no clear dependence of SMR_{long} on the ionic radius r of the dopants is visible. The dependence of SMR_{long} on r resembles more that of M_S on r determined by SQUID magnetometry. The Al, Ir and Ce doped bilayers exhibit a small M_S as well as a small SMR_{long}. For the Ga and Zn doped bilayers, the opposite effect is observed.

5. Summary and outlook

In the following, the key findings of this thesis are summarized in Section 5.1 and an outlook on further research is given in Section 5.2.

5.1. Summary

The aim of this thesis is tuning the amplitude of the spin Hall magnetoresistance (SMR) in α-Fe_2O_3/Pt and γ-Fe_2O_3/Pt heterostructures by doping the corresponding magnetic ordered insulator (MOI) with various dopants at different dopant concentrations. The replacement of magnetic Fe^{3+} ions with diamagnetic dopants reduces the magnetic moment density in the MOI. Since the SMR amplitude depends on the magnetic moment surface density n_s, a decrease in the SMR amplitude is expected. To complement the investigation of the most common iron oxides, also Fe_3O_4 thin film and Fe_3O_4/Pt bilayer samples are fabricated and analyzed in terms of its structural, magnetic and magnetoresistive effects in analogon to the α-Fe_2O_3/Pt and γ-Fe_2O_3/Pt heterostructures.

All discussed α-Fe_2O_3, γ-Fe_2O_3 and Fe_3O_4 thin films fabricated by pulsed-laser deposition with and without an electron-beam evaporated top Pt electrode reveal excellent crystalline qualities indicated by finite thickness fringes around the thin film and the Pt (111) layer reflections as well as narrow rocking curves. Furthermore, these thin films exhibit an excellent surface quality with low surface roughness.

The α-Fe_2O_3/Pt thin films exhibit a small saturation magnetization of $M_S = 8.7\,\mathrm{kA\,m^{-1}}$ at $300\,\mathrm{K}$ due to a Dzyaloshinskii–Moriya interaction (DMI) induced canting of the magnetic sublattices. No Morin transition is found down to $10\,\mathrm{K}$, which is expected at approximately $T_M = 263\,\mathrm{K}$ for bulk α-Fe_2O_3 [15]. The suppression of the Morin transition might be caused by slight changes of the uniaxial anisotropy by strain, size or vacancy effects overtuning the delicate balance with the single-ion anisotropy. The γ-Fe_2O_3 thin film and the γ-Fe_2O_3/Pt bilayer sample have saturation magnetizations below $200\,\mathrm{kA\,m^{-1}}$ and thus much smaller than the literature bulk value of $400\,\mathrm{kA\,m^{-1}}$ [60]. Also the Fe_3O_4 thin film and the Fe_3O_4/Pt bilayer sample exhibit saturation magnetizations well below the literature bulk value of $471\,\mathrm{kA\,m^{-1}}$ [63]. The strong reduction in M_S might be due to the formation of antiferromagnetically coupled antiphase boundaries (APBs) in spinel-based γ-Fe_2O_3 and Fe_3O_4 thin films grown on MgO substrates (see Secs. 3.2.2 and 3.3.2). Broadband ferromagnetic resonance (bbFMR) measurements performed on the γ-Fe_2O_3 thin films reveal an almost vanishing effective magnetization M_{eff} most probably by strain effects (see Fig. 3.2.5). For fitting the resonance line width $\mu_0\Delta H$ a slow relaxer damping contribution needs to be taken into account (cf. Eq. 3.2), which might be caused by structural defects like APBs or impurities in the thin film sample.

The α-Fe_2O_3/Pt bilayer shows the expected SMR effect of an antiferromagnetic insulator (AFI)/ heavy metal (HM) heterostructure under consideration of the domain structure within the magnetic easy plane (see Fig. 3.1.4). The resistivity ρ measured with an applied magnetic field $\mathbf{H}$ rotated in the magnetic easy plane (ip) exhibits a $90°$ phase shift with respect to the SMR effect in ferrimagnetic insulator (FMI)/HM bilayers. In out-of-plane rotations of the magnetic field perpendicular to the current direction $\mathbf{j}$ (oopj) and perpendicular to the transverse direction $\mathbf{t}$ (oopt), ρ is discontinuous for $\mathbf{H}$ being parallel to the surface normal $\mathbf{n}$. Thereby, the domain structure changes from a single domain to a multidomain state (see Sec. 3.1.3 for further explanations). The longitudinal SMR amplitude $\mathrm{SMR}_{\mathrm{long}}$ saturates with a maximum value of 2.55×10^{-3}, which is significantly larger than for the prototype bilayer YIG/Pt with $\mathrm{SMR}_{\mathrm{long}} = 1.3 \times 10^{-3}$ [10] and confirms the recently reported record high SMR amplitude in α-Fe_2O_3/Pt bilayers [12]. The γ-Fe_2O_3/Pt heterostructure reveals the SMR effect for a FMI/HM bilayer with a $\cos^2$ dependence of the longitudinal resistivity ρ_{long} in ip and oopj magnetic field rotations and a constant high resistive state, while rotating the magnetic field in oopt. The SMR amplitude as a function of H reveals a nonsaturating behavior with $\mathrm{SMR}_{\mathrm{long}} = 1.07 \times 10^{-3}$ at $7\,\mathrm{T}$ (cf. Fig. 3.2.7), which is comparable to YIG/Pt. This could be explained by APBs leading to domain wall pinning. The Fe_3O_4/Pt bilayer exhibits a mixture of spin Hall magnetoresistance and anisotropic magnetoresistance (AMR). Above the Verwey transition temperature T_{V} at around $127\,\mathrm{K}$, which can also be considered as a metal to insulator transition, the AMR and below T_{V} the SMR effect is expected to dominate. Surprisingly, a small oscillation of ρ_{long} in oopt magnetic field rotations is observed at $300\,\mathrm{K} > T_{\mathrm{V}}$ as well as at $50\,\mathrm{K} < T_{\mathrm{V}}$ together with a phase change, although the SMR effect claims a constant value for ρ_{long} in oopt rotations.

The respective α-$Fe_{2-x}Ga_xO_3$ thin films of the α-$Fe_{2-x}Ga_xO_3$/Pt bilayers with $x = 0.1$ and 0.2 exhibit similar in-plane lattice constants a of approximately the bulk value of α-Fe_2O_3. The out-of-plane lattice constant c is reduced with increasing Ga content x as expected due to the slightly smaller ionic radius of Ga^{3+} compared to Fe^{3+}. These have larger saturation magnetizations M_{S} than the undoped one (cf. Fig. 4.1.4), although M_{S} is expected to be smaller than for α-Fe_2O_3, if the diamagnetic Ga^{3+} ions are equally distributed on both sublattices. To ensure the growth of the α-phase of Fe_2O_3 and improve the thin film quality of α-$Fe_{2-x}Ga_xO_3$ a α-Fe_2O_3 seed layer is introduced between the Al_2O_3 substrate and the α-$Fe_{2-x}Ga_xO_3$ thin film to reduce the lattice mismatch of the α-$Fe_{2-x}Ga_xO_3$ thin film. These trilayers confirm the structural behavior of the α-$Fe_{2-x}Ga_xO_3$/Pt bilayers. For the α-Fe_2O_3/α-$Fe_{2-x}Ga_xO_3$/Pt trilayers M_{S} is reduced for $x = 0.1$ and 0.2, but increased for $x = 0.3$ (cf. Fig. 4.2.4). The enhanced M_{S} for the respective outliers indicates an increased canting of the magnetic sublattices, which might be induced by Ga^{3+} doping.

In case of the γ-$Fe_{2-x}Ga_xO_3$/Pt bilayer series a remains nearly constant and fully epitaxial strained by the MgO substrates and c is strongly increased with x and saturates at about $c \approx a$. Also the dopant bilayer series γ-Fe$_{1.9}X_{0.1}$O$_3$/Pt with the dopants X = Al^{3+}, Ga^{3+}, Ir$^{3+,4+}$, Zn^{2+} and Ce^{4+} confirm nearly constant values for a and the tendency of an increase in c with increasing ionic radius r of the dopants. With the incorporation of dopants vacancy disorder is induced in γ-Fe$_2$O$_3$, which can be observed as a nearly cubic lattice symmetry of the doped γ-Fe$_2$O$_3$ thin films (see Fig. 4.3.3, cf. Sec. 2.4.2).

The γ-Fe$_{2-x}$Ga$_x$O$_3$/Pt bilayers reveal saturation magnetizations below the one of undoped γ-Fe$_2$O$_3$/Pt except for $x = 0.1$ (cf. Fig. 4.3.4). FMR studies of the γ-Fe$_{2-x}$Ga$_x$O$_3$/Pt heterostructures exhibit a decreasing damping with increasing Ga concentration although the opposite effect is expected due to a possible higher impurity density. In case of the γ-Fe$_{1.9}X_{0.1}$O$_3$/Pt bilayer series the bilayers with X = Al^{3+}, Ir$^{3+,4+}$ and Ce^{4+} have smaller M_S and the bilayers with X = Ga^{3+} and Zn^{2+} have higher M_S than the undoped heterostructure (cf. Fig. 4.4.4). For the dopants Ir, Zn and Ce the occupation of octahedral lattice sites is expected in a simple picture due to their larger ionic radii compared to the one of Fe^{3+} leading to a reduction in M_S. Al^{3+}, instead, has a significantly smaller r resulting in the occupation of the tetrahedral sites and thus an increase in M_S. Since Ga^{3+} has a slightly smaller, but similar r to Fe^{3+}, the assumption of a slightly preferred occupation of the tetrahedral sites could be too simple (see Sec. 2.4.4). In summary, no clear dependence of M_S on the doping concentration and ionic radii of the dopands could be found in the α-Fe$_{2-x}$Ga$_x$O$_3$/Pt as well as the γ-Fe$_{2-x}X_x$O$_3$/Pt bilayer samples.

Although the Ga-doped α-Fe$_2$O$_3$ as well as the γ-Fe$_2$O$_3$ samples exhibit different magnetic bulk properties, a clear dependence of the longitudinal SMR amplitudes SMR$_\mathrm{long}$ as a function of the doping concentration could be found. This is also illustrated in Fig. 5.1.1, which provides an overview of the longitudinal SMR amplitudes SMR$_\mathrm{long}$ of the MOI/HM heterostructures measured within the scope of this thesis. The data are classified by the respective MOI, i.e., in antiferromagnetic insulators (AFI) (left panels) and ferrimagnetic insulators (FMI) with spinel structure (right panels). Thereby in Fig. 5.1.1 (a), (b), SMR$_\mathrm{long}$ is plotted as a function of the magnetic moment volume density nS and in (c), (d) of the saturation magnetization M_S. For the determination of nS a statistical distribution of the dopants in the respective magnetic material is assumed, which might be too simple for the spinel based systems depicted in the right panels, but simplifies the picture. M_S is measured by SQUID magnetometry. Figure 5.1.1 (a) reveals a strong decrease of SMR$_\mathrm{long}$ with decreasing nS for α-Fe$_{2-x}$Ga$_x$O$_3$/Pt and α-Fe$_2$O$_3$/α-Fe$_{2-x}$Ga$_x$O$_3$/Pt heterostructures. In terms of the respective saturation magnetizations, SMR$_\mathrm{long}$ even decreases linearly with increasing M_S indicating a dependence of SMR$_\mathrm{long}$ on M_S, which is the net magnetization presumably originating from sublattice canting in the AFI (cf. Fig. 5.1.1 (c)). However, the only slightly increased canting angle found in the α-Fe$_{2-x}$Ga$_x$O$_3$ samples and therefore the slightly reduced projection $m_t^{\mathrm{A,B}}$ of the sublattice magnetizations on $\mathbf{t}$ for $\alpha = 0°$ cannot explain the strong decrease in SMR$_\mathrm{long}$ as discussed in Sec. 4.1.3. For the spinel based ferrimagnetic insulators SMR$_\mathrm{long}$ of the corresponding bilayers seems to just slightly increase with increasing nS as indicated by the dashed line in Fig. 5.1.1 (b). SMR$_\mathrm{long}$ as a function

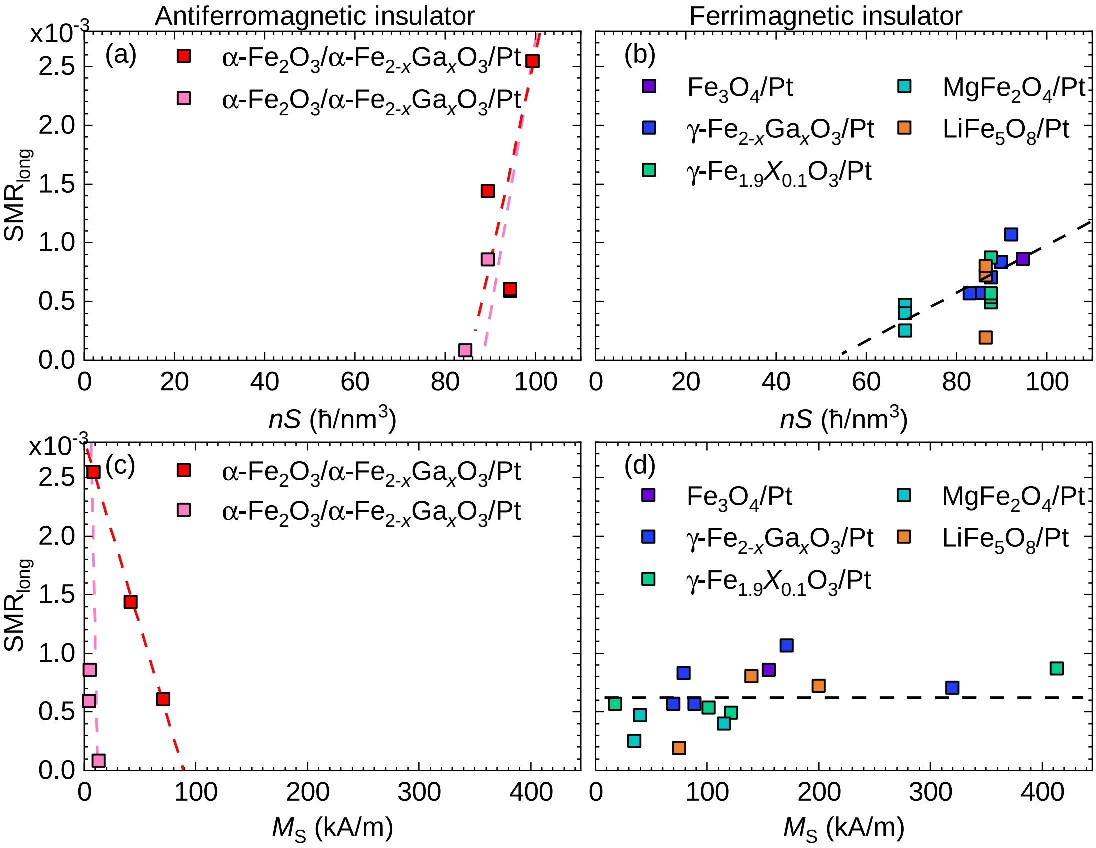

Figure 5.1.1.: Longitudinal SMR amplitudes $\mathrm{SMR_{long}}$ of all heterostructures presented in this thesis as (a), (b) a function of the magnetic moment volume density nS and (c), (d) a function of the saturation magnetization M_S measured at a temperature of 300 K. The data are categorized by the magnetic ordering of the insulator of the corresponding heterostructures - (a), (c) represent antiferromagnetic and (b), (d) ferrimagnetic insulators with spinel structure. The dashed lines are guides to the eye. The data of the $MgFe_2O_4$/Pt and the $LiFe_5O_8$/Pt heterostructures are adapted from Ref. [43].

of M_S is nearly constant over a wide range with a larger scattering of the data points at lower M_S (see Fig. 5.1.1 (d)), which is mostly caused by different SMR amplitudes found in differently fabricated $MgFe_2O_4$/Pt and $LiFe_5O_8$/Pt bilayers [43].

All in all, a general reduction of the SMR amplitude is observed with a decrease of nS by doping with nonmagnetic ions. But this reduction is much stronger than the simple linear dependence assumed in Fig. 2.3.4. Surprisingly, the AFI/HM heterostructures exhibit a linear dependence of $\mathrm{SMR_{long}}$ on the total net magnetization M_S of both sublattice magnetizations, whereas the FMI/HM heterostructures have no dependence of $\mathrm{SMR_{long}}$ on the net magnetization at all. The former paves the way for further tuning the SMR amplitude in AFI/HM bilayer samples.

5.2. Outlook

The results of this thesis provide a variety of ideas for possible measurements and thin film fabrications in future to clarify issues arised in the thesis and to intensify specific measurements. The bbFMR measurements performed on γ-Fe$_2$O$_3$ thin films pave the way for possible magnon transport measurements. The vanishingly small M_eff leads to a nearly circular magnetization precession, which suppresses nonlinear damping effects and therefore increases the magnon conductivity [88]. Subsequently, the nonlinear frequency dependency of the resonance line width $\mu_0 \Delta H$ provokes further investigations to identify the origin of the slow relaxer damping contribution such as antiphase boundaries, which could be visualized by tunneling electron microscopy (TEM).

Furthermore, the ADMR measurements on the Fe$_3$O$_4$/Pt bilayer exhibited a phase change in oopt magnetic field rotation going down to low T. Therefore, also blank Fe$_3$O$_4$ thin films should be measured at 50 K and compared with Fe$_3$O$_4$/Pt to study the effect of the crystalline Pt electrode on the phase of ρ_long. Furthermore, thinner Fe$_3$O$_4$ layers might increase the insulating behavior of Fe$_3$O$_4$ and therefore reduce possible AMR effects in Fe$_3$O$_4$/Pt bilayer samples.

Site and element-selective analysis of doped α-Fe$_2$O$_3$ and γ-Fe$_2$O$_3$ would be advantageous to identify the site-occupation of the different dopants. Especially in spinel-based ferrimagnets such as γ-Fe$_2$O$_3$ the knowledge of the concentration of the different ions on the two different sites is important to calculate the change of the sublattice magnetizations and therefore possible effects on the amplitude of the spin Hall magnetoresistance. In addition to that, measurement outliers should be fabricated once again and characterized by HR-XRD, SQUID magnetometry, bbFMR and ADMR measurements. For example, the α-Fe$_2$O$_3$/α-Fe$_{1.7}$Ga$_{0.3}$O$_3$/Pt trilayer exhibits a linear decrease of M as a function of T, which is clearly different from that of the other trilayers. Also ADMR measurements reveal a different angle-dependence of the longitudinal resistivity showing strong oscillations with larger amplitudes in oopj and oopt magnetic field rotations. In case of the γ-Fe$_{2-x}$Ga$_x$O$_3$/Pt bilayer series, the bilayer with $x = 0.1$ has a much higher saturation magnetization than the other bilayers and therefore also a larger M_eff in bbFMR measurements.

SQUID magnetometry measurements of α-Fe$_2$O$_3$ doped with Ga indicate an increased canting of the magnetic sublattices suggesting an increased Dzyaloshinskii–Moriya interaction (DMI) in these samples. This could pave the way for tuning the DMI in α-Fe$_2$O$_3$ also for magnon Hanle-based experiments [105]. However, doping α-Fe$_2$O$_3$ with other nonmagnetic ions could be a possiblity to verify this behavior. Furthermore, an optimization of the α-Fe$_2$O$_3$ thin film quality could lead to the desired Morin transition, which could then be tuned by thin film doping (cf. Refs. [53, 69, 72, 77, 78, 106]). This would provide the possibility to investigate the SMR amplitude in doped α-Fe$_2$O$_3$/Pt heterostructures below the Morin transition, i.e. without sublattice canting.

In case of γ-Fe$_{2-x}$Ga$_x$O$_3$/Pt heterostructures, the SMR amplitude SMR$_\mathrm{long}$ has similar values for $x = 0.15$ and $x = 0.2$ (cf. Fig. 4.3.7). The fabrication and measurement of γ-$\mathrm{Fe}_{2-x}\mathrm{Ga}_x\mathrm{O}_3$/Pt bilayers with $x \geq 0.2$ could give a hint, if $\mathrm{SMR}_{\mathrm{long}}$ saturates or if the value for $x = 0.2$ is an outlier. Furthermore, a sample series with different doping concentrations using the other dopants Al, Ir, Zn and Ce would reveal, if they exhibit a similar dependence of $\mathrm{SMR}_{\mathrm{long}}$ on the dopant concentration x or not. However, it is striking that such a clear dependence occurs in γ-$\mathrm{Fe}_{2-x}\mathrm{Ga}_x\mathrm{O}_3$/Pt, although magnetic properties are quite different most probably due to the possibility of the Ga ions occupying vacancy sites within the spinel structure.

Additionally, bbFMR of the γ-$\mathrm{Fe}_{1.9}X_{0.1}\mathrm{O}_3$/Pt bilayer series would be interesting, since the γ-$\mathrm{Fe}_{2-x}\mathrm{Ga}_x\mathrm{O}_3$/Pt series exhibited an unexpected reduced damping with increasing x. As the SMR amplitude could be affected by various factors, an extensive bbFMR study on all fabricated thin films could give information about a possible dependence of the SMR on the damping in the MOI.

Furthermore, the interface roughness influences the spin mixing conductance and thus the SMR amplitude [42]. AFM images on blank MOI thin films could help characterizing the interface quality of the MOI/HM bilayer samples.

Doping more simpler magnetic ordered insulators for ADMR measurements could lead to a better prediction of the physical behavior of corresponding MOI/HM bilayers. Since Fig. 5.1.1 suggests that antiferromagnetic insulators with only one crystallographic site of the magnetic ion are best suitable to investigate effects on the SMR amplitude, further AFI/HM heterostructures with different simple AFIs could be considered in the studies.

A. Appendix

A.1. Experimental methods

In the following Sections A.1.1 and A.1.2 the thin film fabrication and analysis methods are discussed in more detail.

A.1.1. Thin film fabrication and structuring

The heterostructures are fabricated by pulsed laser deposition (Sec. A.1.1.1) and electron beam evaporation (Sec. A.1.1.2). Afterwards, the heterostructures are patterned into Hall bar mesa structures (see Sec. A.1.1.3) for magnetotransport measurements.

A.1.1.1. Sample preparation and pulsed laser depostion (PLD)

Before the thin film deposition an approximately $180\,\mathrm{nm}$ thick Pt layer is sputtered on the unpolished backside of the used single crystalline substrates Al_2O_3 and MgO, respectively. During the pulsed laser deposition (PLD) an infrared laser heats up the substrate. The Pt layer provides a better absorption of the infrared light and a more homogeneous heat distribution on the sample and therefore a constant substrate temperature T_S. After the sputtering process, the substrates are cleaned with aceton and isopropanol in an ultrasonic bath. Then the substrates are inserted into the load-lock of the ultra high vacuum (UHV) cluster. The UHV cluster consists of multiple chambers as depicted in Fig. A.1.1. Hereby, the respective substrate can be transferred on a transfer arm accross the transfer chamber into the different chambers without breaking the vacuum.

The fabrication of α-$Fe_{2-x}Ga_xO_3$ thin films on Al_2O_3 (0001) and of γ-$Fe_{2-x}Ga_xO_3$, γ-$Fe_{1.9}X_{0.1}O_3$ and Fe_3O_4 thin films on MgO (001) substrates is done by pulsed laser deposition (PLD). Thereby, the backside of the substrate is heated up to a substrate temperature $T_\mathrm{S} = 320\,°\mathrm{C}$ in a controlled way. A pulsed UV KrF excimer laser with a wavelength of $248\,\mathrm{nm}$ hits the selected stochiometric, polycrystalline target on the target carousel (see Fig. A.1.2). Due to the high energy density at the target, the target material ionizes and a plasma plume forms, which diffuses towards the substrate. The energy density ρ_L can be controlled by an automatic lens system and is set to $2.5\,\mathrm{J\,cm^{-2}}$. The growth process of (doped) α-Fe_2O_3 and γ-Fe_2O_3 takes place in an oxygen atmosphere with a pressure of $p_{\mathrm{O}_2} = 25\,\mathrm{\mu bar}$ to avoid oxygen vacancies. The Fe_3O_4 phase can be accomplished by reducing the amount of oxygen by growing in an argon atmosphere with a pressure of $p_\mathrm{Ar} = 10\,\mathrm{\mu bar}$. The pressure of the respective gas atmosphere is regulated at a constant

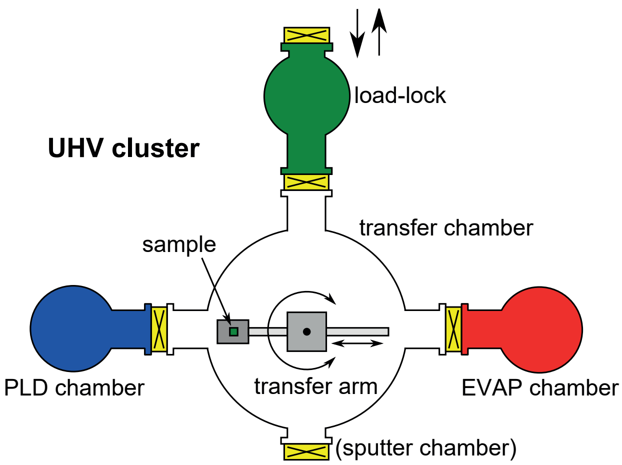

Figure A.1.1.: Scheme of the ultra high vacuum (UHV) cluster. The pulsed laser deposition (PLD), the electron beam evaporation (EVAP) and the sputter chamber (neglected in the scheme here) are accessible by inserting the respective sample into the load-lock and transferring it on the transfer arm accross the transfer chamber. Figure taken from Ref. [107].

gas flow. In the framework of this thesis for every thin film deposition a repetition rate of $f = 2\,\mathrm{Hz}$ is used with a relaxation time of $t_\mathrm{R} = 10\,\mathrm{s}$ inbetween the pulse packages with respectively 250 pulses. For further information about the epitaxial growth of thin films by pulsed laser deposition it is referred to Refs. [108, 109].

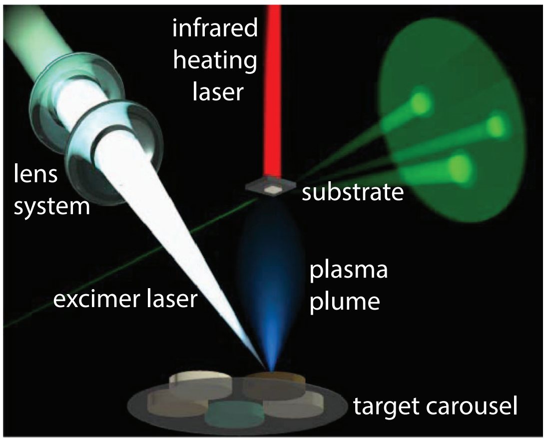

Figure A.1.2.: Working scheme of a pulsed laser deposition (PLD) process. An excimer laser hits a rotating target pellet in the target carousel. The energy density at the target can be regulated via an automatic lens system. A plasma plume then diffuses towards the substrate, which is heated up with an infrared laser. Figure adapted from Ref. [110].

A.1.1.2. Electron beam evaporation (EVAP)

For the bilayer and trilayer samples, a Pt electrode is deposited on top of the respective PLD-grown thin films, in-situ and without breaking the vacuum by electron beam evaporation (EVAP). The EVAP process takes place in a vacuum chamber with a pressure of about 5×10^{-7} mbar. Thereby, a filament with a filament current of 30 A emits electrons that are accelerated in an electric field with an applied voltage of $7.5\,\mathrm{kV}$. The electron beam with a current of approximately $135\,\mathrm{mA}$ is deflected onto a crucible filled with Pt by a magnetic field. Pt is vaporized by the electron beam and deposited on the sample (see Fig. A.1.3). A quartz crystal is used to control the Pt layer thickness that is set to $5\,\mathrm{nm}$ beforehand. Thereby, Pt is also deposited on the oscillating crystal. From the oscillation frequency the mass of the evaporated Pt and therefore the deposition rate can be determined. For a more accurate determination of the Pt thickness X-ray reflectometry is indispensable (cf. Sec. A.1.2.1).

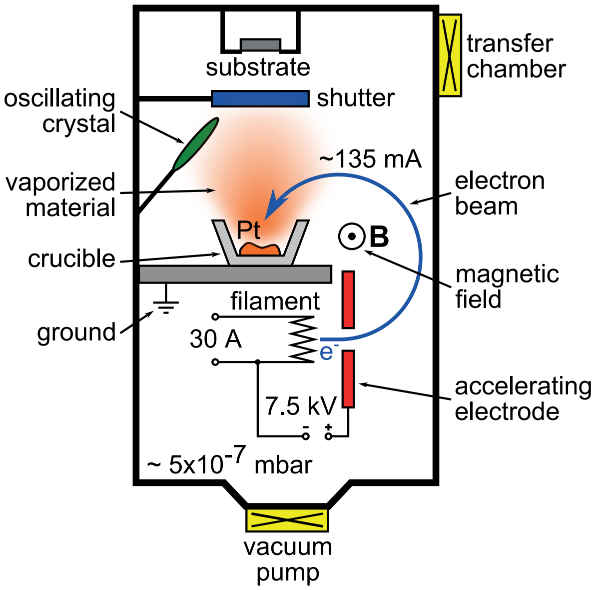

Figure A.1.3.: Principle of electron beam evaporation (EVAP). An electron beam is emitted from the filament, accelerated and then focussed on the Pt crucible by a magnetic field. The Pt is heated up until it evaporates and is deposited onto the sample. An oscillating crystal controls the deposition rate. Figure taken from Ref. [107].

A.1.1.3. Optical lithography and argon ion milling

To perform magnetotransport measurements the heterostructures are patterned into Hall bar mesa structures by optical lithography and argon ion milling. For the optical lithography the samples are cleaned by aceton and isopropanol in an ultrasonic bath and then covered by a photoresist (AZ MIR 701 by Microchemicals), which is spincoated on top of the heterostructure and baked at $90\,^{\circ}\mathrm{C}$ for $90\,\mathrm{s}$ by putting the sample on a hot plate. The lithography process is done by a halogen vapor lamp exposing a dia with UV light. The dia contains the desired Hall bar structure, which is then projected onto the positive optical resist of the sample by a microscope. After the exposure with UV light, the samples are developed in the developer AZ MIF 726 for about $60\,\mathrm{s}$ and then dipped into water. Thereby, the exposed parts of the photoresist are removed.

Via argon ion milling the Hall bar mesa structure is etched into the heterostructure. Argon ions hit the surface of the sample, which is partially covered by the photoresist. The parts that are not protected by the photoresist are etched away. Afterwards, the sample is again cleaned to remove the remaining resist. The sample then contains the desired Hall bar mesa structure. To investigate the SMR, bilayer samples with Pt electrodes are etched for $90\,\mathrm{s}$ to define Hall bar mesa structures within the Pt layer. Samples without a Pt electrode on top are etched for a longer time to define Hall bar mesa structures within the magnetic insulator, which allows the investigation of the electric properties of the respective magnetic insulator. Since the corresponding thin films are not very conducting, the samples are again structured by optical lithography after the etching process. The resist then covers the entire sample except for the Hall bar pads. After the lithography step, $2\,\mathrm{nm}$ titanium (Ti) and then $50\,\mathrm{nm}$ gold (Au) are sputtered on top of the sample. In a lift-off process the resist and the metals on top of the resist are removed in aceton and isopropanol and only the Hall bar structure with pads covered with Ti and Au remains. This structure provides a better electrical contact for magnetotransport measurements.

A.1.2. Analysis methods

This Section provides an overview of the analysis methods used within this thesis, among others high resolution X-ray diffraction (Sec. A.1.2.1), atomic force microscopy (Sec. A.1.2.2), SQUID magnetometry (Sec. A.1.2.3), ferromagnetic resonance (Sec. A.1.2.4) and magnetotransport measurements (Sec. A.1.2.5).

A.1.2.1. High resolution X-ray diffraction (HR-XRD)

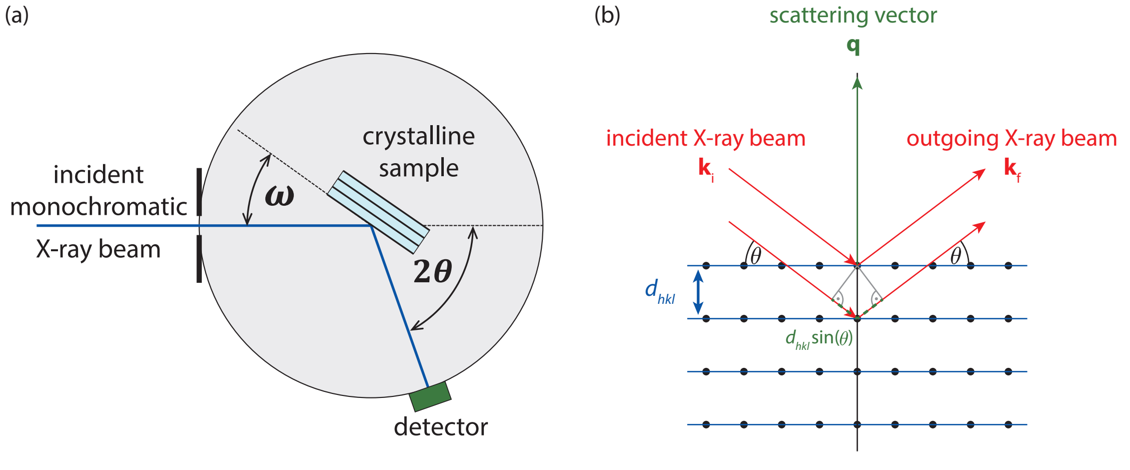

Figure A.1.4.: (a) Schematic of a X-ray diffractometer and (b) diffraction of a X-ray beam at the lattice planes of a crystalline sample. Figure adapted from Ref. [111] in analogy to Refs. [24, 110].

High-resolution X-ray diffraction (HR-XRD) is used to study the crystalline quality of the fabricated thin films and the polycrystalline PLD targets. Within this thesis the 4-circle X-ray diffractometer D8 Discover from Bruker is used. For technical details about the diffractometer it is referred to Ref. [107]. As shown in Fig. A.1.4 (a) a X-ray diffractometer consists of a X-ray source, a sample stage with the mounted sample and a detector measuring the intensity of the reflected radiation. The X-rays hit the sample under an angle ω and are diffracted at the lattice planes of the crystalline sample with a diffraction angle 2θ (see Fig. A.1.4 (b)). The X-rays have a wavelength of $\lambda = 0.154\,06\,\mathrm{nm}$ (Cu-K_{α_1} line). The constructive interference of the reflected X-rays is described by Bragg's law [24]

$$2d_{hkl}\sin(\theta) = n\lambda \tag{A.1}$$

with the distance d_{hkl} between neighboring lattice planes and the diffraction order n. By Eq. (A.1) the out-of-plane lattice constant c of a crystalline thin film is determined. Within this thesis thin films with a tetragonal and a hexagonal symmetry are fabricated. With the Miller indices h, k and l the distance d_{hkl} between lattice planes of a hexagonal crystal is described by

$$\frac{1}{d_{hkl}^2} = \frac{1}{a^2}\left(\frac{4}{3}(h^2+k^2+hk) + l^2\frac{a^2}{c^2}\right), \tag{A.2}$$

and of a tetragonal crystal by

$$\frac{1}{d_{hkl}^2} = \frac{h^2+k^2}{a^2} + \frac{l^2}{c^2}. \tag{A.3}$$

For the determination of the in-plane and the out-of-plane lattice constant of the polycrystalline PLD targets the Nelson-Riley method is used. This method considers different misalignments of the samples for the calculation of the lattice constants and is defined as [112]

$$\mathrm{NR} \propto \frac{1}{2}\left(\frac{\cos^2(\theta)}{\sin(\theta)} + \frac{\cos^2(\theta)}{\theta}\right). \tag{A.4}$$

With the reflections appearing in the 2θ-ω-scans depicted Fig. A.7.1, Bragg's equation (A.1) and Eq. (A.2) a and c are determined for multiple reflections. The respective lattice constants are plotted as a function of the Nelson-Riley function NR of Eq. (A.4). Fitting the data with a linear function gives the intersections a_0 and c_0 at $\mathrm{NR} = 0$, which are a good estimation for the lattice constants in the polycrystalline targets.

A 4-circle X-ray diffractometer provides a variety of scan types, which are discussed in the following:

- **2θ-ω-scan:** In this scan mode information about the crystalline symmetry, the lattice constants and crystalline impurity phases is obtained. Thereby, ω as well as 2θ is varied simultaneously so that the direction of the scattering vector $\mathbf{q}$ remains constant, but its magnitude is changed. The angle 2θ is not exactly twice the incident angle ω due to a possible miscut of the substrate surface described by the angle ω_{offset}, i.e. $2\theta = 2(\omega - \omega_{\mathrm{offset}})$. In 2θ-ω-scans an intensity spectrum is measured as a function of 2θ, where distinct reflection peaks are visible that fulfil Bragg's condition according to Eq. A.1. Samples with high crystalline quality do not only exhibit the respective sample reflections, but also finite thickness fringes, so-called Laue oscillations. These fringes indicate a coherent growth of the lattice planes with low surface roughness. Laue oscillations appear due to the finite thickness of the thin film layers. This enables the determination of the crystalline layer thickness by Laue oscillations using [103]

$$t = \frac{(n_1 - n_2)\lambda}{2(\sin(\theta_1) - \sin(\theta_2))}. \tag{A.5}$$

The 2θ positions of the Laue oscillations in 2θ-ω-scans are determined by fitting a Gaussian function. The thickness t is calculated for neighboring Laue oscillations with positions $2\theta_1$ and $2\theta_2$ ($n_1 - n_2 = -1$). Finally, it is averaged over all values for t.

- **Reflectometry:** X-ray reflectometry (XRR) is a special case of the 2θ-ω-scan with a scan range from $2\theta = 0.5°$ to $5°$. Under a very small angle the X-rays are reflected at the sample surface and at interfaces between layers with different refractive indices. XRR scans exhibit so-called Kiessig fringes due to constructive and destructive interference of the reflected X-rays. The measured intensity $I(2\theta)$ can be simulated with the software LEPTOS to obtain sample parameters such as layer thicknesses or roughnesses.

- **Rocking curve:** Hereby, the ω-angle is varied at a fixed 2θ value. The linewidth of the rocking curve entails information about the mosaicity of the crystal. A small full width at half maximum (FWHM) of the rocking curve therefore indicates a high crystalline quality with low mosaic spread of the layer.

- **Reciprocal space map:** The reciprocal lattice of a thin film can be illustrated by reciprocal space mappings (RSMs) with respect to the substrate reflection. Multiple scans are performed in horizontal and vertical direction of the reciprocal space around selected reflections. RSMs reveal information about the crystalline quality of the sample and a possible tilt of the lattice planes. Additionally the in-plane and the out-of-plane lattice constants a and c can be determined. This includes information about the strain state of the thin films, in particular, if a thin film grows epitaxial strained on a substrate (pseudomorphic growth) or if the thin film is already relaxed. Generally, with the relation

$$\frac{q_{\text{thin film}}}{q_{\text{substrate}}} = \frac{d_{hkl,\text{ substrate}}}{d_{hkl,\text{ thin film}}} \tag{A.6}$$

a as well as c can be calculated from the substrate and thin film reflection positions $q_{\text{thin film}}$ and $q_{\text{substrate}}$ appearing in the RSM.

As some asymmetric the thin film reflections might have a low intensity (see Figs. 4.1.2, 4.1.2 and A.3.3), rocking curves and detector scans are performed around the asymmetric thin film reflections over a long scan time to improve the signal-to-noise ratio. The extracted ω peak position of the rocking curve can be transformed into reciprocal lattice units together with the 2θ value. The absolute value of the outgoing wave vector $\mathbf{k}_\text{f}$ of the X-ray beam equals the absolute value of the incident wave vector $\mathbf{k}_\text{i}$, since it is an elastic scattering process. Therefore is

$$|\mathbf{k}_\mathrm{i}| = |\mathbf{k}_\mathrm{f}| = |\mathbf{k}| = \frac{2\pi}{\lambda}. \tag{A.7}$$

The magnitude of the scattering vector $\mathbf{q} = \mathbf{k}_\mathrm{f} - \mathbf{k}_\mathrm{i}$ can be defined as

$$|\mathbf{q}| = 2|\mathbf{k}|\cos(90^\circ - \theta) = 2|\mathbf{k}|\sin(\theta). \tag{A.8}$$

Geometric considerations lead to the contributions q_H and q_L of the scattering vector parallel and perpendicular to the thin film surface as functions of ω and θ:

$$q_\mathrm{H} = q_\parallel = \frac{4\pi}{\lambda}\sin(\theta)\sin(\omega - \theta), \tag{A.9}$$

$$q_\mathrm{L} = q_\perp = \frac{4\pi}{\lambda}\sin(\theta)\cos(\omega - \theta). \tag{A.10}$$

A.1.2.2. Atomic force microscopy (AFM)

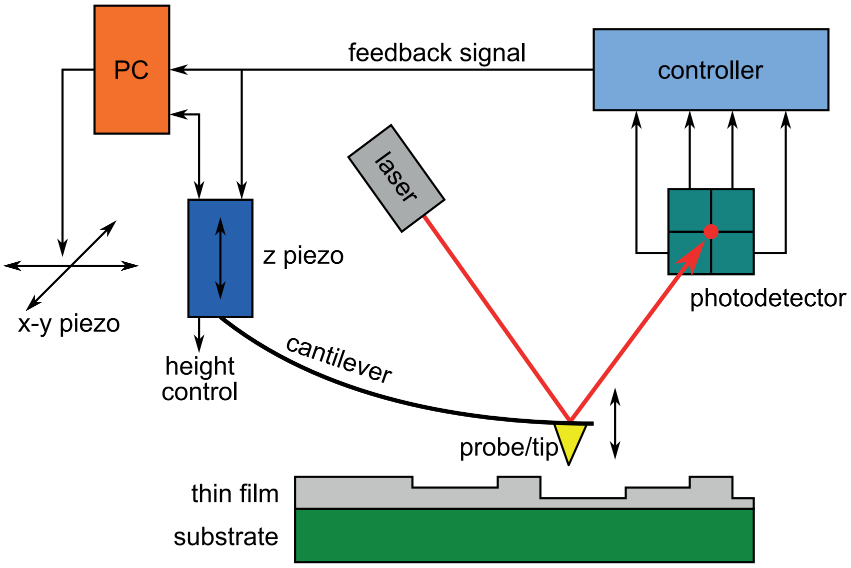

Figure A.1.5.: Schematic of an atomic force microscope (AFM). The sample is moved underneath the sharp cantilever tip. A laser beam is focused on the back of the tip and reflected onto a photodetector. Deflections of the cantilever are detected by the photodetector and a feedback signal is sent to a z piezo that controls the height of the tip. Figure taken from Ref. [107].

The surface quality of thin films can be investigated by atomic force microscopy (AFM) as depicted in Fig. A.1.5. The sample is placed on a sample stage that can be moved by a x-y piezo beneath the sharp AFM tip mounted on a cantilever. A laser beam is focused on the back of the tip and the reflected light is detected with a photodetector. If the cantilever is deflected due to forces between tip and sample, the displacement of the reflected laser light can be measured by the photodetector. The signal is processed and fed back to a z piezo to control the oscillation of the cantilever. For further information about AFM, in particular about the different oparation modes, it is referred to Ref. [107].

A.1.2.3. SQUID magnetometry

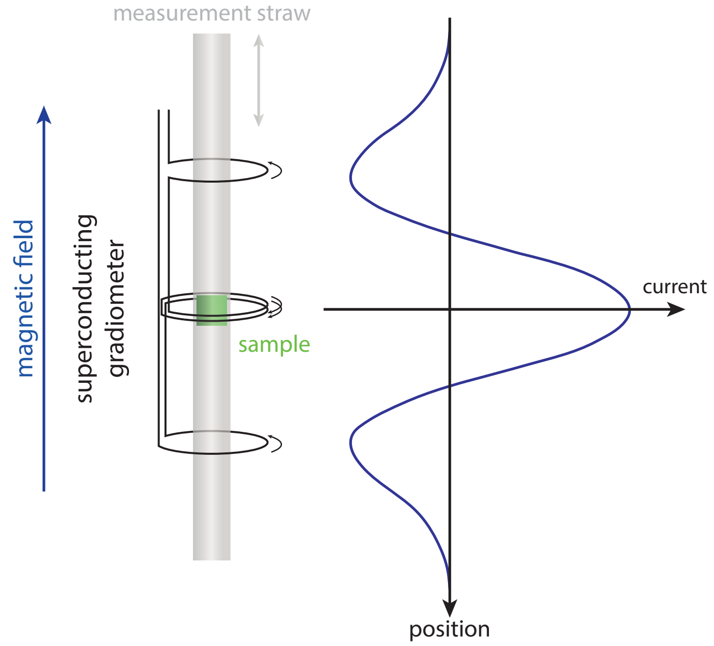

Figure A.1.6.: Detection-scheme of a SQUID magnetometer with a second order gradiometer and the corresponding measured current while moving the sample along the magnetic field direction. Figure taken from Ref. [110].

A superconducting quantum interference device (SQUID) magnetometer was used to investigate the magnetic properties of the thin film samples and the polycrystalline targets (cf. Fig. A.7.3). As depicted in Fig. A.1.6 the detection mechanism in a SQUID magnetometer consists of a system of superconducting induction coils. The sample is glued into a plastic straw and the straw is moved between the coils along the magnetic field direction. There are three coils in total with a distance of $1.5\,\mathrm{cm}$ between neighboring coils. The outer coils have one turn, respectively, the inner coil has two turns in opposite direction. While moving the sample through the coils a current is induced in the coils and converted into a voltage by a rf-SQUID. The current flowing in the inner coil is opposite to the current flowing in the outer ones. Therefore this system of superconducting detection coils is a so-called second order gradiometer, which suppresses interfering fields. The software fits the voltage curve and provides the total magnetic moment. Since SQUID magnetometry is an integral measurement method, the signal of the respective thin film as well as the much larger signal of the substrate is measured at the same time. Therefore, the substrate signal has to be subtracted from the total signal. Afterwards the magnetization M of the thin film is calculated by dividing the magnetic moment m through the thin film volume V.

A.1.2.4. Ferromagnetic resonance (FMR)

Ferromagnetic resonance is a popular tool to extract various magnetization dynamics parameters of ferromagnetic materials such as the g factor, the damping parameter α and the effective magnetization M_{eff}. Anisotropies within the sample can also be investigated. In its equilibrium position the magnetization of a ferromagnet is aligned along an effective magnetic field $\mathbf{H}_{\text{eff}}$ consisting of different magnetic field contributions. Next to the applied external magnetic field $\mathbf{H}_{\text{ext}}$, the anisotropy field $\mathbf{H}_{\text{aniso}}$ and the demagnetizing field $\mathbf{H}_{\text{demag}}$ in the ferromagnetic sample have to be considered leading to [113]

$$\mathbf{H}_{\text{eff}} = \mathbf{H}_{\text{ext}} + \mathbf{H}_{\text{aniso}} - \mathbf{H}_{\text{demag}}. \tag{A.11}$$

If the magnetization $\mathbf{M} = \mathbf{m}/M_{\text{S}}$ is brought out of its thermal equilibrium, the precession of the magnetization direction $\mathbf{m}$ around $\mathbf{H}_{\text{eff}}$ can be described by the Landau-Lifshitz-Gilbert (LLG) equation taking into account a damping of the precession by introducing the Gilbert damping parameter α. This results in

$$\frac{\mathrm{d}\mathbf{m}}{\mathrm{d}t} = -\gamma \mathbf{m} \times \mu_0 \mathbf{H}_{\text{eff}} + \alpha \mathbf{m} \times \frac{\mathrm{d}\mathbf{m}}{\mathrm{d}t} \tag{A.12}$$

with the gyromagnetic ratio $\gamma = g\mu_{\text{B}}/\hbar$, where g is the Landé-factor and μ_{B} the Bohr magneton [114].

Applying a radio frequency driving field $\mathbf{h}_{\text{rf}}$ perpendicular to $\mathbf{H}_{\text{eff}}$ excites $\mathbf{m}$ to the desired precessional motion. If the frequency $\omega_{\text{rf}} = 2\pi f$ of the driving field matches the resonance frequency $\omega = \gamma\mu_0|\mathbf{H}_{\text{eff}}|$ of $\mathbf{m}$, the energy of the driving field is absorbed. The corresponding resonance field $\mathbf{H}_{\text{res}}$ as a function of the driving field frequency f is described by the Kittel equation

$$\mu_0 H_{\text{res}} = \mu_0 H_{\text{ani}} - \frac{1}{2}\mu_0 M_{\text{eff}} + \sqrt{\left(\frac{\mu_0 M_{\text{eff}}}{2}\right)^2 + \left(\frac{2\pi f}{\gamma}\right)^2}. \tag{A.13}$$

with an external magnetic field applied in the thin film plane assuming an uniaxial anisotropy of the thin film sample [115]. For $\mathbf{H}_{\text{ext}}$ applied out of the thin film plane the resonance obeys the equation

$$\mu_0 H_{\text{res}} = \frac{2\pi f}{\gamma} + \mu_0 M_{\text{eff}} \tag{A.14}$$

By fitting $\mu_0 H_{\text{res}}(f)$ with Eqs. (A.13) and (A.14), respectively, M_{eff}, the g factor and H_{ani} can be extracted. In addition to that, the resonance line width $\mu_0 \Delta H$ gives the damping parameter α using the relation

$$\mu_0 \Delta H = \frac{4\pi\alpha f}{\gamma} + \mu_0 H_{\text{inh}} \tag{A.15}$$

with the inhomogeneous line width broadening H_{inh} caused by inhomogeneities in the sample [116, 117]. For a detailed derivation of Eqs. (A.13) - (A.15) it is referred to Refs. [113, 118].

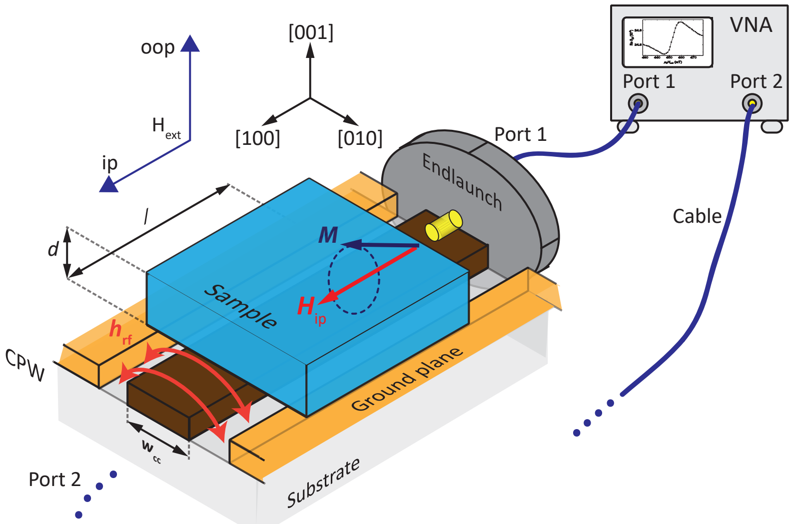

Figure A.1.7.: Scheme of the broadband FMR setup. The sample is placed on top of a coplanar waveguide (CPW) in an external magnetic field $\mathbf{H}_{\mathrm{ext}}$. The CPW consists of the ground planes (orange) and the center conductor (CC, brown). $\mathbf{H}_{\mathrm{ext}}$ can point in the sample plane parallel to the CC (ip) or out of the sample plane (oop). Microwaves are generated by a vector network analyzer (VNA) connected to the CPW at the endlaunches. The induced driving field $\mathbf{h}_{\mathrm{rf}}$ excites the magnetization $\mathbf{M}$ of the sample to a precessional motion. Figure adapted from [113].

The broadband FMR measurements are performed with the setup illustrated in Fig. A.1.7. The sample is placed upside down on a coplanar waveguide (CPW), which consists of two grounded planes and a center conductor (CC). The static magnetic field $\mathbf{H}_{\mathrm{ext}}$ of an electromagnet is applied either in the sample plane parallel to the CC (ip) or out of the plane (oop). A vector network analyzer (VNA) is connected to the endlaunches of the CPW with coaxial cables. A microwave is generated at port 1 and the transmission signal is measured at port 2. The microwave signal induces a radio-frequency driving field $\mathbf{h}_{\mathrm{rf}}$ around the CC, perpendicular to H_{ext}. If the frequency of the driving field is in resonance with the precession of the magnetization $\mathbf{M}$ of the ferromagnetic sample, the microwave is absorbed and the measured transmittive signal described by the S parameter S_{21} is reduced.

A.1.2.5. Magnetotransport measurements

After optical lithography and argon ion milling (see Sec. A.1.1.3) the heterostructures are glued on a copper cuboid and the Hall bar pads are connected to the pads of a chip carrier with aluminum wires via bonding. The angle dependent magnetoresistance (ADMR) measurements are performed in a magnet cryostat by rotating the sample from $-20°$ to $380°$ in $5°$ steps and then rotating back from $380°$ to $-20°$ in $10°$ steps at a constant temperature of the dipstick and a constant external magnetic field. The sample can be mounted on the dipstick in two possible configurations so that the magnetic field direction can be in the thin film plane or out of the thin film plane. The magnetic field rotation planes are defined in Sec. 2.3. With a source meter a current of $I_\mathrm{c} = 100\,\mu\mathrm{A}$ is applied on the Hall bars. The longitudinal and transverse voltages V_long and V_trans are measured in a standard four probe technique as depicted in Fig. A.1.8. With the Hall bar width w of $80\,\mu\mathrm{m}$ and a distance $l = 600\,\mu\mathrm{m}$ between contacted Hall bar pads the longitudinal and the transverse resistivities can be calculated by $\rho_\mathrm{long} = V_\mathrm{long} w t_\mathrm{Pt}/(I_\mathrm{c} l)$ and $\rho_\mathrm{trans} = V_\mathrm{trans} t_\mathrm{Pt}/I_\mathrm{c}$.

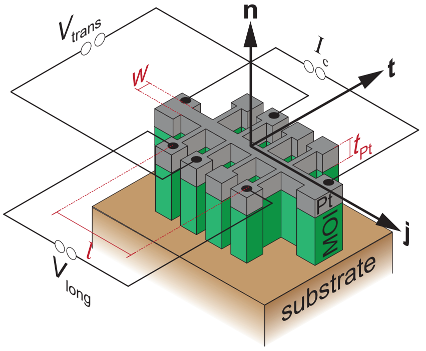

Figure A.1.8.: Scheme of a standard four probe measurement on a magnetic ordered insulator (MOI)/Pt bilayer with a Pt thickness t_Pt patterned into a Hall bar structure. A charge current I_c is applied along the Hall bar. The longitudinal and transverse voltages V_long and V_trans are measured at contacted Hall bar pads with a longitudinal distance $l = 600\,\mu\mathrm{m}$ and a Hall bar width $w = 80\,\mu\mathrm{m}$.

In a more detailed picture, the current reversal method is used to get V_long as well as V_trans. For every rotation angle the current is applied alternately in positive and then in negative $\mathbf{j}$-direction. In the following, the voltage V_+ is measured for I_c applied in $+\mathbf{j}$-direction and the voltage V_- is measured for I_c applied in $-\mathbf{j}$-direction. The current reversal method allows a separation of the thermal and the resistive parts of the voltage using the relations

$$V_\mathrm{res} = \frac{V_+ - V_-}{2} \tag{A.16}$$

and

$$V_\mathrm{therm} = \frac{V_+ + V_-}{2}, \tag{A.17}$$

since V_res depends on the current direction and V_therm does not. The voltages are measured six times in total for each rotation angle - three times the voltage V_+ and three times the voltage V_-. Hence, it can be averaged over three values for V_res and V_therm, respectively. In the framework of this thesis, only V_res is discussed without further notice, since V_therm is negligible at the used current densities.

In magnetically ordered insulator/heavy metal bilayers, the resistive voltages behaves within the SMR theory described in Sec. 2.3. However, in ferro- and ferrimagnetic conductors the anisotropic magnetoresistance (AMR) needs to be taken into account.

A.2. Anisotropic magnetoresistance (AMR) in magnetite

The longitudinal resistivity ρ of a conductor depends on the direction of the charge current $\mathbf{J}_\mathrm{c}$ with respect to the orientation of the magnetization $\mathbf{M}$. If $\mathbf{J}_\mathrm{c}$ is parallel to $\mathbf{M}$ the resistivity is higher than for $\mathbf{J}_\mathrm{c} \perp \mathbf{M}$. This effect can be traced back to the partially filled d-shells in the ferro- or ferrimagnetic conductor that are not spherically symmetric due to spin orbit interaction. The spin orbit interaction couples the orientation of the charge distribution with the orientation of $\mathbf{M}$. Therefore, s-d-scattering is depending on the orientation of $\mathbf{M}$, since the conduction electrons face a larger scattering cross section for $\mathbf{J}_\mathrm{c} \parallel \mathbf{M}$ than for $\mathbf{J}_\mathrm{c} \perp \mathbf{M}$. For a detailed explanation of the AMR it is referred to Ref. [119]. In analogy to the spin Hall magnetoresistance (SMR) effect explained by Eqs. (2.5) and (2.6) the longitudinal resistivity ρ_long can be expressed within the AMR theory as

$$\rho_\mathrm{long} = \rho_0 + \rho_1 m_j^2 \tag{A.18}$$

with the AMR resistivity coefficient ρ_1 and the projection m_j of the magnetization direction $\mathbf{m}$ on the direction $\mathbf{j}$ [120]. In angle dependent magnetoresistance (ADMR) experiments (cf. Fig. 2.3.2 (a)) this results in

$$\rho_\mathrm{long}^\mathrm{ip} = \rho_0 + \frac{\rho_1}{2}(1 + \cos(2\alpha)), \qquad \rho_\mathrm{long}^\mathrm{oopj} = \rho_0, \qquad \rho_\mathrm{long}^\mathrm{oopt} = \rho_0 + \frac{\rho_1}{2}(1 - \cos(2\beta)), \tag{A.19}$$

Hence, for the longitudinal resistivity an oscillation in ip and oopt magnetic field rotation and a low resistive state in oopj rotation is expected. This is only valid, if the crystal symmetry of the conductor is neglected, i.e. a polycrystalline material is assumed. Now the crystal symmetry is taken into account to explain the longitudinal AMR observed in $\mathrm{Fe_3O_4}$ as depicted in Fig. 3.3.5. The following deviation of ρ_long is adapted from Limmer *et al.*, Ref. [97]. First of all, the resistivity tensor is written as a series expansion up to the second order under consideration of a cubic crystal symmetry, hence

$$\begin{aligned}\bar{\rho}^\mathrm{cubic} = (a_{11} + a_{1122}) \begin{pmatrix} 1 & 0 & 0 \\ 0 & 1 & 0 \\ 0 & 0 & 1 \end{pmatrix} + (a_{1111} - a_{1122}) \begin{pmatrix} m_j^2 & 0 & 0 \\ 0 & m_t^2 & 0 \\ 0 & 0 & m_n^2 \end{pmatrix} \\ + a_{2323} \begin{pmatrix} 0 & m_j m_t & m_j m_n \\ m_j m_t & 0 & m_t m_n \\ m_j m_n & m_t m_z & 0 \end{pmatrix} + a_{123} \begin{pmatrix} 0 & m_n & -m_t \\ -m_n & 0 & m_j \\ m_t & -m_j & 0 \end{pmatrix}\end{aligned} \tag{A.20}$$

with the tensor elements a_{11}, a_{1122}, a_{1111}, a_{2323} and a_{123}. Hereby, again the charge current is applied along the crystallographic [100]-direction of the $\mathrm{Fe_3O_4}$ (001) crystal, e.g. $\mathbf{j} \parallel [100]$, $\mathbf{t} \parallel [010]$ and $\mathbf{n} \parallel [001]$. With Ohm's law $\mathbf{E} = \bar{\rho} \cdot \mathbf{J}$, where $\mathbf{E}$ is the electric field and $\mathbf{J} = J\mathbf{j}$

the current density, one gets the longitudinal resistivity

$$\rho_{\text{long}} = \frac{E_{\text{long}}}{J} = \frac{\mathbf{j} \cdot \mathbf{E}}{J} = \mathbf{j} \cdot \bar{\rho} \cdot \mathbf{j}. \tag{A.21}$$

Plugging Eq. (A.20) into Eq. (A.21) results in

$$\rho_{\text{long}}^{\text{cubic}} = a_{11} + a_{1122} + (a_{1111} - a_{1122}) m_j^2, \tag{A.22}$$

which is in accordance with Eq. (A.18) with $\rho_0 = a_{11} + a_{1122}$ and $\rho_1 = a_{1111} - a_{1122}$. A strain induced tetragonal symmetry of Fe_3O_4 as observed in Fe_3O_4 thin films leads to a modulation of the resistivity tensor given by Eq. (A.20). The resulting resistivity tensor $\bar{\rho}^{\text{tetra}}$ can be described by a cubic system with a tetragonal lattice distortion in [001]-direction expressed with the tensor $\Delta\bar{\rho}$:

$$\bar{\rho}^{\text{tetra}} = \bar{\rho}^{\text{cubic}} + \Delta\bar{\rho} \tag{A.23}$$

with

$$\Delta\bar{\rho} = (a_{33} - a_{11} + a_{1133} - a_{1122}) \begin{pmatrix} 0 & 0 & 0 \\ 0 & 0 & 0 \\ 0 & 0 & 1 \end{pmatrix} + (a_{312} - a_{123}) \begin{pmatrix} 0 & m_z & 0 \\ -m_z & 0 & 0 \\ 0 & 0 & 0 \end{pmatrix}$$
$$+ \begin{pmatrix} (a_{3311} - a_{1122}) m_n^2 & (a_{1212} - a_{2323}) m_j m_t & 0 \\ (a_{1212} - a_{2323}) m_j m_t & (a_{3311} - a_{1122}) m_n^2 & 0 \\ 0 & 0 & (a_{3333} - a_{1111} - a_{1133} + a_{1122}) m_n^2 \end{pmatrix}. \tag{A.24}$$

The longitudinal resistivity is then

$$\rho_{\text{long}}^{\text{tetra}} = a_{11} + a_{1122} + (a_{1111} - a_{1122}) m_j^2 + (a_{3311} - a_{1122}) m_n^2. \tag{A.25}$$

In oopj and oopt magnetic field rotation an additional $\cos^2(\beta, \gamma)$ dependence of ρ_{long} appears, which leads to the pronounced oscillation observed in Figs. 3.3.5 and 3.3.6 in oopj rotation.

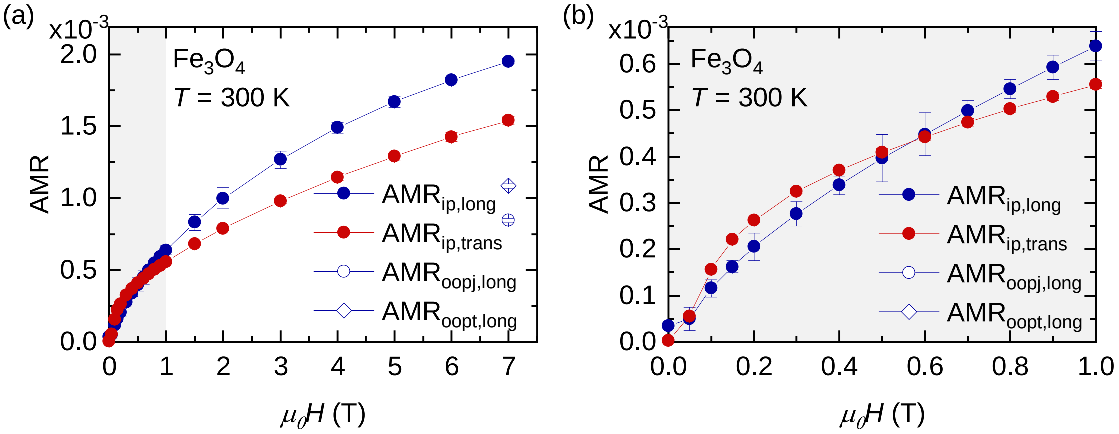

Figure A.2.1.: Longitudinal (blue symbols) and transverse (red symbols) AMR amplitude of the Fe_3O_4 thin film at $300\,\mathrm{K}$ in ip, oopj and oopt magnetic field rotation. (b) The longitudinal ip AMR amplitude exceeds the transverse ip AMR amplitude at $0.6\,\mathrm{T}$.

For the blank Fe_3O_4 thin film the AMR amplitude in ip, oopj and oopt magnetic field rotation is extracted at a temperature of $300\,\mathrm{K}$ and magnetic fields from $0\,\mathrm{T}$ to $7\,\mathrm{T}$ as depicted in Fig. A.2.1.

A.3. Reciprocal space mappings

This Section provides reciprocal space maps (RSMs) of the following bilayer and trilayer samples: γ-Fe_2O_3/Pt (Fig. A.3.1), Fe_3O_4/Pt (Fig. A.3.2), α-Fe_2O_3/α-$Fe_{1.7}Ga_{0.3}O_3$/Pt (Fig. A.3.3), γ-$Fe_{2-x}Ga_xO_3$/Pt with $x = 0.05$, 0.15, 0.2 (Fig. A.3.4) and γ-$Fe_{1.9}X_{0.1}O_3$/Pt with $X =$ Al, Ir, Ce (Fig. A.3.5).

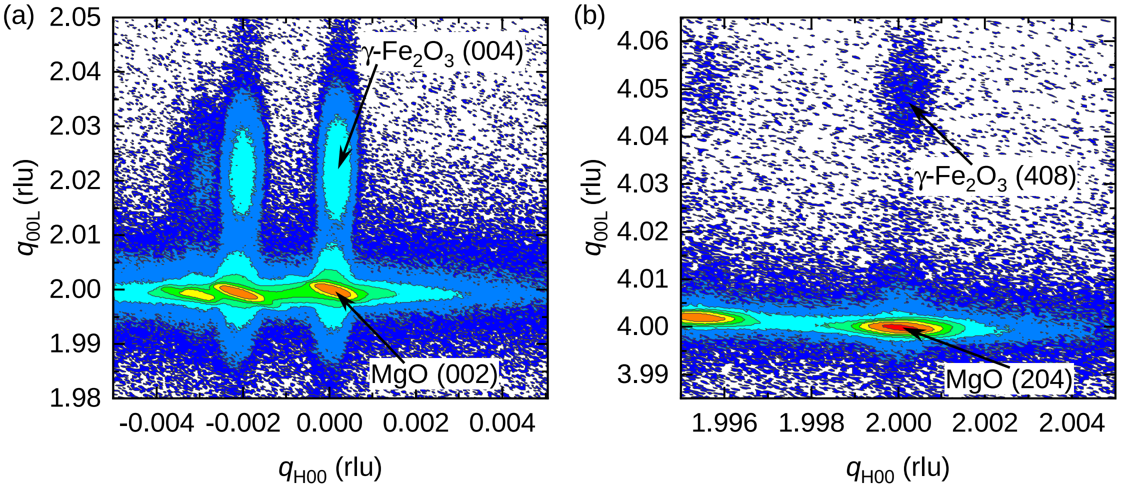

Figure A.3.1.: Reciprocal space maps of the γ-Fe_2O_3/Pt bilayer sample on MgO around (a) the symmetric γ-Fe_2O_3 (004) reflection and (b) the asymmetric γ-Fe_2O_3 (408) reflection. The corresponding substrate reflections are (a) MgO (002) and (b) MgO (204). The double peak structure with reflections along $q_{H00} = 0$ and $q_{H00} \approx -0.002$ is caused by differently oriented crystallites in the sample. The γ-Fe_2O_3 is epitaxial strained by the MgO substrate. The units are given in reciprocal lattice units (rlu) with respect to the MgO substrate.

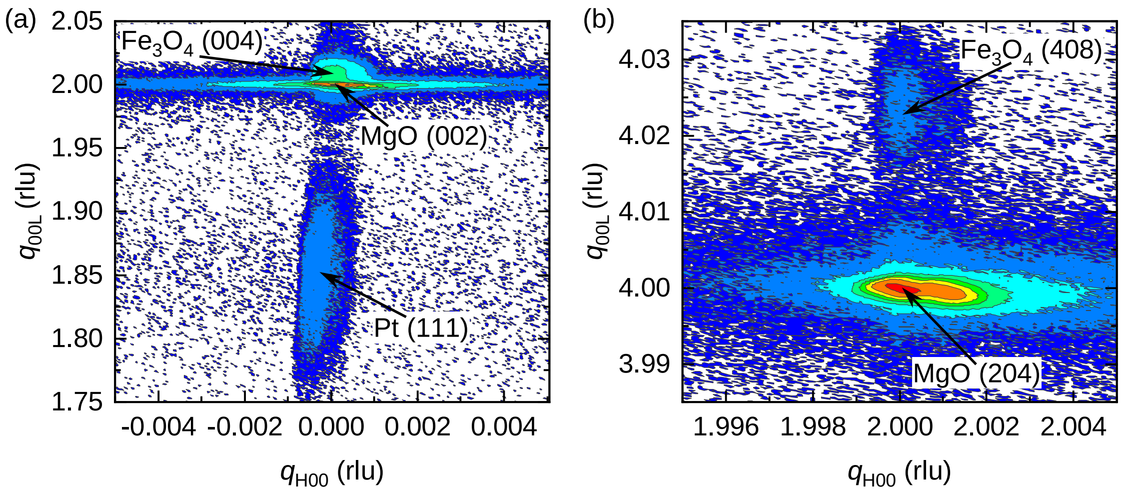

Figure A.3.2.: Reciprocal space mapping of the Fe_3O_4/Pt bilayer sample around (a) the symmetric Fe_3O_4 (004) (MgO (002)) reflection and (b) the asymmetric Fe_3O_4 (408) (MgO (204)) reflection. In this sample the Pt layer is crystalline and exhibits the Pt (111) reflection. The in-plane lattice constant is epitaxial strained. The units are given in reciprocal lattice units (rlu) with respect to the MgO substrate.

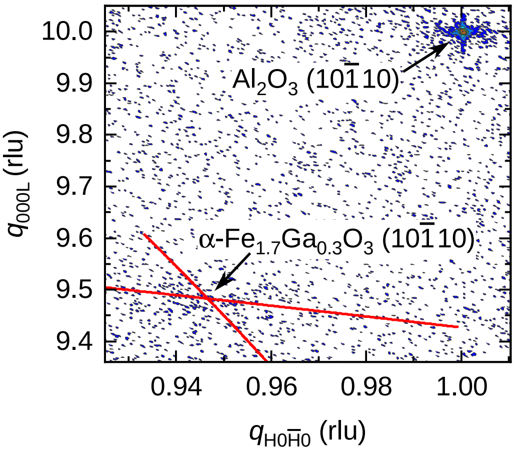

Figure A.3.3.: Reciprocal space map of the α-Fe_2O_3/α-$Fe_{1.7}Ga_{0.3}O_3$/Pt trilayer sample around the asymmetric $Fe_{1.7}Ga_{0.3}O_3$ $(10\bar{1}\,10)$ reflection. The thin film reflection position is determined by a rocking curve and a detector scan indicated by the red lines. The units are given in reciprocal lattice units (rlu) with respect to the Al_2O_3 substrate.

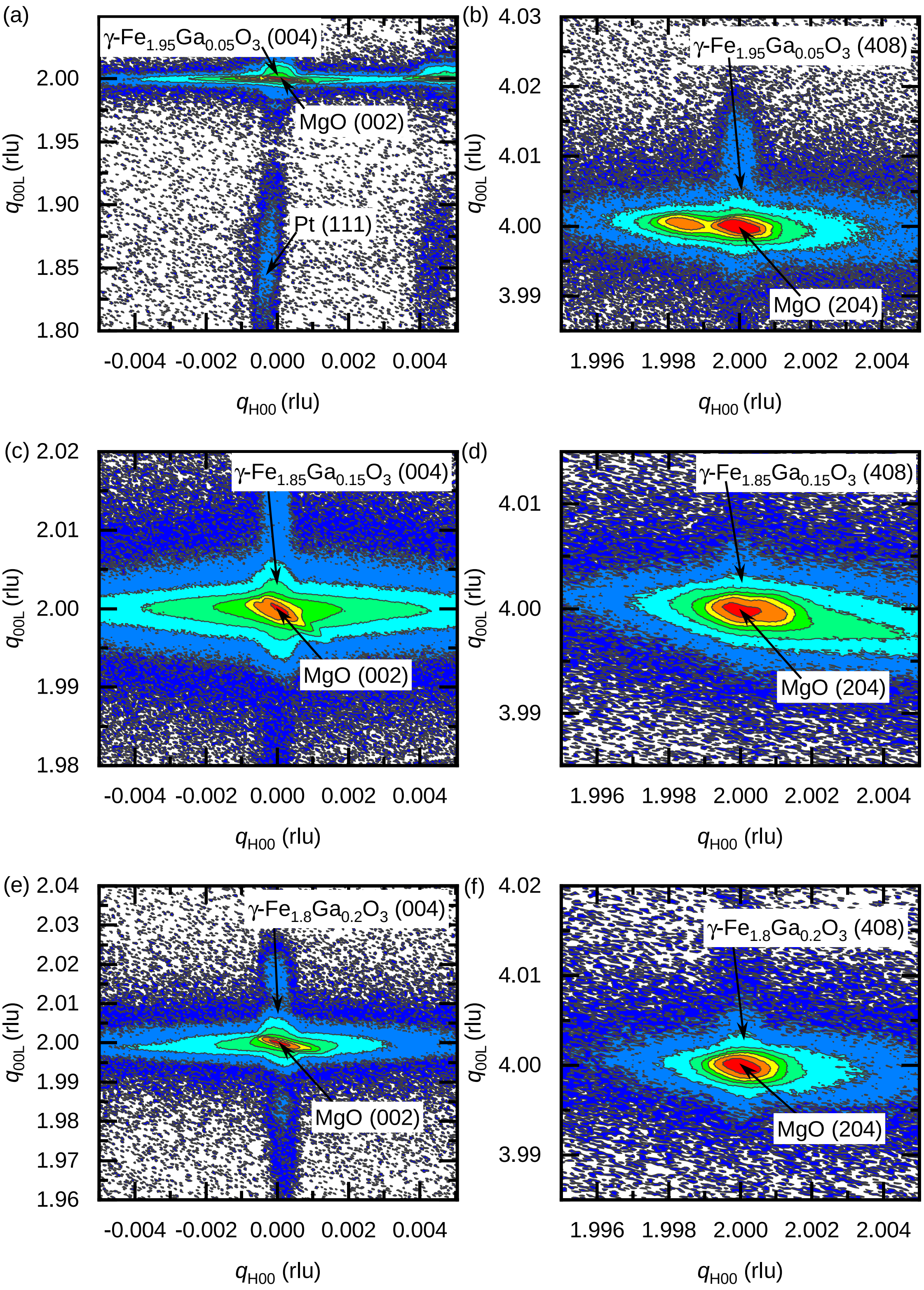

Figure A.3.4.: Reciprocal space maps of γ-Fe$_{2-x}$Ga$_x$O$_3$/Pt bilayer samples with $x = 0.05$, 0.15 and 0.2 on MgO around (a), (c), (e) the symmetric γ-Fe$_{2-x}$Ga$_x$O$_3$ (004) reflections and (b), (d), (f) the asymmetric γ-Fe$_{2-x}$Ga$_x$O$_3$ (408) reflections. The corresponding substrate reflections are MgO (002) (left panels) and MgO (204) (right panels). The units are given in reciprocal lattice units (rlu) with respect to the MgO substrates.

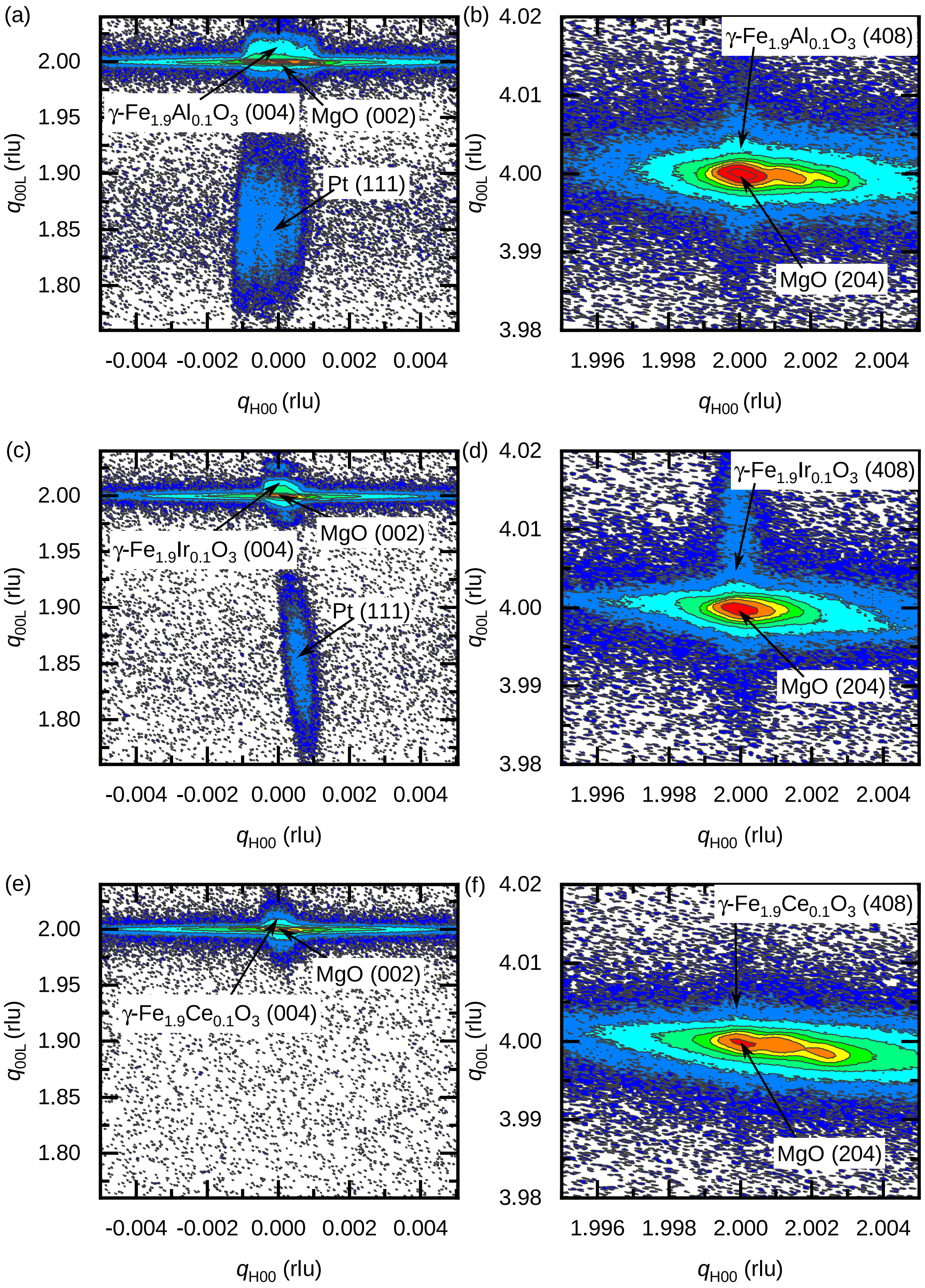

Figure A.3.5.: Reciprocal space maps of γ-Fe$_{1.9}X_{0.1}$O$_3$/Pt bilayer samples with X = Al, Ir and Ce on MgO around (a), (c), (e) the symmetric γ-Fe$_{1.9}X_{0.1}$O$_3$ (004) (MgO (002)) reflections and (b), (d), (f) the asymmetric γ-Fe$_{1.9}X_{0.1}$O$_3$ (408) (MgO (204)) reflections. The units are given in reciprocal lattice units (rlu) with respect to the MgO substrates.

A.4. SQUID magnetometry of iron oxide thin films

Additional SQUID magnetometry data is provided in the next Figures. Thereby, the γ-Fe_2O_3 thin film and the γ-Fe_2O_3/Pt bilayer sample measured at $100\,\mathrm{K}$ are presented in Fig. A.4.1. The temperature dependent magnetization M of a MgO substrate is given in Fig. A.4.2. In Figs. A.4.3, A.4.4 and A.4.5 the magnetization M as a function of the magnetic field $\mu_0 H$ at $100\,\mathrm{K}$ is depicted for Fe_3O_4 thin films, α-$Fe_{2-x}Ga_xO_3$/Pt bilayer samples and α-Fe_2O_3/α-$Fe_{2-x}Ga_xO_3$/Pt trilayer samples, respectively. For the γ-$Fe_{2-x}Ga_xO_3$/Pt bilayers and the γ-$Fe_{1.9}X_{0.1}O_3$/Pt bilayers SQUID magnetometry data is provided in Figs. A.4.6 and A.4.7.

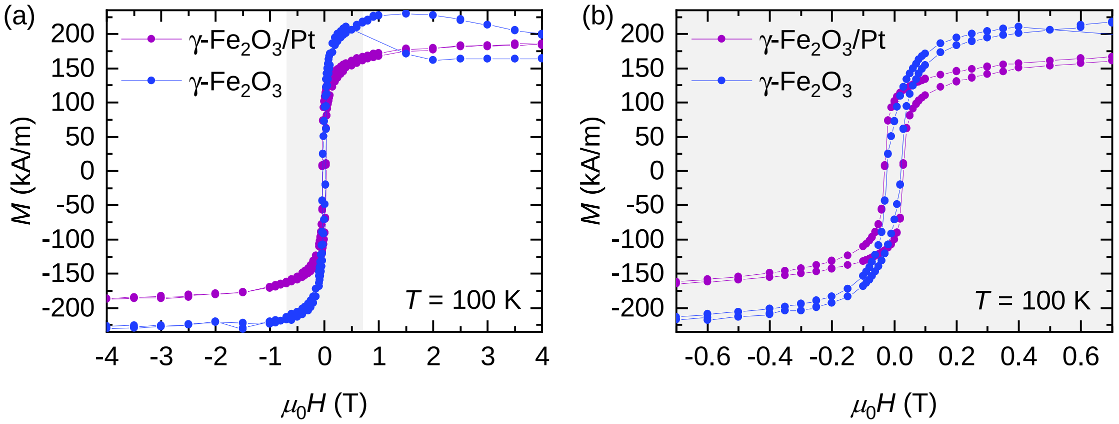

Figure A.4.1.: SQUID magnetometry measurements performed on γ-Fe_2O_3 thin films with (purple dots) and without Pt on top (blue dots). (b) For a better analysis of the hysteresis loops at $100\,\mathrm{K}$ it is zoomed into the grey area of figure (a).

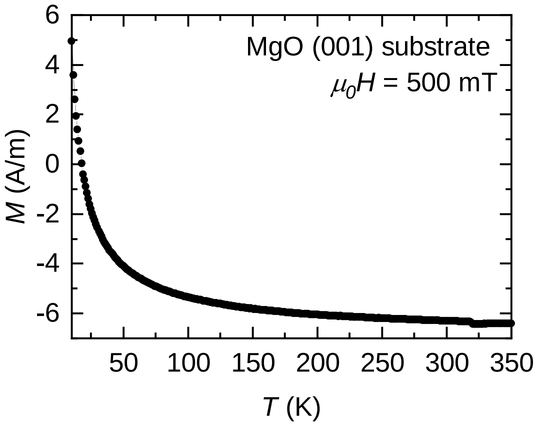

Figure A.4.2.: Temperature dependence of the magnetization M of a MgO substrate measured by SQUID magnetometry at a magnetic field of $500\,\mathrm{mT}$.

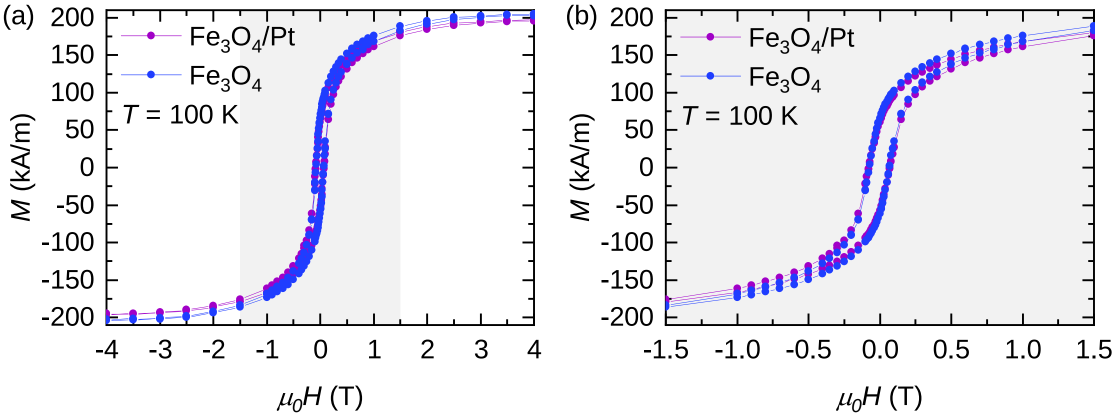

Figure A.4.3.: SQUID magnetometry measurements performed on Fe_3O_4 thin films with and without a Pt electrode. (a) Hysteresis loops at $100\,\mathrm{K}$ and (b) zoom into the grey area of figure (a).

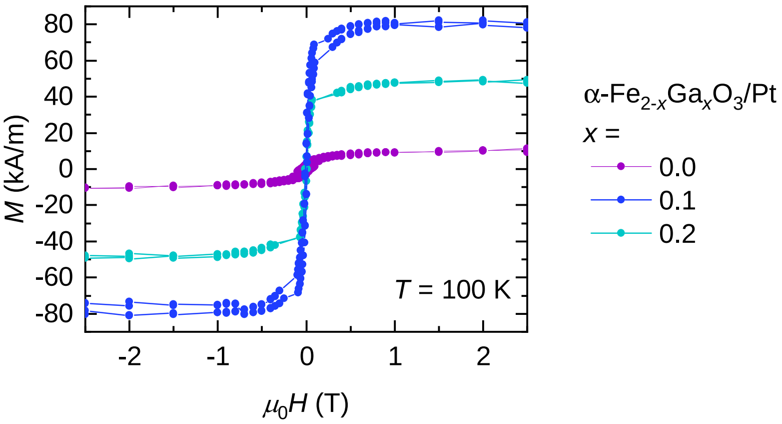

Figure A.4.4.: SQUID magnetometry data of α-$Fe_{2-x}Ga_xO_3$/Pt bilayer samples ($x = 0.0$ in purple, $x = 0.1$ in blue and $x = 0.2$ in cyan). The hysteresis loops are recorded at $T = 100\,\mathrm{K}$ with a magnetic field applied in-plane.

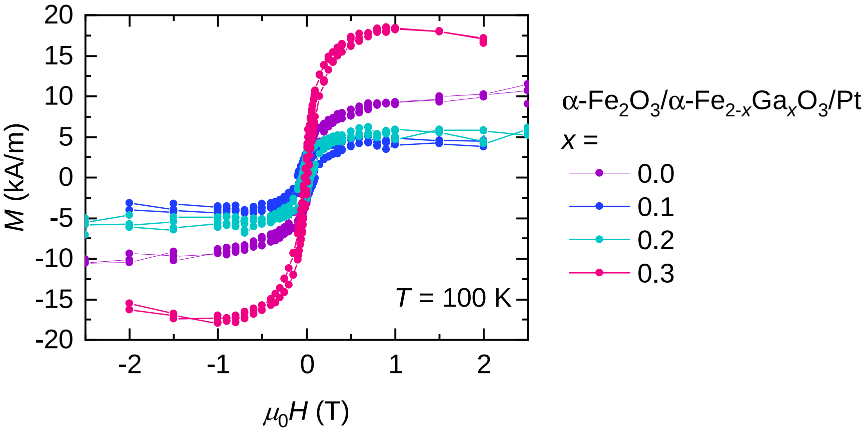

Figure A.4.5.: SQUID magnetometry with M measured as a function of $\mu_0 H$ at $100\,\mathrm{K}$. The α-Fe_2O_3/α-$Fe_{2-x}Ga_xO_3$/Pt trilayers are depicted in blue ($x = 0.1$), cyan ($x = 0.2$) and pink ($x = 0.3$) and the undoped α-Fe_2O_3/Pt bilayer in purple dots.

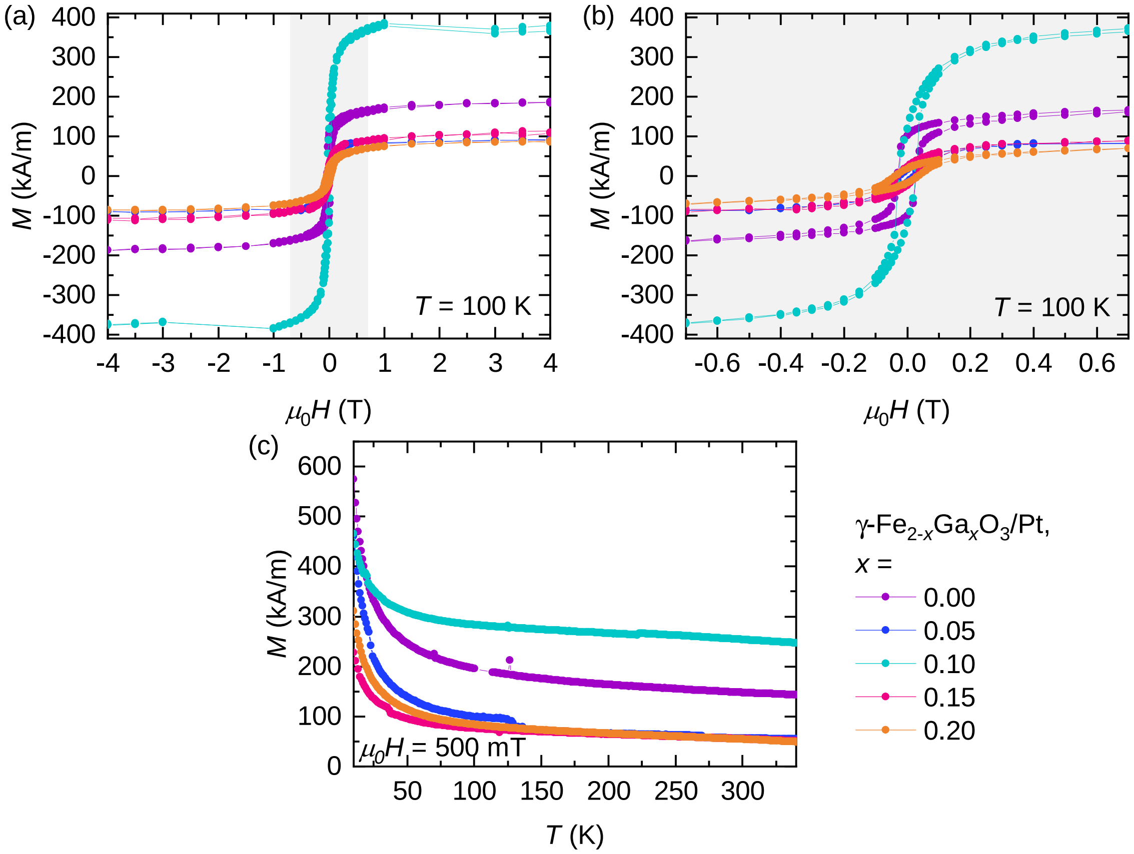

Figure A.4.6.: SQUID magnetometry data of γ-Fe$_{2-x}$Ga$_x$O$_3$/Pt bilayers with $x = 0.0$ (purple), 0.05 (blue), 0.1 (cyan), 0.15 (pink) and 0.2 (orange). (a) Hysteresis loops measured at $100\,\mathrm{K}$, (b) zoom into the grey area of figure (a) and (c) temperature dependence of the magnetization M at $500\,\mathrm{mT}$.

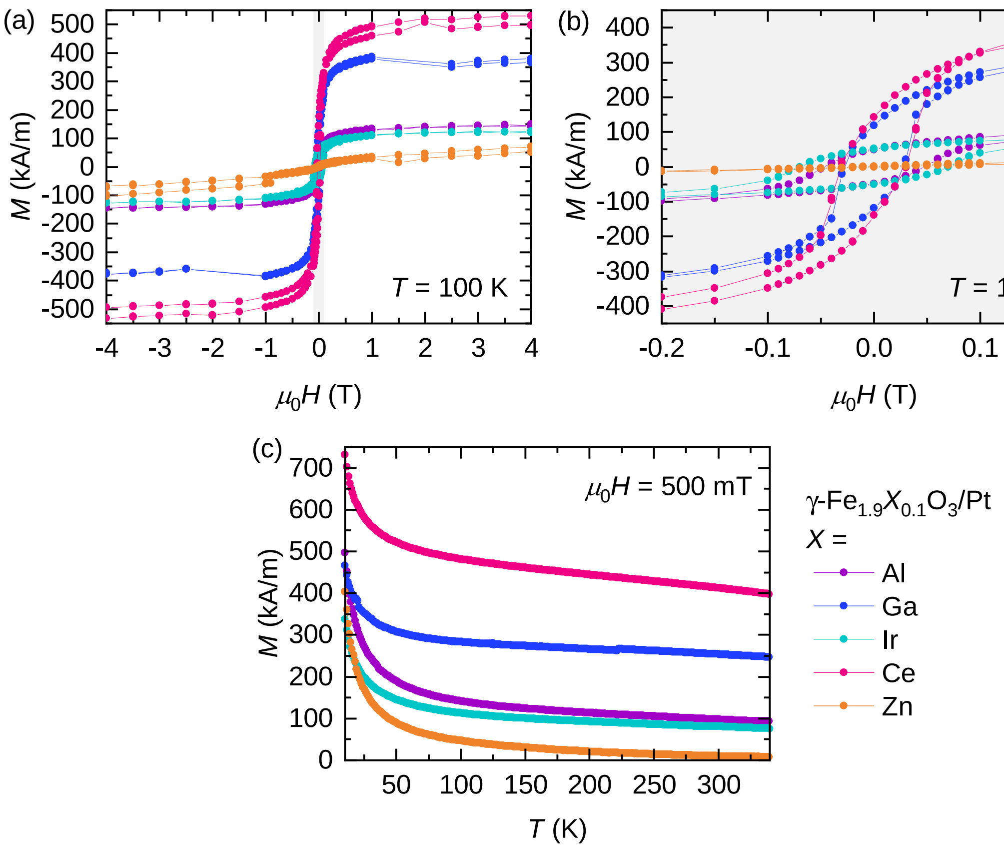

Figure A.4.7.: SQUID magnetometry of γ-Fe$_{1.9}X_{0.1}$O$_3$/Pt bilayers with X = Al (purple), Ga (blue), Ir (cyan), Zn (pink) and Ce (orange). (a) Hysteresis loops measured at $100\,\mathrm{K}$, (b) zoom into the grey area of figure (a) and (c) temperature dependence of the magnetization M at $500\,\mathrm{mT}$.

A.5. FMR in Ga:γ-Fe$_2$O$_3$

Supplemental results of broadband FMR measurements performed on the γ-Fe$_2$O$_3$ thin film sample (Fig. A.5.1 and Table A.5.1) and on the γ-Fe$_{2\text{-x}}$Ga$_\text{x}$O$_3$/Pt bilayer samples (Fig. A.5.2 and Table A.5.2) are presented in the following.

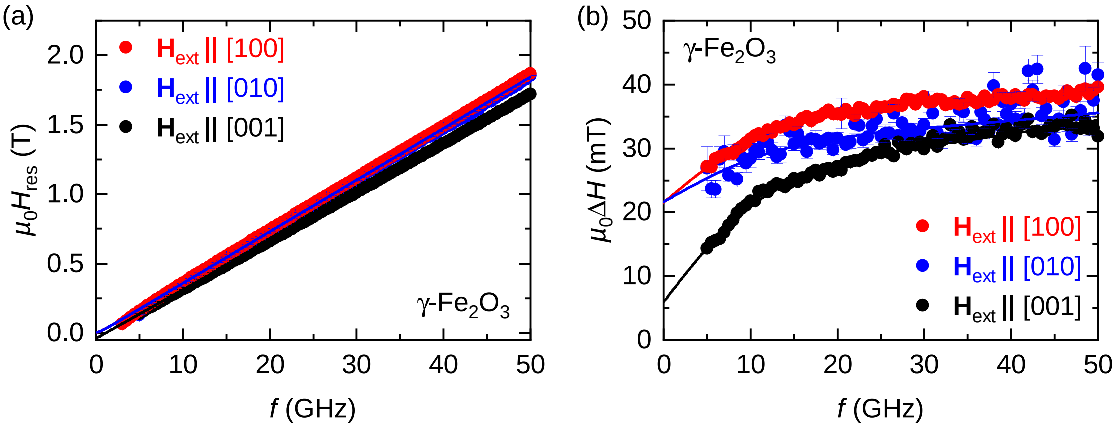

Figure A.5.1.: Broadband ferromagnetic resonance (bbFMR) measurements of the γ-Fe_2O_3 thin film. The measurements are performed with the external magnetic field $\mathbf{H}_{ext}$ being parallel to the crystallographic [100], [010] and [001] directions of the γ-Fe_2O_3 thin film (cf. Fig. A.1.7). (a) Extracted resonance fields $\mu_0 H_{res}$ as well as (b) line widths $\mu_0 \Delta H$. The respective line widths $\mu_0 \Delta H$ are fitted according to Eq. (3.1).

	$\mu_0 M_{eff}$ (mT)	g ($\gamma = \frac{g\mu_B}{\hbar}$)	$\mu_0 H_{ani}$ (mT)	α (10^{-3})	$\mu_0 H_{inh}$ (mT)
$\mathbf{H}_{ext}$ || [100]	-39 (fixed)	1.897 ± 0.002	-34 ± 1	2.7 ± 0.2	21.5 ± 0.6
$\mathbf{H}_{ext}$ || [010]	-39 (fixed)	1.920 ± 0.003	-34 ± 1	2.6 ± 0.7	21.6 ± 0.5
$\mathbf{H}_{ext}$ || [001]	-39 ± 1	2.038 ± 0.001		5.3 ± 0.3	5.9 ± 0.7

Table A.5.1.: Extracted effective Magnetization $\mu_0 M_{eff}$, g-factor g, anisotropy field $\mu_0 H_{ani}$, damping parameter α and inhomogeneity field $\mu_0 H_{inh}$ from fittings of the bbFMR data of the γ-Fe_2O_3 thin film sample using Eqs. (A.13), (A.14) and (3.1).

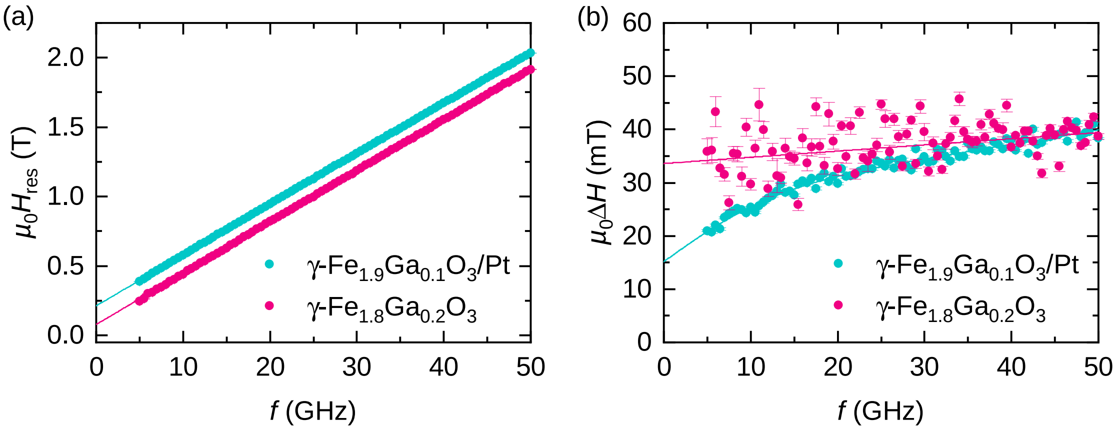

Figure A.5.2.: Broadband ferromagnetic resonance (bbFMR) measurements of the γ-$Fe_{1.9}Ga_{0.1}O_3$/Pt bilayer and the γ-$Fe_{1.8}Ga_{0.2}O_3$ thin film. The measurements are performed with the external magnetic field $\mathbf{H}_{ext}$ being parallel to the crystallographic [001] direction of the Ga:γ-Fe_2O_3 layer. (a) Extracted resonance fields $\mu_0 H_{res}$ as well as (b) line widths $\mu_0 \Delta H$.

x	$\mu_0 M_{\mathrm{eff}}$ (T)	g	α (10^{-3})	$\mu_0 H_{\mathrm{inh}}$ (mT)
0	-0.01 ± 0.0001	2.023 ± 0.001	10.5 ± 0.2	2.7 ± 0.6
0 (without Pt)	-0.039 ± 0.001	2.038 ± 0.001	5.3 ± 0.3	5.9 ± 0.7
0.05	0.100 ± 0.001	1.919 ± 0.002	6.2 ± 0.5	32 ± 1
0.1	0.214 ± 0.001	1.959 ± 0.001	5.0 ± 0.4	15 ± 1
0.15	0.079 ± 0.001	1.916 ± 0.002	3.1 ± 0.8	45 ± 2
0.2	0.079 ± 0.001	1.910 ± 0.002	6.1 ± 0.4	33 ± 1
0.2 (without Pt)	0.079 ± 0.001	1.943 ± 0.001	1.6 ± 0.4	36 ± 1

Table A.5.2.: Extracted effective Magnetization $\mu_0 M_{\mathrm{eff}}$, g-factor g damping parameter α and inhomogeneity field $\mu_0 H_{\mathrm{inh}}$ from fittings of the bbFMR data of the γ-Fe$_{2\text{-x}}$Ga$_\text{x}$O$_3$/Pt bilayers and the γ-Fe$_{2\text{-x}}$Ga$_\text{x}$O$_3$ thin films.

A.6. HR-XRD of the α-Fe$_{1.9}$Ga$_{0.1}$O$_3$ pressure series

Figure A.6.1 presents the 2θ-ω-scans of Ga doped iron oxide thin films fabricated by pulsed laser deposition at different pressures of the oxygen atmosphere.

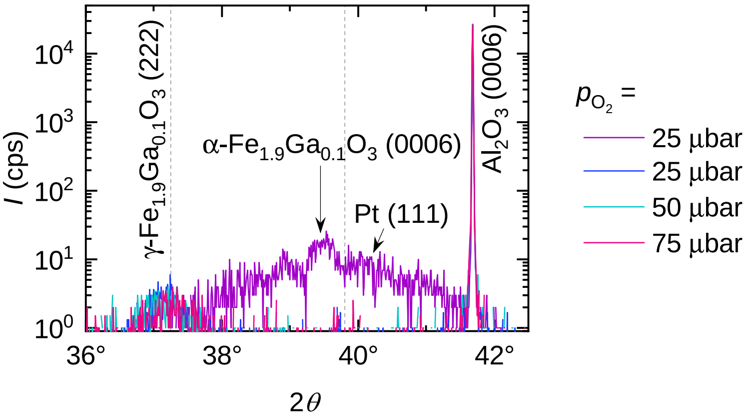

Figure A.6.1.: 2θ-ω-scans of Ga doped iron oxide thin films fabricated on Al$_2$O$_3$ (0001) substrates in an oxygen atmosphere at a pressure ranging from $p_{\mathrm{O_2}} = 25\,\mu\mathrm{bar}$ to $75\,\mu\mathrm{bar}$. The hexagonal α-Fe$_{1.9}$Ga$_{0.1}$O$_3$ phase is indended, but is only grown once at a pressure of $25\,\mu\mathrm{bar}$ (purple). The corresponding reflection is the α-Fe$_{1.9}$Ga$_{0.1}$O$_3$ (0006) reflection. Otherwise, cubic γ-Fe$_{1.9}$Ga$_{0.1}$O$_3$ grows on hexagonal Al$_2$O$_3$ as indicated by the appearance of the γ-Fe$_{1.9}$Ga$_{0.1}$O$_3$ (222) reflection.

A.7. HR-XRD and SQUID magnetometry of polycrystalline Ga:α-Fe$_2$O$_3$ targets

Polycrystalline Ga:α-Fe$_2$O$_3$ targets are investigated by high resolution X-ray diffraction (HR-XRD) and SQUID magnetometry. Figure A.7.1 presents the respective 2θ-ω-scans and Fig. A.7.2 the lattice constants calculated from the positions of the reflections in those 2θ-ω-scans. Figure A.7.3 reveals the temperature and magnetic field dependence of the magnetization of the respective α-Fe$_{2-x}$Ga$_x$O$_3$ targets.

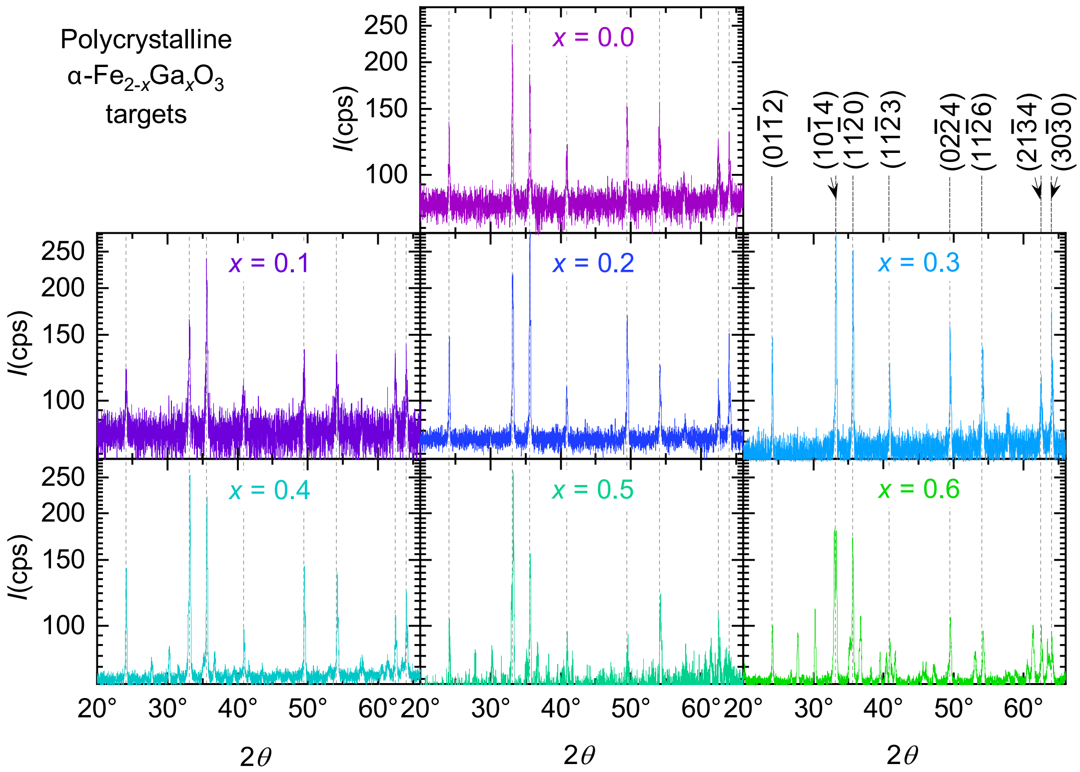

Figure A.7.1.: 2θ-ω-scans of polycrystalline α-Fe$_{2-x}$Ga$_x$O$_3$ targets with $x = 0.0$ - 0.6 in 0.1 steps. The targets show the expected reflections of the α-Fe$_2$O$_3$ phase as indicated by vertical dashed lines. By increasing the Ga concentration more and more parasitic phases occur that are most visible for $x = 0.6$.

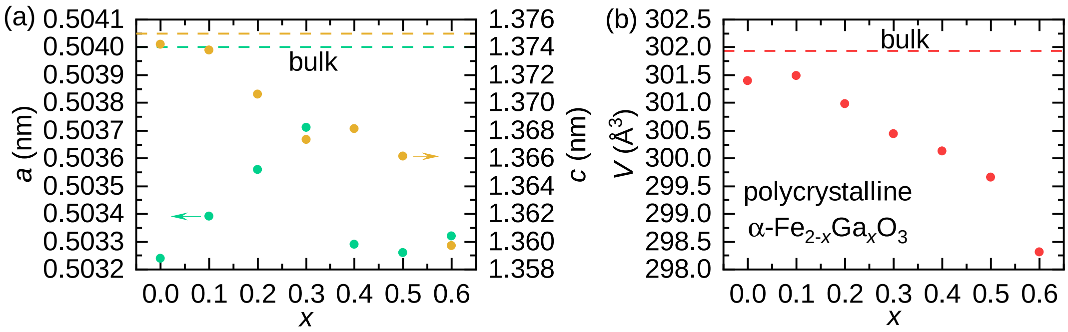

Figure A.7.2.: (a) In-plane lattice constant a (green) and out-of-plane lattice constant c (yellow) and (b) resulting unit cell volume V as functions of the Ga content x in polycrystalline α-Fe$_{2-x}$Ga$_x$O$_3$ targets. a increases linearly for a Ga content of up to $x = 0.3$ and exhibits a strong reduction for higher x. c decreases continously with increasing x, instead, and V also decreases with increasing x. The horizontal dashed lines indicate the literature values for bulk α-Fe$_2$O$_3$ adapted from Ref. [48]. With the occupation of Ga^{3+} on Fe^{3+} lattice sites a decrease in V is expected due to the slightly smaller ionic radius of Ga^{3+} compared to Fe^{3+} [75].

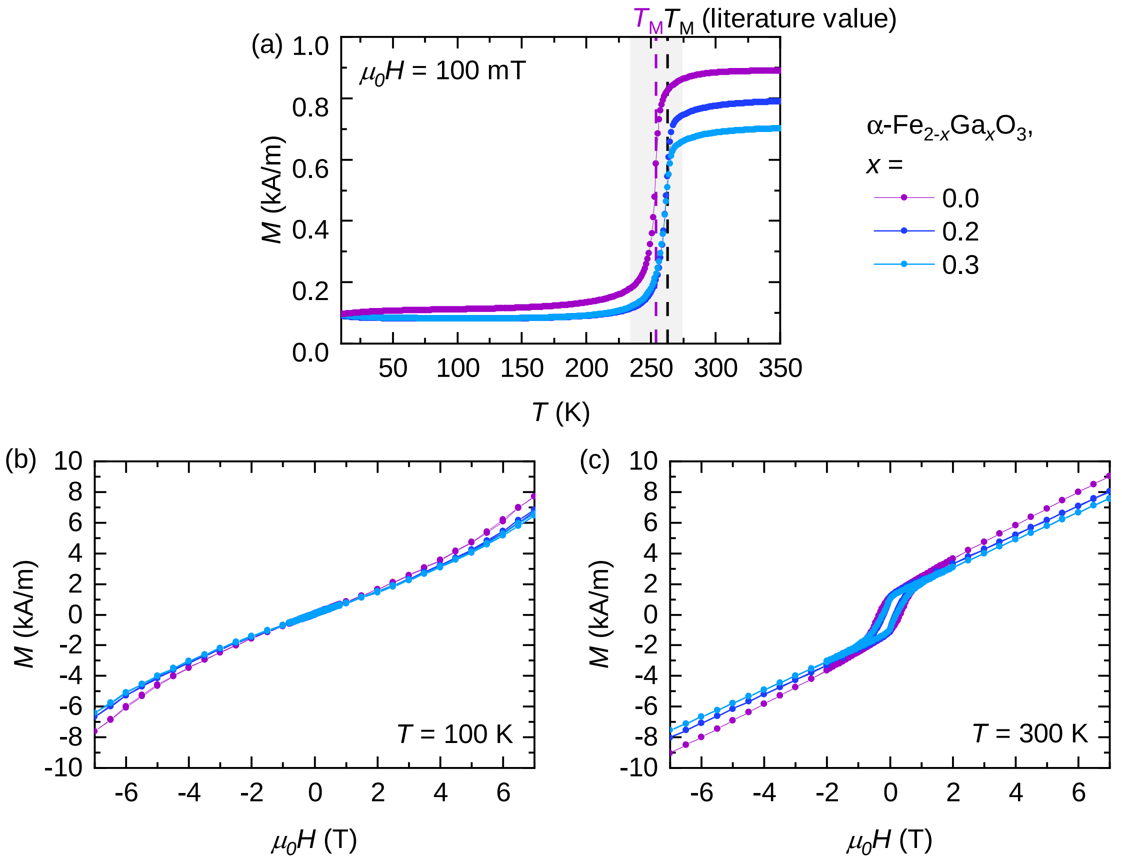

Figure A.7.3.: SQUID magnetometry measurements performed on polycrystalline α-$Fe_{2-x}Ga_xO_3$ targets with $x = 0.0, 0.2$ and 0.3. Magnetization M as (a) a function of the temperature T at a magnetic field of $100\,\mathrm{mT}$ and as a function of the magnetic field $\mu_0 H$ at a temperature of (b) $100\,\mathrm{K}$ and of (c) $300\,\mathrm{K}$. In (a) the Morin transition is clearly visible (cf. Sec. 2.4.1). Therefore in (b) no hysteresis is observable. The Morin transition decreases with increasing x due to the reduction in the number of magnetic moments.

A.8. Additional resistance measurements of Ga:γ-Fe_2O_3 thin films

Resistance measurements are performed on the γ-Fe_2O_3 and the γ-$Fe_{1.8}Ga_{0.2}O_3$ thin film sample and presented in Fig. A.8.1.

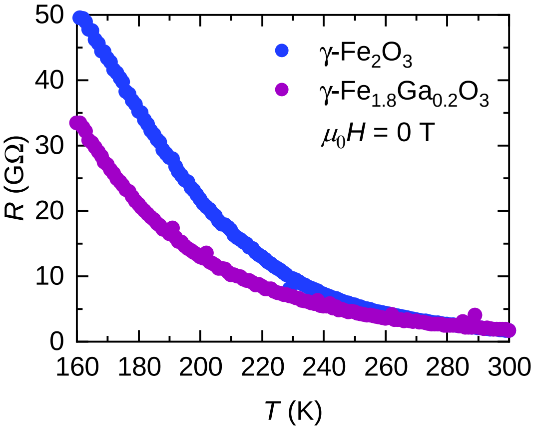

Figure A.8.1.: Zero field measurement of the resistance R as a function of the temperature T of the γ-Fe_2O_3 and the γ-$Fe_{1.8}Ga_{0.2}O_3$ thin film. The latter thin film has a slightly smaller resistance, but both thin films still exhibit a high resistance in the range of tens of GΩ with a strong increase going down to lower T.

Bibliography

[1] M. M. Waldrop, *The chips are down for Moore's law*, Nature **530**, 144 (2016).

[2] J. Puebla, J. Kim, K. Kondou, and Y. Otani, *Spintronic devices for energy-efficient data storage and energy harvesting*, Communications Materials **1** (2020), 10.1038/s43246-020-0022-5.

[3] M. Althammer, *All–Electrical Magnon Transport Experiments in Magnetically Ordered Insulators*, physica status solidi (RRL) – Rapid Research Letters **15**, 2100130 (2021).

[4] L. Belkhir and A. Elmeligi, *Assessing ICT global emissions footprint: Trends to 2040 & recommendations*, Journal of Cleaner Production **177**, 448 (2018).

[5] M. Althammer, in *Topology in Magnetism*, Springer Series in Solid-State Sciences, Vol. 192, edited by J. Zang, V. Cros, and A. Hoffmann (Springer International Publishing, 2018) pp. 209–237.

[6] E. V. Gomonay and V. M. Loktev, *Spintronics of antiferromagnetic systems (Review Article)*, Low Temperature Physics **40**, 17 (2014).

[7] P. Wadley, B. Howells, J. Železný, C. Andrews, V. Hills, R. P. Campion, V. Novák, K. Olejník, F. Maccherozzi, S. S. Dhesi, S. Y. Martin, T. Wagner, J. Wunderlich, F. Freimuth, Y. Mokrousov, J. Kuneš, J. S. Chauhan, M. J. Grzybowski, A. W. Rushforth, K. W. Edmonds, B. L. Gallagher, and T. Jungwirth, *Electrical switching of an antiferromagnet*, Science (New York, N.Y.) **351**, 587 (2016).

[8] H. Nakayama, M. Althammer, Y.-T. Chen, K. Uchida, Y. Kajiwara, D. Kikuchi, T. Ohtani, S. Geprägs, M. Opel, S. Takahashi, R. Gross, G. E. W. Bauer, S. T. B. Goennenwein, and E. Saitoh, *Spin Hall magnetoresistance induced by a nonequilibrium proximity effect*, Physical review letters **110**, 206601 (2013).

[9] J. Fischer, O. Gomonay, R. Schlitz, K. Ganzhorn, N. Vlietstra, M. Althammer, H. Huebl, M. Opel, R. Gross, S. T. B. Goennenwein, and S. Geprägs, *Spin Hall magnetoresistance in antiferromagnet/heavy-metal heterostructures*, Physical Review B **97**, 014417 (2018).

[10] S. Geprägs, M. Opel, J. Fischer, O. Gomonay, P. Schwenke, M. Althammer, H. Huebl, and R. Gross, *Spin Hall magnetoresistance in antiferromagnetic insulators*, Journal of Applied Physics **127**, 243902 (2020).

[11] J. FISCHER, *Spin Hall magnetoresistance in antiferromagnetic NiO and a-Fe2O3*, Master's thesis, TU Munich (2017).

[12] J. FISCHER, M. ALTHAMMER, N. VLIETSTRA, H. HUEBL, S. T. GOENNENWEIN, R. GROSS, S. GEPRÄGS, AND M. OPEL, *Large Spin Hall Magnetoresistance in Antiferromagnetic a−Fe2O3/Pt Heterostructures*, Physical Review Applied **13**, 014019 (2020).

[13] M. ALTHAMMER, *Pure spin currents in magnetically ordered insulator/normal metal heterostructures*, Journal of Physics D: Applied Physics **51**, 313001 (2018).

[14] S. VÉLEZ, V. N. GOLOVACH, J. M. GOMEZ-PEREZ, A. CHUVILIN, C. T. BUI, F. RIVADULLA, L. E. HUESO, F. S. BERGERET, AND F. CASANOVA, *Spin Hall magnetoresistance in a low-dimensional Heisenberg ferromagnet*, Physical Review B **100**, 180401 (2019).

[15] F. J. MORIN, *Magnetic Susceptibility of aFe2O3 and aFe2O3 with Added Titanium*, Physical Review **78**, 819 (1950).

[16] S. N. ABED, P. K. DEB, H. S. SURCHI, S. F. KOKAZ, S. M. JAMAL, S. BANDOPADHYAY, AND R. K. TEKADE, in *Basic Fundamentals of Drug Delivery*, Advances in Pharmaceutical Product Development and Research Ser, edited by R. K. Tekade (Elsevier Science & Technology, 2018) pp. 685–731.

[17] H. SHOKROLLAHI, *A review of the magnetic properties, synthesis methods and applications of maghemite*, Journal of Magnetism and Magnetic Materials **426**, 74 (2017).

[18] X. WANG, Y. LIAO, D. ZHANG, T. WEN, AND Z. ZHONG, *A review of Fe3O4 thin films: Synthesis, modification and applications*, Journal of Materials Science & Technology **34**, 1259 (2018).

[19] R. TAKAHASHI, Y. CHO, AND M. LIPPMAA, *Interfacial capacitance between a ferroelectric Fe 3 O 4 thin film and a semiconducting Nb:SrTiO 3 substrate*, Journal of Applied Physics **117**, 014104 (2015).

[20] W. KAISER, *Spinabhängiger Transport in Magnetit*, Master's thesis, TU Munich (2006).

[21] T. WIMMER, *Spin Transport in Magnetic Nanostructures*, Master's thesis, TU Munich (2016).

[22] M. JULLIERE, *Tunneling between ferromagnetic films*, Physics Letters A **54**, 225 (1975).

[23] F. D. CZESCHKA, *Spin Currents in Metallic Nanostructures*, PhD thesis, TU Munich (2011).

[24] R. GROSS, *Festkörperphysik*, 3rd ed., De Gruyter Studium Ser (De Gruyter Inc, 2018).

[25] J. SMIT, *The spontaneous hall effect in ferromagnetics II*, Physica **24**, 39 (1958).

[26] L. Berger, *Side-Jump Mechanism for the Hall Effect of Ferromagnets*, Physical Review B **2**, 4559 (1970).

[27] Di Xiao, M.-C. Chang, and Q. Niu, *Berry phase effects on electronic properties*, Reviews of Modern Physics **82**, 1959 (2010).

[28] M. Althammer, S. Meyer, H. Nakayama, M. Schreier, S. Altmannshofer, M. Weiler, H. Huebl, S. Geprägs, M. Opel, R. Gross, D. Meier, C. Klewe, T. Kuschel, J.-M. Schmalhorst, G. Reiss, L. Shen, A. Gupta, Y.-T. Chen, G. E. W. Bauer, E. Saitoh, and S. T. B. Goennenwein, *Quantitative study of the spin Hall magnetoresistance in ferromagnetic insulator/normal metal hybrids*, Physical Review B **87**, 224401 (2013).

[29] H. L. Wang, C. H. Du, Y. Pu, R. Adur, P. C. Hammel, and F. Y. Yang, *Scaling of spin Hall angle in 3d, 4d, and 5d metals from Y3Fe5O12/metal spin pumping*, Physical review letters **112**, 197201 (2014).

[30] Y.-T. Chen, S. Takahashi, H. Nakayama, M. Althammer, S. T. B. Goennenwein, E. Saitoh, and G. E. W. Bauer, *Theory of spin Hall magnetoresistance (SMR) and related phenomena*, Journal of Physics: Condensed Matter **28**, 103004 (2016).

[31] F. P. Witek, *Spin Hall Magnetoresistive Noise*, Masters's thesis, TU Munich (2013).

[32] L. J. Cornelissen, J. Liu, R. A. Duine, J. B. Youssef, and B. J. van Wees, *Long-distance transport of magnon spin information in a magnetic insulator at room temperature*, Nature Physics **11**, 1022 (2015).

[33] Y.-T. Chen, S. Takahashi, H. Nakayama, M. Althammer, S. T. B. Goennenwein, E. Saitoh, and G. E. W. Bauer, *Theory of spin Hall magnetoresistance*, Physical Review B **87**, 144411 (2013).

[34] S. A. Bender and Y. Tserkovnyak, *Interfacial spin and heat transfer between metals and magnetic insulators*, Physical Review B **91**, 140402 (2015).

[35] T. Wimmer, *Control and Manipulation of Magnonic Spin Currents in Magnetic Insulators*, PhD thesis, TU Munich (2021).

[36] R. Nathans, S. J. Pickart, H. A. Alperin, and P. J. Brown, *Polarized-Neutron Study of Hematite*, Physical Review **136**, A1641 (1964).

[37] J. C. Marmeggi, D. Hohlwein, and E. F. Bertaut, *Magnetic neutron laue diffraction study of the domain distribution in a-Fe2O3*, Physica Status Solidi (a) **39**, 57 (1977).

[38] E. Uchida, N. Fukuoka, H. Kondoh, T. Takeda, Y. Nakazumi, and T. Nagamiya, *Magnetic Anisotropy of Single Crystals of NiO and MnO*, Journal of the Physical Society of Japan **23**, 1197 (1967).

[39] E. V. Gomonay and V. M. Loktev, *On the theory of the formation of equilibrium domain structure in antiferromagnets*, Low Temperature Physics **30**, 804 (2004).

[40] H. V. Gomonay and V. M. Loktev, *Shape-induced phenomena in finite-size antiferromagnets*, Physical Review B **75**, 174439 (2007).

[41] X.-P. Zhang, F. S. Bergeret, and V. N. Golovach, *Theory of Spin Hall Magnetoresistance from a Microscopic Perspective*, Nano letters **19**, 6330 (2019).

[42] T. K. H. Pham, M. Ribeiro, J. H. Park, N. J. Lee, K. H. Kang, E. Park, Q. van Nguyen, A. Michel, C. S. Yoon, S. Cho, and T. H. Kim, *Interface morphology effect on the spin mixing conductance of Pt/Fe3O4 bilayers*, Scientific reports **8**, 13907 (2018).

[43] A. Haslberger, *Untersuchung des Spin Hall Magnetwiderstands in Spinell-basierten Heterostrukturen*, Bachelor's thesis, TU Munich (2020).

[44] O. Mauit, K. Fleischer, B. O'Dowd, D. Mullarkey, and I. V. Shvets, *Growth and characterization of epitaxial magnesium ferrite thin films*, Thin Solid Films **612**, 290 (2016).

[45] S. Singhal and K. Chandra, *Cation Distribution in Lithium Ferrite (LiFe5O8) Prepared via Aerosol Route*, Journal of Electromagnetic Analysis and Applications **02**, 51 (2010).

[46] C. G. Shull, W. A. Strauser, and E. O. Wollan, *Neutron Diffraction by Paramagnetic and Antiferromagnetic Substances*, Physical Review **83**, 333 (1951).

[47] M. Lübbe, *Präparation und magnetische Eigenschaften dünner Fe2O3- und FeTi1−xO3-Schichten auf Al2O3(0001)*, PhD thesis, Ludwig-Maximilians-Universität (2009).

[48] P. Villars and K. Cenzual, *a-Fe2O3 hematite (Fe2O3 hem) Crystal Structure: Datasheet from "PAULING FILE Multinaries Edition – 2012" in SpringerMaterials* ().

[49] G. W. van Oosterhout and C. J. M. Rooijmans, *A New Superstructure in Gamma-Ferric Oxide*, Nature **181**, 44 (1958).

[50] R. Dronskowski, *The Little Maghemite Story: A Classic Functional Material*, Advanced Functional Materials **11**, 27 (2001).

[51] A. H. Morrish, *Canted Antiferromagnetism: Hematite* (World Scientific, 1994).

[52] J. M. D. Coey, *Magnetism and magnetic materials*, repr ed. (Cambridge Univ. Press, 2013).

[53] P. J. Besser, A. H. Morrish, and C. W. Searle, *Magnetocrystalline Anisotropy of Pure and Doped Hematite*, Physical Review **153**, 632 (1967).

[54] Y. Bando, M. Kiyama, N. Yamamoto, T. Takada, T. Shinjo, and H. Takaki, *The Magnetic Properties of a-Fe 2 O 2 Fine Particles*, Journal of the Physical Society of Japan **20**, 2086 (1965).

[55] R. Grau-Crespo, A. Y. Al-Baitai, I. Saadoune, and N. H. de Leeuw, *Vacancy ordering and electronic structure of g-Fe2O3 (maghemite): a theoretical investigation*, Journal of Physics: Condensed Matter **22**, 255401 (2010).

[56] P. Villars and K. Cenzual, *g-Fe2O3 (Fe2O3 tet, T = 578 K) Crystal Structure: Datasheet from "PAULING FILE Multinaries Edition – 2012" in SpringerMaterials* ().

[57] M. Coduri, P. Masala, L. Del Bianco, F. Spizzo, D. Ceresoli, C. Castellano, S. Cappelli, C. Oliva, S. Checchia, M. Allieta, D.-V. Szabo, S. Schlabach, M. Hagelstein, C. Ferrero, and M. Scavini, *Local Structure and Magnetism of Fe2O3 Maghemite Nanocrystals: The Role of Crystal Dimension*, Nanomaterials (Basel, Switzerland) **10** (2020), 10.3390/nano10050867.

[58] R. Zboril, M. Mashlan, and D. Petridis, *Iron(III) Oxides from Thermal ProcessesSynthesis, Structural and Magnetic Properties, Mössbauer Spectroscopy Characterization, and Applications*, Chemistry of Materials **14**, 969 (2002).

[59] H. L. Andersen, B. A. Frandsen, H. P. Gunnlaugsson, M. R. V. Jørgensen, S. J. L. Billinge, K. M. Ø. Jensen, and M. Christensen, *Local and long-range atomic/magnetic structure of non-stoichiometric spinel iron oxide nanocrystallites*, IUCrJ **8**, 33 (2021).

[60] X. L. Huang, Y. Yang, and J. Ding, *Epitaxial growth of g-Fe2O3 thin films on MgO substrates by pulsed laser deposition and their properties*, Acta Materialia **61**, 548 (2013).

[61] P. Villars and K. Cenzual, *magnetite (Fe3O4 rt, T = 300 K) Crystal Structure: Datasheet from "PAULING FILE Multinaries Edition – 2012" in SpringerMaterials* ().

[62] K. Dehnicke, *Hollemann-Wiberg, Lehrbuch der Anorganischen Chemie. 101. Auflage. VonNils Wiberg. Walter de Gruyter, Berlin/New York, 1995. 2033 S., geb. 158.00 DM. ISBN 3–11–012641–9*, Angewandte Chemie **108**, 2696 (1996).

[63] D. Reisinger, P. Majewski, M. Opel, L. Alff, and R. Gross, *Hall effect, magnetization, and conductivity of Fe3O4 epitaxial thin films*, Applied Physics Letters **85**, 4980 (2004).

[64] A. Mitra, J. Mohapatra, S. S. Meena, C. V. Tomy, and M. Aslam, *Verwey Transition in Ultrasmall-Sized Octahedral Fe 3 O 4 Nanoparticles*, The Journal of Physical Chemistry C **118**, 19356 (2014).

[65] E. J. W. Verwey, *Electronic Conduction of Magnetite (Fe3O4) and its Transition Point at Low Temperatures*, Nature **144**, 327 (1939).

[66] M. S. Senn, J. P. Wright, and J. P. Attfield, *Charge order and three-site distortions in the Verwey structure of magnetite*, Nature **481**, 173 (2011).

[67] J.-X. Yin, Z.-G. Liu, S.-F. Wu, W.-H. Wang, W.-D. Kong, P. Richard, L. Yan, and H. Ding, *Unconventional magnetization of Fe 3 O 4 thin film grown on amorphous SiO 2 substrate*, AIP Advances **6**, 065111 (2016).

[68] Zhang and Satpathy, *Electron states, magnetism, and the Verwey transition in magnetite*, Physical review. B, Condensed matter **44**, 13319 (1991).

[69] J. Z. Liu, *Morin transition in hematite doped with iridium ions*, Journal of Magnetism and Magnetic Materials **54-57**, 901 (1986).

[70] J. Velev, A. Bandyopadhyay, W. H. Butler, and S. Sarker, *Electronic and magnetic structure of transition-metal-doped a -hematite*, Physical Review B **71**, 205208 (2005).

[71] U. Khan, A. Akbar, H. Yousaf, S. Riaz, and S. Naseem, *Ferromagnetic Properties of Al-doped Fe2O3 Thin Films by Sol-gel*, Materials Today: Proceedings **2**, 5415 (2015).

[72] S. Krehula, G. Štefanić, K. Zadro, L. Kratofil Krehula, M. Marciuš, and S. Musić, *Synthesis and properties of iridium-doped hematite (a-Fe2O3)*, Journal of Alloys and Compounds **545**, 200 (2012).

[73] P. Kumar, V. Sharma, J. P. Singh, A. Kumar, S. Chahal, K. Sachdev, K. H. Chae, A. Kumar, K. Asokan, and D. Kanjilal, *Investigations on magnetic and electrical properties of Zn doped Fe2O3 nanoparticles and their correlation with local electronic structures*, Journal of Magnetism and Magnetic Materials **489**, 165398 (2019).

[74] J. Ning, P. Shi, M. Jiang, C. Liu, and X. Li, *Effect of Ce Doping on the Structure and Chemical Stability of Nano-a-Fe2O3*, Nanomaterials (Basel, Switzerland) **9**, 1039 (2019).

[75] R. D. Shannon, *Revised effective ionic radii and systematic studies of interatomic distances in halides and chalcogenides*, Acta Crystallographica Section A **32**, 751 (1976).

[76] P. Villars and K. Cenzual, *Al2O3 Crystal Structure: Datasheet from "PAULING FILE Multinaries Edition – 2012" in SpringerMaterials* ().

[77] N. Shimomura, S. P. Pati, Y. Sato, T. Nozaki, T. Shibata, K. Mibu, and M. Sahashi, *Morin transition temperature in (0001)-oriented a-Fe 2 O 3 thin film and effect of Ir doping*, Journal of Applied Physics **117**, 17C736 (2015).

[78] K. Mibu, K. Mikami, M. Tanaka, R. Masuda, Y. Yoda, and M. Seto, *Thickness dependence of Morin transition temperature in iridium-doped hematite layers studied through nuclear resonant scattering*, Hyperfine Interactions **238** (2017), 10.1007/s10751-017-1470-2.

[79] S. Park, H. Jang, J.-Y. Kim, B.-G. Park, T.-Y. Koo, and J.-H. Park, *Strain control of Morin temperature in epitaxial a -Fe 2 O 3 (0001) film*, EPL (Europhysics Letters) **103**, 27007 (2013).

[80] H. Jani, J. Linghu, S. Hooda, R. V. Chopdekar, C. Li, G. J. Omar, S. Prakash, Y. Du, P. Yang, A. Banas, K. Banas, S. Ghosh, S. Ojha, G. R. Umapathy, D. Kanjilal, A. Ariando, S. J. Pennycook, E. Arenholz, P. G. Radaelli, J. M. D. Coey, Y. P. Feng, and T. Venkatesan, *Reversible hydrogen control of antiferromagnetic anisotropy in a-Fe2O3*, Nature communications **12**, 1668 (2021).

[81] S. Meyer, M. Althammer, S. Geprägs, M. Opel, R. Gross, and S. T. B. Goennenwein, *Temperature dependent spin transport properties of platinum inferred from spin Hall magnetoresistance measurements*, Applied Physics Letters **104**, 242411 (2014).

[82] Y. J. Zhou, X. Z. Chen, X. F. Zhou, H. Bai, R. Y. Chen, F. Pan, and C. Song, *A comparative study of spin Hall magnetoresistance in Fe 2 O 3 -based systems*, Journal of Applied Physics **127**, 163904 (2020).

[83] P. Villars and K. Cenzual, *MgO Crystal Structure: Datasheet from "PAULING FILE Multinaries Edition – 2012" in SpringerMaterials* ().

[84] S. Alraddadi, *The Electronic and Magnetic Properties of Ultrathin g-Fe 2 O 3 Films*, IOP Conference Series: Materials Science and Engineering **842**, 012012 (2020).

[85] A. Nielsen, *Magnetit - ein Material für die Spinelektronik*, PhD thesis, TU Munich (2009).

[86] S. Geprägs, S. Meyer, S. Altmannshofer, M. Opel, F. Wilhelm, A. Rogalev, R. Gross, and S. T. B. Goennenwein, *Investigation of induced Pt magnetic polarization in Pt/Y 3 Fe 5 O 12 bilayers*, Applied Physics Letters **101**, 262407 (2012).

[87] E. Popova, N. Keller, F. Jomard, L. Thomas, M.-C. Brianso, F. Gendron, M. Guyot, and M. Tessier, *Exchange coupling in ultrathin epitaxial yttrium iron garnet films*, The European Physical Journal B - Condensed Matter **31**, 69 (2003).

[88] J. Gückelhorn, T. Wimmer, M. Müller, S. Geprägs, H. Hübl, R. Gross, and M. Althammer, *Magnon transport in Y3Fe5O12/Pt nanostructures with reduced effective magnetization* (06.08.2021).

[89] T. Wimmer, M. Althammer, L. Liensberger, N. Vlietstra, S. Geprägs, M. Weiler, R. Gross, and H. Huebl, *Spin Transport in a Magnetic Insulator with Zero Effective Damping*, Physical review letters **123**, 257201 (2019).

[90] G. Woltersdorf, M. Kiessling, G. Meyer, J.-U. Thiele, and C. H. Back, *Damping by slow relaxing rare earth impurities in Ni80Fe20*, Physical review letters **102**, 257602 (2009).

[91] H. T. Nembach, T. J. Silva, J. M. Shaw, M. L. Schneider, M. J. Carey, S. Maat, and J. R. Childress, *Perpendicular ferromagnetic resonance measurements of damping and Landé g− factor in sputtered (Co_2Mn)_1xGe_x thin films*, Physical Review B **84**, 054424 (2011).

[92] M. Haertinger, C. H. Back, J. Lotze, M. Weiler, S. Geprägs, H. Huebl, S. T. B. Goennenwein, and G. Woltersdorf, *Spin pumping in YIG/Pt bilayers as a function of layer thickness*, Physical Review B **92**, 054437 (2015).

[93] I. Knittel, J. Wei, Y. Zhou, S. K. Arora, I. V. Shvets, M. Luysberg, and U. Hartmann, *Observation of antiferromagnetic coupling in epitaxial ferrite films*, Physical Review B **74**, 132406 (2006).

[94] S. Geprägs, C. Klewe, S. Meyer, D. Graulich, F. Schade, M. Schneider, S. Francoual, S. P. Collins, K. Ollefs, F. Wilhelm, A. Rogalev, Y. Joly, S. T. B. Goennenwein, M. Opel, T. Kuschel, and R. Gross, *Static magnetic proximity effects and spin Hall magnetoresistance in Pt/Y3Fe5O12 and inverted Y3Fe5O12/Pt bilayers*, Physical Review B **102**, 214438 (2020).

[95] M. G. Chapline and S. X. Wang, *Observation of the Verwey transition in thin magnetite films*, Journal of Applied Physics **97**, 123901 (2005).

[96] R. R. Birss, *Symmetry and magnetism* (North-Holland Publishing Company, 1964).

[97] W. Limmer, M. Glunk, J. Daeubler, T. Hummel, W. Schoch, R. Sauer, C. Bihler, H. Huebl, M. S. Brandt, and S. T. B. Goennenwein, *Angle-dependent magnetotransport in cubic and tetragonal ferromagnets: Application to (001)- and (113)A - oriented (Ga,Mn)As*, Physical Review B **74**, 205205 (2006).

[98] Z. Ding, B. L. Chen, J. H. Liang, J. Zhu, J. X. Li, and Y. Z. Wu, *Spin Hall magnetoresistance in Pt/Fe3O4 thin films at room temperature*, Physical Review B **90**, 134424 (2014).

[99] R. N. Bhowmik, G. Vijayasri, and A. K. Sinha, *Study of magnetic field induced spin order in diluted antiferromagnetic states in a Ga doped a-Fe 2 O 3 system prepared by a chemical route and air annealing*, RSC Advances **6**, 112960 (2016).

[100] A. G. Lone and R. N. Bhowmik, *Effect of magnetic spins flipping process on the dielectric properties of a -Fe 1.6 Ga 0.4 O 3 system*, AIP Advances **5**, 047117 (2015).

[101] M. Sharmin and J. Podder, *Influence of Al doping on the structure and properties of Fe 2 O 3 thin films: high transparency, wide band gap, ferromagnetic behavior*, Semiconductor Science and Technology **34**, 075033 (2019).

[102] R. N. Bhowmik, G. Vijayasri, and R. Ranganathan, *Structural characterization and ferromagnetic properties in Ga 3+ doped a-Fe 2 O 3 system prepared by coprecipitation route and vacuum annealing*, Journal of Applied Physics **116**, 123905 (2014).

[103] Arturas Vailionis, *Introduction to Experimental X-ray Diffraction Techniques*.

[104] M. R. Anantharaman, K. A. Malini, P. D. Sindhu, S. Sindhu, and H. V. Keer, *Influence of dopants on the properties of maghemite*, Indian Journal of Pure & Applied Physics **37**, 842 (1999).

[105] T. Wimmer, A. Kamra, J. Gückelhorn, M. Opel, S. Geprägs, R. Gross, H. Huebl, and M. Althammer, *Observation of Antiferromagnetic Magnon Pseudospin Dynamics and the Hanle Effect*, Physical review letters **125**, 247204 (2020).

[106] T. Nozaki, S. P. Pati, Y. Shiokawa, M. Suzuki, T. Ina, K. Mibu, M. Al-Mahdawi, S. Ye, and M. Sahashi, *Identifying valency and occupation sites of Ir dopants in antiferromagnetic a-Fe 2 O 3 thin films with X-ray absorption fine structure and Mössbauer spectroscopy*, Journal of Applied Physics **125**, 113903 (2019).

[107] F. M. Schade, *Fabrication and Characterization of Y3Fe5O12|Pt|Y3Fe5O12 Trilayers for Spin Current Based Experiments*, Bachelor's thesis, TU Munich (2013).

[108] M. Opel, S. Geprägs, M. Althammer, T. Brenninger, and R. Gross, *Laser molecular beam epitaxy of ZnO thin films and heterostructures*, Journal of Physics D: Applied Physics **47**, 034002 (2014).

[109] M. Opel, *Spintronic oxides grown by laser-MBE*, Journal of Physics D: Applied Physics **45**, 033001 (2012).

[110] K.-W. Nielsen, *Ursache der magnetischen Kopplung in Kobalt-dotiertem ZnO*, PhD thesis, TU Munich (2007).

[111] M. Dietlein, *Spin Seebeck effect: a powerful probe for magnon properties in compensated ferrimagnets*, Master's thesis, TU Munich (2020).

[112] J. B. Nelson and D. P. Riley, *An experimental investigation of extrapolation methods in the derivation of accurate unit-cell dimensions of crystals*, Proceedings of the Physical Society **57**, 160 (1945).

[113] L. Flacke, *Spin-Pumping and Spin Wave Damping in Co25Fe75 Thin-Film Heterostructures*, Master's thesis, TU Munich (2018).

[114] T. L. Gilbert, *Classics in Magnetics A Phenomenological Theory of Damping in Ferromagnetic Materials*, IEEE Transactions on Magnetics **40**, 3443 (2004).

[115] C. Kittel, *On the Theory of Ferromagnetic Resonance Absorption*, Physical Review **73**, 155 (1948).

[116] T. D. Rossing, *Resonance Linewidth and Anisotropy Variation in Thin Films*, Journal of Applied Physics **34**, 995 (1963).

[117] H. Maier-Flaig, S. T. B. Goennenwein, R. Ohshima, M. Shiraishi, R. Gross, H. Huebl, and M. Weiler, *Note: Derivative divide, a method for the analysis of broadband ferromagnetic resonance in the frequency domain*, The Review of scientific instruments **89**, 076101 (2018).

[118] L. Liensberger, *Magnon Hybrid Dynamics*, PhD thesis, TU Munich (2021).

[119] R. Gross and A. Marx, *Lecture Notes on Spinelectronics*.

[120] T. McGuire and R. Potter, *Anisotropic magnetoresistance in ferromagnetic 3d alloys*, IEEE Transactions on Magnetics **11**, 1018 (1975).

Acknowledgements

I would like to thank several people who contributed to this master thesis and supported me during my time at the Walther-Meißner-Institut:

First of all, Prof. Gross for giving me the opportunity to write my master's thesis at the WMI.

My advisor Dr. Stephan Geprägs, who invested a lot of time in the careful proofreading of this thesis. I would also like to thank you, Steve, for the detailed and interesting discussions about the measurement data and the resulting new ideas on how to interpret them. Besides answering all the questions I had, you helped me a lot, when things went wrong in the lab and cheered me up.

Manuel Müller, who performed and evaluated the bbFMR and AFM measurements presented in this thesis. I also thank Janine Gückelhorn for showing me the atomic force microscope.

Philipp Schwenke for explaining me the EVAP and the laserwriter. In addition, I would like to thank Elisabeth Meidinger, Niklas Bruckmoser and Leonhard Hölscher for helping me with problems concerning the laserwriter.

Andreas Haslberger for his support as a working student - specifically, for the fabrication of several samples and their preparation for ADMR measurements.

My (former) office colleagues Elisabeth Meidinger, Christopher Waas, Korbinian Rubenbauer and Philipp Krüger, for the productive working atmosphere, the many sweets and the interesting conversations in between - and of course for the open ear when lab and writing frustration arose now and then. In particular, I would like to thank Elisabeth for her constant support on a personal level and Philipp for his funny life stories. I also thank Lukas Vetter, who never sat in our office but was always interested in my writing progress.

The master students sitting in room 128, including Ramona Stumberger, Niklas Bruckmoser, Leonhard Hölscher, Philipp Schwenke, Matthias Grammer, Mayank Sharma, Johannes Schirk and Max Nägele for all the funny moments, the "Weißwurstfrühstück", the ice cream and lunch breaks and all the cake. I also thank Niklas and Ramona for the interesting conversations in my office and the last minute LaTeX hacks to complete this thesis.

Thomas Brenninger for the technical support in the PLD lab and Astrid Habel for making the polycrystalline targets.

All other unnamed people of the WMI for the friendly working atmosphere and the constant help.

My family for their financial support and my friends for the funny times inside and outside of university life.

My boyfriend for his emotional support and the time we had together during the bachelor's and master's studies with all the ups and downs that it brought. Most of all, I want to thank you, Fabi, for always believing in me and helping me in stressful times. I also want to thank your family for their constant interest in my work.